MMNSA

Mathematical Modelling and Numerical Simulation with Applications

ISSN Online : 2791-8564

Year : 2024

Volume : 4

Issue : 3

https://dergipark.org.tr/en/pub/mmnsa

Editor-in-Chief
Mehmet Yavuz, PhD

VOLUME: 4 ISSUE: 3
ISSN ONLINE: 2791-8564

September 2024
https://dergipark.org.tr/en/pub/mmnsa

MATHEMATICAL MODELLING AND NUMERICAL SIMULATION WITH APPLICATIONS

Editor-in-Chief and Publisher

Mehmet Yavuz
Department of Mathematics and Computer Sciences,
Faculty of Science, Necmettin Erbakan University,
Meram Yeniyol, 42090 Meram, Konya / TÜRKİYE
mehmetyavuz@erbakan.edu.tr

Associate Editors (In Alphabetical Order)

Editorial Board Members (In Alphabetical Order)

Scientific Managing Editor

Technical Editor

English Editors (In Alphabetical Order)

Editorial Secretariat

Contents

Research Articles

1 Optimizing tuberculosis control: a comprehensive simulation of integrated interventions using a mathematical model
Olumuyiwa James Peter, Afeez Abidemi, Fatmawati Fatmawati, Mayowa M. Ojo, Festus Abiodun Oguntolu **238-255**

2 A three-dimensional discrete fractional-order HIV-1 model related to cancer cells, dynamical analysis and chaos control
Haneche Nabil, Tayeb Hamaizia **256-279**

3 Mathematical model for IP_3 dependent calcium oscillations and mitochondrial associate membranes in non-excitable cells
Neeraj Manhas **280-295**

4 Mathematical analysis of Ebola considering transmission at treatment centres and survivor relapse using fractal-fractional Caputo derivatives in Uganda
Isaac Kwasi Adu, Fredrick Asenso Wireko, Samuel Akwasi Adarkwa, Gerald Ohene Agyekum **296-334**

5 Column generation approach for 1.5-dimensional cutting stock problem with technical constraints
Müjgan Sağır, Tuğba Saraç **335-350**

6 A multi-step mathematical model-based predictive strategy for software release timing during testing stage
Poonam Panwar, Satish Kumar, Shkauntla Singla, Yeliz Karaca **351-369**

7 A seismic-risk-based bi-objective stochastic optimization framework for the pre-disaster allocation of earthquake search and rescue units
Nadi Serhan Aydın **370-394**

Mathematical Modelling and Numerical Simulation with Applications, 2024, 4(3), 238–255

https://dergipark.org.tr/en/pub/mmnsa
ISSN Online: 2791-8564 / Open Access
https://doi.org/10.53391/mmnsa.1461011

RESEARCH PAPER

Optimizing tuberculosis control: a comprehensive simulation of integrated interventions using a mathematical model

Olumuyiwa James Peter [1,2,3,‡], **Afeez Abidemi** [4,‡], **Fatmawati Fatmawati** [3,*,‡], **Mayowa M. Ojo** [5,‡] **and Festus Abiodun Oguntolu** [6,‡]

[1]Department of Mathematical and Computer Sciences, University of Medical Sciences, Ondo City, Ondo State, Nigeria, [2]Department of Epidemiology and Biostatistics, School of Public Health, University of Medical Sciences, Ondo City, Ondo State, Nigeria, [3]Department of Mathematics, Faculty of Science and Technology, Universitas Airlangga, Surabaya 60115, Indonesia, [4]Department of Mathematical Sciences, Federal University of Technology, Akure, Ondo State, Nigeria, [5]Department of Mathematical Sciences, University of South Africa, Florida, South Africa, [6]Department of Mathematics, Federal University of Technology, P.M.B 65 Minna, Nigeria

* Corresponding Author
‡ peterjames4real@gmail.com (Olumuyiwa James Peter); aabidemi@futa.edu.ng (Afeez Abidemi); fatmawati@fst.unair.ac.id (Fatmawati Fatmawati); mmojomth@gmail.com (Mayowa M. Ojo); festus.tolu@futminna.edu.ng (Festus Abiodun Oguntolu)

Abstract

Tuberculosis (TB) remains a formidable global health challenge, demanding effective control strategies to alleviate its burden. In this study, we introduce a comprehensive mathematical model to unravel the intricate dynamics of TB transmission and assess the efficacy and cost-effectiveness of diverse intervention strategies. Our model meticulously categorizes the total population into seven distinct compartments, encompassing susceptibility, vaccination, diagnosed infectious, undiagnosed infectious, hospitalized, and recovered individuals. Factors such as susceptible individual recruitment, the impact of vaccination, immunity loss, and the nuanced dynamics of transmission between compartments are considered. Notably, we compute the basic reproduction number, providing a quantitative measure of TB transmission potential. Through this comprehensive model, our study aims to offer valuable insights into optimal control measures for TB prevention and control, contributing to the ongoing global efforts to combat this pressing health challenge.

Keywords: Tuberculosis; basic reproduction number; drug resistance; preventive strategies

AMS 2020 Classification: 37M05; 37N25; 92B05; 92C60

➤ **Received:** 29.03.2024 ➤ **Revised:** 06.07.2024 ➤ **Accepted:** 15.07.2024 ➤ **Published:** 30.09.2024

1 Introduction

Tuberculosis (TB) is a highly infectious disease caused by the bacterium Mycobacterium tuberculosis. It primarily affects the lungs but can also target other organs such as the kidneys, spine, and brain. TB is a significant global health concern, with a long history of affecting humanity. Despite the advances in healthcare, it remains a major cause of morbidity and mortality worldwide. In this introduction, we will provide an overview of the epidemiology of tuberculosis, including disease burden, transmission, symptoms, and control measures [1, 2].

Tuberculosis is one of the top 10 causes of death worldwide, accounting for significant morbidity and mortality. According to the World Health Organization (WHO), in 2020, an estimated 10 million people fell ill with TB, and 1.5 million died from the disease. Approximately 95% of TB deaths occur in low- and middle-income countries, with sub-Saharan Africa and Asia bearing the highest burden. The disease disproportionately affects vulnerable populations, such as those living with HIV, malnourished individuals, and those with compromised immune systems. TB is primarily transmitted through the air when an infected individual coughs, sneezes, speaks, or sings, releasing droplets containing the bacteria. People in close contact with an active TB patient, especially in crowded and poorly ventilated settings, are at higher risk of contracting the infection. It is worth noting that not everyone exposed to the bacteria becomes infected. Factors such as the infectiousness of the source case, duration of exposure, proximity, and individual immunity contribute to the likelihood of transmission [3, 4].

The clinical presentation of TB can vary depending on the site of infection and the individual's immune response. Pulmonary tuberculosis, the most common form, often presents with symptoms such as persistent cough, chest pain, weight loss, fatigue, night sweats, and hemoptysis (coughing up blood). Extra-pulmonary TB can affect various organs, leading to symptoms specific to those sites. However, some individuals may remain asymptomatic, referred to as latent TB infection, with no signs of active disease but carrying the bacteria and being at risk of developing active TB in the future [5, 6]. The control of TB relies on a comprehensive approach that includes early detection, prompt treatment, and preventive interventions. Key strategies involve active case finding through targeted screening and improved diagnostic techniques. The introduction of GeneXpert and other rapid molecular tests has greatly enhanced the detection of TB and drug-resistant strains. Treatment primarily consists of a combination of antibiotics administered over a specified duration to ensure a cure and prevent the emergence of drug resistance. Furthermore, preventive measures such as isoniazid preventive therapy (IPT) for individuals with latent TB infection and Bacillus Calmette-Guérin (BCG) vaccination in certain populations have demonstrated efficacy in reducing the risk of TB transmission and progression. Strengthening health systems, ensuring access to quality healthcare services, and addressing social determinants of TB are critical for effective control and elimination efforts [7, 8]. Mathematical models have become valuable tools in understanding the dynamics and control of tuberculosis (TB) epidemics. These models provide insights into the complex interactions between various factors involved in TB transmission, the impact of control measures, and the potential outcomes of different interventions. This introduction discusses the existing mathematical models used to study TB, highlighting their contributions and key findings. In recent years, numerous studies have utilized mathematical models to explore effective strategies for disease control within populations [9–23]. Within the realm of tuberculosis, several models have been developed and investigated to enhance our understanding of transmission dynamics and control measures [24–28]. For instance, Yang et al. [24] explored the role of partial therapy in tuberculosis transmission, shedding light on its implications. Zhang et al. [25] studied a dynamical tuberculosis model that considered both infected and non-infected compartments. Egonmwan and Daniel developed a model to determine

the rate of treatment and its impact on infected individuals, [26]. Investigations into the stability of tuberculosis with partial treatment were conducted by Ullah et al. [27]. Additionally, Intan et al. [28] investigated tuberculosis transmission by incorporating a latent group and assessing the effects of vaccine administration. While these deterministic models have provided valuable insights, there remains a gap in understanding the role of vaccination, contact rates, vaccine efficacy, and coverage rates in disease control. Vaccination has long been recognized as a highly effective preventive strategy against various diseases, including tuberculosis. It plays a crucial role in protecting populations from infection and reducing the potential for community-wide transmission. Therefore, considering these factors in disease modelling is essential for developing robust control strategies. Further contributions to the dynamics of tuberculosis models can be found in studies such as [29–37]. These investigations have expanded our knowledge of TB dynamics, including the disease's global stability and the impact of heterogeneity on its dispersion. In this study, we aim to address the aforementioned research gap by developing a mathematical model for tuberculosis that incorporates vaccination, contact rates, vaccine efficiency, and coverage rates. By considering these factors, we can gain a more comprehensive understanding of the dynamics and control of tuberculosis in the population and ultimately contribute to the development of effective strategies for disease prevention and control. The novelty of this study lies in the comprehensive integration of various epidemiological factors within a structured compartmental model for Tuberculosis (TB) transmission. Specifically, the model incorporates detailed compartments representing vaccinated individuals, diagnosed and undiagnosed infectious cases, exposed individuals, hospitalizations, and recovered individuals. This granularity allows for a nuanced analysis of TB dynamics, considering the different states of infection and treatment. Additionally, the study introduces the concept of immunity loss in vaccinated individuals over time, providing a realistic perspective on the long-term efficacy of TB vaccination programs. The differentiation between diagnosed and undiagnosed cases, along with the varying progression rates between these states and the hospitalization phase, adds complexity to the model, making it more reflective of real-world scenarios. Furthermore, the consideration of distinct death rates for diagnosed and undiagnosed infectious individuals, along with additional disease-induced mortality in the hospitalized class, adds a layer of realism to the outcomes of the model. Overall, the study's novelty lies in its detailed and multifaceted approach, capturing the complexities of TB transmission, vaccination dynamics, and disease progression, which provides a robust foundation for understanding and potentially optimizing TB control strategies.

2 Model formulation

In this section, we develop a new model that describes the disease transmission between each compartment based on the health status of individuals in the population under consideration. In the present work, we consider seven distinct populations. $S(t)$ represents susceptible individuals not exposed to TB infection, $V(t)$ represents vaccinated individuals against TB infection, $E(t)$ exposed individuals to TB infection but not infectious, I_D represents diagnosed infectious individuals, those in this category have been infected with TB and diagnosed in the hospital. I_U undiagnosed infectious, those in this class have been infected with TB but not diagnosed in the hospital. $H(t)$ represent the hospitalised class and $R(t)$ represents recovered individuals. The susceptible population is increased due to the daily recruitment rate Π, susceptible individuals received vaccination against TB infection at a constant rate ρ, and lose immunity at a rate τ. We assume that individuals vaccinated against TB infection lose immunity after a period of time and can be infected after effective contact with diagnosed and undiagnosed infectious individuals at a reduced rate of 1-ε so that the force of infection for the vaccinated individuals is at the rate $\beta(1-\varepsilon)(zI_D + I_U + zH)V$ where z represent the reduction in the infection rate in undiagnosed infectious individuals. We

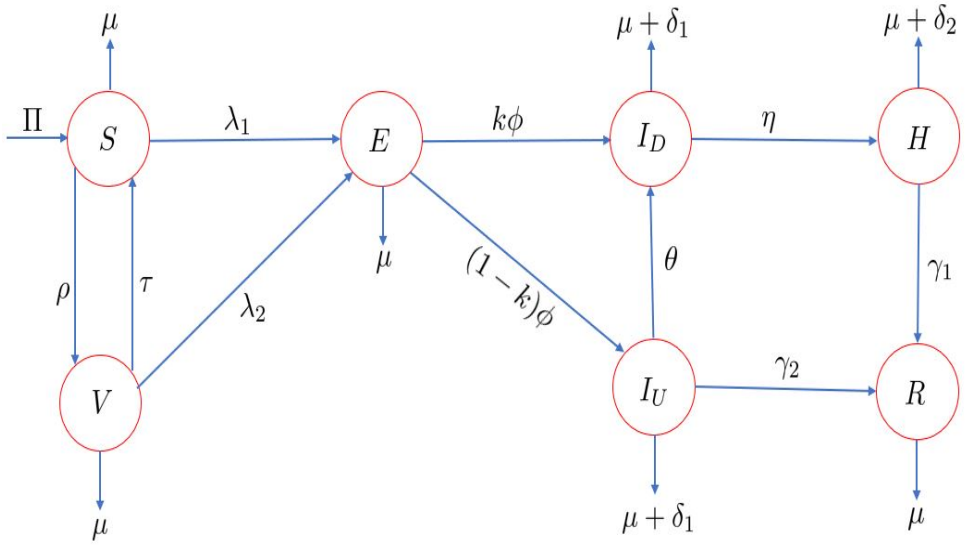

Figure 1. Schematic illustration of the TB model. For illustration suitability, we defined $\lambda_1 = \beta(zI_D + I_U + zH)$ and $\lambda_2 = \beta(1-\varepsilon)(zI_D + I_U + zH)$

also assume that only diagnosed, undiagnosed and hospitalised individuals can transfer the infection, thus, the force of infection is given as $\beta(1-\varepsilon)(zI_D + I_U + zH)S$. There is a fraction k of individuals who are diagnosed with TB and $1-k$ undiagnosed, where ϕ is the progression rate to infectious, θ represent progression rate from undiagnosed class to diagnosed infectious class, η the progression rate from diagnosed infectious to hospitalised class. Individuals in the hospitalised class recover through hospital treatment at a rate γ_1 and γ_2 represent the natural recovery rate of individuals in the undiagnosed class. The parameter μ represents the natural death rate in all the compartments, we assume that the disease-induced death rates in I_U and I_D occur at equal rates δ_1, while additional death due to the disease occurs in H at a rate δ_2 with $\delta_1 > \delta_2$.
The above illustration gives a clear picture of the disease dynamics and this can also be represented in a system differential equations in (1), while the model's compartmental flow diagram is shown in Figure 1. Moreover, the description of model variables (compartments) are given in Table 1.

$$
\begin{aligned}
\frac{dS}{dt} &= \Pi + \tau V - \beta S(zI_D + I_U + zH) - (\mu + \rho)S,\\
\frac{dV}{dt} &= \rho S - \beta(1-\varepsilon)(zI_D + I_U + zH) - (\mu + \tau)V,\\
\frac{dE}{dt} &= \beta S(zI_D + I_U + zH) + \beta(1-\varepsilon)(zI_D + I_U + zH)V - (\phi + \mu)E,\\
\frac{dI_D}{dt} &= k\phi E + \theta I_U - (\mu + \delta_1 + \eta)I_D,\\
\frac{dI_U}{dt} &= (1-k)\phi E - (\theta + \mu + \delta_1 + \gamma_2)I_U,\\
\frac{dH}{dt} &= \eta I_D - (\mu + \delta_2 + \gamma_1)H,\\
\frac{dR}{dt} &= \gamma_2 I_U + \gamma_1 H - \mu R.
\end{aligned}
\tag{1}
$$

Table 1. Description of the model variables

Variable	Description
S	Susceptible class
V	Vaccinated class
E	Exposed humans
I_D	Diagnosed infectious class
I_U	Undiagnosed infectious class
H	Hospitalised class
R	Recovered class

3 Model analysis

Fundamental properties of the TB model

It should be noted that all the parameters used for the TB model are non-negative since the model depicts human population dynamics. On this note, it is called to show that all the seven state variables of the proposed model are non-negative at all times.

Positivity and boundedness of solutions

It is easy to show that, from the first differential equation of model (1), the differential inequality in (2) is satisfied

$$\frac{dS}{dt} + [\beta(zI_D + I_U + zH) + (\rho + \mu)]S > 0. \tag{2}$$

The integrating factor related to the differential inequality (2) is

$$\exp\left\{(\rho+\mu)t + \int_0^t (\beta(I_D(\tilde{w}) + zI_U(\tilde{w}) + H(\tilde{w}))d\tilde{w})\right\}.$$

The use of this integrating factor in (2) leads to

$$\frac{d}{dt}\left[S(t)\exp\left\{-[(\rho+\mu)t + \int_0^t (\beta(zI_D(\tilde{w}) + I_U(\tilde{w}) + zH(\tilde{w}))d\tilde{w})]\right\}\right] > 0,$$

so that

$$S(t) \geq S(0)\exp\left\{-[(\rho+\mu)t + \int_0^t (\beta(zI_D(\tilde{w}) + I_U(\tilde{w}) + zH(\tilde{w}))d\tilde{w})]\right\} > 0,$$

for all time time $t > 0$. The other six state variables V, E, I_D, I_U, H and R can be shown using a similar approach. Thus, the solution set $\{S, V, E, I_D, I_U, H, R\}$ is non-negative for all time t. This leads to claiming the following result:

Theorem 1 *Every solutions of the TB model* (1)*, expressed by the set* $\{S, V, E, I_D, I_U, H, R\}$*, with non-negative initial conditions* $S(0)$*,* $V(0)$*,* $E(0)$*,* $I_D(0)$*,* $I_U(0)$*,* $H(0)$*,* $R(0)$*, remain non-negative for all time* $t > 0$*.*

Moreover, it is sufficient to analyze the transmission dynamics of TB described by model (1) in a biologically feasible region defined by

$$\Psi = \left\{(S, V, E, I_D, I_U, H, R) \in \mathbb{R}_+^7 : S + V + E + I_D + I_U + H + R \leq \frac{\Pi}{\mu}\right\}. \tag{3}$$

Following the ideas of the authors in [38–45], we can demonstrate that the region Ψ in (3) is non-negative invariant. Thus, the solution of the model is contained in the region Ψ meaning that the proposed TB model is well-posed.

Existence and stability analysis of equilibria

TB model (1) is rigorously analyzed with respect to the equilibrium points in this part. At steady state, the TB model (1) becomes

$$\begin{aligned}
&\Pi + \tau V - \beta S(zI_D + I_U + zH) - m_1 S = 0,\\
&\rho S - m_2 V - \beta(1-\varepsilon)(zI_D + I_U + zH)V = 0,\\
&\beta S(zI_D + I_U + zH) + \beta(1-\varepsilon)(zI_D + I_U + zH)V - m_3 E = 0,\\
&k\phi E + \theta I_U - m_4 I_D = 0,\\
&(1-k)\phi E - m_5 I_U = 0,\\
&\eta I_D - m_6 H = 0,\\
&\gamma_2 I_U + \gamma_1 H - \mu R = 0,
\end{aligned} \tag{4}$$

where $m_1 = (\mu + \rho)$, $m_2 = (\mu + \tau)$, $m_3 = (\phi + \mu)$, $m_4 = (\mu + \delta_1 + \eta)$, $m_5 = (\theta + \mu + \delta_1 + \gamma_2)$, and $m_6 = (\mu + \delta_2 + \gamma_1)$.

Disease-free equilibrium

The disease-free equilibrium (DFE) of the TB model (1) is obtained by setting $E = I_D = I_U = H = 0$ in system (4). Thus, DFE, denoted by Ω_1, of model (1) is given by

$$\Omega_1 = (S^*, V^*, E^*, I_D^*, I_U^*, H^*, R^*) = \left(\frac{m_2\Pi}{\mu(\rho+\tau+\mu)}, \frac{\rho\Pi}{\mu(\rho+\tau+\mu)}, 0, 0, 0, 0, 0\right). \tag{5}$$

Effective reproduction number

To calculate the effective (or control) reproduction number of model (1), the popular next-generation operator method and notation studied in depth by [46] is employed. Assume that $x = \{E, I_D, I_U, H\}$ is the set of infected compartments. Then, the subsystem describing the dynamics of these compartments is extracted from the TB model (1), and is given by

$$\begin{aligned}
\frac{dE}{dt} &= \beta S(zI_D + I_U + zH) + \beta(1-\varepsilon)(zI_D + I_U + zH)V - (\phi + \mu)E,\\
\frac{dI_D}{dt} &= k\phi E + \theta I_U - (\mu + \delta_1 + \eta)I_D,\\
\frac{dI_U}{dt} &= (1-k)\phi E - (\theta + \mu + \delta_1 + \gamma_2)I_U,\\
\frac{dH}{dt} &= \eta I_D - (\mu + \delta_2 + \gamma_1)H.
\end{aligned} \tag{6}$$

It follows from (6) that

$$\frac{dx}{dt} = \mathcal{F} - \mathcal{V},$$

where

$$\mathcal{F} = \begin{bmatrix} \beta S(zI_D + I_U + zH) + \beta(1-\varepsilon)V(zI_D + I_U + zH) \\ 0 \\ 0 \\ 0 \end{bmatrix}, \tag{7}$$

and

$$\mathcal{V} = \begin{bmatrix} m_3 E \\ m_4 I_D - \kappa\phi E - \theta I_U \\ m_5 I_U - (1-\kappa)\phi E \\ m_6 H - \eta I_D \end{bmatrix}. \tag{8}$$

From (7), the matrix F of new infection terms is derived as

$$F = \begin{pmatrix} 0 & \frac{\beta[m_2+(1-\varepsilon)\rho]\Pi}{\mu(\rho+\tau+\mu)} & \frac{z\beta[m_2+(1-\varepsilon)\rho]\Pi}{\mu(\rho+\tau+\mu)} & \frac{\beta[m_2+(1-\varepsilon)\rho]\Pi}{\mu(\rho+\tau+\mu)} \\ 0 & 0 & 0 & 0 \\ 0 & 0 & 0 & 0 \\ 0 & 0 & 0 & 0 \end{pmatrix}.$$

Similarly, the matrix V of the transition terms and its inverse V^{-1} are obtained from (8) as

$$V = \begin{pmatrix} m_3 & 0 & 0 & 0 \\ -\kappa\phi & m_4 & -\theta & 0 \\ -(1-\kappa)\phi & 0 & m_5 & 0 \\ 0 & -\eta & 0 & m_6 \end{pmatrix},$$

$$V^{-1} = \begin{pmatrix} \frac{1}{m_3} & 0 & 0 & 0 \\ \frac{\phi(m_5\kappa+\theta(1-\kappa))}{m_3m_4m_5} & \frac{1}{m_4} & \frac{\theta}{m_4m_5} & 0 \\ \frac{(1-\kappa)\phi}{m_3m_5} & 0 & \frac{1}{m_5} & 0 \\ \frac{\eta\phi(m_5\kappa+\theta(1-\kappa))}{m_3m_4m_5m_6} & \frac{\eta}{m_4m_6} & \frac{\eta\theta}{m_4m_5m_6} & \frac{1}{m_6} \end{pmatrix}.$$

Thus,

$$\mathcal{R}_e = G\left(FV^{-1}\right) = \frac{\beta\phi\Pi[m_2+(1-\varepsilon)\rho]\{m_6[m_5\kappa+\theta(1-\kappa)]+zm_4m_6(1-\kappa)+\eta[m_5\kappa+\theta(1-\kappa)]\}}{m_3m_4m_5m_6\mu(\rho+\tau+\mu)}, \tag{9}$$

where G represents the spectral radius of the next generation matrix FV^{-1}. Following Theorem 2 in [46], the result in Lemma 1 holds which states that: The disease-free equilibrium, Ω_1, of the TB model (1) is locally asymptotically stable (LAS) in Ψ if $\mathcal{R}_e < 1$ and unstable if $\mathcal{R}_e > 1$.

Endemic equilibrium

Let the endemic equilibrium (EE) of the TB model (1) be defined by

$$\Omega_2 = (S^{**}, V^{**}, E^{**}, I_D^{**}, I_U^{**}, H^{**}, R^{**}). \tag{10}$$

Assume further that, in the steady state system (4), the force of infection at the endemic state is defined by

$$\lambda^{**} = \beta\left(zI_D^{**} + I_U^{**} + zH^{**}\right). \tag{11}$$

Then, solving the steady state system (4) with the hypothesis that $E \neq 0$, $I_D \neq 0$, $I_U \neq 0$, and $H \neq 0$, we obtain

$$\begin{aligned}
S^{**} &= \frac{\Pi[m_2 + (1-\varepsilon)\lambda^{**}]}{\{(\lambda^{**} + m_1)[m_2 + (1-\varepsilon)\lambda^{**}] - \rho\tau\}},\\
V^{**} &= \frac{\rho\Pi}{\{(\lambda^{**} + m_1)[m_2 + (1-\varepsilon)\lambda^{**}] - \rho\tau\}},\\
E^{**} &= \frac{\Pi\{[m_2 + (1-\varepsilon)\lambda^{**}] + (1-\varepsilon)\rho\}\lambda^{**}}{m_3\{(\lambda^{**} + m_1)[m_2 + (1-\varepsilon)\lambda^{**}] - \rho\tau\}},\\
I_D^{**} &= \frac{\Pi\phi[m_5\kappa + \theta(1-\kappa)]\{[m_2 + (1-\varepsilon)\lambda^{**}] + (1-\varepsilon)\rho\}\lambda^{**}}{m_3m_4m_5\{(\lambda^{**} + m_1)[m_2 + (1-\varepsilon)\lambda^{**}] - \rho\tau\}},\\
I_U^{**} &= \frac{\Pi(1-\kappa)\phi\{[m_2 + (1-\varepsilon)\lambda^{**}] + (1-\varepsilon)\rho\}\lambda^{**}}{m_3m_5\{(\lambda^{**} + m_1)[m_2 + (1-\varepsilon)\lambda^{**}] - \rho\tau\}},\\
H^{**} &= \frac{\Pi\phi\eta[m_5\kappa + \theta(1-\kappa)]\{[m_2 + (1-\varepsilon)\lambda^{**}] + (1-\varepsilon)\rho\}\lambda^{**}}{m_3m_4m_5m_6\{(\lambda^{**} + m_1)[m_2 + (1-\varepsilon)\lambda^{**}] - \rho\tau\}},\\
R^{**} &= \frac{\Pi\phi[m_4m_6(1-\kappa)\gamma_2 + \eta\gamma_1[m_5\kappa + \theta(1-\kappa)]]\{[m_2 + (1-\varepsilon)\lambda^{**}] + (1-\varepsilon)\rho\}\lambda^{**}}{m_3m_4m_5m_6\mu\{(\lambda^{**} + m_1)[m_2 + (1-\varepsilon)\lambda^{**}] - \rho\tau\}}.
\end{aligned} \tag{12}$$

Now, using the results of I_D^{**}, I_U^{**}, and H^{**} from (12) in the force of infection (11) and simplifying yields the quadratic equation satisfied by the endemic equilibria of the TB model (1), and is given by

$$n_1\left(\lambda^{**}\right)^2 + n_2\lambda^{**} + n_3 = 0, \tag{13}$$

where

$$\begin{aligned}
n_1 &= (1-\varepsilon)m_3m_4m_5m_6,\\
n_2 &= m_3m_4m_5m_6[m_2 + (1-\varepsilon)m_1]\\
&\quad -\beta(1-\varepsilon)\Pi\phi\{m_6[m_5\kappa + \theta(1-\kappa)] + zm_4m_6(1-\kappa) + \eta[m_5\kappa + \theta(1-\kappa)]\},\\
n_3 &= m_3m_4m_5m_6\mu(\rho + \tau + \mu)\left(1 - \mathcal{R}_e\right).
\end{aligned}$$

Thus, the endemic equilibrium Ω_2 of the TB model (1) is derived from (13) for a non-negative values of λ^{**} and substituting back into the components of Ω_2 in (12). Thus, to obtain the required solutions of (13), we arrive at the following assumptions: n_1 is always positive, while n_2 and n_3 may be positive or negative depending on the signs of $\mathcal{R}_e$. That is,

$$n_1 > 0, \quad n_2 = \begin{cases} > 0, \\ < 0, \end{cases} \quad \text{and} \quad n_3 = \begin{cases} > 0 & \text{if } \mathcal{R}_e < 1, \\ < 0 & \text{if } \mathcal{R}_e > 1. \end{cases} \tag{14}$$

From (14), the five cases below are obtained:

Case I: If $\mathcal{R}_e < 1$, then $n_3 > 0$ so that (13) has two non-negative roots when $n_2 < 0$.

Case II: If $\mathcal{R}_e < 1$, then $n_3 > 0$ so that (13) has no non-negative roots (2 negative roots) when $n_2 < 0$.

Case III: If $\mathcal{R}_e > 1$, then $n_3 < 0$ so that (13) has one non-negative root when $n_2 > 0$.

Case IV: If $\mathcal{R}_e > 1$, then $n_3 < 0$ so that (13) also has one non-negative root when $n_2 < 0$.

Case V: When $\mathcal{R}_e = 1$, Eq. (13) reduces to $(n_1\lambda^{**} + n_2)\,\lambda^{**} = 0$. The trivial solution $\lambda^{**} = 0$ coincides with the disease-free equilibrium Ω_1, while the non-trivial solution $\lambda^{**} = -\frac{n_2}{n_1}$ is a non-negative root when $n_2 < 0$ and negative root (which is meaningless in the biological sense) when $n_2 > 0$.

Consequently, the existence of the endemic equilibrium of model (1) is summarized as follows:

Theorem 2 *The TB model has:*

i. an endemic equilibrium provided that if $n_2 > 0$ or $n_2 < 0$ and $\mathcal{R}_e > 1$,
ii. double endemic equilibria provided that if $n_2 < 0$ and $\mathcal{R}_e < 1$,
iii. no endemic equilibrium otherwise whenever $\mathcal{R}_e < 1$.

The backward bifurcation has been studied subject to some TB models and those of other infectious diseases' dynamics (For more details, see [47–49]). It points to a possible coexistence of equilibria when the effective reproduction number is less than unity, in which case conditions of a backward bifurcation at a disease-free and endemic equilibrium condition are satisfied. To rule out this possibility and ensure the existence of a unique endemic equilibrium point for TB model (1), let the vaccine efficacy, denoted by ε, be set to 1. Hence, the quadratic equation (13) becomes

$$n_2\lambda^{**} + n_3 = 0, \tag{15}$$

so that $n_2 = m_2m_3m_4m_5m_6$, and $n_3 = m_3m_4m_5m_6\mu(\rho+\tau+\mu)\,(1-\mathcal{R}_e|_{\varepsilon=1})$, where

$$\mathcal{R}_e|_{\varepsilon=1} = \frac{\beta\Pi\phi m_2\{m_6[m_5\kappa+\theta(1-\kappa)] + zm_4m_6(1-\kappa) + \eta[m_5\kappa+\theta(1-\kappa)]\}}{m_3m_4m_5m_6\mu(\rho+\tau+\mu)}. \tag{16}$$

It can be seen that $n_2 > 0$ and $n_3 \geq 0$ whenever $\mathcal{R}_e|_{\varepsilon=1} \leq 1$. It follows from (15) that $\lambda^{**} = -\frac{n_3}{n_2} \leq 0$ at $\mathcal{R}_e|_{\varepsilon=1} \leq 1$. Therefore, the TB model (1), with $\varepsilon = 1$, has no positive (endemic) equilibrium at $\mathcal{R}_e|_{\varepsilon=1} \leq 1$. On the other hand, $n_3 < 0$ at $\mathcal{R}_e|_{\varepsilon=1} > 1$, so that $\lambda^{**} = -\frac{n_3}{n_2} > 0$. Thus, the TB model (1), with $\varepsilon = 1$, has a unique positive (endemic) equilibrium when $\mathcal{R}_e|_{\varepsilon=1} > 1$. This result is summarized as follows:

Theorem 3 *The TB model (1) in the absence of imperfect vaccine ($\varepsilon = 1$) has no endemic equilibrium whenever $\mathcal{R}_e|_{\varepsilon=1} \leq 1$, and a unique endemic equilibrium exists if $R_e|_{\varepsilon=1} > 1$.*

Global asymptotic dynamics of equilibria

Global stability of Ω_1

Theorem 4 *The given disease-free equilibrium Ω_1 in (5) of TB model (1) in the absence of imperfect vaccine ($\varepsilon = 1$) is globally asymptotically stable in the feasible region Ψ if $\mathcal{R}_e|_{\varepsilon=1} < 1$.*

Proof Consider the following Lyapunov functional $\mathbb{U}(E(t), I_D(t), I_U(t), H(t))$ for TB model (1) with $\varepsilon = 1$ defined by

$$\mathbb{U} = b_1E + b_2I_D + b_3I_U + b_4H, \tag{17}$$

where

$$
\begin{aligned}
b_1 &= 1,\\
b_2 &= \frac{\beta m_2 \Pi (m_6+\eta)}{m_4 m_6 \mu(\rho+\tau+\mu)},\\
b_3 &= \frac{m_3}{(1-\kappa)\phi} - \frac{\beta m_2 \Pi \phi\kappa (m_6+\eta)}{m_4 m_6 \mu(\rho+\tau+\mu)(1-\kappa)\phi},\\
b_4 &= \frac{\beta m_2 \Pi}{m_6 \mu(\rho+\tau+\mu)}.
\end{aligned}
$$

Obviously, $\mathbb{U}(0) = 0$, and $\mathbb{U}(E(t), I_D(t), I_U(t), H(t)) > 0$, $\forall\ (E(t), I_D(t), I_U(t), H(t)) \neq 0$, implying that $\mathbb{U}$ is positive definite. Furthermore, the time derivative of the Lyapunov functional (17) along the solution path of the TB model (1) is obtained as

$$
\begin{aligned}
\frac{d\mathbb{U}}{dt} &= \frac{dE}{dt} + \frac{\beta m_2 \Pi (m_6+\eta)}{m_4 m_6 \mu(\rho+\tau+\mu)}\frac{dI_D}{dt} + \left[\frac{m_3}{(1-\kappa)\phi} - \frac{\beta m_2 \Pi \phi\kappa (m_6+\eta)}{m_4 m_6 \mu(\rho+\tau+\mu)(1-\kappa)\phi}\right]\frac{dI_U}{dt} + \frac{\beta m_2 \Pi}{m_6 \mu(\rho+\tau+\mu)}\frac{dH}{dt}\\
&= [\beta S(I_D + zI_U + H) - m_3 E] + \frac{\beta m_2 \Pi (m_6+\eta)}{m_4 m_6 \mu(\rho+\tau+\mu)}[\kappa\phi + \theta I_U - m_4 I_D]\\
&+ \left[\frac{m_3}{(1-\kappa)\phi} - \frac{\beta m_2 \Pi \phi\kappa (m_6+\eta)}{m_4 m_6 \mu(\rho+\tau+\mu)(1-\kappa)\phi}\right][(1-\kappa)\phi E - m_5 I_U] + \frac{\beta m_2 \Pi}{m_6 \mu(\rho+\tau+\mu)}[\eta I_D - m_6 H].
\end{aligned}
\tag{18}
$$

Since $S \leq S^* = \frac{m_2\Pi}{\mu(\rho+\tau+\mu)}$ in the positively-invariant region Ψ, then by further simplification of (18), we get

$$
\begin{aligned}
\frac{d\mathbb{U}}{dt} &\leq \left[\beta z S^* + \frac{\beta S^*(m_6+\eta)\theta}{m_4 m_6} + \frac{\beta S^* \kappa\phi (m_6+\eta) m_5}{m_4 m_6 (1-\kappa)\phi} - \frac{m_3 m_5}{(1-\kappa)\phi}\right] I_U\\
&= \left[\frac{\beta S^*\{z m_4 m_6 (1-\kappa)\phi + \theta(m_6+\eta)(1-\kappa)\phi + \kappa\phi(m_6+\eta)m_5\}}{m_4 m_6 (1-\kappa)\phi} - \frac{m_3 m_5}{(1-\kappa)\phi}\right] I_U\\
&= \frac{m_3 m_5}{(1-\kappa)\phi}\left[\frac{\beta m_2 \Pi \phi\{m_6[m_5\kappa + \theta(1-\kappa)] + z m_4 m_6(1-\kappa) + \eta[m_5\kappa + \theta(1-\kappa)]\}}{m_3 m_4 m_5 m_6 \mu(\rho+\tau+\mu)} - 1\right] I_U\\
&= \frac{m_3 m_5}{(1-\kappa)\phi}\left(\mathcal{R}_e|_{\varepsilon=1} - 1\right) I_U.
\end{aligned}
$$

Since the variables and parameters of the TB model (1) are non-negative, it implies that $\frac{d\mathbb{U}}{dt} \leq 0$ if and only if $\mathcal{R}_e|_{\varepsilon=1} \leq 1$, and $E = I_D = I_U = H = 0$. Thus, by LaSalle's invariance principle [50],

$$
(E, I_D, I_U, H) \to (0,0,0,0) \text{ as } t \to \infty. \tag{19}
$$

It therefore follows from the first and second equations of TB model (1) that $\lim_{t\to\infty}(S(t), V(t)) = \left(\frac{m_2\Pi}{\mu(\rho+\tau+\mu)}, \frac{\rho\Pi}{\mu(\rho+\tau+\mu)}\right)$, while $\lim_{t\to\infty} R(t) = 0$ from the last equation of the model. Therefore, every solution that starts in Ψ converges to Ω_1 as $t \to \infty$ whenever $\mathcal{R}_e|_{\varepsilon=1} \leq 1$.

4 Numerical simulation

In this section, we run a numerical simulation using the formulated model described in system (1) to examine TB dynamics under different control interventions. We first investigate the impact of vaccination as a preventive intervention in mitigating the burden of TB in the human population. This was achieved by simulating the impact of the vaccination rate of TB-susceptible individuals

with different levels of vaccine efficacy. Following this, the impact of the detection rate of TB infection, the hospitalization rate of diagnosed TB-infectious individuals, and the recovery rate of hospitalized individuals were examined to understand the impact of these control interventions on mitigating TB burden in the populace. The combination of all aforementioned interventions was then simulated to explore the optimum impact on the control of tuberculosis in the human population. The values of parameters used for simulation are given in Table 2.

Table 2. Model parameter values and description

Parameter	Description	Value	Source
Π	Recruitment rate	5	[51]
ρ	Vaccination rate	0.1 - 0.98	[51]
τ	Vaccine wane rate	0.067	[51]
ε	Vaccine efficacy rate	0 - 1	[51]
β	Effective contact rate	0.6501	[51]
μ	Natural death rate	0.0148	[51]
η	Progression rate from diagnosed infectious to hospitalised class	0.60	Assumed
δ_1	TB induced death rate	0.10	[51]
δ_2	TB induced death rate	0.05	Assumed
θ	Progression rate from undiagnosed to diagnosed infectious class	0.45	Assumed
γ_1	Rate of recovery after hospital treatment	0.01	[51]
γ_2	Natural recovery rate of undiagnosed infectious	0.005	Assumed
z	Reduction in infectious rate for diagnosed and hospitalized infectious	0.5	Assumed
k	fraction of individuals who are diagnosed of TB	0.40	Assumed
ϕ	Progression rate to infectious	0.00375	[51]

The total TB infected population in Figure 2, Figure 3, and Figure 4 are in thousand. It is observed that the variation in parameters remains around the mean level. We assume a decrease of 50% from the baseline value for parameters with variation. Important Notice: If the value of the associated variable is smaller or larger than the parameter value at the lower boundary (0 or 1), then no significant perturbation in vaccination rates has been associated with higher relative and absolute autism rates. The high point of the associated variable exceeds approximately 100% more than the parameter value at the lower boundary of the variable. Therefore, in Figure 2, vaccination policymakers are depicted assuming vaccination rates should be set at low (ρ = 0.25), medium (ρ = 0.50), or high (ρ = 1.00), while vaccine efficacy remains either low (ε The rates of detection of TB infection, hospitalization of an infectious individual after diagnosis, recovery, and case fatality among diagnosed TB infectious individuals were varied at three levels of scenarios—low, medium, and high. The detection rate of TB-infection was varied at levels: θ = low = 0.225, θ = medium = 0.45, Aggregate simulated active TB infectious population consists of undiagnosed infectious population and diagnosed infectious population in addition to hospitalized infectious population in this simulation. Throughout the simulation, we defined the total TB infectious population as the sum of both the undiagnosed infectious population, the diagnosed infectious population, and the hospitalized infectious population. This is justified because both undiagnosed infectious humans, diagnosed infectious humans, and hospitalized infectious humans can transmit the disease as presented in the force of infection of the developed model (1).

In Figure 2, we simulate the impact of vaccination as a preventive intervention in mitigating the burden of TB in the human population. This was carried out by examining different levels of vaccination rates of TB-susceptible humans and TB vaccine efficacy simultaneously. The result shows that a high level of vaccination rate with a corresponding high vaccine efficacy leads

to a higher reduction in the total TB-infectious human population. This result implies that, to effectively reduce the tuberculosis burden in the human population, a higher vaccine efficacy with a higher rate of vaccination against the disease is required. Furthermore, this result suggests that while vaccine development is contingent on different factors, efforts should be made to ensure the development of vaccines with higher efficacy is highly prioritized to obtain optimum results in preventing disease spread. Also, to attain a high vaccination rate against tuberculosis, efforts should be made towards awareness and educational campaigns to ensure people are educated on the need for vaccination against the deadly disease especially in the developing regions.

While vaccination is a preventive intervention against tuberculosis, several control intervention strategies are also used in mitigating the spread of tuberculosis including but not limited to hospitalization of infected individuals for treatment. Based on this fact, in Figure 3 we examine the impact of the detection rate of TB infection, hospitalization rate of diagnosed TB-infectious individuals, and recovery rate of hospitalized individuals to understand the impact of these control interventions on mitigating TB burden in the populace. As expected, the result shows that a high level of detection rate of TB infection, a high level of hospitalization rate of diagnosed TB-infectious individuals, and a high level of recovery rate of hospitalized individuals due to treatment resulted in a higher reduction in the total TB-infectious human in the populace. The result suggests that efforts should be made to facilitate the resources in detecting TB-infectious individuals and the hospitalization of diagnosed humans for effective treatment. This will contribute to the reduction of tuberculosis transmission in the human population. In Figure 4, we combined different interventions (vaccination rate of TB-susceptible humans, TB vaccine efficacy, detection rate of TB infection, hospitalization rate of diagnosed TB-infectious individuals, and recovery rate of hospitalized individuals) to examine the optimum impact they have on the control of tuberculosis in the human population. The result shows that a high level of vaccination rate of TB-susceptible humans, a high level of TB vaccine efficacy, a high level of detection rate of TB infection, a high level of hospitalization rate of diagnosed TB-infectious individuals, and a high level of recovery rate of hospitalized individuals due to treatment resulted into a huge reduction in the total TB-infectious human in the populace when compared with a single intervention usage. The overall result suggests that, by combining several intervention strategies, the TB burden can be reduced faster and more effectively when compared to a single usage of intervention.

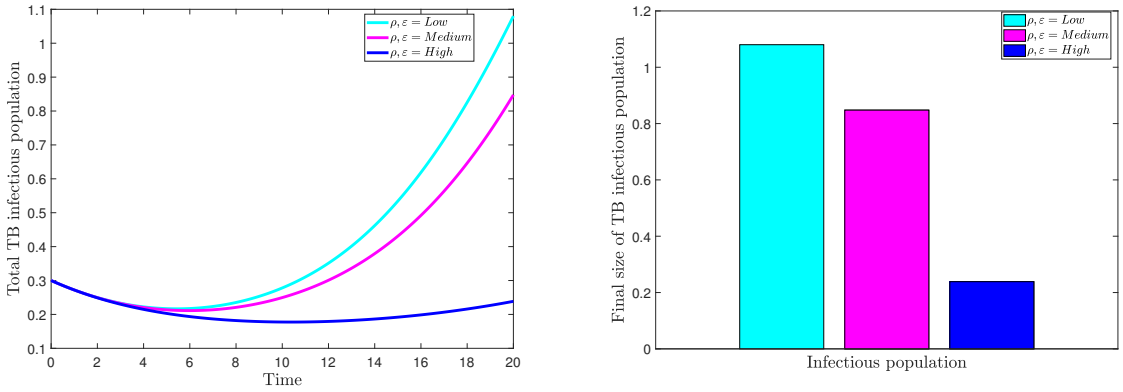

(a) **(b)**

Figure 2. Numerical simulation of TB model (1), illustrating the impact of varying vaccination rates ρ and vaccine efficacy ε on the dynamics and final sizes of the total TB infectious human population. Baseline parameter values are set as follows: ρ=Low=0.25, ρ=Medium=0.50, and ρ=High=1.00; and ε=Low=0.245, ε=Medium=0.490, and ε=High=0.980

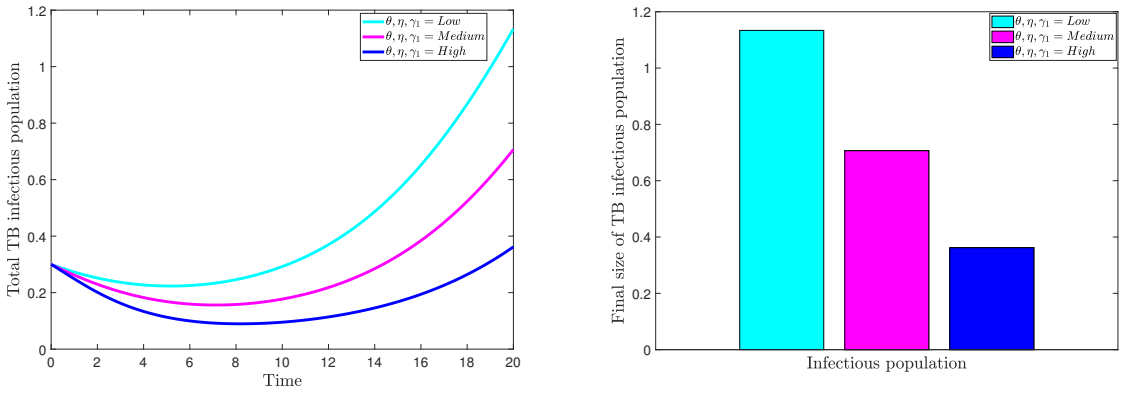

(a) **(b)**

Figure 3. Numerical simulations of the TB model illustrate the impact of varying levels of the detection rate of TB infection, θ, the hospitalization rate of diagnosed TB-infected individuals, η, and the recovery rate of hospitalized individuals, γ_1, on the dynamics and final sizes of the total TB infectious human population. Baseline parameter values are set as follows: θ=Low=0.225, θ=Medium=0.450, and θ=High=0.900; η=Low=0.30, η=Medium=0.60, and η=High=1.20; and γ_1=Low=0.005, γ_1=Medium=0.01, and γ_1=High=0.02

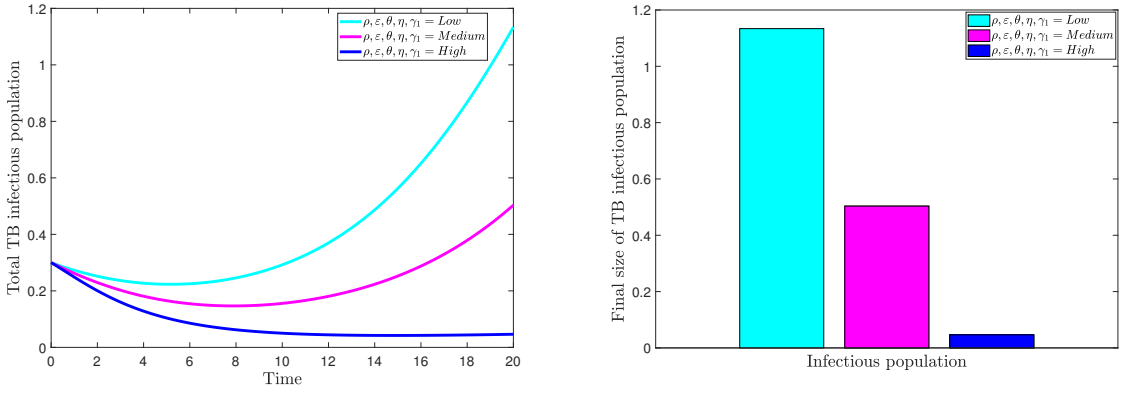

(a) **(b)**

Figure 4. Numerical simulation of TB model, illustrating the impact of varying vaccination rates ρ, vaccine efficacy ε, TB infection detection rate θ, hospitalization rate of diagnosed TB-infected individuals η, and recovery rate of hospitalized individuals γ_1 on the dynamics and final sizes of the total TB infectious human population. Baseline parameter values are set as follows: ρ=Low=0.25, ρ=Medium=0.50, and ρ=High=1.00; ε=Low=0.245, ε=Medium=0.490, and ε=High=0.980; θ=Low=0.225, θ=Medium=0.450, and θ=High=0.900; η=Low=0.30, η=Medium=0.60, and η=High=1.20; and γ_1=Low=0.005, γ_1=Medium=0.01, and γ_1=High=0.02

5 Conclusion

The mathematical model presented in this study investigates the dynamics of tuberculosis (TB), considering detected, undetected, and hospitalized individuals. The numerical simulations focus on the impact of diverse control interventions. The study evaluates the effectiveness of vaccination as a preventive measure, highlighting the crucial role of high vaccine efficacy and the need for increased vaccination rates, especially in developing regions. Additionally, the investigation explores the influence of detecting infections, hospitalizing diagnosed individuals,

and promoting recovery in the hospitalized population. The results demonstrate that higher rates of detection, hospitalization, and recovery significantly reduce the total TB-infectious human population. Importantly, combining multiple interventions, including vaccination, yields a more substantial reduction compared to individual measures. The study underscores the importance of a comprehensive strategy involving various control measures for efficient and rapid TB burden reduction, providing valuable insights for healthcare practitioners and policymakers.

Declarations

Use of AI tools

The authors declare that they have not used Artificial Intelligence (AI) tools in the creation of this article.

Data availability statement

There are no data associated with this article.

Ethical approval (optional)

The authors state that this research complies with ethical standards. This research does not involve either human participants or animals.

Consent for publication

Not applicable

Conflicts of interest

The authors declare that they have no conflict of interest.

Funding

No funding was received for this research.

Author's contributions

O.J.P.: Methodology, Conceptualization, Validation, Foftware, Data Curation, Writing the Original Draft. A.A., F.F., M.M.O. and F.A.O.: Writing - Review & Editing, Supervision. All authors have read and agreed to the published version of the manuscript.

Acknowledgements

Not applicable

References

[1] World Health Organization, Global Tuberculosis Report 2021, (2021). https://www.who.int/teams/global-tuberculosis-programme/tb-reports/global-tuberculosis-report-2021

[2] World Health Organization, Global Tuberculosis Report 2022, (2022). https://www.who.int/teams/global-tuberculosis-programme/tb-reports/global-tuberculosis-report-2022

[3] World Health Organization, Latent Tuberculosis Infection: Updated and Consolidated Guidelines for Programmatic Management, (2023). https://www.who.int/tb/publications/201

[4] World Health Organization, The END TB Strategy, (2015). https://www.who.int/publications/i/item/WHO-HTM-TB-2015.19

[5] Zumla, A., Raviglione, M., Hafner, R. and Von Reyn, C.F. Tuberculosis. *The New England Journal of Medicine*, 368(8), 745-755, (2013). [CrossRef]

[6] Dodd, P.J., Sismanidis, C. and Seddon, J.A. Global burden of drug-resistant tuberculosis in children: a mathematical modelling study. *The Lancet Infectious Diseases*, 16(10), 1193-1201, (2016). [CrossRef]

[7] Centers for Disease Control and Prevention, Tuberculosis (TB)-Data and Statistics, (2023). https://www.cdc.gov/tb/statistics/default.htm

[8] Gupta, R.K., Lipman, M., Story, A., Hayward, A., De Vries, G., Van Hest, R. et al. Active case finding and treatment adherence in risk groups in the tuberculosis pre-elimination era. *The International Journal of Tuberculosis and Lung Disease*, 22(5), 479-487, (2018). [CrossRef]

[9] Goufo, E.F.D., Maritz, R. and Pene, M.K. A mathematical and ecological analysis of the effects of petroleum oil droplets breaking up and spreading in aquatic environments. *International Journal of Environment and Pollution*, 61(1), 64-71, (2017). [CrossRef]

[10] Atangana, A. and Doungmo Goufo, E.F. Computational analysis of the model describing HIV infection of CD4+ T cells. *BioMed Research International*, 2014, 618404, (2014). [CrossRef]

[11] Tchepmo Djomegni, P.M., Govinder, K.S. and Doungmo Goufo, E.F. Movement, competition and pattern formation in a two prey–one predator food chain model. *Computational and Applied Mathematics*, 37, 2445-2459, (2018). [CrossRef]

[12] Peter, O.J., Yusuf, A., Oshinubi, K., Oguntolu, F.A., Lawal, J.O., Abioye, A.I. et al. Fractional order of pneumococcal pneumonia infection model with Caputo-Fabrizio operator. *Results in Physics*, 29, 104581, (2021). [CrossRef]

[13] Atangana, A. and Qureshi, S. Mathematical modeling of an autonomous nonlinear dynamical system for malaria transmission using Caputo derivative. In *Fractional Order Analysis: Theory, Methods and Applications* (pp. 225-252). New York, United States: John Wiley & Sons, (2020). [CrossRef]

[14] Peter, O.J., Shaikh, A.S., Ibrahim, M.O., Nisar, K.S., Baleanu, D., Khan, I. et al. Analysis and dynamics of fractional order mathematical model of COVID-19 in Nigeria using Atangana-Baleanu operator. *Computers, Materials, & Continua*, 66(2), 1823-1848, (2021). [CrossRef]

[15] Peter, O.J., Qureshi, S., Yusuf, A., Al-Shomrani, M. and Idowu, A.A. A new mathematical model of COVID-19 using real data from Pakistan. *Results in Physics*, 24, 104098, (2021). [CrossRef]

[16] Khan, H., Gómez-Aguilar, J.F., Alkhazzan, A. and Khan, A. A fractional order HIV-TB coinfection model with nonsingular Mittag-Leffler law. *Mathematical Methods in the Applied Sciences*, 43(6), 3786-3806, (2020). [CrossRef]

[17] Akinpelu, F.O. and Ojo, M.M. Mathematical analysis of effect of isolation on the transmission of Ebola virus disease in a population. *Asian Research Journal of Mathematics*, 1(5), 1-12, (2016). [CrossRef]

[18] Ahmad, S., Ullah, A., Al-Mdallal, Q.M., Khan, H., Shah, K. and Khan, A. Fractional order mathematical modeling of COVID-19 transmission. *Chaos, Solitons & Fractals*, 139, 110256, (2020). [CrossRef]

[19] Arafa, A.A.M., Khalil, M. and Sayed, A. A non-integer variable order mathematical model of human immunodeficiency virus and malaria coinfection with time delay. *Complexity*, 2019,

4291017, (2019). [CrossRef]

[20] Ojo, M.M. and Goufo, E.F.D. Modeling, analyzing and simulating the dynamics of Lassa fever in Nigeria. *Journal of the Egyptian Mathematical Society,* 30, 1, (2022). [CrossRef]

[21] Demongeot, J., Griette, Q., Magal, P. and Webb, G. Modeling vaccine efficacy for COVID-19 outbreak in New York city. *Biology,* 11(3), 345, (2022). [CrossRef]

[22] Musa, S.S., Qureshi, S., Zhao, S., Yusuf, A., Mustapha, U.T. and He, D. Mathematical modeling of COVID-19 epidemic with effect of awareness programs. *Infectious Disease Modelling,* 6, 448-460, (2021). [CrossRef]

[23] Memon, Z., Qureshi, S. and Memon, B.R. Assessing the role of quarantine and isolation as control strategies for COVID-19 outbreak: a case study. *Chaos, Solitons & Fractals,* 144, 110655, (2021). [CrossRef]

[24] Yang, Y., Li, J., Ma, Z. and Liu, L. Global stability of two models with incomplete treatment for tuberculosis. *Chaos, Solitons & Fractals,* 43(1-12), 79-85, (2010). [CrossRef]

[25] Zhang, J., Li, Y. and Zhang, X. Mathematical modeling of tuberculosis data of China. *Chaos, Solitons & Fractals,* 365, 159-163, (2015). [CrossRef]

[26] Egonmwan, A.O. and Okuonghae, D. Analysis of a mathematical model for tuberculosis with diagnosis. *Journal of Applied Mathematics and Computing,* 59, 129-162, (2019). [CrossRef]

[27] Ullah, I., Ahmad, S., Al-Mdallal, Q., Khan, Z.A., Khan, H. and Khan, A. Stability analysis of a dynamical model of tuberculosis with incomplete treatment. *Advances in Difference Equations,* 2020, 499, (2020). [CrossRef]

[28] Syahrini, I., Sriwahyuni, Halfiani, V., Yuni, S.M., Iskandar, T., Rasudin, et al. The epidemic of tuberculosis on vaccinated population. In Proceedings, *Journal of Physics: Conference Series* (Vol. 890, No. 1), p. 012017, (2017, September). [CrossRef]

[29] Okuonghae, D. A mathematical model of tuberculosis transmission with heterogeneity in disease susceptibility and progression under a treatment regime for infectious cases. *Applied Mathematical Modelling,* 37(10-11), 6786-6808, (2013). [CrossRef]

[30] Liu, J. and Zhang, T. Global stability for a tuberculosis model. *Mathematical and Computer Modelling,* 54(1-2), 836-845, (2011). [CrossRef]

[31] Andrawus, J., Eguda, F.Y., Usman, I.G., Maiwa, S.I., Dibal, I.M., Urum, T.G. et al. A mathematical model of a tuberculosis transmission dynamics incorporating first and second line treatment. *Journal of Applied Sciences and Environmental Management,* 24(5), 917-922, (2020). [CrossRef]

[32] Kasereka Kabunga, S., Doungmo Goufo, E.F. and Ho Tuong, V. Analysis and simulation of a mathematical model of tuberculosis transmission in Democratic Republic of the Congo. *Advances in Difference Equations,* 2020, 642, (2020). [CrossRef]

[33] Kim, S., De Los Reyes V, A.A. and Jung, E. Country-specific intervention strategies for top three TB burden countries using mathematical model. *PloS One,* 15(4), e0230964, (2020). [CrossRef]

[34] Nkamba, L.N., Manga, T.T., Agouanet, F. and Mann Manyombe, M.L. Mathematical model to assess vaccination and effective contact rate impact in the spread of tuberculosis. *Journal of Biological Dynamics,* 13(1), 26-42, (2019). [CrossRef]

[35] Gerberry, D.J. Practical aspects of backward bifurcation in a mathematical model for tuberculosis. *Journal of Theoretical Biology,* 388, 15-36, (2016). [CrossRef]

[36] Ludji, D.G., Sianturi, P. and Nugrahani, E. Dynamical system of the mathematical model for tuberculosis with vaccination. *ComTech: Computer, Mathematics and Engineering Applications*, 10(2), 59-66, (2019). [CrossRef]

[37] Mishra, B.K. and Srivastava, J. Mathematical model on pulmonary and multidrug-resistant tuberculosis patients with vaccination. *Journal of the Egyptian Mathematical Society*, 22(2), 311-316, (2014). [CrossRef]

[38] Olaniyi, S. Dynamics of Zika virus model with nonlinear incidence and optimal control strategies. *Applied Mathematics & Information Sciences*, 12(5), 969-982, (2018). [CrossRef]

[39] Peter, O.J., Oguntolu, F.A., Ojo, M.M., Olayinka Oyeniyi, A., Jan, R. and Khan, I. Fractional order mathematical model of monkeypox transmission dynamics. *Physica Scripta*, 97(8), 084005, (2022). [CrossRef]

[40] Abidemi, A., Zainuddin, Z.M. and Aziz, N.A.B. Impact of control interventions on COVID-19 population dynamics in Malaysia: a mathematical study. *The European Physical Journal Plus*, 136, 237, (2021). [CrossRef]

[41] Joshi, H. and Yavuz, M. Transition dynamics between a novel coinfection model of fractional-order for COVID-19 and tuberculosis via a treatment mechanism. *The European Physical Journal Plus*, 138, 468, (2023). [CrossRef]

[42] Joshi, H., Jha, B.K. and Yavuz, M. Modelling and analysis of fractional-order vaccination model for control of COVID-19 outbreak using real data. *Mathematical Biosciences and Engineering*, 20(1), 213-240, (2023). [CrossRef]

[43] Joshi, H. Mechanistic insights of COVID-19 dynamics by considering the influence of neurodegeneration and memory trace. *Physica Scripta*, 99(3), 035254, (2024). [CrossRef]

[44] Allegretti, S., Bulai, I.M., Marino, R., Menandro, M.A. and Parisi, K. Vaccination effect conjoint to fraction of avoided contacts for a SARS-CoV-2 mathematical model. *Mathematical Modelling and Numerical Simulation with Applications*, 1(2), 56-66, (2021). [CrossRef]

[45] Bolaji, B., Onoja, T., Agbata, C., Omede, B.I. and Odionyenma, U.B. Dynamical analysis of HIV-TB co-infection transmission model in the presence of treatment for TB. *Bulletin of Biomathematics*, 2(1), 21-56, (2024). [CrossRef]

[46] Van den Driessche, P. and Watmough, J. Reproduction numbers and sub-threshold endemic equilibria for compartmental models of disease transmission. *Mathematical Biosciences*, 180(1-2), 29-48, (2002). [CrossRef]

[47] Gumel, A.B. Causes of backward bifurcations in some epidemiological models. *Journal of Mathematical Analysis and Applications*, 395(1), 355-365, (2012). [CrossRef]

[48] Singer, B.H. and Kirschner, D.E. Influence of backward bifurcation on interpretation of R_0 in a model of epidemic tuberculosis with reinfection. *Mathematical Biosciences and Engineering*, 1(1), 81-93, (2004). [CrossRef]

[49] Egbelowo, O.F., Munyakazi, J.B., Dlamini, P.G., Osaye, F.J. and Simelane, S.M. Modeling visceral leishmaniasis and tuberculosis co-infection dynamics. *Frontiers in Applied Mathematics and Statistics*, 9, 1153666, (2023). [CrossRef]

[50] La Salle, J.P. *The Stability of Dynamical Systems*. SIAM: United States of America, (1976).

[51] Ojo, M.M., Peter, O.J., Goufo, E.F.D., Panigoro, H.S. and Oguntolu, F.A. Mathematical model for control of tuberculosis epidemiology. *Journal of Applied Mathematics and Computing*, 69, 69-87, (2023). [CrossRef]

Mathematical Modelling and Numerical Simulation with Applications (MMNSA)
(https://dergipark.org.tr/en/pub/mmnsa)

How to cite this article: Peter, O.J., Abidemi, A., Fatmawati, F., Ojo, M.M. & Oguntolu, F.A. (2024). Optimizing tuberculosis control: a comprehensive simulation of integrated interventions using a mathematical model. *Mathematical Modelling and Numerical Simulation with Applications,* 4(3), 238-255. https://doi.org/10.53391/mmnsa.1461011

Mathematical Modelling and Numerical Simulation with Applications, 2024, 4(3), 256–279

https://dergipark.org.tr/en/pub/mmnsa

ISSN Online: 2791-8564 / Open Access

https://doi.org/10.53391/mmnsa.1484994

RESEARCH PAPER

A three-dimensional discrete fractional-order HIV-1 model related to cancer cells, dynamical analysis and chaos control

Haneche Nabil [1,*,‡] and **Hamaizia Tayeb** [2,‡]

[1]Applied Mathematics & Modeling Laboratory, Department of Mathematics, University of Mentouri Brothers, 25000 Constantine, Algeria, [2]Department of Mathematics, University of Mentouri Brothers, 25000 Constantine, Algeria

* Corresponding Author

‡ nabil.haneche@doc.umc.edu.dz (Haneche Nabil); el.tayyeb@umc.edu.dz (Hamaizia Tayeb)

Abstract

In this paper, we study a three-dimensional discrete-time model to describe the behavior of cancer cells in the presence of healthy cells and HIV-infected cells. Based on the Caputo-like difference operator, we construct the fractional-order biological system. This study's significance lies in developing a new approach to presenting a biological dynamical system. Since the qualitative analysis related to existence, uniqueness, and stability is almost the same as can be found in numerous existing papers, and comparing this study to other research, constructing a biological discrete system using the Caputo difference operator can be particularly important. Using powerful tools of nonlinear theory such as phase plots, bifurcation diagrams, Lyapunov exponent spectrum, and the 0-1 test, we establish that the proposed system can exhibit different biological states, including stable, periodic, and chaotic behaviors. Here, the route leading to chaos is period-doubling bifurcation. Furthermore, the level of chaos in the system is quantified using C_0 complexity and approximate entropy algorithms. The stabilization or suppression of chaotic motions in the fractional-order system is presented, where an efficient controller is designed based on the stability theory of the discrete-time fractional-order systems. Numerical simulations are provided to validate the theoretical results derived in this research paper.

Keywords: Fractional-order; discrete chaos; HIV-1 model; bifurcation diagram; chaos control

AMS 2020 Classification: 26A33; 34H10; 35B41; 37D45; 37G35

1 Introduction

In recent years, the modeling of infectious diseases has become an important topic that has been studied to describe the mechanisms by which disease spreads and then to predict the future behavior of the disease. The goal of this study is to find solutions and strategies to fight and

➤ **Received:** 16.05.2024 ➤ **Revised:** 06.07.2024 ➤ **Accepted:** 15.07.2024 ➤ **Published:** 30.09.2024

control epidemics and diseases such as cancers and immunodeficiency disease [1]. Mathematical systems can be used to design new experiments by formulating hypotheses about the spread and dynamics of disease. In particular, nowadays, mathematical models of HIV-1 have been extensively studied by researchers around the world to show the interactions between healthy cells, infected cells, and cancer cells. There are many existing reviews of HIV-1 models that describe the coexistence of HIV-infected cells with cancer cells, see [2–5]. Our contribution is to construct a discrete fractional-order model that describes the interactions between these cells, and then to control the constructed system via an effective fractional-order controller.

Recently, discrete-time systems have been more commonly used than continuous-time systems to study biological and epidemiological models because discrete-time systems are easier to compute and numerically simulate [6]. In fact, fractional calculus is a broad field in modern mathematics that allows us to investigate and describe a new phenomenon modeled with fractional-order equations. To our best knowledge, the first idea of the fractional derivative is associated with Leibniz when he discussed the possibility of the construction of a fractional derivative in correspondence with Bernoulli and Wallis in 1695 [7]. Then, the complete definition of such fractional derivative was not established until the 19^{th} century as a result of the works of Letnikov, Grunwald, Liouville, Riemann, etc [8]. It should be noted that Letnikov established the first exact theoretical formulation of the fractional derivation. Today, many types of fractional derivatives exist, with and without singular kernels. With singular kernels, we have the well-known fractional derivatives, Caputo fractional derivative [9] and Riemann-Liouville fractional derivative [10]. Without singular kernels, we have two categories: fractional derivative with the exponential kernel which is the Caputo-Fabrizio fractional derivative [11], and fractional derivative with Mittag-Leffler kernel which is called as Atangana-Baleanu fractional derivative [12].

Modeling biological systems with fractional derivatives becomes an important topic due to the involvement of memory and hereditary properties in the study of the interaction between cancer cells and HIV-infected cells [13]. The non-integer models incorporate all prior information from the past due to the memory effect, then we can understand well the dynamics of the model and predict the spread of the disease [14]. The topics of stability of the equilibrium points, existence and uniqueness, positivity and boundedness of the solution in the fractional order cancer models are discussed in detail in [15–20]. Several numerical solutions to solve fractional-order biological systems are proposed in [21–23].

Nowadays, among several fractional derivatives that exist, the Riemann-Liouville derivative and the Caputo derivative are the most commonly used [24]. Today, many systems in physics, chemistry, biology, epidemiology, neurology, viscoelasticity, cryptography, cardiology, etc. have been studied and developed using fractional calculus theory [25].

On the side of discrete dynamical systems, Diaz and Osler published in 1974 the first concept of a fractional difference operator defined as a generalization of the binomial formula for the n^{th}-order difference operator Δ^n [26]. Furthermore, Atici et al. introduced the fractional nabla difference operator, which is analogous to the forward fractional difference proposed by Miller and Ross in 1989 [27]. Then, Abdeljawad introduced the Caputo fractional delta and nabla difference operators [28]. Recently, Abdeljawad et al. derived the delta and nabla discrete formulas for fractional integral and derivative, adopting the binomial theorem [29].

Discrete fractional calculus allows us to study systems in biology and ecology using fractional-order equations to get better results and understand the interactions between species. Another advantage of this theory is the speed of calculations with high precision. Additionally, it consumes minimal computer resources [30]. While discrete fractional calculus offers benefits such as high flexibility and robustness, it also poses challenges related to nonlinearity and complexity when we numerically solve a fractional-order system. Furthermore, this theory's analytical tools have

limitations in determining the convergence and stability of numerical schemes. Using numerical methods and approximations to solve a fractional-order equation can lead to significant errors [31].

Recently, there has been great interest shown in the literature on chaotic dynamical systems due to their important applications in practice. A chaotic system is defined as a dynamical system that displays what is called sensitive dependence on initial conditions [32]. A small change in the initial state of a chaotic system may lead to completely different outcomes. In nonlinear dynamical analysis, a chaotic system has at least one positive Lyapunov exponent, in which the Lyapunov exponent is a numerical quantity that measures the rate of convergence and divergence of neighboring trajectories in nonlinear dynamical system [33].

In the current paper, we report a 3-D discrete-time fractional-order HIV-1 model involving AIDS-related cancer cells. This model can exhibit chaotic dynamics for some parameter values. By employing theoretical results and numerical simulations, we can show the chaotic behavior of the proposed system, which is a popular phenomenon in nonlinear dynamical systems. In Section 2, basic notions related to discrete fractional calculus are introduced. In Section 3, the discrete fractional-order system is constructed based on the Caputo-like delta difference operator. In Section 4, the dynamics of the fractional-order system are analyzed in both commensurate and non-commensurate fractional-order using powerful tools in nonlinear dynamic analysis such as phase portraits, bifurcation diagrams, maximum Lyapunov exponent, dynamical maps, etc. In Section 5, the complexity of the fractional-order system is measured by the 0-1 test, C_0 complexity, and approximate entropy algorithms. In Section 6, a suitable control scheme for stabilizing the chaotic dynamics in the fractional-order system is constructed. In Section 7, the data analysis and discussion have been presented. Section 8 contains the conclusions.

2 Mathematical background

In this section, we give some results of discrete fractional calculus, which helped us build this manuscript.

Definition 1 *[27] Consider the real-valued function $\phi(\tau) : \mathbb{N}_\alpha \to \mathbb{R}$ with $\mathbb{N}_\alpha = \mathbb{N}_0 + \{\alpha\} = \{\alpha, \alpha+1, \alpha+2, \ldots\}$ where $\alpha \in \mathbb{R}$. Let $\nu > 0$, the ν^{th}-order fractional sum of $\phi(\tau)$ is defined as*

$$\Delta_\alpha^{-\nu}\phi(\tau) = \frac{1}{\Gamma(\nu)}\sum_{\xi=\alpha}^{\tau-\nu}(\tau-\xi-1)^{(\nu-1)}\phi(\xi), \tag{1}$$

where the falling factorial $\tau^{(\nu)}$ is expressed using the Γ-function as

$$\tau^{(\nu)} = \frac{\Gamma(\tau+1)}{\Gamma(\tau+1-\nu)} = \tau\,(\tau-1)\ldots(\tau-\nu+1)\,. \tag{2}$$

Definition 2 *[28] Let $\phi(\tau) : \mathbb{N}_{\alpha+(m-\nu)} \to \mathbb{R}$ a real-valued function and $\nu \notin \mathbb{N}$, the Caputo-like discrete fractional difference operator of $\phi(\tau)$ is defined as*

$${}^{C}\Delta_\alpha^{\nu}\phi(\tau) = \Delta_\alpha^{-(m-\nu)}\Delta^m\phi(\tau) = \frac{1}{\Gamma(m-\nu)}\sum_{\xi=\alpha}^{\tau-(m-\nu)}(\tau-\xi-1)^{(m-\nu-1)}\Delta_\xi^m\phi(\xi), \tag{3}$$

where $\nu \notin \mathbb{N}$, $m = [\nu]+1$ and $\tau \in \mathbb{N}_{\alpha+(m-\nu)}$.

By adopting the following theorem, we can define the numerical solution of a discrete fractional-

order system.

Theorem 1 *[34] Given the following Caputo-type discrete initial value problem*

$$\begin{cases} {}^{C}\Delta_{\alpha}^{\nu}\phi(\tau) = \psi(\tau+\nu-1,\phi(\tau+\nu-1)), \\ \Delta^{k}\phi(\alpha) = \phi_{k}, \quad m=[\nu]+1, \quad k=0,1,2,\ldots,m-1, \end{cases} \tag{4}$$

then the unique solution of problem (4) is given by

$$\phi(\tau) = \phi_{0}(\tau) + \frac{1}{\Gamma(\nu)} \sum_{\xi=\alpha+(m-\nu)}^{\tau-\nu} (\tau-\xi-1)^{(\nu-1)}\psi(\xi+\nu-1,\phi(\xi+\nu-1)), \quad \tau \in \mathbb{N}_{\alpha+m}, \tag{5}$$

where

$$\phi_{0}(\tau) = \sum_{k=0}^{m-1} \frac{(\tau-\alpha)^{(k)}}{\Gamma(k+1)}\Delta^{k}\phi(\alpha) = \sum_{k=0}^{m-1} \frac{(\tau-\alpha)^{(k)}}{k!}\Delta^{k}\phi(\alpha). \tag{6}$$

The next theorem allows us to construct a stability condition for an equilibrium point of a discrete fractional-order system in the case of commensurate fractional order.

Theorem 2 *[35] For the discrete commensurate fractional-order system*

$${}^{C}\Delta_{\alpha}^{\nu}S(\tau) = BW(\tau+\nu-1), \tag{7}$$

where $W(\tau) = (w_{1}(\tau), w_{2}(\tau), \ldots, w_{n}(\tau))^{T}$, $B \in \mathbb{R}^{n\times n}$, *and* $\tau \in \mathbb{N}_{(\alpha-\nu)+1}$, *the zero equilibrium point of (7) is asymptotically stable if*

$$\lambda_{j} \in \left\{ z_{0} \in \mathbb{C} : |z_{0}| < \left(2\cos\frac{|\arg z_{0}|-\pi}{2-\nu}\right)^{\nu} \quad \text{and} \quad |\arg z_{0}| > \nu\frac{\pi}{2} \right\}, \qquad j=1,2,\ldots,n, \tag{8}$$

where λ_{j} *is an eigenvalue of the matrix* B *and* $\nu \in (0,1)$.

3 Discrete fractional-order HIV-1 model

Recently, Lou et al. [36] proposed a three-dimensional continuous-time HIV-1 system with cancer cells related to AIDS, which is described by the following dynamics:

$$\begin{cases} \frac{dC}{dt} = C\left[\alpha_{1}\left(1-\frac{C+S+R}{\mu}\right)-\delta_{1}S\right], \\ \frac{dS}{dt} = S\left[\alpha_{2}\left(1-\frac{C+S+R}{\mu}\right)-\eta\delta_{1}C-\delta_{2}R\right], \\ \frac{dR}{dt} = R\left(\delta_{2}S-\varrho\right), \end{cases} \tag{9}$$

where C represents the number of cancer cells, S represents the number of healthy cells, and R represents the number of HIV-infected cells. α_{1}, α_{2}, μ, δ_{1}, δ_{2}, η, and ϱ are constant positive parameters. Here α_{1} and α_{2} represent the rate at which cancer cells proliferate uncontrollably and the healthy cells' inherent growth rate respectively, with always $\alpha_{1} > \alpha_{2}$, then the cancer cells reproduce faster than the healthy cells. δ_{1} represents the immune system's capacity to eliminate cancerous cells, δ_{2} represents the rate coefficient of infection, μ represents the effective carrying capacity of the system, the rate in which cancer cells destroy immune cells is represented by η, ϱ represents the killing impact on the infected cells.

In order to enrich the study of the system described in (9) and to contribute to the field of modeling using the techniques of fractional calculus, the fractional-order version of system (9) is given as [37]

$$\begin{cases} {}^{C}D^{\nu_1}C(t) = C\left[\alpha_1\left(1-\frac{C+S+R}{\mu}\right)-\delta_1 S\right], \\ {}^{C}D^{\nu_2}S(t) = S\left[\alpha_2\left(1-\frac{C+S+R}{\mu}\right)-\eta\delta_1 C-\delta_2 R\right], \\ {}^{C}D^{\nu_3}R(t) = \delta_2 SR-\varrho R, \end{cases} \tag{10}$$

where ν_1, ν_2, and ν_3 are the fractional-orders such that $\nu_i \in (0,1)$ for $i = 1,2,3$, and ${}^{C}D^{\nu}$ is the Caputo fractional derivative defined in [38].

Definition 3 *The Caputo fractional derivative of order $\nu \in \mathbb{R}^+$ of a continuous function $g(t) : [t_0, +\infty[\to \mathbb{R}$ is defined as*

$${}^{C}D^{\nu}_{t_0} g(t) = \frac{1}{\Gamma(m-\nu)} \int_{t_0}^{t} \frac{g^{(m)}(s)}{(t-s)^{\nu+1-m}} ds, \tag{11}$$

where $t > t_0$, $m-1 < \nu \leq m$, and $m = \lceil \nu \rceil$.

For $\nu_1 = \nu_2 = \nu_3 = \nu = 0.98$ and the parameter values listed in Table 1 under the initial conditions $(C(0), S(0), R(0)) = (678, 452, 0.25)$, the attractor of the commensurate fractional-order system (10) is shown in Figure 1(a). In addition, when $(\nu_1, \nu_2, \nu_3) = (0.96, 0.97, 0.98)$, the attractor of the non-commensurate fractional-order system (10) is shown in Figure 1(b).

Table 1. Parameter values of the continuous-time fractional-order system (10)

Parameter	Value
α_1	0.1785
α_2	0.03
δ_1	0.0001
δ_2	0.0005
η	0.01
μ	1500
ϱ	0.3

To simplify the study, we nondimensionalize the system (9) in order to obtain the scaled system. We set

$$u = \frac{C}{\mu}, \qquad v = \frac{S}{\mu}, \qquad w = \frac{R}{\mu}, \qquad \tau = \alpha_1 t, \tag{12}$$

where the new parameters are given by

$$b_{12} = \frac{\mu\delta_1}{\alpha_1}, \qquad b_{23} = \frac{\delta_2\mu}{\alpha_1}, \qquad b_{22} = \frac{\eta\delta_1\mu}{\alpha_1}, \qquad b_{31} = \frac{\delta_2\mu}{\alpha_1}, \qquad r = \frac{\alpha_2}{\alpha_1}, \qquad b_{32} = \frac{\varrho}{\alpha_1}. \tag{13}$$

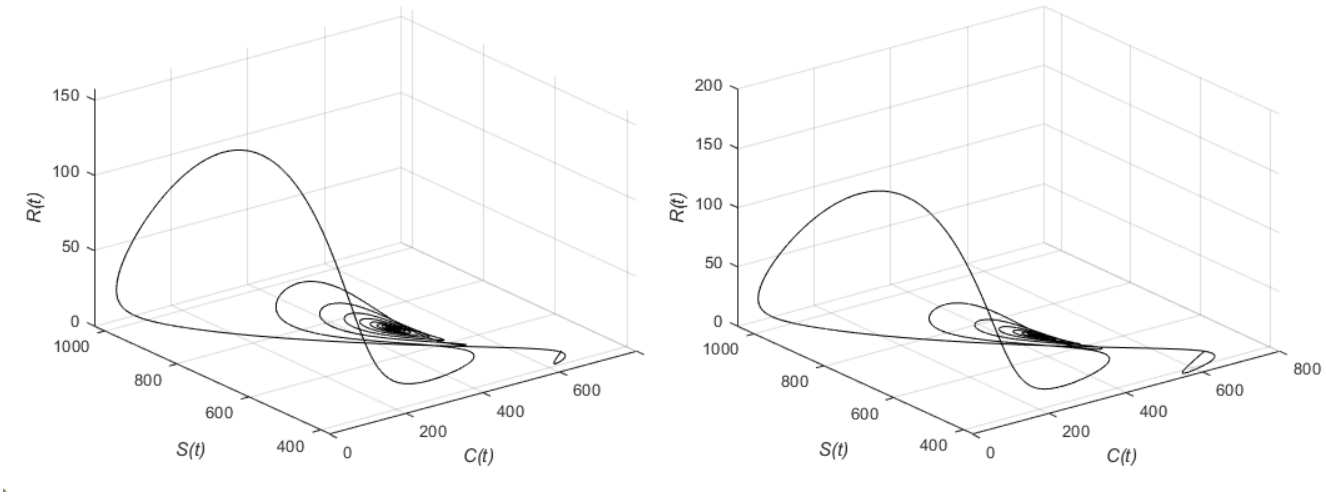

(a) commensurate fractional-order (b) non-commensurate fractional-order

Figure 1. Phase portrait of the fractional-order system (10)

Hence, the nondimensionalized system can be expressed as

$$\begin{cases} \frac{du}{d\tau} = u\left(1-(u+v+w)\right) - b_{12}uv, \\ \frac{dv}{d\tau} = rv\left(1-(u+v+w)\right) - b_{22}uv - b_{23}vw, \\ \frac{dw}{d\tau} = b_{31}vw - b_{32}w. \end{cases} \tag{14}$$

We can obtain the discrete fractional-order HIV-1 model with cancer cells related to AIDS by substituting the fractional derivatives ${}^{C}D^{\nu_i}$ with the Caputo-like discrete fractional difference operator ${}^{C}\Delta_{\alpha}^{\nu_i}$ as follows

$$\begin{cases} {}^{C}\Delta_{\alpha}^{\nu_1}u(\tau) = u(\tau+\nu_1-1)(1-(u(\tau+\nu_1-1)+v(\tau+\nu_1-1)+w(\tau+\nu_1-1)) \\ \qquad\qquad -b_{12}u(\tau+\nu_1-1)v(\tau+\nu_1-1), \\ {}^{C}\Delta_{\alpha}^{\nu_2}v(\tau) = rv(\tau+\nu_2-1)\left(1-(u(\tau+\nu_2-1)+v(\tau+\nu_2-1)+w(\tau+\nu_2-1))\right) \\ \qquad\qquad -b_{22}u(\tau+\nu_2-1)v(\tau+\nu_2-1)-b_{23}v(\tau+\nu_2-1)w(\tau+\nu_2-1), \\ {}^{C}\Delta_{\alpha}^{\nu_3}w(\tau) = b_{31}v(\tau+\nu_3-1)w(\tau+\nu_3-1)-b_{32}w(\tau+\nu_3-1). \end{cases} \tag{15}$$

For simplification, we will replace u, v, and w by x, y, and z, respectively. Using Theorem 1 with $\alpha = 0$, the numerical solution of the discrete fractional-order system (15) is given by

$$\begin{cases} x(n) = x(0) + \frac{1}{\Gamma(\nu_1)}\sum_{s=1}^{n}\frac{\Gamma(n-s+\nu_1)}{\Gamma(n-s+1)}(x(s-1)(1-(x(s-1)+y(s-1)+z(s-1))) \\ \qquad -b_{12}x(s-1)y(s-1)), \\ y(n) = y(0) + \frac{1}{\Gamma(\nu_2)}\sum_{s=1}^{n}\frac{\Gamma(n-s+\nu_2)}{\Gamma(n-s+1)}(ry(s-1)(1-(x(s-1)+y(s-1)+z(s-1))) \\ \qquad -b_{22}x(s-1)y(s-1)-b_{23}y(s-1)z(s-1)), \\ z(n) = z(0) + \frac{1}{\Gamma(\nu_3)}\sum_{s=1}^{n}\frac{\Gamma(n-s+\nu_3)}{\Gamma(n-s+1)}\left(b_{31}y(s-1)z(s-1)-b_{32}z(s-1)\right), \end{cases} \tag{16}$$

where $x(n)$, $y(n)$, and $z(n)$ represent the number of cancer cells, healthy cells, and HIV-infected cells respectively.b_{12}, b_{22}, b_{23}, b_{31}, b_{32}, and r are constant positive parameters.

4 Dynamics of the fractional-order discrete system

This section focuses on the analysis of the dynamics of the discrete fractional-order HIV-1 model with cancer cells related to AIDS (15) in both commensurate and non-commensurate fractional orders.

Case 1. Commensurate fractional-order

Existence and stability of equilibria

In this part, we study the existence and stability of equilibria in the fractional-order system (15). The equilibrium points of the fractional-order system (15) are the solutions of the following system of equations:

$$\begin{cases} x\left(1-(x+y+z)\right)-b_{12}xy=0, \\ ry\left(1-(x+y+z)\right)-b_{22}xy-b_{23}yz=0, \\ b_{31}yz-b_{32}z=0. \end{cases} \tag{17}$$

If we assume that $b_{22} \neq b_{23}$, the equilibrium points of (15) are:

$$\begin{aligned} F_0 &= (0,0,0), \quad F_1=(1,0,0), \quad F_2=(0,1,0), \quad F_3=\left(0,\frac{b_{32}}{b_{31}},\frac{-3r}{r+b_{23}}\right), \\ F_4 &= \left(\frac{rb_{12}}{rb_{12}+b_{22}b_{12}+b_{22}},\frac{b_{22}}{rb_{12}+b_{22}b_{12}+b_{22}},0\right), \\ F_5 &= \left(\frac{b_{31}b_{23}-(b_{23}b_{12}+rb_{12}+b_{23})b_{32}}{b_{31}(b_{23}-b_{22})},\frac{b_{32}}{b_{31}},\frac{(rb_{12}+b_{22}b_{12}+b_{22})b_{32}-b_{31}b_{22}}{b_{31}(b_{23}-b_{22})}\right). \end{aligned}$$

Fix $b_{31}=0.01$, $b_{22}=0.08$, $b_{23}=0.01$, $b_{12}=0.08$, $b_{32}=0.04$, $r=3.4$, the fixed points and the corresponding eigenvalues are shown in Table 2.

Table 2. Equilibria of the fractional-order discrete system (15)

Fixed points	Eigenvalues
F_0	$\lambda_1=1,\ \lambda_2=3.4,\ \lambda_3=-0.04$
F_1	$\lambda_1=-1,\ \lambda_2=-0.08,\ \lambda_3=-0.04$
F_2	$\lambda_1=-3.4,\ \lambda_2=-1.08,\ \lambda_3=-0.03$
F_3	$\lambda_1=0.0299,\ \lambda_2=-13.6299,\ \lambda_3=-0.3288$
F_4	$\lambda_1=-1.5569,\ \lambda_2=0.039,\ \lambda_3=-0.0378$
F_5	$\lambda_1=-30.4586,\ \lambda_2=0.8061,\ \lambda_3=0.0353$

The equilibrium points F_0, F_3, F_4, F_5 have real positive eigenvalue, then the condition $\arg(\lambda_j) > \nu\frac{\pi}{2}$ is not achieved. Based on Theorem 2, the equilibrium points F_0, F_3, F_4, and F_5 are unstable. Also, the equilibrium point F_2 is unstable. We found that the corresponding eigenvalues are $\lambda_1=-3.4$, $\lambda_2=-1.08$, $\lambda_3=-0.03$. Then we have $\arg(\lambda_1)=\pi > \nu\frac{\pi}{2}$, but any value of ν can verify $|\lambda_1| < \left(2\cos\frac{|\arg(\lambda_1)|-\pi}{2-\nu}\right)^{\nu}$.

Theorem 3 *The equilibrium point F_1 of the fractional-order discrete system (15) is locally asymptotically stable.*

Proof The Jacobian matrix of the system (15) evaluated at the equilibrium point (x, y, z) is given by

$$J = \begin{pmatrix} 1-2x-(y+z)-b_{12}y & -(1+b_{12})x & -x \\ -(r+b_{22})y & r(1-(x+y+z))-ry-b_{22}x-b_{23}z & -(r+b_{23})y \\ 0 & b_{31}z & b_{31}y-b_{32} \end{pmatrix}. \tag{18}$$

The eigenvalues of the matrix J at F_1 are $\lambda_1 = -1$, $\lambda_2 = -0.08$, $\lambda_3 = -0.04$. Using Theorem 2, the equilibrium point F_1 is asymptotically stable.

Bifurcation diagrams and maximum Lyapunov exponent

This part focuses on the investigation of the dynamics properties of the commensurate fractional-order discrete HIV-1 model (15) and the influence of the parameters on the dynamic behavior of system (15). Fix $b_{31} = 0.01$, $b_{22} = 0.08$, $b_{23} = 0.01$, $b_{12} = 0.08$, $b_{32} = 0.04$ and vary r in the interval $[2, 3.8]$ when $\nu = 0.4$, then when $\nu = 0.92$ under the initial conditions $(x(0), y(0), z(0)) = (0.1, 0.2, 0.25)$. The bifurcation diagrams of the discrete system (15) are shown in Figure 2. We see that when $\nu = 0.4$, the system is stable for $r \in [2, 3.23]$, but when r increases, the system (15) exhibits chaotic dynamics in the range $r \in [3.23, 3.8]$. For $\nu = 0.92$, the dynamics of the system are complex, and the chaotic behavior is dominated. Clearly, when $r \in [2, 2.6]$, the system (15) is periodic, but when $r \in [2.6, 3.6]$, the system (15) exhibits chaotic behavior, but when r increases, the chaotic behavior gradually disappears.

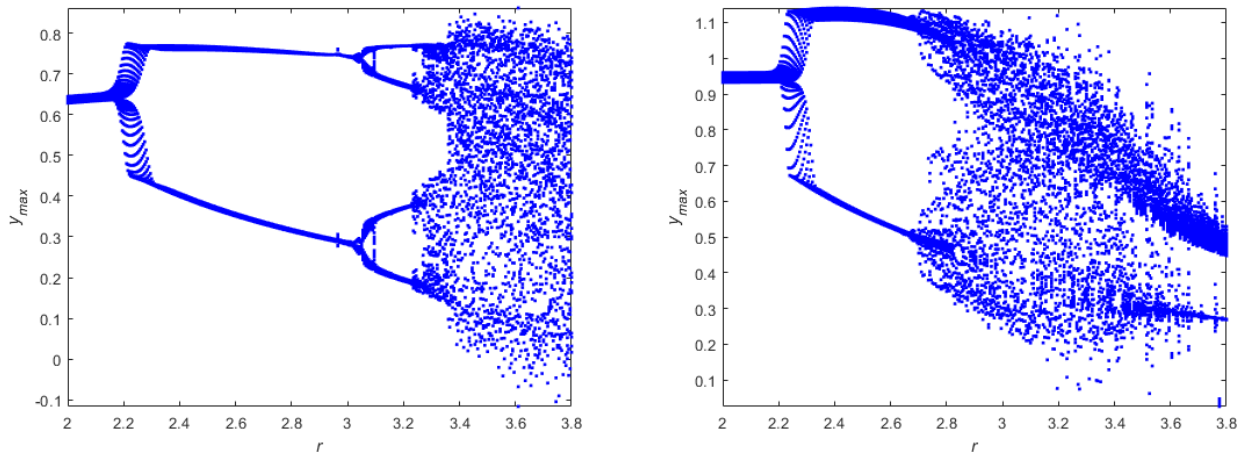

(a) for $\nu = 0.4$ (b) for $\nu = 0.92$

Figure 2. Bifurcation diagrams of the fractional-order system (15) as r varies

Now, we investigate the influence of the fractional order on the dynamics of the fractional-order system (15). Figure 3 represents the bifurcation diagram of the commensurate fractional-order discrete system (15) for the parameter values $b_{31} = 0.01$, $b_{22} = 0.08$, $b_{23} = 0.01$, $b_{12} = 0.08$, $b_{32} = 0.04$, and $r = 3.4$. As can be observed, the system (15) is periodic at first, but if ν increases, the dynamics of the system become unstable with the appearance of a chaotic state in the range $\nu \in [0.14, 1]$.

We can also investigate the chaotic behavior in the system (15) by exploiting the maximum Lyapunov exponent. It should be noted that the maximum Lyapunov exponent can be approximated using the Jacobian matrix algorithm [39]. We set $r_0 = (x(0), y(0), z(0))^T$, the Lyapunov exponent

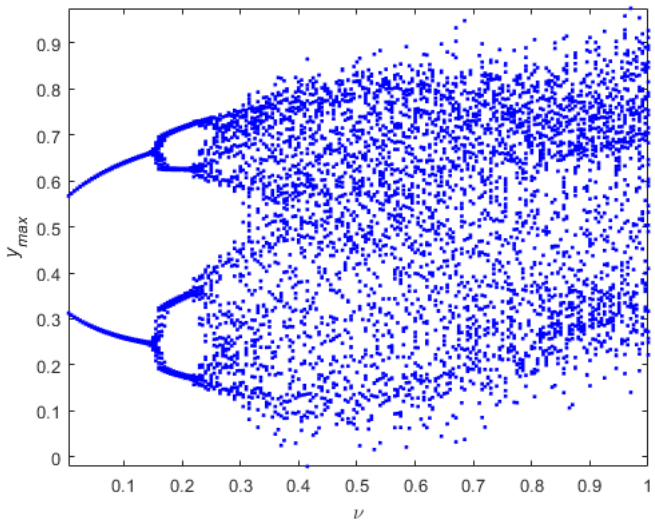

Figure 3. Bifurcation diagram of the fractional-order system (15) as ν varies

is defined as

$$\lambda_i(r_0) = \lim_{n\to\infty} \frac{1}{n} \ln|\lambda_i^{(n)}|, \quad i = 1, 2, 3, \tag{19}$$

where λ_i $(i = 1, 2, 3)$ are the eigenvalues of the tangent map J_n given by

$$J_n = \begin{pmatrix} \theta_1(n) & \theta_2(n) & \theta_3(n) \\ \theta_4(n) & \theta_5(n) & \theta_6(n) \\ \theta_7(n) & \theta_8(n) & \theta_9(n) \end{pmatrix}, \tag{20}$$

where

$$\begin{aligned}
\theta_1(n) &= \theta_1(0) + \frac{1}{\Gamma(\nu)} \sum_{s=1}^{n} \frac{\Gamma(n-s+\nu)}{\Gamma(n-s+1)} (\theta_1(s-1)(1-2x(s-1)-y(s-1)-z(s-1)-b_{12}y(s-1)) \\
&\quad +\theta_4(s-1)(-x(s-1)-b_{12}x(s-1))-\theta_7(s-1)x(s-1)), \\
\theta_2(n) &= \theta_2(0) + \frac{1}{\Gamma(\nu)} \sum_{s=1}^{n} \frac{\Gamma(n-s+\nu)}{\Gamma(n-s+1)} (\theta_2(s-1)(1-2x(s-1)-y(s-1)-z(s-1)-b_{12}y(s-1)) \\
&\quad +\theta_5(s-1)(-x(s-1)-b_{12}x(s-1))-\theta_8(s-1)x(s-1)), \\
\theta_3(n) &= \theta_3(0) + \frac{1}{\Gamma(\nu)} \sum_{s=1}^{n} \frac{\Gamma(n-s+\nu)}{\Gamma(n-s+1)} (\theta_3(s-1)(1-2x(s-1)-y(s-1)-z(s-1)-b_{12}y(s-1)) \\
&\quad +\theta_6(s-1)(-x(s-1)-b_{12}x(s-1))-\theta_9(s-1)x(s-1)), \\
\theta_4(n) &= \theta_4(0) + \frac{1}{\Gamma(\nu)} \sum_{s=1}^{n} \frac{\Gamma(n-s+\nu)}{\Gamma(n-s+1)} (\theta_1(s-1)(-ry(s-1)-b_{22}y(s-1)) + \theta_4(s-1)(r-rx(s-1) \\
&\quad -2ry(s-1)-rz(s-1)-b_{22}x(s-1)-b_{23}z(s-1)) + \theta_7(s-1)(-ry(s-1)-b_{23}y(s-1)), \\
\theta_5(n) &= \theta_5(0) + \frac{1}{\Gamma(\nu)} \sum_{s=1}^{n} \frac{\Gamma(n-s+\nu)}{\Gamma(n-s+1)} (\theta_2(s-1)(-ry(s-1)-b_{22}y(s-1)) + \theta_5(s-1)(r-rx(s-1) \\
&\quad -2ry(s-1)-rz(s-1)-b_{22}x(s-1)-b_{23}z(s-1)) + \theta_8(s-1)(-ry(s-1)-b_{23}y(s-1)),
\end{aligned}$$

$$
\begin{aligned}
\theta_6(n) &= \theta_6(0) + \frac{1}{\Gamma(\nu)} \sum_{s=1}^{n} \frac{\Gamma(n-s+\nu)}{\Gamma(n-s+1)} (\theta_3(s-1)(-ry(s-1) - b_{22}y(s-1)) \\
&\quad + \theta_6(s-1)(r - rx(s-1) - 2ry(s-1) - rz(s-1) - b_{22}x(s-1) - b_{23}z(s-1)) \\
&\quad + \theta_9(s-1)(-ry(s-1) - b_{23}y(s-1)), \\
\theta_7(n) &= \theta_7(0) + \frac{1}{\Gamma(\nu)} \sum_{s=1}^{n} \frac{\Gamma(n-s+\nu)}{\Gamma(n-s+1)} (b_{31}\theta_4(s-1)z(s-1) + \theta_7(s-1)(b_{31}y(s-1) - b_{32}), \\
\theta_8(n) &= \theta_8(0) + \frac{1}{\Gamma(\nu)} \sum_{s=1}^{n} \frac{\Gamma(n-s+\nu)}{\Gamma(n-s+1)} (b_{31}\theta_5(s-1)z(s-1) + \theta_8(s-1)(b_{31}y(s-1) - b_{32}), \\
\theta_9(n) &= \theta_9(0) + \frac{1}{\Gamma(\nu)} \sum_{s=1}^{n} \frac{\Gamma(n-s+\nu)}{\Gamma(n-s+1)} (b_{31}\theta_6(s-1)z(s-1) + \theta_9(s-1)(b_{31}y(s-1) - b_{32}),
\end{aligned}
$$

with $\theta_1(0) = \theta_5(0) = \theta_9(0) = 1$, $\theta_i(0) = 0$ $(i = 2, 3, 4, 6, 7, 8)$. Figure 4(a) and Figure 4(b) show the maximum Lyapunov exponent of the fractional-order system (15) with respect to parameter r under the parameter values $b_{31} = 0.01$, $b_{22} = 0.08$, $b_{23} = 0.01$, $b_{12} = 0.08$, $b_{32} = 0.04$, and the fractional-orders $\nu = 0.4$ and $\nu = 0.92$ respectively. In Figure 4(a), when $r \in [2, 3.8]$, we see that the MLE is equal to zero when $r \in [2, 3.22]$ and the system (15) is periodic, but when r increases, the MLE has positive values, meaning that the discrete fractional-order system (15) transitions from a periodic state to a chaotic state. In Figure 4(b), the MLE of the system (15) is negative at the minimum values of r, then the system (15) is periodic. In addition, when $r \in [2.6, 3.4]$, the MLE is positive, then the system (15) is chaotic. As can be observed, when r increases, the MLE takes positive and negative values, and then the appearance of periodic orbits in the chaotic regions is confirmed. Now, we analyze the MLE of the discrete fractional-order system (15) when the

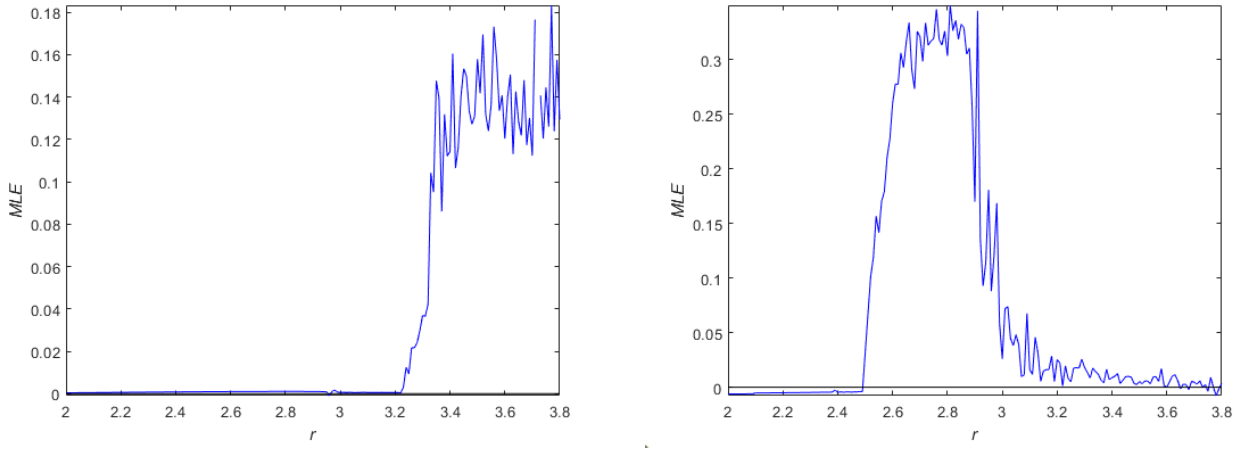

(a) for $\nu = 0.4$ (b) for $\nu = 0.92$

Figure 4. MLE spectrum of the fractional-order system (15) as r varies

fractional-order varies. Figure 5 represents the maximum Lyapunov exponent when ν ranges from 0 to 1. As can be observed, the MLE of system (15) is equal to zero when $\nu \in (0, 0.15]$, and then the system (15) remains in periodic state, but when $\nu \geq 0.15$, the MLE is positive, and then the system (15) exhibits chaotic behavior. The attractor of the fractional-order discrete system (15) for various ν-values is depicted in Figure 6.

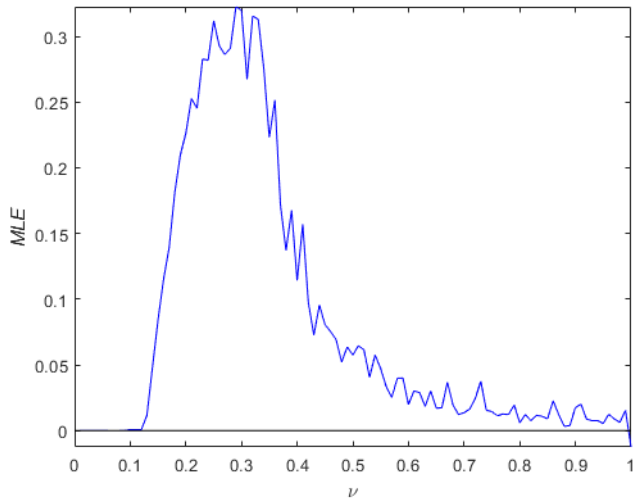

Figure 5. MLE spectrum of the fractional-order system (15) as ν varies

Case2. Non-commensurate fractional-order

Now, we study the dynamic behavior of the system (15) in the non-commensurate fractional-order case. Fix $b_{31} = 0.01$, $b_{22} = 0.08$, $b_{23} = 0.01$, $b_{12} = 0.08$, $b_{32} = 0.04$, $r = 3.4$, $\nu_1 = 0.21$, $\nu_3 = 0.34$, and vary ν_2 from 0 to 1. Figure 7 shows the bifurcation diagram and its corresponding MLE spectrum. By examining the MLE and the bifurcation diagram displayed in Figure 7, we find that the fractional-order discrete system (15) may experience two scenarios according to the values of ν_2. When $\nu_2 \in [0, 0.18]$, the MLE is negative or equal to zero, then the state of system (15) is periodic, but when $\nu_2 \in [0.18, 0.91]$, the MLE is positive, then the system (15) exhibits robust chaos across this parameter ν_2 range. Finally, when $\nu_2 > 0.91$, the MLE is equal to zero once again, meaning that the system (15) is periodic.

Now, we study the dynamics of the discrete incommensurate fractional-order system (15) when ν_1 varies. Figure 8 represents the bifurcation diagram and its corresponding MLE spectrum for $\nu_2 = 0.3$, and $\nu_3 = 0.4$. We see that the MLE is positive when $\nu_1 \in [0, 0.4]$, and then the system (15) exhibits robust chaos, but when $\nu_1 > 0.4$, the chaotic state arises with the appearance of the periodic state, as shown by the MLE's oscillation between positive and negative values.

Moreover, to show the dynamic behavior of the non-commensurate fractional-order system (15), we vary ν_3 when $\nu_1 = 0.5$, and $\nu_2 = 0.6$. Figure 9 shows the bifurcation diagram and the MLE spectrum of the fractional-order system (15). As we can see, at the minimum values of ν_3, the discrete non-commensurate fractional-order system (15) has a negative or zero MLE, but when ν_3 increases, the MLE has strictly positive values, meaning that the system transitions from a periodic state to a chaotic state.

To provide further clarification, the phase portrait of the non-commensurate fractional-order system (15) is shown in Figure 10 for different values of (ν_1, ν_2, ν_3).

5 0-1 test and complexity of the fractional-order system

Test 0-1 for Chaos

The 0-1 test is an efficient technique to detect chaos in discrete fractional-order systems. We review the steps of this algorithm [40]. Based on the state $x(n)$ in Eq. (16), we construct the translation

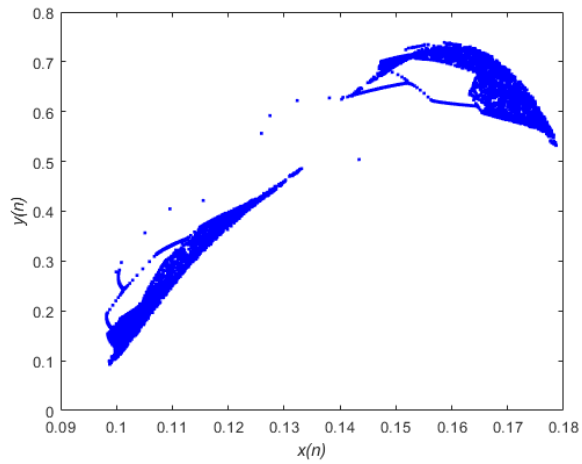

(a) for $\nu = 0.12$

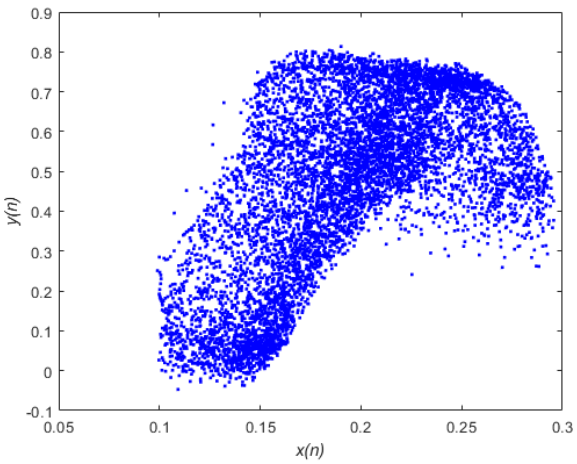

(b) for $\nu = 0.24$

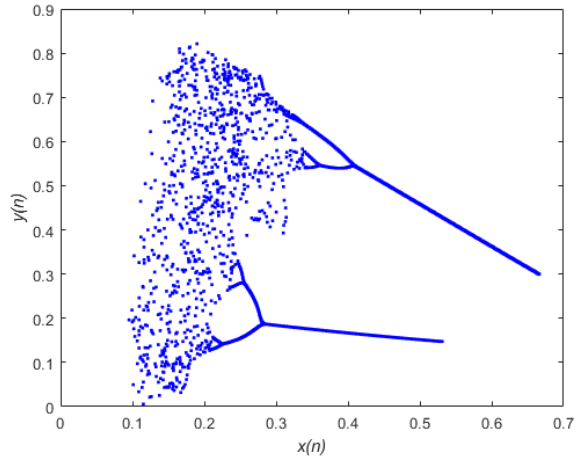

(c) for $\nu = 0.36$

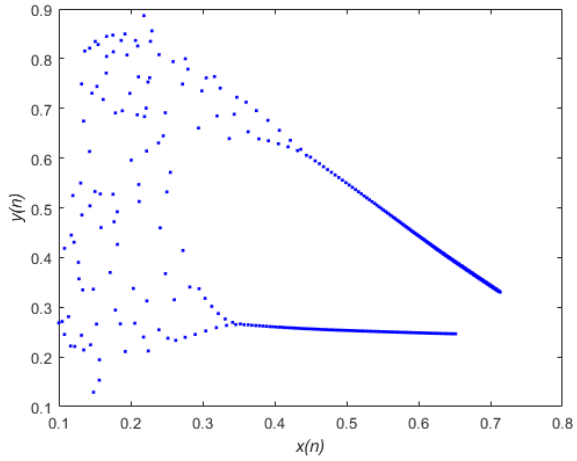

(d) for $\nu = 0.75$

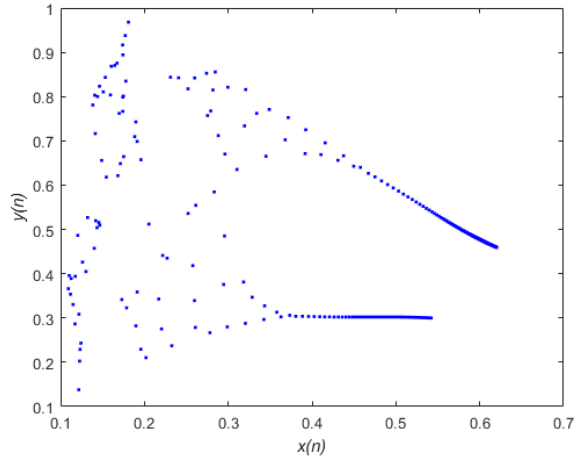

(e) for $\nu = 0.89$

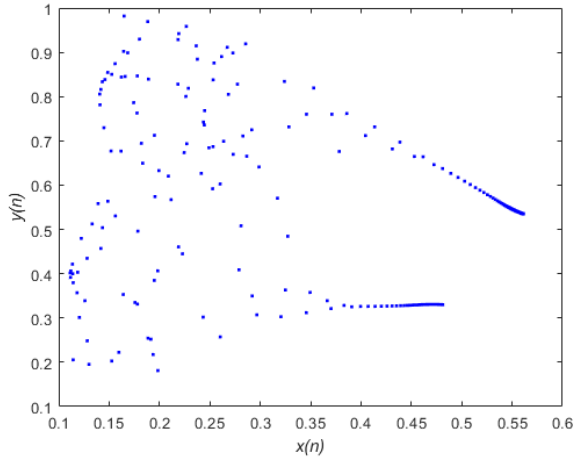

(f) for $\nu = 0.96$

Figure 6. Attractor of the fractional-order discrete system (15) for different values of ν

components p_c and q_c as follows

$$p_c(n) = \sum_{k=1}^{n} x(k)\cos(kc), \qquad q_c(n) = \sum_{k=1}^{n} x(k)\sin(kc), \tag{21}$$

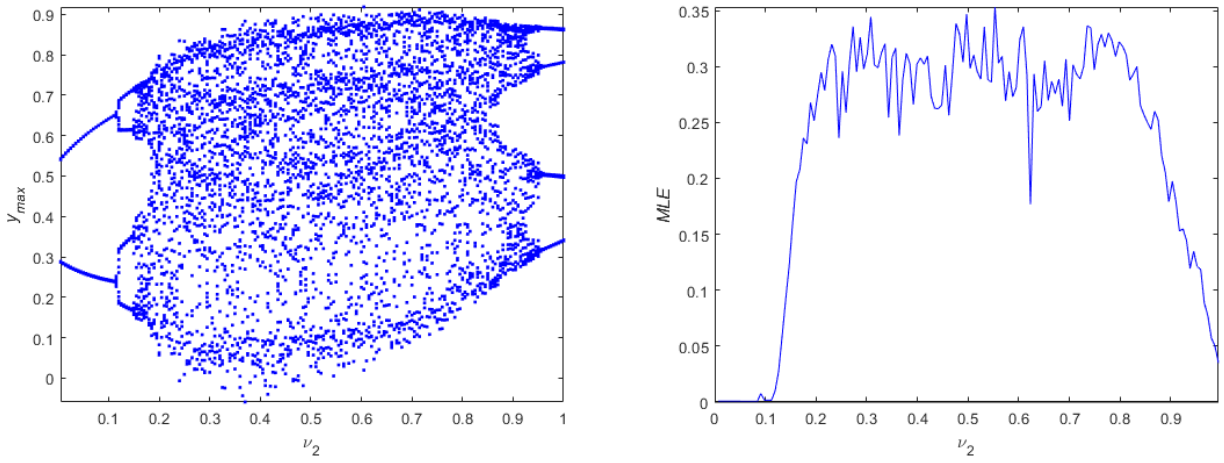

(a) Bifurcation diagram as ν_2 varies (b) The MLE spectrum as ν_2 varies

Figure 7. Bifurcation and MLE spectrum diagrams for ν_2

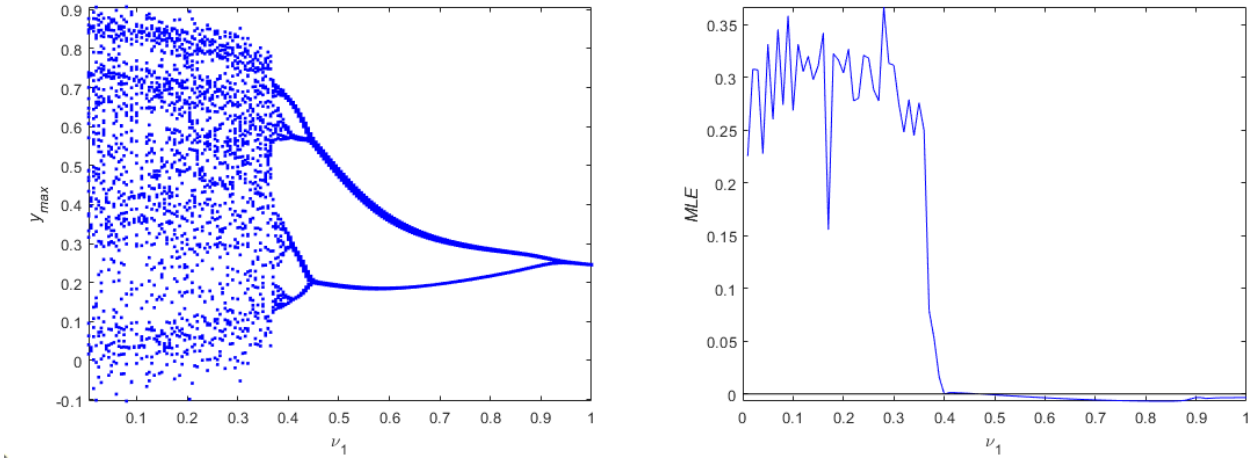

(a) Bifurcation diagram as ν_1 varies (b) The MLE spectrum as ν_1 varies

Figure 8. Bifurcation and MLE spectrum diagrams for ν_1

where c is a random constant selected from $(0, \pi)$. We can plot p_c and q_c to verify if the chaotic behavior appears when the bounded motions of p_c and q_c imply regular dynamics, whereas the asymptotic Brownian movement implies chaotic dynamics. Figure 11 shows the results.

C_0 complexity

We can evaluate the complexity of a discrete chaotic system via the C_0 algorithm. Assume that $x(j)$ $(j = 0, 1, \ldots, L-1$, where $L \geq 1$ is a sequence of data selected from the discrete system (15). The corresponding discrete Fourier transformation for this data set is given by

$$X_L(k) = \sum_{j=0}^{L-1} x(j) \exp\left[\frac{-2\pi ijk}{L}\right], \tag{22}$$

where $k = 0, 1, \ldots, L-1$, and i is the imaginary unit. Next, the mean of X_L is obtained as

$$M_L = \frac{1}{L} \sum_{k=0}^{L-1} |X_L(k)|^2. \tag{23}$$

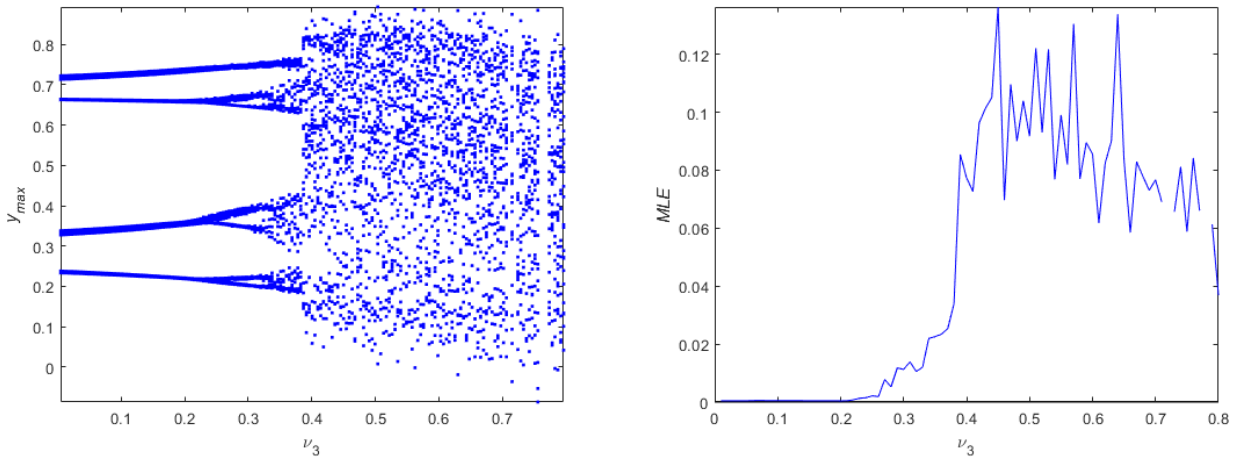

(a) Bifurcation diagram as ν_3 varies

(b) The MLE spectrum as ν_3 varies

Figure 9. Bifurcation and MLE spectrum diagrams for ν_3

A control parameter υ is introduced as

$$\tilde{X}_L(k) = \begin{cases} X(k) & \text{if} \quad |X_L(k)|^2 > \upsilon M_L, \\ 0 & \text{if} \quad |X_L(k)|^2 \leq \upsilon M_L. \end{cases} \tag{24}$$

The inverse discrete Fourier transformation of $\tilde{X}_L$ is given by

$$\tilde{x}(j) = \frac{1}{L} \sum_{k=0}^{L-1} \tilde{X}_L(k) \exp[\frac{2\pi i j k}{L}], \tag{25}$$

where $j = 0, 1, \ldots, L-1$. Finally, the C_0 complexity is defined as [41]

$$C_0(x, \upsilon, L) = \frac{\sum_{j=0}^{L-1} |x(j) - \tilde{x}(j)|^2}{\sum_{j=0}^{L-1} |x(j)|^2}. \tag{26}$$

Fix $b_{31} = 0.01$, $b_{22} = 0.08$, $b_{23} = 0.01$, $b_{12} = 0.08$, $b_{32} = 0.04$, $r = 3.4$, $\nu_1 = 0.21$, $\nu_3 = 0.34$, the C_0 complexity with respect to fractional-order ν_2 is shown in Figure 12. As can be observed, the complexity of the fractional-order system (15) changes as we vary ν_2, which agrees well with the findings of the bifurcation diagram and maximum Lyapunov exponent.

Approximate entropy

In the dynamical analysis of nonlinear chaotic systems, approximate entropy (ApEn) is an efficient technique that allows us to measure the level of complexity in chaotic systems. In brief, we review the steps to evaluate the approximate entropy for the fractional-order system (15). We select a sequence of data $x(j)$ $(j = 1, 2, \ldots, N)$ from the system (15), then we construct a sequence of vectors $\mu(1), \mu(2), \ldots, \mu(N - m + 1)$ as: $\mu(j) = [x(j), x(j+1), x(j+2), \ldots, x(j+m-1)]$, and $\mu(i) = [x(i), x(i+1), x(i+2), \ldots, x(i+m-1)]$, where m is a positive integer representing the embedding dimension. The distance between two vectors is given by

$$d\left(\mu(j), \mu(i)\right) = \max\{|x(j+s-1) - x(i+s-1)|\}, \quad s = 1, 2, \ldots, m. \tag{27}$$

We take a non-negative number r and we denote by L the number of j where $d\left(\mu(j), \mu(i)\right) \leq r$, the approximate entropy is defined as [42]

$$\text{ApEn} = \Lambda^m(r) - \Lambda^{m+1}(r), \tag{28}$$

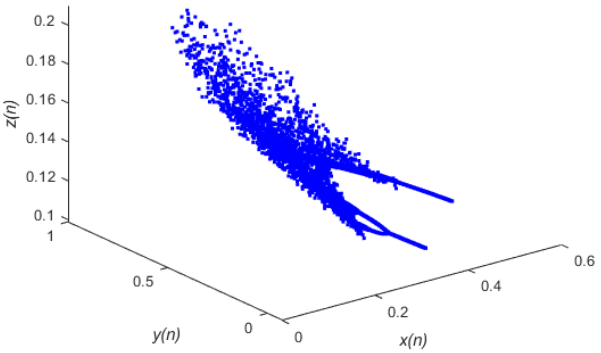

(a) for $(\nu_1, \nu_2, \nu_3) = (0.3, 0.3, 0.4)$

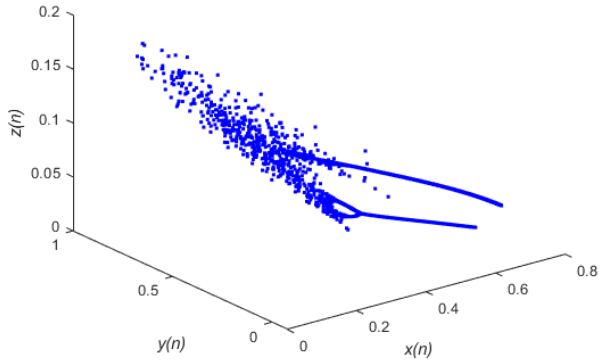

(b) for $(\nu_1, \nu_2, \nu_3) = (0.4, 0.55, 0.6)$

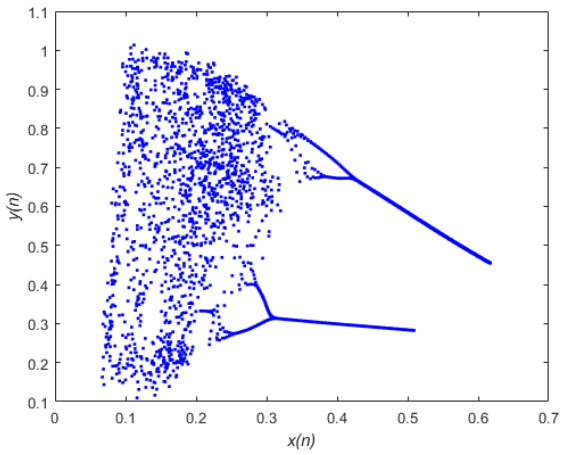

(c) for $(\nu_1, \nu_2, \nu_3) = (0.6, 0.96, 0.58)$

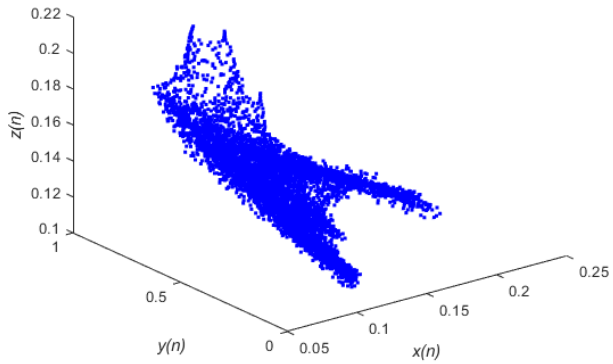

(d) for $(\nu_1, \nu_2, \nu_3) = (0.4, 0.9, 0.4)$

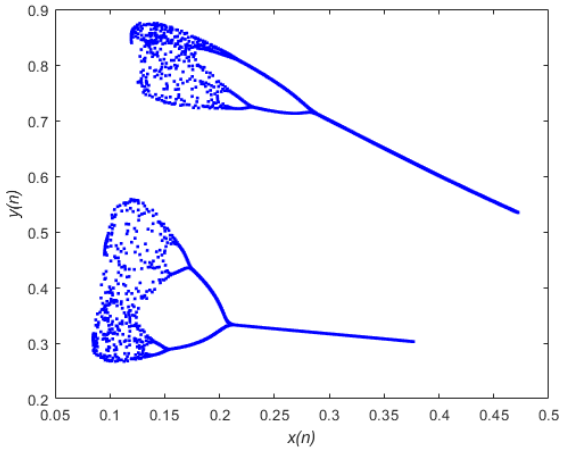

(e) for $(\nu_1, \nu_2, \nu_3) = (0.6, 0.9, 0.4)$

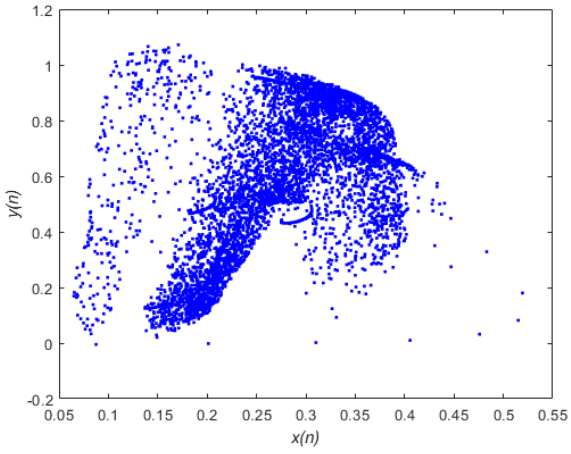

(f) for $(\nu_1, \nu_2, \nu_3) = (0.36, 0.98, 0.7)$

Figure 10. Attractor of the non-commensurate fractional-order system (15)

where $\Lambda^m(r)$ is determined as

$$\Lambda^m(r) = \frac{1}{N-m+1} \sum_{j=1}^{N-m+1} \log Q_j^m(r), \tag{29}$$

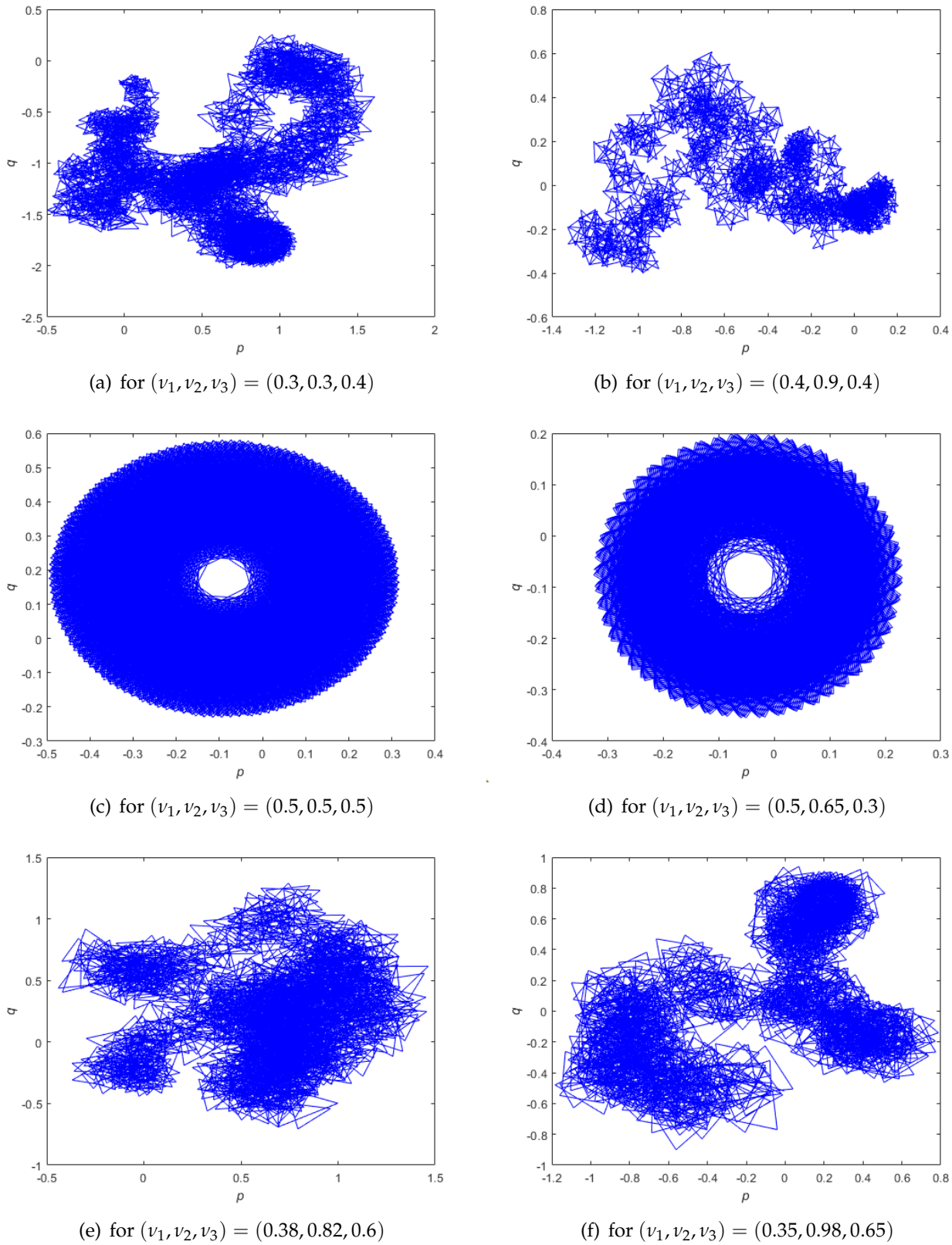

(a) for $(\nu_1, \nu_2, \nu_3) = (0.3, 0.3, 0.4)$

(b) for $(\nu_1, \nu_2, \nu_3) = (0.4, 0.9, 0.4)$

(c) for $(\nu_1, \nu_2, \nu_3) = (0.5, 0.5, 0.5)$

(d) for $(\nu_1, \nu_2, \nu_3) = (0.5, 0.65, 0.3)$

(e) for $(\nu_1, \nu_2, \nu_3) = (0.38, 0.82, 0.6)$

(f) for $(\nu_1, \nu_2, \nu_3) = (0.35, 0.98, 0.65)$

Figure 11. Dynamics of the translation components p_c and q_c

and $Q_j^m(r)$ is given by

$$Q_j^m(r) = \frac{L}{N - m + 1}. \tag{30}$$

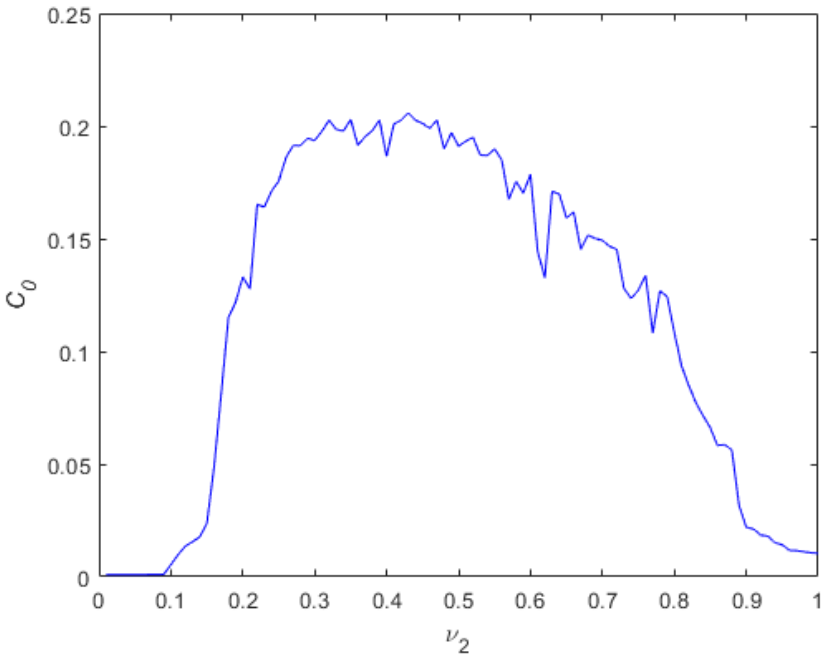

Figure 12. C_0 complexity of the fractional-order system (15) as ν_2 varies

Fix $b_{31} = 0.01$, $b_{22} = 0.08$, $b_{23} = 0.01$, $b_{12} = 0.08$, $b_{32} = 0.04$, $r = 3.4$, $\nu_1 = 0.21$, and $\nu_3 = 0.34$, the approximate entropy of the fractional-order system (15) with respect to ν_2 is shown in Figure 13. As can be observed, the approximate entropy of the system (15) changes when we vary ν_2, which agrees well with the findings derived in Section 4.

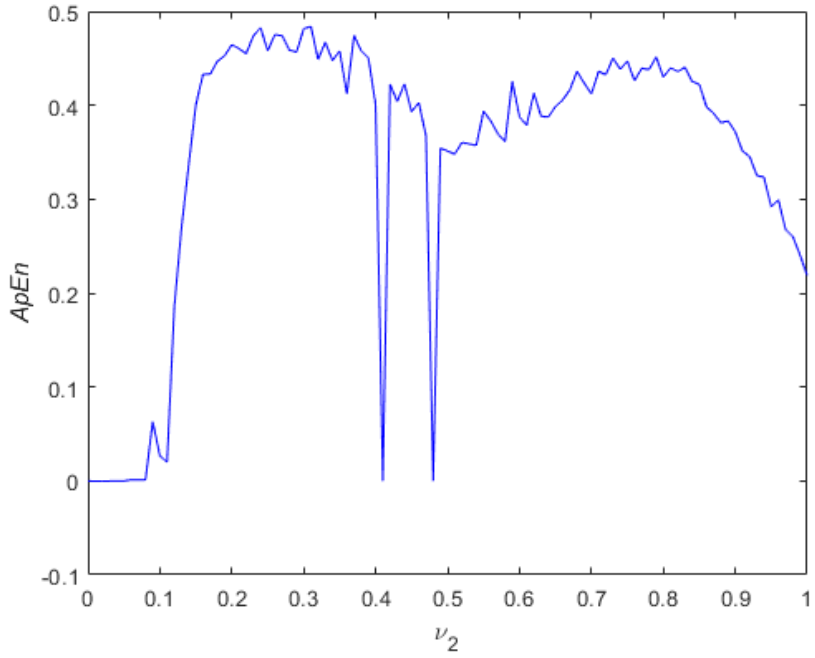

Figure 13. Approximate entropy of the fractional-order system (15) as ν_2 varies

6 Control scheme for the discrete fractional-order chaotic system

This section is devoted to the chaos control in the discrete commensurate fractional-order system (15) where an active fractional-order controller is designed.
The fractional-order system (15) with the controller $(u_1, u_2, u_3)^T$ is described as

$$\begin{cases} {}^{C}\Delta_{\theta}^{\nu} x(\tau) = x(\tau+\nu-1)\left(1-(x(\tau+\nu-1)+y(\tau+\nu-1)+z(\tau+\nu-1))\right) \\ \qquad\qquad -b_{12}x(\tau+\nu-1)y(\tau+\nu-1)+u_1(\tau+\nu-1), \\ {}^{C}\Delta_{\theta}^{\nu} y(\tau) = ry(\tau+\nu-1)\left(1-(x(\tau+\nu-1)+y(\tau+\nu-1)+z(\tau+\nu-1))\right) \\ \qquad\qquad -b_{22}x(\tau+\nu-1)y(\tau+\nu-1)-b_{23}y(\tau+\nu-1)z(\tau+\nu-1)+u_2(\tau+\nu-1), \\ {}^{C}\Delta_{\theta}^{\nu} z(\tau) = b_{31}y(\tau+\nu-1)z(\tau+\nu-1)-b_{32}z(\tau+\nu-1)+u_3(\tau+\nu-1), \end{cases} \tag{31}$$

where $\tau \in \mathbb{N}(\alpha-\nu)+1$. Our goal is to design a suitable control law that guarantees that all states of the fractional-order system (15) converge towards zero asymptotically.

Theorem 4 *The discrete fractional-order chaotic system* (15) *is stabilized under the following* 3*-D control law*

$$\begin{cases} u_1(\tau) = x(\tau)\left(x(\tau)+y(\tau)+z(\tau)-2\right)+b_{12}x(\tau)y(\tau), \\ u_2(\tau) = ry(\tau)\left(x(\tau)+y(\tau)+z(\tau)\right)-4y(\tau)+b_{22}x(\tau)y(\tau)+b_{23}y(\tau)z(\tau), \\ u_3(\tau) = -0.96z(\tau)-b_{31}y(\tau)z(\tau). \end{cases} \tag{32}$$

Proof Substituting (32) into (31), we obtain

$$\begin{cases} {}^{C}\Delta_{\theta}^{\gamma} x(\tau) = -x(\tau+\nu-1), \\ {}^{C}\Delta_{\theta}^{\gamma} y(\tau) = (r-4)y(\tau+\nu-1), \\ {}^{C}\Delta_{\theta}^{\gamma} z(\tau) = -(b_{32}+0.96)z(\tau+\nu-1), \end{cases} \tag{33}$$

which can be expressed as

$${}^{C}\Delta_{\theta}^{\nu}\left(x(\tau),y(\tau),z(\tau)\right)^T = N\left(x(\tau),y(\tau),z(\tau)\right)^T, \tag{34}$$

where

$$N = \begin{pmatrix} -1 & 0 & 0 \\ 0 & r-4 & 0 \\ 0 & 0 & -(b_{32}+0.96) \end{pmatrix}. \tag{35}$$

Then, the eigenvalues of the matrix N are $\lambda_1 = -1$, $\lambda_2 = r-4$, $\lambda_3 = -(b_{32}+0.96)$. It is easy to verify that λ_j $(j = 1,2,3)$ satisfy

$$|\arg\lambda_j| = \pi > \nu\frac{\pi}{2}, \quad \text{and} \quad |\lambda_j| < \left(2\cos\frac{|\arg\lambda_j|-\pi}{2-\nu}\right)^{\nu}, \quad \nu \in (0,1). \tag{36}$$

Therefore, using Theorem 2, we can conclude that the zero equilibrium of (34) is asymptotically stable. Thus, the stabilization of the fractional-order discrete system (31) is achieved.

For numerical simulations, the parameter values are selected as $b_{31} = 0.01$, $b_{22} = 0.08$, $b_{23} = 0.01$, $b_{12} = 0.08$, $b_{32} = 0.04$, $r = 3.4$, and the fractional-order as $\nu = 0.82$, under the initial conditions $(x(0),y(0),z(0)) = (0.1,0.2,0.25)$. Figure 14 shows the time evolution of the controlled states of the system (31). As we can see, the states $x(n)$, $y(n)$, and $z(n)$ converge towards zero asymptotically. This shows the accuracy and feasibility of the constructed control scheme.

7 Data analysis, results and discussion

We conclude our analysis using time-series plots in order to obtain a better comprehension of the proposed fractional-order biological model. For the parameter values mentioned in Table 1, Figure 15(a) and Figure 16(a) show the time evolution of cancer cells (C), healthy CD4+T lymphocyte cells (S), and

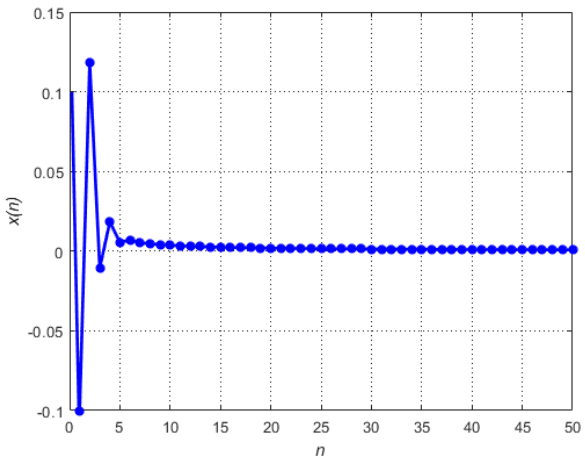

(a) $x(n)$ with n

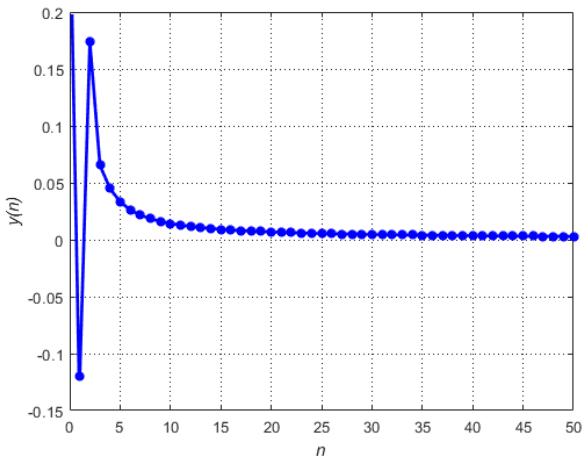

(b) $y(n)$ with n

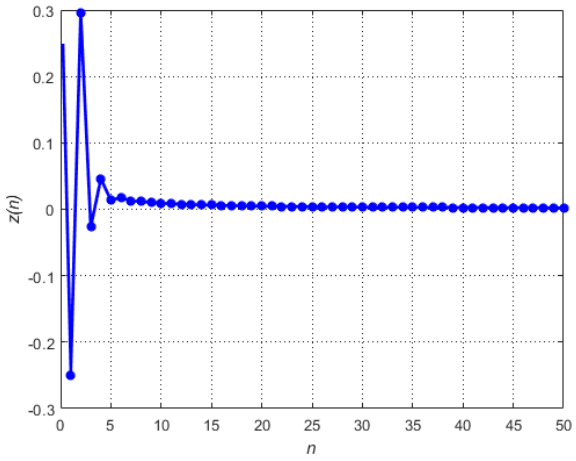

(c) $z(n)$ with n

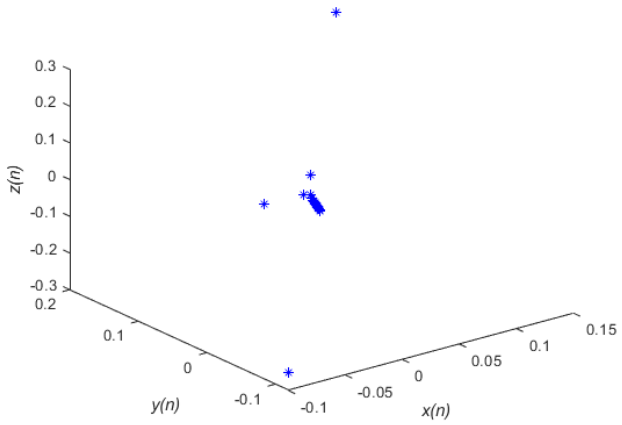

(d) phase space

Figure 14. Evolution of the controlled states of the commensurate fractional-order system (31) for $\nu = 0.82$

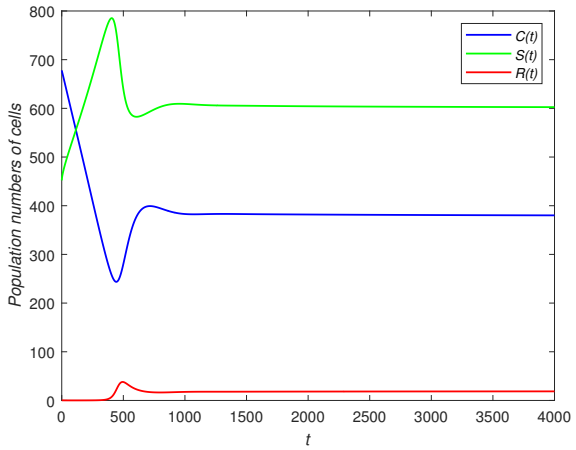

(a) Continuous F-O model for $\nu_1 = \nu_2 = \nu_3 = 0.69$

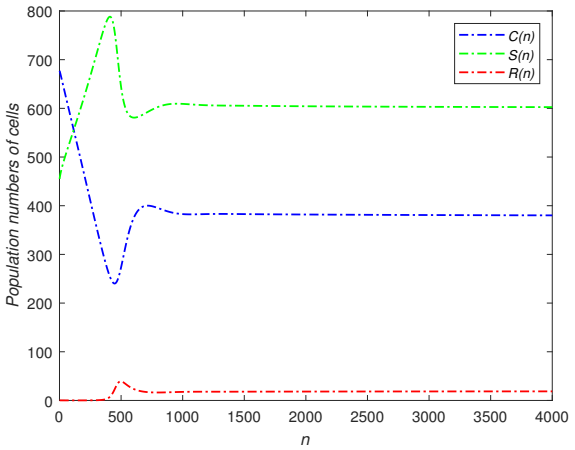

(b) Discrete F-O model for $\nu_1 = \nu_2 = \nu_3 = 0.69$

Figure 15. Time series of the fractional-order (F-O) models

Table 3. The minimum and maximum numbers of biological cells in the commensurate case $\nu_1 = \nu_2 = \nu_3 = 0.69$

Biological cells	Continuous fractional-order model (min,max)	Discrete fractional-order model (min,max)	Average number of biological cells
Cancer cells C	$(245, 678)$	$(240, 678)$	380
Healthy cells S	$(452, 784)$	$(452, 787)$	602
HIV-Infected Cells R	$(0, 37)$	$(0, 38)$	18

HIV-infected cells (R) of the continuous fractional-order model (10) for $\nu_1 = \nu_2 = \nu_3 = 0.69$ (commensurate fractional-order) and $(\nu_1, \nu_2, \nu_3) = (0.91, 0.92, 0.93)$ (non-commensurate fractional-order), respectively, while the time series plots obtained from the corresponding discrete fractional-order system constructed using the Caputo-like delta difference operator are shown in Figure 15(b) and Figure 16(b), respectively. By comparing the findings, we find that the results obtained from the continuous fractional-order system are identical to the results of the discrete fractional system. Using the time series results, we expect the population numbers of the three biological cells in sufficient time when the oscillations are stabilized for commensurate and non-commensurate fractional orders. The results are shown in Table 3 and Table 4. The average number of cell populations can help biologists collect statistical data to fight the disease.

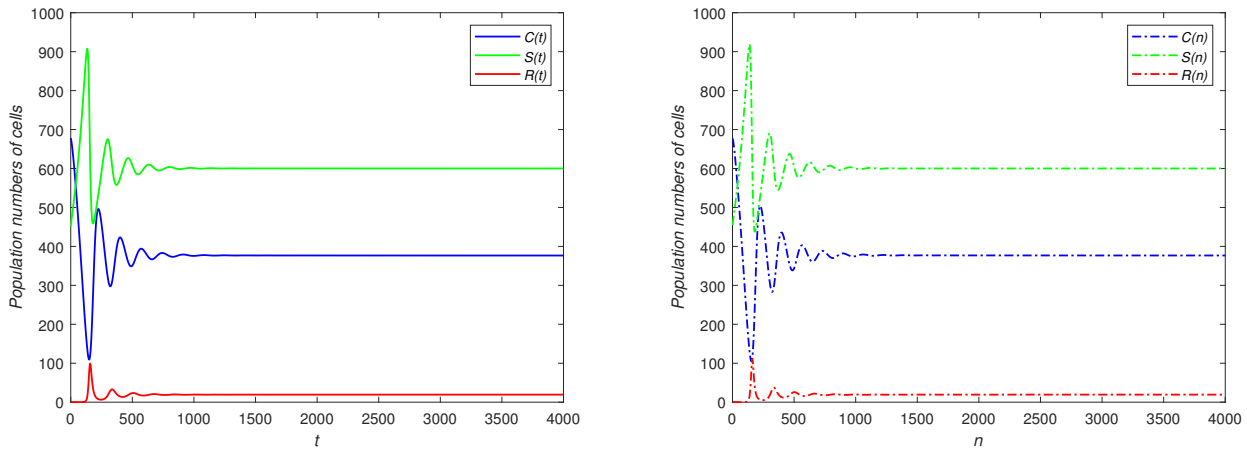

(a) Continuous model for $(\nu_1, \nu_2, \nu_3) = (0.91, 0.92, 0.93)$ (b) Discrete model for $(\nu_1, \nu_2, \nu_3) = (0.91, 0.92, 0.93)$

Figure 16. Time series of the fractional-order models

Table 4. The numbers of biological cells in the non-commensurate case $(\nu_1, \nu_2, \nu_3) = (0.91, 0.92, 0.93)$

Biological cells	Continuous fractional-order model (min,max)	Discrete fractional-order model (min,max)	Average number of biological cells
Cancer cells C	$(111, 678)$	$(114, 678)$	376
Healthy cells S	$(452, 907)$	$(452, 918)$	602
HIV-Infected Cells R	$(0, 99)$	$(0, 110)$	19

8 Conclusion

In this paper, a 3-D discrete-time fractional-order chaotic system which is composed of cancer, healthy, and HIV-infected cells is analyzed. We demonstrated that the biological system can exhibit chaotic behavior

for some parameter values. The dynamical behaviors are analyzed using powerful nonlinear dynamic analysis tools such as phase plots, bifurcation diagrams, and the maximum Lyapunov exponent, which show that the discrete system constructed using the Caputo-like-delta difference operator has rich dynamic behaviors. Furthermore, an efficient fractional-order controller is designed to stabilize the chaotic motions of the discrete system states. In biological systems, chaos and bifurcation are common phenomena. The biological implications of chaos and bifurcation in such a model involve studying population dynamics, where bifurcation points represent critical transitions. When the parameters change, the system can shift from a stable state to a chaotic state. Moreover, the chaotic dynamics can lead to population fluctuations, and then the extinction risk increases. Stable equilibria in a dynamical system are essential for species persistence, and bifurcation can lead to unstable fixed points. Thus, the transition to a chaotic state can lead to complex and unpredictable behavior. Understanding bifurcation behavior allows us to suggest efficient strategies to control chaotic dynamics in biological systems for the reasons stated above. Furthermore, researchers and biologists can use these insights to explain many biologically observed HIV-cancer states, including stable, periodic, quasiperiodic, and chaotic behaviors. Then, they can develop control techniques for suppressing chaos in biological dynamical systems.
In the near future, we plan to work on this topic, since we believe that controlling or suppressing chaos in fractional-order HIV-1 models involving AIDS-related cancer cells can help biologists and scientists in the fight against AIDS and cancer.

Declarations

Use of AI tools

he authors declare that they have not used Artificial Intelligence (AI) tools in the creation of this article.

Data availability statement

There are no external data associated with this article.

Ethical approval (optional)

The authors state that this research complies with ethical standards. This research does not involve either human participants or animals.

Consent for publication

Not applicable

Conflicts of interest

The authors declare that they have no conflict of interest.

Funding

No funding was received for this research.

Author's contributions

H.N.: Conceptualization, Methodology, Writing-Original draft preparation, Software. H.T.: Data Curation, Methodology, Supervision, Writing-original draft preparation, Validation. All authors have read and agreed to the published version of the manuscript.

Acknowledgements

The authors like to express their gratitude to everyone who helped to complete this research work.

References

[1] Daley, D.J. and Gani, J.M. *Epidemic Modelling: An Introduction*. Cambridge University Press: New York, (1999).

[2] Duarte, J., Januário, C., Martins, N., Ramos, C.C., Rodrigues, C. and Sardanyés, J. Optimal homotopy analysis of a chaotic HIV-1 model incorporating AIDS-related cancer cells. *Numerical Algorithms*, 77, 261–88, (2018). [CrossRef]

[3] Boshoff, C. and Weiss, R. AIDS-related malignancies. *Nature Reviews Cancer*, 2, 373–382, (2002). [CrossRef]

[4] Callaway, D.S. and Perelson, A.S. HIV-1 infection and low steady state viral loads. *Bulletin of Mathematical Biology*, 64(1), 29–64, (2002). [CrossRef]

[5] Naik, P.A., Yeolekar, B.M., Qureshi, S., Yeolekar, M. and Madzvamuse, A. Modeling and analysis of the fractional-order epidemic model to investigate mutual influence in HIV/HCV co-infection. *Nonlinear Dynamics*, 112, 11679–11710, (2024). [CrossRef]

[6] Saeed, T., Djeddi, K., Guirao, J.L., Alsulami, H.H. and Alhodaly, M.S. A discrete dynamics approach to a tumor system. *Mathematics*, 10(10), 1774, (2022). [CrossRef]

[7] Rogosin, S. and Dubatovskaya, M. Fractional calculus in Russia at the end of XIX century. *Mathematics*, 9(15), 1736, (2021). [CrossRef]

[8] Miller, K.S. and Ross, B. *An Introduction to the Fractional Calculus and Fractional Differential Equations*. Wiley-Interscience: New York, (1993).

[9] Samko, S.G., Kilbas, A.A. and Marichev, O.I. *Fractional Integrals and Derivatives: Theory and Applications*. Gordon and Breach Science Publishers: Philadelphia, USA, (1993).

[10] Kilbas, A.A., Srivastava, H.M. and Trujillo, J.J. *Theory and Applications of Fractional Differential Equations* (Vol. 204). Elsevier: Tokyo, (2006).

[11] Caputo, M. and Fabrizio, M. A new definition of fractional derivative without singular kernel. *Progress in Fractional Differentiation and Applications*, 1(2), 73-85, (2015). [CrossRef]

[12] Atangana, A. and Baleanu, D. New fractional derivatives with nonlocal and non-singular kernel: theory and application to heat transfer model. *Thermal Science*, 20(2), 763-769, (2016). [CrossRef]

[13] Debbouche, N., Ouannas, A., Grassi, G., Al-Hussein, A.B.A., Tahir, F.R., Saad, K.M. and Aly, A.A. Chaos in cancer tumor growth model with commensurate and incommensurate fractional-order derivatives. *Computational and Mathematical Methods in Medicine*, 2022, 5227503, (2022). [CrossRef]

[14] Chamgoué, A.C., Ngueuteu, G.S.M., Yamapi, R. and Woafo, P. Memory effect in a self-sustained birhythmic biological system. *Chaos, Solitons & Fractals*, 109, 160-169, (2018). [CrossRef]

[15] Gholami, M., Ghaziani, R.K. and Eskandari, Z. Three-dimensional fractional system with the stability condition and chaos control. *Mathematical Modelling and Numerical Simulation with Applications*, 2(1), 41-47, (2022). [CrossRef]

[16] Naik, P.A., Yavuz, M., Qureshi, S., Zu, J. and Townley, S. Modeling and analysis of COVID-19 epidemics with treatment in fractional derivatives using real data from Pakistan. *The European Physical Journal Plus*, 135, 795, (2020). [CrossRef]

[17] Naik, P.A. Global dynamics of a fractional-order SIR epidemic model with memory. *International Journal of Biomathematics*, 13(08), 2050071, (2020). [CrossRef]

[18] Yapışkan, D. and Eroğlu, B.B.İ. Fractional-order brucellosis transmission model between interspecies with a saturated incidence rate. *Bulletin of Biomathematics*, 2(1), 114-132, (2024). [CrossRef]

[19] Atede, A.O., Omame, A. and Inyama, S.C. A fractional order vaccination model for COVID-19 incorporating environmental transmission: a case study using Nigerian data. *Bulletin of Biomathematics*, 1(1), 78-110, (2023). [CrossRef]

[20] Omame, A., Onyenegecha, I.P., Raezah, A.A. and Rihan, F.A. Co-dynamics of COVID-19 and viral

hepatitis B using a mathematical model of non-integer order: impact of vaccination. *Fractal and Fractional*, 7(7), 544, (2023). [CrossRef]

[21] Nwajeri, U.K., Omame, A. and Onyenegecha, C.P. Analysis of a fractional order model for HPV and CT co-infection. *Results in Physics*, 28, 104643, (2021). [CrossRef]

[22] Omame, A. and Zaman, F.D. Analytic solution of a fractional order mathematical model for tumour with polyclonality and cell mutation. *Partial Differential Equations in Applied Mathematics*, 8, 100545, (2023). [CrossRef]

[23] Munir, S., Omame, A. and Zaman, F.D. Mathematical analysis of a time-fractional coupled tumour model using Laplace and finite Fourier transforms. *Physica Scripta*, 99(2), 025241, (2024). [CrossRef]

[24] Holm, M. *The Theory of Discrete Fractional Calculus: Development and Application*. Ph.D. Thesis, Department of Mathematics, The University of Nebraska-Lincoln, (2011). [https://digitalcommons.unl.edu/mathstudent/27/]

[25] Podlubny, I. *Fractional Differential Equations* (Vol. 198). Academic Press: San Diego, (1999).

[26] Diaz, J.B. and Osler, T.J. Differences of fractional order. *Mathematics of Computation*, 28(125), 185-202, (1974). [CrossRef]

[27] Atici, F.M. and Eloe, P. Discrete fractional calculus with the nabla operator. *Electronic Journal of Qualitative Theory of Differential Equations*, 3, 1-12, (2009). [CrossRef]

[28] Abdeljawad, T. On Riemann and Caputo fractional differences. *Computers & Mathematics with Applications*, 62(3), 1602-1611, (2011). [CrossRef]

[29] Abdeljawad, T., Baleanu, D., Jarad, F. and Agarwal, R.P. Fractional sums and differences with binomial coefficients. *Discrete Dynamics in Nature and Society*, 2013, 104173, (2013). [CrossRef]

[30] Andreichenko, K.P., Smarun, A.B. and Andreichenko, D.K. Dynamical modelling of linear discrete-continuous systems. *Journal of Applied Mathematics and Mechanics*, 64(2), 177-188, (2000). [CrossRef]

[31] Goodrich, C. and Peterson, A.C. *Discrete Fractional Calculus*. Springer Cham: Switzerland, (2015). [CrossRef]

[32] Devaney, R. *An Introduction to Chaotic Dynamical Systems*. CRC Press: USA, (2003). [CrossRef]

[33] Strogatz, S.H. *Nonlinear Dynamics and Chaos With Applications to Physics, Biology, Chemistry, and Engineering*. CRC Press: USA, (2018). [CrossRef]

[34] Anastassiou, G.A. Principles of delta fractional calculus on time scales and inequalities. *Mathematical and Computer Modelling*, 52(3-4), 556-566, (2010). [CrossRef]

[35] Cermák, J., Gyori, I. and Nechvátal, L. On explicit stability conditions for a linear fractional difference system. *Fractional Calculus and Applied Analysis*, 18, 651-672, (2015). [CrossRef]

[36] Lou, J., Ruggeri, T. and Tebaldi, C. Modeling cancer in HIV-1 infected individuals: equilibria, cycles and chaotic behavior. *Mathematical Biosciences and Engineering*, 3(2), 313-324, (2006). [CrossRef]

[37] Naik, P.A., Owolabi, K.M., Yavuz, M. and Zu, J. Chaotic dynamics of a fractional order HIV-1 model involving AIDS-related cancer cells. *Chaos, Solitons & Fractals*, 140, 110272, (2020). [CrossRef]

[38] Cafagna, D. and Grassi, G. Fractional-order systems without equilibria: the first example of hyperchaos and its application to synchronization. *Chinese Physics B*, 24(8), 080502, (2015). [CrossRef]

[39] Wu, G.C. and Baleanu, D. Jacobian matrix algorithm for Lyapunov exponents of the discrete fractional maps. *Communications in Nonlinear Science and Numerical Simulation*, 22(1-3), 95-100, (2015). [CrossRef]

[40] Sun, K.H., Liu, X. and Zhu, C.X. The 0-1 test algorithm for chaos and its applications. *Chinese Physics B*, 19(11), 110510, (2010). [CrossRef]

[41] En-Hua, S., Zhi-Jie, C. and Fan-Ji, G. Mathematical foundation of a new complexity measure. *Applied Mathematics and Mechanics*, 26, 1188-1196, (2005). [CrossRef]

[42] Pincus, S.M. Approximate entropy as a measure of system complexity. *Proceedings of the National Academy of Sciences*, 88(6), 2297-2301, (1991). [CrossRef]

Mathematical Modelling and Numerical Simulation with Applications (MMNSA)
(https://dergipark.org.tr/en/pub/mmnsa)

How to cite this article: Nabil, H. & Tayeb, H. (2024). A three-dimensional discrete fractional-order HIV-1 model related to cancer cells, dynamical analysis and chaos control. *Mathematical Modelling and Numerical Simulation with Applications*, 4(3), 256-279. https://doi.org/10.53391/mmnsa.1484994

Mathematical Modelling and Numerical Simulation with Applications, 2024, 4(3), 280–295

https://dergipark.org.tr/en/pub/mmnsa

ISSN Online: 2791-8564 / Open Access

https://doi.org/10.53391/mmnsa.1503948

RESEARCH PAPER

Mathematical model for IP_3 dependent calcium oscillations and mitochondrial associate membranes in non-excitable cells

Neeraj Manhas [1,*,‡]

[1]Department of Mathematics, National Institute of Technology Raipur, Chhattisgarh, 492010, India

* Corresponding Author

‡ nmanhas.maths@nitrr.ac.in (Neeraj Manhas)

Abstract

Theoretical studies on calcium oscillations within the cytosolic $[Ca^{2+}]$, and mitochondria $[Ca^{2+}]_{mit}$ have been conducted using a mathematical model-based approach. The model incorporates the mechanism of calcium-induced calcium release (CICR) through the activation of inositol-trisphosphate receptors (IPR), with a focus on the endoplasmic reticulum (ER) as an internal calcium store. The production of 1,4,5 inositol-trisphosphate (IP_3) through the phospholipase *C* isoforms and its degradation via Ca^{2+} are considered, with IP_3 playing a crucial role in modulating calcium release from the ER. The model includes a simple kinetic mechanism for mitochondrial calcium uptake, release and physical connections between the ER and mitochondria, known as mitochondrial associate membrane complexes (MAMs), which influence cellular calcium homeostasis. Bifurcation analysis is used to explore the different dynamic properties of the model, identifying various regimes of oscillatory behavior and how these regimes change in response to different levels of stimulation, highlighting the complex regulatory mechanisms governing intracellular calcium signaling.

Keywords: Mitochondria-associated membranes; Hopf bifurcation; periodic doubling bifurcation; calcium oscillation

AMS 2020 Classification: 34C23; 92B99; 92-10

1 Introduction

Calcium (Ca^{2+}) contributes to the vast array of various physiology and pathophysiology. The extremely rapid increase in cytosolic Ca^{2+} leads to a multitude of cellular responses, such as release of neurotransmitters, muscle contraction, gene transcription, and cell proliferation [1–4]. Although the fluctuations observed in cytoplasmic Ca^{2+} provided valuable insights into the complexity of Ca^{2+} signaling. However, the toolkit involved in these regulations has a very fine control over its

➤ **Received:** 24.06.2024 ➤ **Revised:** 20.08.2024 ➤ **Accepted:** 23.08.2024 ➤ **Published:** 30.09.2024

components. However, non-excitable cells exhibit Ca^{2+} oscillations of different frequencies and amplitudes on hormone stimulation [5–7]. These Ca^{2+} oscillations are meticulously controlled by a network of receptors, pumps, exchangers, Ca^{2+}-ATPase, etc. The ER has IPR on its membrane. They released Ca^{2+} on activation. Intracellular IP_3 binds to IPR with Ca^{2+} as a co-agonist and opens them. Active IPR mediates the CICR process that enhances cytosolic Ca^{2+}. Physiologically low Ca^{2+} concentrations are required for cell function. Thus, Ca^{2+} is quickly pumped back into the ER lumen through Ca^{2+} ATPase pumps from the sarco / endoplasmic reticulum (SERCA). It is also sent to the extracellular medium by Ca^{2+} ATPase pumps (PMCA). Mitochondria uptakes Ca^{2+} via uniporter (MCU). It releases Ca^{2+} into the cytosol via the Na^{+}/Ca^{2+} exchanger (NCX). Moreover, the direct flow of Ca^{2+} ions occurs from the ER to the mitochondria through MAMs [8, 9].

Mathematical models are powerful tools for advancing scientific knowledge. However, models have an attractive ability to make experimentally testable predictions. In the field of Ca^{2+} dynamics, researchers develop foundational models based on the available data, facilitating Ca^{2+} dynamics within cells. Initially, models were built that have the capability to produce Ca^{2+} oscillations at constant IP_3. For example: to understand rhythmic Ca^{2+} fluctuations, a one-pool model is developed. It includes IPR activation both by Ca^{2+} and constant IP_3 [10]. Atri et al. [11] constructed a biphasic form of the IPR channel, which produces Ca^{2+} oscillation at constant IP_3. Few advanced models of this kind are seen here [12–14]. However, several models pointed out that the activation of IP_3 metabolism by Ca^{2+} could lead to oscillations in IP_3. These models helped to clarify how changes in Ca^{2+} levels might affect the dynamics of IP_3 and cause cells to oscillate. Models of these types are shown here [15, 16]. Furthermore, theoretically, the modelling approaches show that Ca^{2+} oscillations occur in different types of cells: like acinar cells [17–20], hepatocytes [21–23], oocytes [24–26], cardiac myocytes [27–29], neuron [30, 31], fibroblast [32], etc. Regardless of the cell type, mitochondria are necessary for cells to survive [33–35]. Specialized subdomains or MAM, exist in the ER closest to mitochondria. It facilitates the entry of Ca^{2+} ions and lipids into the mitochondria. The physical connection between mitochondria and the ER is quantitatively investigated here [36]. Marhl et al., [37] model served as the framework for that one. It is assumed that MCU perceives Ca^{2+} are thought to be the MAM and the cytosol. Moreover, Moshkforoush et al., [38] Wacquier et al., [39], and Han and Periwal [40] developed models demonstrating Ca^{2+} dynamics oscillations are influenced by ER mitochondrial micro-domains.

However, this article proposes a class II mathematical model for the Ca^{2+} exchange between the cytosol and mitochondria. Experiments with exchangers, uniporters, pumps, Ca^{2+} ATPase, IP_3 dynamics, and IPR validate the model's major components. The goal of this research is to understand the role of MAMs in non-excitable cells. The deterministic modeling technique utilized in this study gives information on the complex Ca^{2+} flow via MAMs and other Ca^{2+} compartments such as the cytosol, ER, and mitochondria, as well as how these routes influence the Ca^{2+} response of each compartment individually. In short, modeling the physiology of non-excitable cells is an effective tool for understanding the relationships outlined above. This study is useful because it provides a comprehensive description of Ca^{2+} signaling in non-excitable cells such as pancreatic acinar cells, hepatocytes, vascular endothelial cells, etc. Overall, this study seeks to analyze the experimental patterns anticipated by the predictions, revealing the process by which agonist concentration turns fundamental rhythmic patterns into complex oscillatory patterns.

The format for the rest of the paper's body is as follows: Following the introduction in Section 1, Section 2 covers the Ca^{2+} toolkit's primary components and describes how to construct the model and create the mathematical equations. Section 3 presents the model's numerical analysis and

outcomes once it has been developed. The argument, conclusions drawn from the model's results, and any potential repercussions are then covered in Section 4.

2 The mathematical model of the problem

This paradigm explains Ca^{2+} release mechanisms in the cytosol, endoplasmic reticulum, and mitochondria, using symbols $[Ca^{2+}]$, $[Ca^{2+}]_{er}$, and $[Ca^{2+}]_{mit}$. It considers fast Ca^{2+} absorption, mitochondrial release, IP_3 generation, degradation, fluxes, leaks, and direct Ca^{2+} exchange from the ER to mitochondria. Then the nonlinear kinetic equations are shown as follows:

$$\begin{aligned}
\frac{d[Ca^{2+}]}{dt} &= (J_{IPR} + J_{ER}) - J_{SERCA} + \delta(J_{IN} - J_{PM}) + J_{NCX} - J_{MCU} - J_{RaM},\\
\frac{d[Ca^{2+}]_{er}}{dt} &= \gamma(-(J_{IPR} + J_{ER}) + J_{SERCA} - J_{MAM}),\\
\frac{d[IP_3]}{dt} &= J_{IP_3prod} - J_{IP_3deg},\\
\frac{d[Ca^{2+}]_{mit}}{dt} &= \tau(J_{MCU} + J_{RaM} - J_{NCX} + J_{MAM}).
\end{aligned} \tag{1}$$

In this model, δ controls the overall calcium flow via plasma membrane, cytoplasm volume to ER volume ratio is γ, and mitochondria volume to cytoplasm volume is τ. The model is solved numerically and analyzed using AUTO [41] and MATLAB 2021b. Also, all the parameters' values are shown in Table 1.

The IPR

The IPR is divided into six states: resting (R), activated (A), shut (S), open (O), and two inactivated (I_1), and (I_2) states. There are four components that make up the IPR. Two binding sites for Ca^{2+} activation, one for Ca^{2+} inactivation, and one for IP_3 are present in each subunit. Ca^{2+} and IP_3 mediate the shift between these states. Consequently, the model equations provided for all states are given below. A thorough explanation of the model is here [42]

$$\begin{aligned}
\frac{dR}{dt} &= \phi_{-2}O - \phi_2[IP_3]R + (k_{-1} + l_{-2})I_1 - \phi_1 R,\\
\frac{dO}{dt} &= \phi_2[IP_3]R - (\phi_{-2} + \phi_4 + \phi_3)O + \phi_{-4}A + k_{-3}S,\\
\frac{dA}{dt} &= \phi_4 O - \phi_{-4}A - \phi_5 A + (k_{-1} + l_{-2})I_2,\\
\frac{dI_1}{dt} &= \phi_1 R - (k_{-1} + l_{-2})I_1,\\
\frac{dI_2}{dt} &= \phi_5 A - (k_{-1} + l_{-2})I_2.
\end{aligned} \tag{2}$$

Here, R, O, A, I_1, I_2 denotes the fraction of receptors in the respective states, and $R + S + O + A + I_1 + I_2 = 1$. All ϕ's that are the functions of $[Ca^{2+}]$ are as follows:

$$\begin{aligned}
\phi_1[Ca^{2+}] &= \frac{(k_1 L_1 + l_2)[Ca^{2+}]}{L_1 + [Ca^{2+}](1 + \frac{L_1}{L_3})},\\
\phi_2[Ca^{2+}] &= \frac{k_2 L_3 + l_4[Ca^{2+}]}{L_3 + [Ca^{2+}](1 + \frac{L_3}{L_1})},
\end{aligned}$$

$$\begin{aligned}
\phi_{-2}[Ca^{2+}] &= \frac{k_{-2} + l_{-4}[Ca^{2+}]}{(1 + \frac{Ca^{2+}}{L_5})}, \\
\phi_3[Ca^{2+}] &= \frac{k_3 L_5}{L_5 + [Ca^{2+}]}, \\
\phi_4[Ca^{2+}] &= \frac{(k_4 L_5 + l_6)[Ca^{2+}]}{L_5 + [Ca^{2+}]}, \\
\phi_{-4}[Ca^{2+}] &= \frac{L_1(k_{-4} + l_{-6})}{L_1 + [Ca^{2+}]}, \\
\phi_5[Ca^{2+}] &= \frac{(k_1 L_1 + l_2)[Ca^{2+}]}{L_1 + [Ca^{2+}]}.
\end{aligned} \tag{3}$$

The open probability of the IPR is taken to be $P_{IPR} = (0.1O + 0.9A)^4$, thus, the calcium flux from the IPR is given as:

$$J_{IPR} = k_{IPR} P_{IPR}([Ca^{2+}]_{er} - [Ca^{2+}]). \tag{4}$$

The SERCA pump and Ca^{2+} ATPase pump (PMCA)

Calcium enters the ER via the SERCA pump, with the quasi-hill form model representing the pump flux, influenced by the ER's calcium content [43]

$$J_{SERCA} = V_{SERCA} \frac{[Ca^{2+}]}{K_{SERCA} + [Ca^{2+}]} \times \frac{1}{[Ca^{2+}]_{er}}. \tag{5}$$

Here, V_{SERCA}, K_{SERCA} are the maximum permeability and half saturation constant of the SERCA pump, respectively. Ca^{2+} is moved from the cytosol to the extracellular medium by the PMCA. As a result, the flow from the cytosol to the extracellular pool is expressed as (4):

$$J_{PM} = V_{PM} \frac{[Ca^{2+}]^2}{K_{PM}^2 + [Ca^{2+}]^2}. \tag{6}$$

Here, V_{PM} is the permeability of the PMCA, and the K_{PM} is a half-saturation constant. When calcium reaches the cytosol, the intracellular calcium is altered. The J_{IN} is modeled as a function of increasing agonist concentration, with agonist-dependent inflow ($\alpha_2 V_{PLC}$) and constant leak (α_1)

$$J_{IN} = \alpha_1 + \alpha_2 v_{PLC}. \tag{7}$$

Calcium leakage from the ER to the cytoplasmic J_{ER} is directly linked to the variation in calcium concentrations.

The IP_3 dynamics

PLC, whose activity is influenced by Ca2+ and agonist dosage, produces IP_3. The expression for the phospholipase C isoform production, also known as PLCβ, and its Ca^{2+} sensitivity is as follows [44]

$$J_{IP_3 prod} = V_{PLC} \frac{[Ca^{2+}]^2}{K_{PLC}^2 + [Ca^{2+}]^2}. \tag{8}$$

In this case, K_{PLC} represents the sensitivity of PLC to calcium, while V_{PLC} indicates the maximum synthesis rate of PLC isoforms. Next, the following kinetic equation for IP_3 degradation modulated by [Ca2+] is given as

$$J_{IP_3deg} = k_{deg}\left(\frac{[Ca^{2+}]^2}{K_{deg}^2 + [Ca^{2+}]^2}\right)[IP_3], \tag{9}$$

where K_{deg} is the IP_3 half saturation constant, and k_{deg} describes the phosphorylation rate. The rate of variation of the cytosolic concentration of (IP_3) is therefore given as

$$\frac{d[IP_3]}{dt} = J_{IP_3prod} - J_{IP_3deg}. \tag{10}$$

The mitochondrial uptake and release

The exchange of Ca^{2+} between the cytosol and mitochondria occurs as the mitochondria absorb Ca^{2+}. The equation is as follows

$$J_{MCU} = k_{mcu}\frac{[Ca^{2+}]^2}{K_{mcu}^2 + [Ca^{2+}]^2}. \tag{11}$$

The K_{mcu} is a half-activation constant, while the maximal permeability is k_{mcu}. The fast mode also removes Ca^{2+} from the cytosol, therefore this exchange is provided by

$$J_{RaM} = k_{RaM}\frac{[Ca^{2+}]^8}{K_{RaM}^8 + [Ca^{2+}]^8}. \tag{12}$$

Here k_{RaM} is the maximal permeability, and K_{RaM}, is the half-activation constant for the rapid mode.

The Na^+/Ca^{2+} exchanger

Within the mitochondria, the Na^+/Ca^{2+} exchanger facilitates the gradual release of Ca^{2+}. The exchanger for it is provided as

$$J_{NCX} = v_{NCX}\frac{[Na^+]_{cyto}^3}{k_{Na}^3 + [Na^+]_{cyto}^3}\frac{[Ca^{2+}]_{mit}}{k_{NCX} + [Ca^{2+}]_{mit}}. \tag{13}$$

The Na^+/Ca^{2+} exchanger's activation constants are k_{Na} and k_{NCX}, with the cytosolic Na^+ concentration being $[Na^+]_{cyto}$, and its maximal activity being V_{NCX}.

Mitochondrial-Associated Membranes (MAMs)

The ER and mitochondria are physically connected to form stanch structural domains known as mitochondria-associated ER membranes. It participates in fundamental biological Ca^{2+} homeostasis processes. Further, the evidence is, that there is a physical contact between ER Ca^{2+} release sites and mitochondrial Ca^{2+} uptake sites [45]. Thus, the Ca^{2+} flux from ER to mitochondria

directly is given by

$$J_{MAM} = k_{MAM_1} \frac{[Ca^{2+}]_{er}^2}{K_{MAM_1}^2 + [Ca^{2+}]_{er}^2} + k_{MAM_2} \frac{[Ca^{2+}]_{er}^8}{K_{MAM_2}^8 + [Ca^{2+}]_{er}^8}, \tag{14}$$

where k_{MAM_1}, k_{MAM_2} are the maximal permeability and K_{MAM_1}, K_{MAM_2} are the half-activation constants for the J_{MAM} fluxes.

3 Results: model analysis

Nonlinear differential Eqs. (1)-(2) in the system determine the dynamic behavior of the model and solve the system of equations numerically. A partial bifurcation analysis of the model is also carried out. The maximum PLC isoform synthesis rate is represented by the parameter V_{PLC}. This parameter, thus, serves as the model's bifurcation parameter.

The bifurcation diagram for $[Ca^{2+}]$ in Figure 1 illustrates how V_{PLC} affects this. In this case, HB1 and HB2 represent the two Hopf Bifurcations. The stable periodic orbits are shown by dark black lines, and the unstable ones are shown by dark blue lines. Period doubling bifurcation point is depicted by PDs. TRs is an acronym for the tour's split point. The inset shows the period of oscillations. Steady-state stability decreases as V_{PLC} rises. The steady state, for positive V_{PLC} values $\approx$ 2.344 to 34.4 μM/s, contains two Hopf bifurcation points: right-most Hopf bifurcation (HB2) and left-most Hopf bifurcation (HB1). Hopf bifurcation arises when the steady state changes the stability. It causes the appearance or disappearance of a periodic orbit.

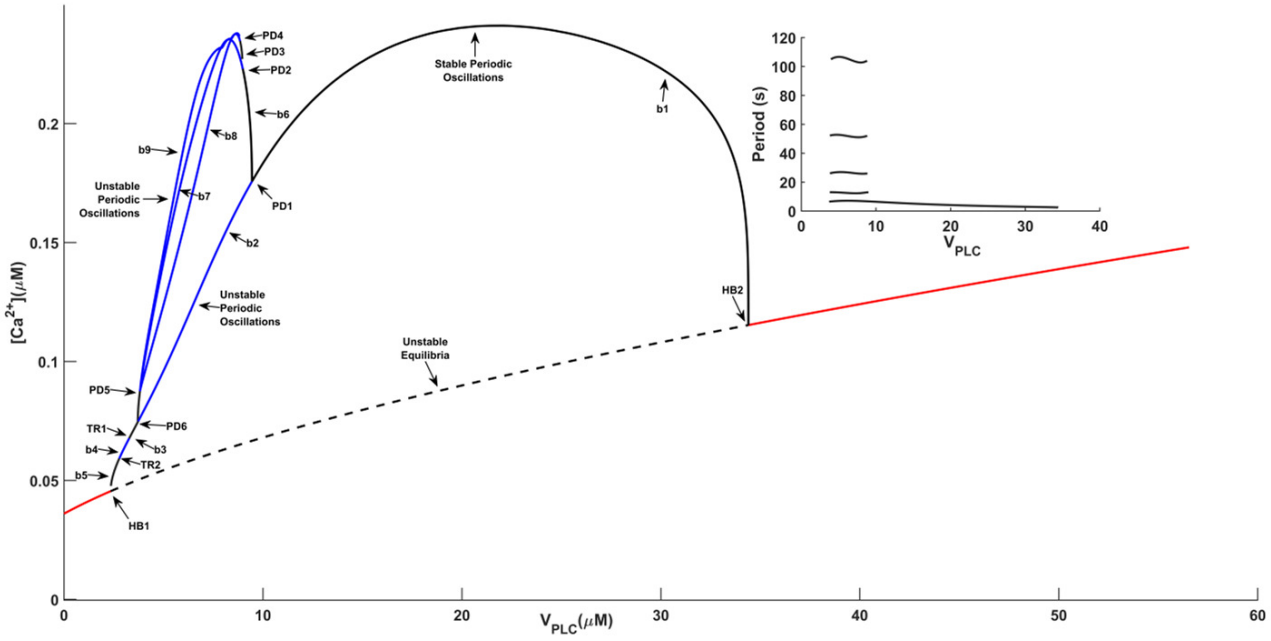

Figure 1. The maximum values of the periodic orbits with respect to V_{PLC} are shown on the bifurcation diagram

Thus, the model enables oscillations between two V_{PLC} values, with stable and unstable periodic oscillations. The steady state is the saddling node type. The stable branch b1 starts at HB2 at V_{PLC} = 34.4 μM/s and ends at PD1 at $V_{PLC} \approx$ 9.449 μM/s, with oscillation periods ranging from 2.465 to 6.526 seconds.

Beginning at PD6, the tiny stable branch b3 stops at the point TR1 $V_{PLC} \approx 3.267 \mu$M/s. The oscillation period of this little branch is 6.526 to 6.245 seconds. After that, the new unstable branch

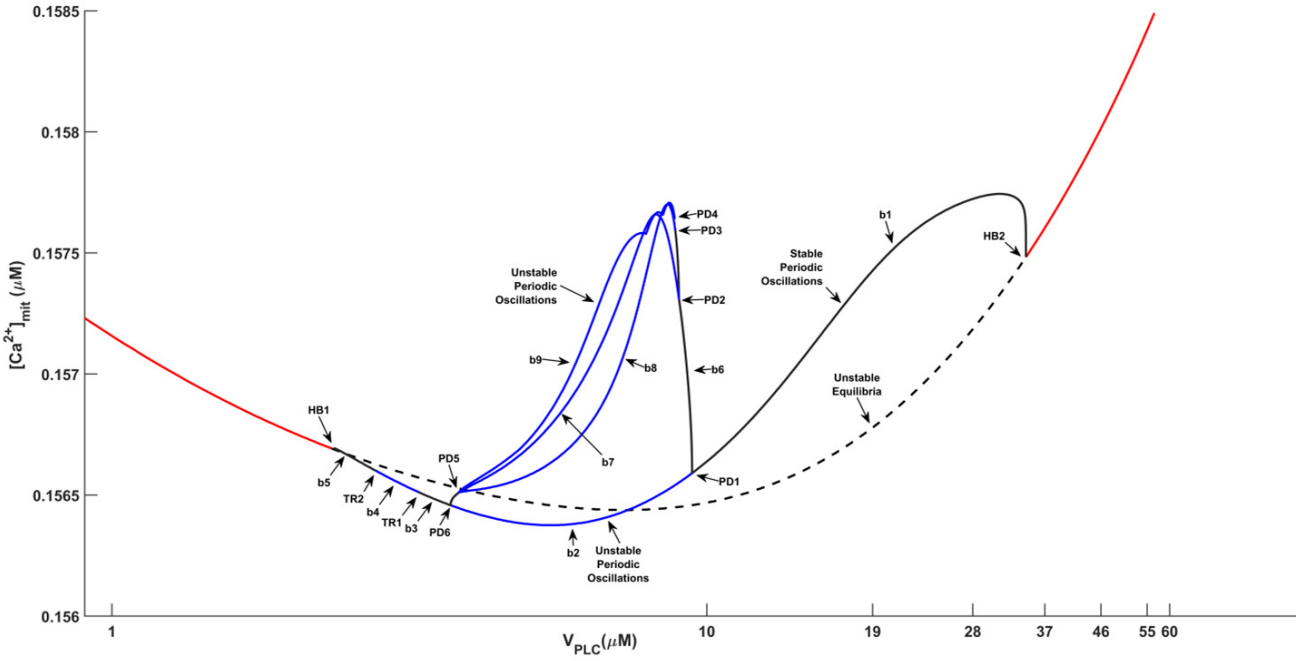

Figure 2. The bifurcation diagram of $[Ca^{2+}]_{mit}$ as a function of V_{PLC}

b4 blue line begins at tour point TR1 (3.267 μM/s) and finishes at TR2 $V_{PLC} \approx 2.777\mu$M/s. In this branch, oscillations occur approximately 6.245 to 5.447 seconds. Next, a little, stable branch called b5 (a solid black line) emerged from TR2 and ended close to HB1. On this branch, the oscillation period varies from approximately 5.853 to 5.447 seconds.

Starting at PD1 and ending at PD2, the new stable branch has a V_{PLC} of roughly 13.05μM/s. At PD5, at $V_{PLC} \approx 3.854$ μM/s, the elongation from PD2 (branch b7) comes to a halt. At $V_{PLC} \approx 8.966$ μM/s, branch b7 has the PD3. Starting at PD3, the branch b8 ends at PD5. This branch oscillates at a period of roughly 26.07 to 26.11 seconds. The unstable branch b9 ends near PD5 and starts at $V_{PLC} \approx 8.816\mu$M/s, originating from PD4. The oscillation period of this branch is 51.98 to 52.21 seconds.

Figure 2 displays the bifurcation diagram that forecasts how V_{PLC} will affect $[Ca^{2+}]_{mit}$. The dotted black lines are unstable equilibrium. The solid black lines represent the stable periodic orbits and dark blue lines represent the unstable periodic orbits. The PDs are the period-doubling bifurcation points. TRs represents the tours bifurcation point. Bifurcation points such as the Hopf bifurcation, period doubling, and Tours points happen at the same V_{PLC} values as they do in Figure 1. As a result, both the stable and unstable branches in Figure 1 and Figure 2 correspond to oscillations whose period and amplitude fall within a scientifically meaningful range. The function of V_{PLC} drives these complex dynamics both in cytosol and mitochondria. It should be mentioned that IP_3 fluctuations in this scenario are the cause of the $[Ca^{2+}]$ oscillations, that lead to $[Ca^{2+}]_{mit}$ oscillations.

Ca^{2+} oscillations are more than just a biological curiosity; they have a substantial impact on cell function. Calcium signals indicate how cells can encode information in the frequency and amplitude of oscillations generated by their oscillatory nature. Thus, it is important to understand the dynamics of time series. Following that, the next several values of V_{PLC} are displayed along with the distinct dynamic profiles of $[Ca^{2+}]$, $[Ca^{2+}]_{mit}$, and $[IP_3]$ oscillations.

The time series is periodic at PD3, $V_{PLC} \approx 8.853\mu$M, with a period of 26.01 seconds. Figure 3A, Figure 3C illustrates the oscillation of the $[Ca^{2+}]$ and $[Ca^{2+}]_{mit}$ time series, which exhibit four spikes in total: two large and two minor spikes. Furthermore, the $[IP_3]$ profile is displayed in

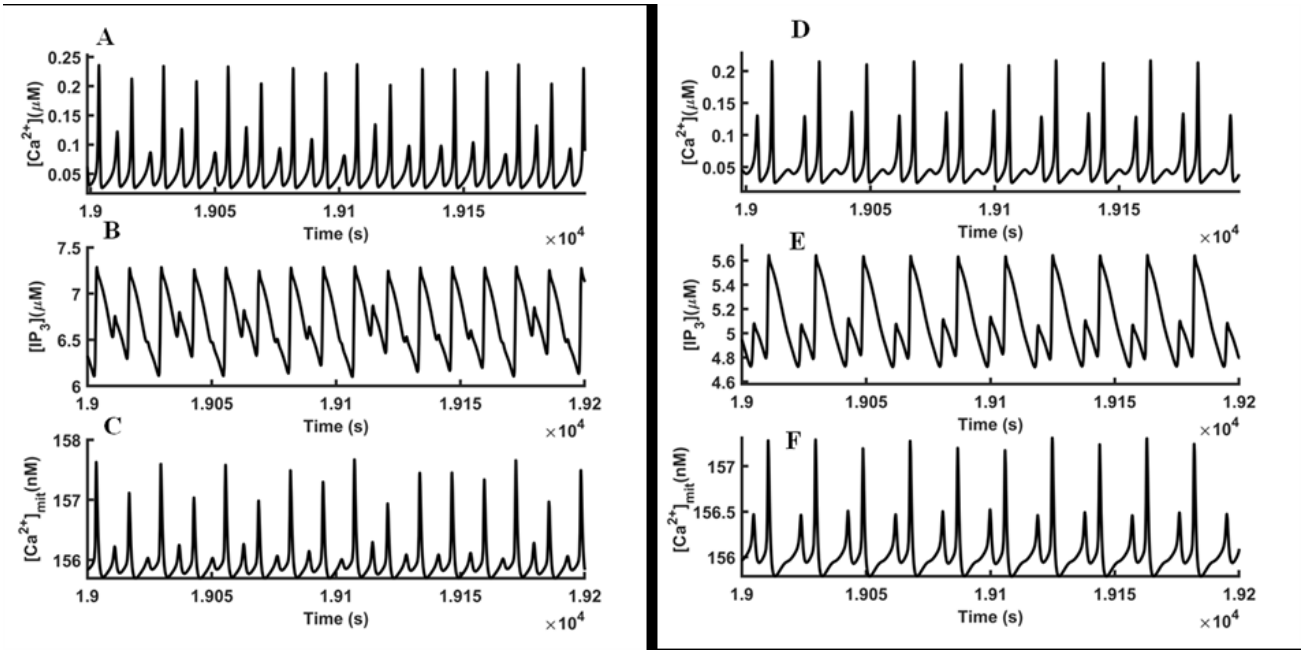

Figure 3. The time series profiles of $[Ca^{2+}]$, $[IP_3]$, and $[Ca^{2+}]_{mit}$ at $V_{PLC} = 8.853\mu M/s$, and $V_{PLC} = 7\mu M/s$, are shown in Panels A, B, and C and Panels D, E, F, respectively

Figure 3B. Three distinct attractors can be found in phase space at $V_{PLC} \approx 8.853\mu M$, When the stable periodic orbits reach the period-doubling bifurcation PD3, a powerful attractor is created. Additionally, there are two additional period doubling bifurcations (PD2 and PD4) that form complex attractors close to PD3. Consequently, there are variations in the amplitudes of the oscillations in $[IP_3]$, $[Ca^{2+}]$, and $[Ca^{2+}]_{mit}$ and. Figure 1 illustrates how it results from the merger of various attractors in the phase plane. Moreover, branch b7 exhibits a two-peak oscillation of $[Ca^{2+}]$ at $V_{PLC} = 7\mu M$, with a huge spike coming first, and a smaller spike following, as depicted in Panel D. In addition, the $[Ca^{2+}]_{mit}$ oscillates, showing two peaks in Panel F. Panel E displays the $[IP_3]$ pattern.

The predicted time series for $[Ca^{2+}]$ and $[Ca^{2+}]_{mit}$ exhibit two abrupt spikes with different small amplitudes at PD6, $V_{PLC} = 3.819\ \mu M/s$, as illustrated in Figure 4A and Figure 4C, respectively. The unstable periodic orbits that merge into the stable periodic orbits, as seen in Figure 1 and Figure 2, complicate the $[Ca^{2+}]$ profile. Moreover, two bifurcation points PD5 and TR1 (torus point) exit near the PD6 area, which results in complex oscillations. TR1 occurs at $V_{PLC} = 3.267\mu M$. Figure 4D illustrates the smaller oscillations of $[Ca^{2+}]$ and $[Ca^{2+}]_{mit}$ having multiple large and small fluctuations having periods of around 6.245 seconds, respectively. When comparing the Ca^{2+} profile in Figure 4E with Figure 4A, the Ca^{2+} oscillates with less amplitude.

Furthermore, steady oscillations develop when V_{PLC} is increased (see branch b1 of Figure 1 and Figure 2). When compared to unstable oscillations, stable oscillations have amplitudes that are comparable. Figure 5A and Figure 5C show that the $[Ca^{2+}]$ and $[Ca^{2+}]_{mit}$ oscillate with significant amplitudes and identical spikes at $V_{PLC} = 20\mu M$. Similar amplitude spikes are also shown in Figure 5B of the $[IP_3]$. Comparing Figure 5 panels Figure 5D, Figure 5E, and Figure 5F with Figure 5A, Figure 5B, and Figure 5C for $[Ca^{2+}]$, $[IP_3]$, and $[Ca^{2+}]_{mit}$ oscillations, respectively, reveals sinusoidal oscillations at $V_{PLC} = 30\mu M$, but the oscillations are also stable at this point. Approximately 2.5 seconds make up the oscillation period. Calcium oscillations with varying amplitudes at smaller frequencies are predicted by the model to be observed when V_{PLC} is modest. Higher V_{PLC} causes higher frequency oscillations. The oscillations in the $[IP_3]$ concentration are by Ca^{2+} induced IP_3 production and degradation. However, the IP_3 plays a key role in the

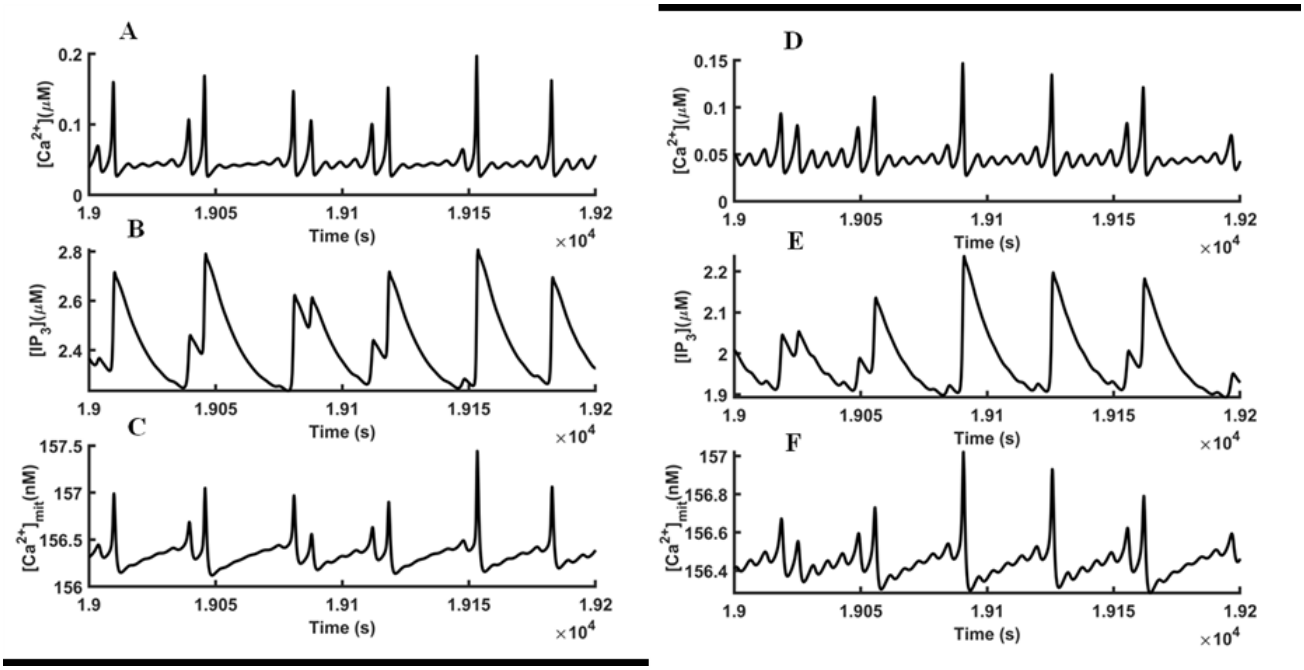

Figure 4. Qualitative oscillation behavior at different agonist concentrations, presenting time series profiles of $[Ca^{2+}]$, $[IP_3]$, and $[Ca^{2+}]_{mit}$ at V_{PLC} = 3.819 μM/s (Panels A, B, C) and 3.267 μM/s, (Panels D, E, F), respectively

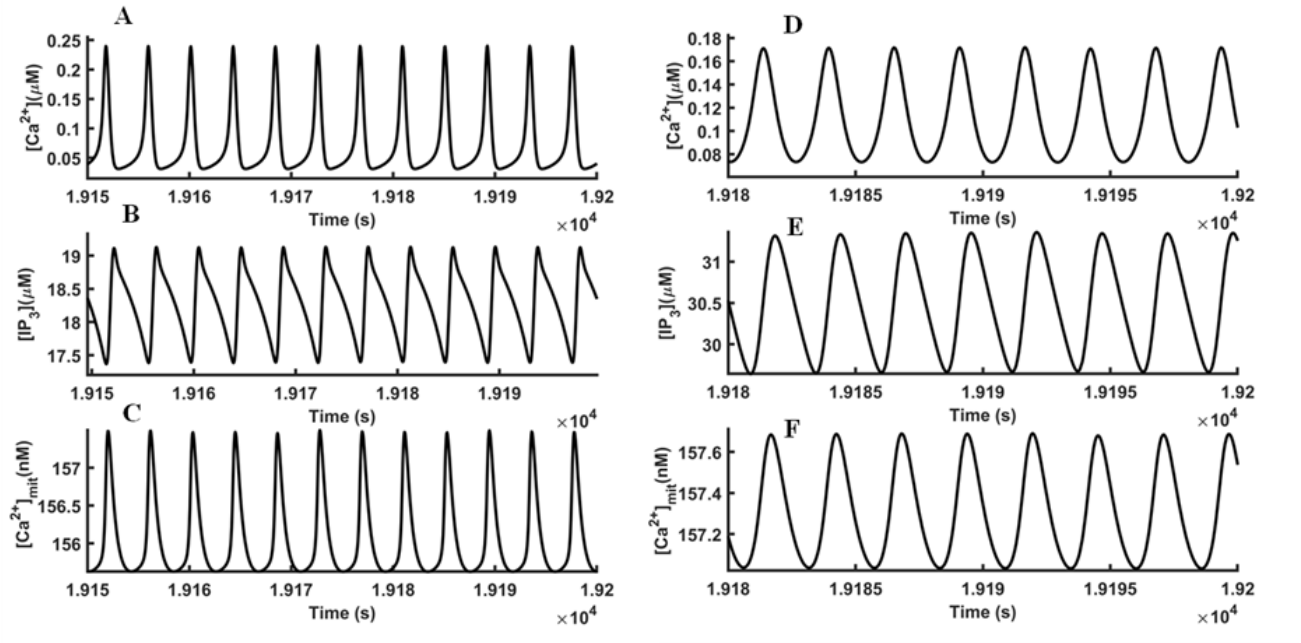

Figure 5. Numerical integration of agonist V_{PLC} at different concentrations, displaying time series profiles of $[Ca^{2+}]$, $[IP_3]$, and $[Ca^{2+}]_{mit}$ at 20μM/s (Panels A, B, and C) and 30μM/s (D, E, and F)

modulation of $[Ca^{2+}]$ oscillations.

4 Discussion and conclusions

The goal of this study is to comprehend sophisticated Ca^{2+} oscillations in the mitochondria and the cytoplasm. Agonist stimulations that cause CICR through IPR entrenched in the ER membrane elicit the calcium transients. Consideration is given to the cytosolic IP_3 synthesis by PLC and its degradation by Ca^{2+}. Through uniporters and the rapid mode mechanism, Ca^{2+} is swiftly

Table 1. Parameter values used in the model taken from [17, 18, 20, 46]

IPR Parameters values					
k_1	0.64 $(\mu M)^{-1}s^{-1}$	k_{-1}	0.04 s^{-1}	l_2	1.7 s^{-1}
k_2	37.4 $(\mu M)^{-1}s^{-1}$	k_{-2}	1.4 s^{-1}	l_4	1.7 $s^{-1}(\mu M)^{-1}$
k_3	0.11 $(\mu M)^{-1}s^{-1}$	k_{-3}	29.8 s^{-1}	l_6	4707 s^{-1}
k_4	4.0 $s^{-1}(\mu M)^{-1}$	k_{-4}	0.54 s^{-1}	L_1	0.12 μM
L_3	0.025 (μM)	L_5	54.7 μM		
IP_3 Parameters values					
K_{PLC}	0.2 μM	k_{deg}	0.5 s^{-1}	K_{deg}	0.1 μM
Calcium Parameters					
k_{IPR}	0.71 s^{-1}	J_{ER}	0.002 s^{-1}	δ	0.1
γ	5.405	τ	1.64	V_{SERCA}	120 $(\mu M)^{-2}s^{-1}$
K_{SERCA}	0.18 μM	V_{PM}	28 μMs^{-1}	K_{PM}	0.425 μM
α_1	0.2 $(\mu M)s^{-1}$	α_2	0.05 s^{-1}		
Mitochondrial Parameters					
k_{mcu}	15 $(\mu M)s^{-1}$	K_{mcu}	20 μM	k_{RaM}	30 $(\mu M)s^{-1}$
K_{RaM}	0.8 μM	V_{NCX}	60 $(\mu M)^{-1}s^{-1}$	K_{NCX}	35 μM
K_{Na}	9.4 μM	$[Na^+]_{cyto}$	10 μM	k_{MaM1}	0.03 $(\mu M)s^{-1}$
K_{MaM1}	20 μM	k_{MaM2}	0.12 $(\mu M)s^{-1}$	K_{MaM2}	1.8 μM

taken up by mitochondria and released slowly via an exchanger back into the cytosol. Cellular organelles, including mitochondria and ER, play distinct biological roles, physically forming MAMs and not being isolated entities, despite evidence suggesting otherwise [9]. MAMs are a dynamic interface that connects the outer mitochondrial membrane (OMM), the ER subdomain, and several proteins, serving as a link between the ER and mitochondria [47]. It helps the material and information flow between the ER and the mitochondria including Ca^{2+} ions [45]. Thus, a straightforward but reliable mathematical model is developed to comprehend the intricacy of Ca^{2+} dynamics, which includes direct Ca^{2+} flow from the ER to the mitochondria, pumps, standard Ca^{2+} fluxes, and the IP_3 metabolism that is associated IPR controls over activation and inactivation.

The bifurcation analysis is performed on the constructed model. The bifurcation analysis reveals the dynamical structures, that govern the oscillations (Figure 1). The existence of such unstable oscillations holds the fact that they exist for very small regions (blue dark lines) as shown in Figure 1 and Figure 2. The stable Ca^{2+} oscillations exist for large regions (black dark lines) discussed above in Figure 1 and Figure 2. As predicted the model shows transient from simple to complex Ca^{2+} oscillations. The model suggests that even at low levels of stimulation, the Ca^{2+} response may exhibit erratic spikes. The Ca^{2+} oscillations remain at high frequency and low amplitude even at large agonist dosages (Figure 2, Figure 3, Figure 4, Figure 5). Moreover, the correlation between agonist and oscillations period indicates that the period sharply decreases as stimulus concentration rises (see the inset in Figure 1). It is also observed that when the model is simulated without MAMs and mitochondrial dynamics. Bifurcation's dynamical structure ($[Ca^{2+}]$ vs. V_{PLC}) differs significantly (results not shown). With few stable and unstable branches, the oscillations happen in the V_{PLC} border range. These oscillations have large amplitudes. The bifurcation diagram ($[Ca^{2+}]$ vs. V_{PLC}) exhibits a complex dynamical structure with more unstable and stable branches in relation to mitochondrial uptakes, releases, and MAM inclusions. The structure is particularly challenging because of the cascade of PDs and TR bifurcations. The dynamical structures are like these models [20, 36, 37, 48–50].

Nevertheless, by emphasizing ER-cytosolic exchange, SERCA pump, PMAC, external intakes as well as mitochondrial uptake, release, and MAMs, this work explains calcium oscillations in non-

excitable cells. Likewise, it addresses mixed IP_3 metabolism that generates a range of morphologies, such as baseline spikes, transient, sinusoidal, and simple to complex oscillations with low to high periods and frequencies. Therefore, here findings are in keeping with previous experimental research showing that agonists like acetylcholine (Ach), and vasopressin (VP) delivery lead in high frequency, sinusoidal baseline spikes, while cholecystokinin (cch), phenylephrine (PE) application results in low-frequency baseline spikes [5–7].

This model has few limitations. Here, we tried to develop a simple mathematical model that shows Ca^{2+} dynamics physiologically accurate. This model is a well-mixed type, and the concentration of each species is homogeneous throughout. However, the Ca^{2+} dynamics in non-excitable cells vary with space and time both. Thus, this model is limited to show the propagating of Ca^{2+} waves from one region to another region of the cells. Also, to investigate Ca^{2+} patterns through MAMs in the non-excitable cells; we use the direct Ca^{2+} passage from the ER to the mitochondria. The more accurate model is to consider the microdomains near the connecting sights of the ER and the mitochondria. However, in the future, we will construct such kinds of models. This model is deterministic in nature. It does not provide any information regarding the stochastic aspects of Ca^{2+} dynamics in the non-excitable cells.

Cell viability is dependent on the production of ATP via mitochondrial oxidative phosphorylation [51]. Moreover, the sustained rise of $[Ca^{2+}]$ is shown to cause oxidative stress leading to the generation of excess ROS [52–56]. ROS are generated as byproducts of normal cellular respiration, particularly during the electron transport chain in the mitochondria. During the electron transport chain (ETC), electrons are transferred through Complex I, II, and III, and molecular oxygen O_2 serves as the final electron acceptor. Sometimes, during this process, some electrons can prematurely interact with O_2, leading to the formation of ROS. ROS includes molecules like superoxide radicals ($O_2\bullet-$), hydrogen peroxide (H_2O_2), and hydroxyl radicals ($\bullet OH$). Few mathematical models to understand these mechanisms are seen here [57–61]. Thus, it is important to understand the crosstalk between MAMs and ROS in non-excitable cells. But it is the avenue of future work.

Declarations

Use of AI tools

The author declares that he has not used Artificial Intelligence (AI) tools in the creation of this article.

Data availability statement

There are no external data associated with this article.

Ethical approval (optional)

The author states that this research complies with ethical standards. This research does not involve either human participants or animals.

Consent for publication

Not applicable

Conflicts of interest

The author declares that he has no conflict of interest.

Funding

No funding was received for this research.

Author's contributions

The author has written, read and agreed to the published version of the manuscript.

Acknowledgements

Not applicable

References

[1] Berridge, M.J. Smooth muscle cell calcium activation mechanisms. *The Journal of Physiology,* 586(21), 5047-5061, (2008).[CrossRef]

[2] Südhof, T.C. Neurotransmitter release: the last millisecond in the life of a synaptic vesicle. *Neuron,* 80(3), 675-690, (2013).[CrossRef]

[3] Berridge, M., Lipp, P. and Bootman, M. Calcium signalling. *Current Biology,* 9(5), R157-R159, (1999).[CrossRef]

[4] Gerasimenko, J.V., Peng, S., Tsugorka, T. and Gerasimenko, O.V. Ca^{2+} signalling underlying pancreatitis. *Cell Calcium,* 70, 95-101, (2018). [CrossRef]

[5] Bartlett, P.J., Cloete, I., Sneyd, J. and Thomas, A.P. IP_3-dependent Ca^{2+} oscillations switch into a dual oscillator mechanism in the presence of PLC-linked hormones. *Iscience,* 23(5), 101062, (2020). [CrossRef]

[6] Yule, D.I. and Gallacher, D.V. Oscillations of cytosolic calcium in single pancreatic acinar cells stimulated by acetylcholine. *FEBS Letters,* 239(2), 358-362, (1988). [CrossRef]

[7] Petersen, O.H. Local calcium spiking in pancreatic acinar cells. *Ciba Foundation Symposium,* 188, 85-103, (1995).

[8] Raturi, A. and Simmen, T. Where the endoplasmic reticulum and the mitochondrion tie the knot: the mitochondria-associated membrane (MAM). *Biochimica et Biophysica Acta (BBA)-Molecular Cell Research,* 1833(1), 213-224, (2013). [CrossRef]

[9] Yang, M., Li, C., Yang, S., Xiao, Y., Xiong, X., Chen, W. et al. Mitochondria-associated ER membranes–the origin site of autophagy. *Frontiers in Cell and Developmental Biology,* 8, 595, (2020). [CrossRef]

[10] De Young, G.W. and Keizer, J. A single-pool inositol 1, 4, 5-trisphosphate-receptor-based model for agonist-stimulated oscillations in Ca^{2+} concentration. *Proceedings of the National Academy of Sciences,* 89(20), 9895-9899, (1992). [CrossRef]

[11] Atri, A., Amundson, J., Clapham, D. and Sneyd, J. A single-pool model for intracellular calcium oscillations and waves in the Xenopus laevis oocyte. *Biophysical Journal,* 65(4), 1727-1739, (1993). [CrossRef]

[12] Dupont, G. and Swillens, S. Quantal release, incremental detection, and long-period Ca^{2+} oscillations in a model based on regulatory Ca^{2+}-binding sites along the permeation pathway. *Biophysical Journal,* 71(4), 1714-1722, (1996). [CrossRef]

[13] Li, Y.X. and Rinzel, J. Equations for $InsP_3$ receptor-mediated $[Ca^{2+}]$ i oscillations derived from a detailed kinetic model: a Hodgkin-Huxley like formalism. *Journal of Theoretical Biology,* 166(4), 461-473, (1994). [CrossRef]

[14] Bezprozvanny, I. Theoretical analysis of calcium wave propagation based on inositol (1, 4, 5)-trisphosphate ($InsP_3$) receptor functional properties. *Cell Calcium,* 16(3), 151-166, (1994). [CrossRef]

[15] Cuthbertson, K.S.R. and Chay, T.R. Modelling receptor-controlled intracellular calcium oscillators. *Cell Calcium,* 12(2-3), 97-109, (1991). [CrossRef]

[16] Meyer, T. and Stryer, L. Molecular model for receptor-stimulated calcium spiking. *Proceedings of the National Academy of Sciences,* 85(14), 5051-5055, (1988). [CrossRef]

[17] Sneyd, J., Tsaneva-Atanasova, K., Bruce, J.I.E., Straub, S.V., Giovannucci, D.R. and Yule, D.I. A model of calcium waves in pancreatic and parotid acinar cells. *Biophysical Journal,* 85(3), 1392-1405, (2003). [CrossRef]

[18] Manhas, N. and Pardasani, K.R. Modelling mechanism of calcium oscillations in pancreatic acinar cells. *Journal of Bioenergetics and Biomembranes,* 46, 403-420, (2014). [CrossRef]

[19] Manhas, N., Sneyd, J. and Pardasani, K.R. Modelling the transition from simple to complex Ca^{2+} oscillations in pancreatic acinar cells. *Journal of Biosciences,* 39, 463-484, (2014). [CrossRef]

[20] Manhas, N. and Anbazhagan, N. A mathematical model of intricate calcium dynamics and modulation of calcium signalling by mitochondria in pancreatic acinar cells. *Chaos, Solitons & Fractals,* 145, 110741, (2021). [CrossRef]

[21] Dupont, G., Falcke, M., Kirk, V. and Sneyd, J. *Models of Calcium Signalling* (Vol. 43). Springer: Switzerland, (2016). [CrossRef]

[22] Dupont, G., Swillens, S., Clair, C., Tordjmann, T. and Combettes, L. Hierarchical organization of calcium signals in hepatocytes: from experiments to models. *Biochimica et Biophysica Acta (BBA)-Molecular Cell Research,* 1498(2-3), 134-152, (2000). [CrossRef]

[23] Kummer, U., Olsen, L.F., Dixon, C.J., Green, A.K., Bornberg-Bauer, E. and Baier, G. Switching from simple to complex oscillations in calcium signaling. *Biophysical Journal,* 79(3), 1188-1195, (2000). [CrossRef]

[24] Ullah, G., Jung, P. and Machaca, K. Modeling Ca^{2+} signaling differentiation during oocyte maturation. *Cell Calcium,* 42(6), 556-564, (2007). [CrossRef]

[25] Naik, P.A. and Pardasani, K.R. Three-dimensional finite element model to study calcium distribution in oocytes. *Network Modeling Analysis in Health Informatics and Bioinformatics*, 6, 16, (2017). [CrossRef]

[26] Naik, P.A. and Pardasani, K.R. Three-dimensional finite element model to study effect of RyR calcium channel, ER leak and SERCA pump on calcium distribution in oocyte cell. *International Journal of Computational Methods,* 16(01), 1850091, (2019). [CrossRef]

[27] Zhang, H., Zhang, S., Wang, W., Wang, K. and Shen, W. A mathematical model of the mouse atrial myocyte with inter-atrial electrophysiological heterogeneity. *Frontiers in Physiology,* 11, 972, (2020). [CrossRef]

[28] Greenstein, J.L. and Winslow, R.L. An integrative model of the cardiac ventricular myocyte incorporating local control of Ca^{2+} release. *Biophysical Journal,* 83(6), 2918-2945, (2002). [CrossRef]

[29] Bers, D.M. Cardiac excitation–contraction coupling. *Nature,* 415, 198-205, (2002). [CrossRef]

[30] Bhattacharyya, R. and Jha, B.K. Analyzing fuzzy boundary value problems: a study on the influence of mitochondria and ER fluxes on calcium ions in neuron cells. *Journal of Bioenergetics and Biomembranes,* 56, 15-29, (2024). [CrossRef]

[31] Jethanandani, H., Jha, B.K. and Ubale, M. The role of calcium dynamics with amyloid beta on neuron-astrocyte coupling. *Mathematical Modelling and Numerical Simulation with Applications,* 3(4), 376-390, (2023). [CrossRef]

[32] Joshi, H., Yavuz, M. and Stamova, I. Analysis of the disturbance effect in intracellular calcium dynamic on fibroblast cells with an exponential kernel law. *Bulletin of Biomathematics,* 1(1), 24-39, (2023). [CrossRef]

[33] Ishii, K., Hirose, K. and Iino, M. Ca^{2+} shuttling between endoplasmic reticulum and mitochondria underlying Ca^{2+} oscillations. *EMBO Reports,* 7, 390-396, (2006). [CrossRef]

[34] Johnson, P.R., Dolman, N.J., Pope, M., Vaillant, C., Petersen, O.H., Tepikin, A.V. and Erdemli, G. Non-uniform distribution of mitochondria in pancreatic acinar cells. *Cell and Tissue Research,* 313, 37-45, (2003). [CrossRef]

[35] Tinel, H., Cancela, J.M., Mogami, H., Gerasimenko, J.V., Gerasimenko, O.V., Tepikin, A.V. and Petersen, O.H. Active mitochondria surrounding the pancreatic acinar granule region prevent spreading of inositol trisphosphate-evoked local cytosolic Ca^{2+} signals. *The EMBO Journal,* 18, 4999-5008, (1999). [CrossRef]

[36] Dyzma, M., Szopa, P. and Kaźmierczak, B. Membrane associated complexes: new approach to calcium dynamics modelling. *Mathematical Modelling of Natural Phenomena,* 7(6), 167-186, (2012). [CrossRef]

[37] Marhl, M., Schuster, S. and Brumen, M. Mitochondria as an important factor in the maintenance of constant amplitudes of cytosolic calcium oscillations. *Biophysical Chemistry,* 71(2-3), 125-132, (1998). [CrossRef]

[38] Moshkforoush, A., Ashenagar, B., Tsoukias, N.M. and Alevriadou, B.R. Modeling the role of endoplasmic reticulum-mitochondria microdomains in calcium dynamics. *Scientific Reports,* 9, 17072, (2019). [CrossRef]

[39] Wacquier, B., Combettes, L., Van Nhieu, G.T. and Dupont, G. Interplay between intracellular Ca^{2+} oscillations and Ca^{2+}-stimulated mitochondrial metabolism. *Scientific Reports,* 6, 19316, (2016). [CrossRef]

[40] Han, J.M. and Periwal, V. A mathematical model of calcium dynamics: Obesity and mitochondria-associated ER membranes. *PLoS Computational Biology,* 15(8), e1006661, (2019). [CrossRef]

[41] Doedel, E.J. AUTO: A program for the automatic bifurcation analysis of autonomous systems. In Proceedings, *10th Manitoba Conference on Numerical Mathematics and Computing*, (Vol. 30) pp. 265-284, Winnipeg, Canada, (1981, September).

[42] Sneyd, J. and Dufour, J.F. A dynamic model of the type-2 inositol trisphosphate receptor. *Proceedings of the National Academy of Sciences,* 99(4), 2398-2403, (2002). [CrossRef]

[43] Tsaneva-Atanasova, K., Yule, D.I. and Sneyd, J. Calcium oscillations in a triplet of pancreatic acinar cells. *Biophysical Journal,* 88(3), 1535-1551, (2005). [CrossRef]

[44] Politi, A., Gaspers, L.D., Thomas, A.P. and Höfer, T. Models of IP_3 and Ca^{2+} oscillations: frequency encoding and identification of underlying feedbacks. *Biophysical Journal,* 90(9), 3120-3133, (2006). [CrossRef]

[45] Csordás, G., Várnai, P., Golenár, T., Roy, S., Purkins, G., Schneider, T. G. et al. Imaging interorganelle contacts and local calcium dynamics at the ER-mitochondrial interface. *Molecular Cell,* 39(1), 121-132, (2010). [CrossRef]

[46] Szopa, P., Dyzma, M. and Kaźmierczak, B. Membrane associated complexes in calcium dynamics modelling. *Physical Biology,* 10(3), 035004, (2013). [CrossRef]

[47] Li, X., Zhang, S., Liu, X., Wang, X., Zhou, A. and Liu, P. Important role of MAMs in bifurcation and coherence resonance of calcium oscillations. *Chaos, Solitons & Fractals*, 106, 131-140, (2018).

[CrossRef]

[48] Cloete, I., Bartlett, P.J., Kirk, V., Thomas, A.P. and Sneyd, J. Dual mechanisms of Ca^{2+} oscillations in hepatocytes. *Journal of Theoretical Biology,* 503, 110390, (2020). [CrossRef]

[49] Ventura, A.C. and Sneyd, J. Calcium oscillations and waves generated by multiple release mechanisms in pancreatic acinar cells. *Bulletin of Mathematical Biology,* 68, 2205-2231, (2006). [CrossRef]

[50] LeBeau, A.P., Yule, D.I., Groblewski, G.E. and Sneyd, J. Agonist-dependent phosphorylation of the inositol 1, 4, 5-trisphosphate receptor: a possible mechanism for agonist-specific calcium oscillations in pancreatic acinar cells. *The Journal of General Physiology,* 113(6), 851-872, (1999). [CrossRef]

[51] Heiske, M., Letellier, T. and Klipp, E. Comprehensive mathematical model of oxidative phosphorylation valid for physiological and pathological conditions. *The FEBS Journal,* 284(17), 2802-2828, (2017). [CrossRef]

[52] Zhang, J., Wang, X., Vikash, V., Ye, Q., Wu, D., Liu, Y. and Dong, W. ROS and ROS-mediated cellular signaling. *Oxidative Medicine and Cellular Longevity,* 2016, 4350965, (2016). [CrossRef]

[53] Murphy, M.P. How mitochondria produce reactive oxygen species. *Biochemical Journal,* 417(1), 1-13, (2009). [CrossRef]

[54] Criddle, D.N. Reactive oxygen species, Ca^{2+} stores and acute pancreatitis; a step closer to therapy?. *Cell Calcium,* 60(3), 180-189, (2016). [CrossRef]

[55] Chouchani, E.T., Pell, V.R., James, A.M., Work, L.M., Saeb-Parsy, K., Frezza, C. et al. A unifying mechanism for mitochondrial superoxide production during ischemia-reperfusion injury. *Cell Metabolism,* 23(2), 254-263, (2016). [CrossRef]

[56] Mazat, J.P., Devin, A. and Ransac, S. Modelling mitochondrial ROS production by the respiratory chain. *Cellular and Molecular Life Sciences,* 77, 455-465, (2020). [CrossRef]

[57] Quinlan, C.L., Orr, A.L., Perevoshchikova, I.V., Treberg, J.R., Ackrell, B.A. and Brand, M.D. Mitochondrial complex II can generate reactive oxygen species at high rates in both the forward and reverse reactions. *Journal of Biological Chemistry,* 287(32), 27255-27264, (2012). [CrossRef]

[58] Duong, Q.V., Levitsky, Y., Dessinger, M.J., Strubbe-Rivera, J.O. and Bazil, J.N. Identifying site-specific superoxide and hydrogen peroxide production rates from the mitochondrial electron transport system using a computational strategy. *Function,* 2(6), zqab050, (2021). [CrossRef]

[59] Manhas, N., Duong, Q.V., Lee, P., Richardson, J.D., Robertson, J.D., Moxley, M.A. and Bazil, J.N. Computationally modeling mammalian succinate dehydrogenase kinetics identifies the origins and primary determinants of ROS production. *Journal of Biological Chemistry,* 295(45), 15262-15279, (2020). [CrossRef]

[60] Manhas, N., Duong, Q.V., Lee, P. and Bazil, J.N. Analysis of mammalian succinate dehydrogenase kinetics and reactive oxygen species production. *bioRxiv,* 870501, (2019). [CrossRef]

[61] Chenna, S., Koopman, W.J., Prehn, J.H. and Connolly, N.M. Mechanisms and mathematical modeling of ROS production by the mitochondrial electron transport chain. *American Journal of Physiology-Cell Physiology,* 323(1), C69-C83, (2022). [CrossRef]

Mathematical Modelling and Numerical Simulation with Applications (MMNSA)
(https://dergipark.org.tr/en/pub/mmnsa)

How to cite this article: Manhas, N. (2024). Mathematical model for IP_3 dependent calcium oscillations and mitochondrial associate membranes in non-excitable cells. *Mathematical Modelling and Numerical Simulation with Applications*, 4(3), 280-295. https://doi.org/10.53391/mmnsa.1503948

Mathematical Modelling and Numerical Simulation with Applications, 2024, 4(3), 296–334

https://dergipark.org.tr/en/pub/mmnsa

ISSN Online: 2791-8564 / Open Access

https://doi.org/10.53391/mmnsa.1514196

RESEARCH PAPER

Mathematical analysis of Ebola considering transmission at treatment centres and survivor relapse using fractal-fractional Caputo derivatives in Uganda

Isaac Kwasi Adu [1,*,‡], **Fredrick Asenso Wireko** [2,‡], **Samuel Akwasi Adarkwa** [3,‡] **and Gerald Ohene Agyekum** [3,‡]

[1]Department of Mathematical Sciences, Faculty of Applied Sciences and Technology, Kumasi Technical University, 854, Kumasi, Ghana, [2]Department of Mathematics, College of Science, Kwame Nkrumah University of Science and Technology, 854, Kumasi, Ghana, [3]Department of Statistical Sciences, Faculty of Applied Sciences and Technology, Kumasi Technical University, 854, Kumasi, Ghana

[*] Corresponding Author

[‡] isaac.kadu@kstu.edu.gh (Isaac Kwasi Adu); fredrick.wireko@knust.edu.gh (Fredrick Asenso Wireko); saadarkwa@gmail.com (Samuel Akwasi Adarkwa); geraldagyekum45@gmail.com (Gerald Ohene Agyekum)

Abstract

In this article, we seek to formulate a robust mathematical model to study the Ebola disease through fractal-fractional operators. The study thus incorporates the transmission rate in the treatment centers and the relapse rate, since the Ebola virus persists or mostly hides in the immunologically protected sites of survivors. The Ebola virus disease (EVD) is one of the infectious diseases that has recorded a high death rate in countries where it is endemic, and Uganda is not an exception. The world at large has suffered from this deadly disease since 1976 when it was declared epidemic by the World Health Organization. The study employed fractal-fractional operators to identify the epidemiological patterns of EVD, especially in treatment centers and relapse. Memory loss and relapse are mostly observed in EVD survivors and this justifies the use of fractional operators to capture the true dynamics of the disease. Through dynamical analysis, the model is proven to be positive and bounded in the region. The model is further explicitly shown to have a solution that is unique and stable. The reproduction number was duly computed by using the next-generation matrix approach. By taking EVD epidemic cases in Uganda, the study fitted all parameters to real data. It has been shown through sensitivity index analysis that the transmission rate outside treatment centers and relapse have a significant effect on the endemic state of the disease, as they lead to an increase in the basic reproduction ratio.

Keywords: Ebola; EVD transmission; Caputo derivatives; numerical simulations; Hyers-Ulam stability

AMS 2020 Classification: 34-02; 34A34; 92B05; 70-10; 34L30

➤ **Received:** 11.07.2024 ➤ **Revised:** 06.09.2024 ➤ **Accepted:** 14.09.2024 ➤ **Published:** 30.09.2024

1 Introduction

The Ebola virus is the source of the highly infectious and often fatal disease known as Ebola virus disease (EVD) [1]. The most typical ways of transmitting the Ebola virus to individuals are via direct interaction with secretions, organs, blood, or additional body fluids of an infected person, in addition to interaction with surfaces and items (clothes and bedding) stained with these fluids. Wild animals, including fruit bats, porcupines, and nonhuman primates, are the main carriers of the disease to people. On average, 50% of cases of EVD result in death. Case death rates have varied from 25% to 90% in prior epidemics [1, 2]. Several epidemics of EVD are initiated by a single overflow event and spread from person to person via intimate interactions, often in remote, densely forested locations. Index cases are often associated with hunting, forest work, or land modification.

Infected individuals can spread the virus to other individuals directly, but close contacts such as family members, caregivers, or medical professionals are at more risk of contracting the disease [3]. For instance, the 2014–2015 West Africa Ebola outbreak claimed 109 lives among healthcare professionals in Guinea, sparking alarm worldwide and subsequent instances in Spain and the US. Ebola Rehabilitation Facility for Medical Personnel in Conakry, Guinea, diagnoses and treats healthcare professionals who are infected (either confirmed or suspected) with EVD and are provided with comprehensive medical care, such as biologic monitoring and blood transfusions [4]. The early symptoms of an Ebola infection are fever, myalgia, and asthenia, progressing to gastrointestinal syndrome, including vomiting and diarrhoea. Subsequently, shock, hypoperfusion, failure of several organs, such as serious kidney damage, and depletion of intravenous fluid may occur. Haemorrhage syndrome, primarily gastrointestinal bleeding, may also occur [5]. Furthermore, an Ebola infection may result in several neurological problems. These comprise tremors, migraines, loss of memory, epilepsy, and anomalies of the cranial nerves [6]. Studies have shown that either waning of immunity or weak immunity can lead to virus reinfection in Ebola victims. Some survivors' immunity declines after recovery, while stronger immune systems experience subclinical or asymptomatic sickness [7, 8]. In 2014, during the West African Ebola outbreak, thousands of people survived. It has been reported that the Ebola virus may relapse and cause a potentially fatal and spreadable illness since survivors can harbour the infection for months in immune-privileged sites like the brain, the testes, the central nervous system, and the eyes [6, 8].

In 1976, the world recorded two significant EVD epidemics in South Sudan and also DR Congo (DRC), which led to the initial recognition of the disease worldwide. From that period, countries like DR Congo (DRC) in 1994 and Uganda in 1995 experienced another Ebola outbreak. Ebola outbreaks following this, outbreaks have been reported often and widely in Nigeria, Gabon, the DR Congo, Guinea, Uganda, Liberia, and Sierra Leone. Additionally, rare outbreaks of EVD have been reported from South Africa, the USA, Italy, and the United Kingdom [9].

Recently, mathematical modelling has come to be seen as an important and valuable instrument for understanding the behaviour and cause of the spread of many prevalent infectious diseases, such as diabetes mellitus [10], Ebola [1], measles [11], monkey pox [12], COVID-19 [13], diarrhoea [14], and query fever [15] as stated in [1, 10]. It can also be employed to demonstrate the effective way to mitigate disease propagation and assist in making decisions during an outbreak of disease [1]. For instance, [14] employed Ghana's Ministry of Health data to validate an epidemiological model for diarrhoea transmission dynamics from 2008-2018. They concluded that reducing transmission rates and increasing treatment can significantly control or eradicate the disease. [16], analysed the Hepatitis E model's dynamics and optimal control analysis using the Atangana-Baleanu derivative. When their reproduction number is below one, their model becomes locally asymptotically stable.

They formulated an optimal control system using appropriate control strategies. Numerical results suggest the proper application of control strategies for early Hepatitis E elimination. The Atangana-Baleanu derivative allows for disease status monitoring and effective strategies. A mathematical model predicting giardiasis spread that considers carriers, preventative measures, and interaction between humans and the environment was proposed by [17].

The model uses the Lyapunov function, Metzler constancy hypothesis, and advanced next-generation matrix. Implementing solutions in endemic areas effectively stops giardiasis spread. [18], proposed an article to review malaria biology, mathematical modelling methods, uncertainties, and controversies, and provides a timeline from Ross and MacDonald's classical works to recent climate-focused studies, contextualising mathematical work within the "million-murdering death" of malaria. [19], conducted a pneumonia and HIV/AIDS deterministic co-infection model and used it to assess the impact of these diseases on each other. Their model includes sub-models and sensitivity analysis, revealing that the spreading rate of HIV and the treatment rates are the most sensitive parameters. Their model incorporated intervention strategies and numerical simulations, which shown that prevention and treatment of both diseases reduce the co-infection burden. For more articles on the application of mathematical modelling to study infectious diseases, see [20, 21].

Now, we concentrate on some mathematical models of EVD that have been published earlier by different authors. A nonlinear mathematical model for Ebola was published in 2024 by [1], with an emphasis on burial practices and environmental contamination. They determine the reproduction number, Ebola-free, and Ebola-present equilibrium, as well as the boundedness, positivity, and well-posedness of the model. The sensitivity analysis reveals forward bifurcation, suggesting suppression of Ebola spread. Control strategies include reducing contact with infected people, educating the public, vaccinating the susceptible, and promoting education against funeral customs. Personal protection, vaccination, and safe burial are the most cost-effective methods. In the research of [22], they presented an Ebola virus disease model built using a novel exponentially nonlinear incidence function, which incorporates the curtailment in disease spread as a result of human behaviour. The steady states of the model were determined, and the model's global stability was demonstrated using Lyapunov functions. Their results indicate a good fit when effectiveness and the rate of change of behaviour are faster, after fitting the model to Liberia and Sierra Leone's Ebola data.

In another study, [23], developed an article to explore the dynamics of EVD in domestic and wild animals. They employ an SEIR-type model developed to study the virus's stability in the human population. Their model comprises a nonlinear coupled differential equation, determining Ebola-free and present equilibrium states. The model is asymptotically stable, and global stabilities are carried out using Lyapunov functions theory. The Runge-Kutta method and non-standard finite difference scheme are used for the SEIR model. They concluded that compared to RK4, the NSFD numerical approach is more dependable, preserving non-negativity and boundedness for different step sizes. State-variable simulations provided a numerical analysis of their disease model.

Further, authors of [24] developed a SIR-type model to study Ebola virus disease (EVD) spread using conformable derivatives. Their model incorporates direct and indirect transmission methods, including funeral practices, tainted bush meat consumption, and environmental contamination. The model also considers the possibility of infected individuals birthing and migrating to the existing population. According to their research, the only state in which there is no sickness is when there is no environmental spread of the Ebola virus. In addition, authors of [25] presented a model on the Ebola virus disease. Their model employed mathematical models to understand the spread of the virus validated a new model incorporating vaccination and applied optimal control

analysis to study its impact on numerous shooting techniques with direct multiple shooting methods. Their numerical simulations indicate that an optimal control strategy implemented significantly reduces the number of people prone to Ebola and Ebola-infected people and increases the number of people who recover.

Notwithstanding this, the Ebola virus disease is known to be deadly as it leaves the survivor with severe neurological effects such as seizures, cranial nerve disorders, and memory loss. Authors of [2] presented a mathematical model to explain the dynamics of Ebola transmission between humans and dogs through fractional operators. Caputo-Fabrizio derivative served as the foundation for their model. Fractional orders were shown to have a considerable influence on the model when it was fitted to Uganda's reported Ebola outbreak. According to them, Controlling the spread of Ebola can be achieved by improving recovery rates and decreasing contact rates between dog compartments. They concluded that it is advisable to implement quarantine procedures to regulate encounters during outbreaks. In [26], the Grunwald-Letnikov fractional operator was applied to study the Ebola disease physical patterns in the population, and in [27], the Atangana-Baleanu Caputo operator was also applied to investigate the outbreak of the contagious Ebola disease.

Our motivation for the current research is that all the related literature discussed considers Ebola spreads and how to mitigate the infection. However, we observed that none of the articles examined the following: transmission of Ebola virus disease at treatment centres; Ebola virus persistent in the immunologically protected sites of survivors' bodies and the associated relapse-symptomatic infection; the application of susceptible, infected, treatment and recovered, SITR-type model to investigate the dynamics of Ebola Virus Disease (EVD). Although the authors of [28] employed SITR-type to examine their Ebola model, there are some limitations to their research. These include the use of some parameter values based on assumptions and parameters from existing literature instead of using real Ebola data to carry out their analysis. There are several neurological side effects linked to Ebola. This includes seizures and loss of memory. The memory effect is a crucial characteristic of biological systems. The use of fractional-order models allowed for the realisation of this [6, 29–31]; however, the deterministic approach that was employed in their research was unable to do that. The current research seeks to address these gaps by:

i. Studying the dynamics of EVD transmission at the treatment centres,
ii. Incorporating the dynamics of relapse in survivors due to virus persistence in their bodies after recovery,
iii. Applying the least square estimation technique to fit all the model parameters to real data from Uganda,
iv. Employing the novel fractal-fractional Caputo derivative to capture the exact dynamics of EVD in the population.

The remaining sections of the article are categorised in this pattern. Section 2 deals with formulating the Ebola model that incorporates transmission dynamics at the treatment centres and the relapse patterns in survived individuals. The basic or preliminary results are presented in Section 3. In Section 4, we investigate the positivity and boundedness of the Ebola model understudy. The Ebola model is now studied through fractal-fractional Caputo operators in Section 5 where we performed thorough existence and uniqueness analysis through the fixed point theorem. Also, the Hyers-Ulam and Hyers-Ulam-Rassias stability criterion is used to establish that the Ebola model is stable and is discussed here. Again, we subjected the Ebola model to real data to estimate all the parameters of the study in Section 6, whereas Section 7 performs the local stability analysis and also measures the fundamental reproduction number. In Section 8, the sensitivity analysis of the model's parameters to the R_0 is discussed. Finally, the numerical simulations and conclusion of

the research study are discussed in Section 9 and Section 10, respectively.

2 Ebola model formulation

We propose an integer Ebola transmission model in this section. The entire population is classified into four classes: Susceptible $S(t)$, these are people who are prone to contracting Ebola disease. Infected $I(t)$ are those actively infected with Ebola, show clinical symptoms, and can spread the disease to other individuals. Treated $T(t)$, these are individuals who have received treatment after infection from Ebola. Some individuals of the treated class can still transmit Ebola diseases to other people through direct or indirect means due to the waning of Ebola virus antibodies after a few years of recovery [32]. People who have recovered from the Ebola infection are denoted by $R(t)$. The natural mortality rate is denoted by μ. β is the transmission rate from the infectious class to the treatment class, δ_1 is the Ebola-induced death rate of individuals, and k is the relapse rate of individuals under treatment. The recruitment rate is given by ψ. α_1 is the transfer rate of susceptible to infectious class. α_2 is the transmission rate of partially recovered individuals at the treatment centres to caregivers, σ_1 is the immunity loss rate, and σ_2 denotes the recovery rate. Hence, the entire populace is denoted by $N = S + I + T + R$. The assumptions below formed the basis of the development of the Ebola model:

i. Ebola can spread to susceptible people via any of the following ways: having interpersonal relationships with recovered Ebola victims, touching contaminated animals, or coming into contact with the bodily fluids and clothing of an infected individual,
ii. Recovered individuals can become susceptible to Ebola infection after recovery,
iii. Recovered individuals can transmit Ebola to other people within a few years after recovery due to waning immunity,

The following four (4) integer-order differential equations were developed using the assumptions as basis. The model equations are therefore given by

$$\begin{aligned}
\frac{dS}{dt} &= \psi + \sigma_1 R(t) - \alpha_1 S(t) I(t) - \mu S(t), \\
\frac{dI}{dt} &= \alpha_1 S(t) I(t) + kT(t) - \alpha_2 I(t) R(t) - (\beta + \delta_1 + \mu) I(t), \\
\frac{dT}{dt} &= \alpha_2 I(t) R(t) + \beta I(t) - (\mu + k + \sigma_2) T(t), \\
\frac{dR}{dt} &= \sigma_2 T(t) - (\sigma_1 + \mu) R(t),
\end{aligned} \tag{1}$$

with initial conditions $S(0) = S_0 > 0$, $I(0) = I_0 \geq 0$,$T(0) = T_0 \geq 0$, and $R(0) = R_0 \geq 0$.

3 Preliminary results

In this section, the studies highlight some essential definitions regarding the dynamical analysis to be carried out on the Caputo fractal-fractional Ebola disease model. The definitions are stated below based on literature [33–35].

Definition 1 *Let us suppose there is a continuous domain $(\mathcal{A}, \mathcal{E})$, and further assume that $\mathcal{H}$ has a derivative existing in the fractal dimension range Φ_2. Then, the Caputo fractal-fractional differential operator of $\mathcal{H}$ with the fractional order Φ_1 is given as*

$$^{\mathcal{FFC}}\mathfrak{D}_{\mathcal{A},\mathcal{E}}^{\Phi_1,\Phi_2}\mathcal{H}(\mathcal{E}) = \frac{1}{\Gamma(q-\Phi_1)} \frac{d}{d\mathcal{E}^{\Phi_2}} \int_{\mathcal{A}}^{\mathcal{E}} (\mathcal{E}-k)^{q-\Phi_1-1} \mathcal{H}(k) dk, \quad (q-1 < \Phi_1, \Phi_2 \leq q \in \mathbb{N}),$$

following differentiation results;

$$\frac{d\mathcal{H}(k)}{dk^{\Phi_2}} = \lim_{\mathcal{E}\to k} \frac{\mathcal{H}(\mathcal{E}) - \mathcal{H}(k)}{\mathcal{E}^{\Phi_2} - k^{\Phi_2}}.$$

By supposing that $\Phi_2 = 1$, then the Caputo fractal-fractional derivative ${}^{\mathcal{FFC}}\mathfrak{D}^{\Phi_1,\Phi_2}_{\mathcal{G},\mathcal{E}}$ yields Φ_1^{th}-Riemann-Liouville derivative ${}^{\mathbf{RL}}\mathfrak{D}^{\Phi_1}_{\mathcal{G},\mathcal{E}}$.

Definition 2 *If we further assume that the map $\mathcal{H}$ is unperturbed in the neighborhood of the open interval $(\mathcal{A},\mathcal{E})$. Then, it is obvious that the Caputo fractal-fractional integral of $\mathcal{H}$ results in*

$${}^{\mathcal{FFC}}\mathfrak{I}^{\Phi_1,\Phi_2}_{\mathcal{A},\mathcal{E}}\mathcal{H}(\mathcal{E}) = \frac{\Phi_2}{\Gamma(\Phi_1)}\int_{\mathcal{A}}^{\mathcal{E}} k^{\Phi_2-1}(\mathcal{E}-k)^{\Phi_1-1}\mathcal{H}(k)dk.$$

By classifying $\mathfrak{A}$ t be a non-decreasing transformation, that is $b : \mathcal{R}_{\geq 0} \to \mathcal{R}_{\geq 0}$ with $b(\mathcal{E}) < \mathcal{E}, \forall \mathcal{E} > 0$,

$$\sum_{u=1}^{\infty} a^u(\mathcal{E}) < \infty.$$

Definition 3 *Let us define the map $\mathcal{H} : \mathbb{V} \to \mathbb{V}$ and $\psi : \mathbb{V}^2 \to \mathcal{R}_{\geq 0}$, with $\mathbb{V}$ to be a normed linear space. We then have*

i. In the case where each $x_1, x_2 \in \mathbb{V}$,

$$\phi(x_1,x_2)\mathbf{d}(\mathcal{H}x_1,\mathcal{H}x_2) < a(d(x_1,x_2)),$$

then $\mathcal{H}$ is $\psi-$a-contraction,

ii. Also, assuming $\psi(x_1,x_2) \geq 1$ yields $\psi(\mathcal{H}x_1,\mathcal{H}x_2) \geq 1$, we have that $\mathcal{H}$ is ψ - admissible.

4 Positivity and boundedness

This section establishes the positivity and boundedness of solutions to the proposed Ebola model. By following a similar procedure as performed in literature [20], we obtain the positivity and boundedness of the Ebola model in this manner.

Positivity of solutions

To establish the positivity of the model's solutions, we show that the solutions to each equation of the model are non-negative for any $t > 0$. Let us begin the proof by first supposing that $S(t)$ and $I(t)$ possess the same signs and $\alpha_1 > 0$. In this manner, we suppose that the following inequality holds for $T(t)$ compartment,

$$T(t) \geq T_0 e^{-(\mu+k+\sigma_2)}, \quad \forall t > 0.$$

Noting from the above that $T(t)$ is positive, it suffices that

$$\begin{aligned} I &= \alpha_1 SI + kT - \alpha_2 IR - (\beta+\delta_1+\mu)I \\ &\geq -(\beta+\delta_1+\mu)I. \end{aligned}$$

Thus, we have

$$I \geq I_0 e^{-(\beta+\delta_1+\mu)}.$$

Subsequently, by following the same approach, we have

$$R \geq R_0 e^{-(\sigma_1+\mu)}.$$

Now, let us suppose that the $I(t)$ and $T(t)$ compartments are integrable, this implies that the following inequality arises:

$$\mathcal{G}(t) \geq \mathcal{G}_0 + \int [\delta_1(I+T)]dt, \quad \forall t > 0.$$

Importantly, we explicitly establish the positivity of the $S(t)$ compartment by first supposing the norm below exists: $\|g\| = \sup_{t\in D_g} |g|$. This suffices that for the susceptible compartment, $S(t)$, we have

$$\begin{aligned}
\dot{S}(t) &= \psi + \sigma_1 R - \alpha_1 SI - \mu S \\
&\geq \sigma_1 R - (\alpha_1 I + \mu)S \geq -(\alpha_1 |I| + \mu)S \\
&\geq -(\alpha_1 \sup_{t\in D_g} |I| + \mu)S \geq -(\alpha_1 \|I\|_\infty + \mu)S \\
&\geq -\varphi S,
\end{aligned}$$

where we define

$$\varphi = (\alpha_1 \|I\|_\infty + \mu).$$

Obviously, this yields

$$S(t) = S_0 e^{-\varphi t}.$$

We observe that these results hold for all other compartments. Hence, all the solutions of the Ebola model are positive.

Boundedness of solutions

To prove the boundedness of solutions to the model, we first consider the total human population,

$$N(t) = S(t) + I(t) + T(t) + R(t). \tag{2}$$

Substituting all equations of the model, we obtain,

$$\begin{aligned}
\frac{dN(t)}{dt} &= \frac{dS(t)}{dt} + \frac{dI(t)}{dt} + \frac{dT(t)}{dt} + \frac{dR(t)}{dt} \\
&= \psi + \sigma_1 R(t) - \alpha_1 S(t)I(t) - \mu S(t) + \alpha_1 S(t)I(t) + kT(t) - \alpha_2 I(t)R(t) \\
&\quad -(\beta+\delta_1+\mu)I(t) + \alpha_2 I(t)R(t) + \beta I(t) - (\mu+k+\sigma_2)T(t) + \sigma_2 T(t) - (\mu+\sigma_1)R(t) \\
&= \psi - \mu N - \delta_1 I(t).
\end{aligned} \tag{3}$$

In the absence of Ebola-related deaths, ($\delta_1 = 0$), we have

$$\frac{dN}{dt} \leq \psi - \mu N. \tag{4}$$

Now taking the Laplace transform of (4), we obtain

$$\begin{aligned} \mathcal{L}\{N'(t)\} + \mu\mathcal{L}\{N(t)\} &\leq \mathcal{L}\{\psi\}, \\ s\mathcal{N}(s) - N(0) + \mu\mathcal{N}(s) &\leq \frac{\psi}{s}, \\ \mathcal{N}(s) &\leq \frac{\psi}{s(s+\mu)} + \frac{N(0)}{s+\mu}. \end{aligned} \tag{5}$$

The inverse Laplace of (5) is

$$N(t) \leq \frac{\psi}{\mu}(1 - e^{-\mu t}) + N(0)e^{-\mu t}. \tag{6}$$

Taking the $\limsup_{t\to\infty}$ of the above equation, we get

$$N(t) \leq \frac{\psi}{\mu}. \tag{7}$$

Now, the solutions of the Ebola model are bounded and feasible in the region

$$\mathcal{V} = \left\{(S, I, T, R) \in \mathbb{R}^4_+ | N \leq \frac{\psi}{\mu}\right\}. \tag{8}$$

5 Caputo fractal-fractional Ebola model

It has been reported in the literature that individuals who have suffered from the Ebola virus disease mostly face severe neurological disorders such as cranial nerve disorders, memory loss, recurring seizures, and others for about six months or more even after recovery [6]. As a result of this, using integer order operator models to study the dynamics of the Ebola disease virus may yield uncertain or unreliable conclusions. In addition, since there occurs mostly structural variability in the dynamics of the Ebola disease, that is, the disease is influenced by physical occurrences, a fractional analysis of the dynamics of the Ebola is the appropriate operator to measure the physical dynamics of the disease [7]. The Caputo fractal-fractional derivative has been chosen for this study due to its enormous advantages over the other fractional operators. For instance, it has been reported in the literature that the Caputo fractal-fractional derivative presents a better description of complex systems, such as biological processes, by accurately measuring these systems' inherent hereditary and memory properties.Again, the Caputo fractal-fractional derivative is quite simplified as it allows the use of standard initial conditions compared to the Riemann-Liouville derivative. As a result, the Caputo fractal-fractional derivative has a minimal computational complexity and requires a minimum storage space when its algorithm is simulated [36–38]. In this study, the Ebola virus disease is thus investigated using the Caputo fractal-fractional operator. From this knowledge, Eq. (1) is reformulated into a non-integer model using Caputo operators in this manner:

$$
\begin{aligned}
{}^{FFC}\mathcal{D}_{0,t}^{\Phi_1,\Phi_2} S(t) &= \psi + \sigma_1 R(t) - \alpha_1 S(t) I(t) - \mu S(t), \\
{}^{FFC}\mathcal{D}_{0,t}^{\Phi_1,\Phi_2} I(t) &= \alpha_1 S(t) I(t) + \kappa T(t) - \alpha_2 I(t) R(t) - (\beta + \delta_1 + \mu) I(t), \\
{}^{FFC}\mathcal{D}_{0,t}^{\Phi_1,\Phi_2} T(t) &= \alpha_2 I(t) R(t) \beta I(t) - (\mu + \kappa + \sigma_2) T(t), \\
{}^{FFC}\mathcal{D}_{0,t}^{\Phi_1,\Phi_2} R(t) &= \sigma_2 T(t) - (\sigma_1 + \mu) R(t),
\end{aligned} \tag{9}
$$

with initial conditions $S(0) = S_0 > 0$, $I(0) = I_0 \geq 0$, $T(0) = T_0 \geq 0$, and $R(0) = R_0 \geq 0$.

Existence and uniqueness of the Caputo fractal-fractional Ebola disease model

A key aspect of mathematical modelling is to examine if there exists a unique solution for the model under study. To establish that model (9) is injective, a thorough existence and uniqueness analysis is carried out using the fixed point theory as done in literature [39–42]. By supposing that there exists the norm $\mathbf{B}(\tau)$ which is defined to be a Banach space and further assumed to be a continuous real-valued map defined in the domain $\tau(0, T)$ with a defined sub norm. Then we note that there is $\mathcal{G} = \mathbf{B}(\tau_1) \times \mathbf{B}(\tau_2) \times \mathbf{B}(\tau_3) \times \mathbf{B}(\tau_4)$ which is imposed on the norm $\|(S, I, T, R)\| = \|S\| + \|I\| + \|T\| + |R\|$, where $\|S\| = \sup_{t\in\tau} |S|, \|I\| = \sup_{t\in\tau} |I|, \|T\| = \sup_{t\in\tau} |T|, \|R\| = \sup_{t\in\tau} |R|$. From the suppositions above, the fractal-fractional Ebola disease model in the Caputo sense is reconstructed as;

$$
\begin{aligned}
S(t) - S(0) &= {}^{C}\mathcal{D}_{t}^{\Phi_1,\Phi_2} \left[\psi + \sigma_1 R(t) - \alpha_1 S(t) I(t) - \mu S(t)\right], \\
I(t) - I(0) &= {}^{C}\mathcal{D}_{t}^{\Phi_1,\Phi_2} \left[\alpha_1 S(t) I(t) + \kappa T(t) - \alpha_2 I(t) R(t) - (\beta + \delta_1 + \mu) I(t)\right], \\
T(t) - T(0) &= {}^{C}\mathcal{D}_{t}^{\Phi_1,\Phi_2} \left[\alpha_2 I(t) R(t) \beta I(t) - (\mu + \kappa + \sigma_2) T(t)\right], \\
R(t) - R(0) &= {}^{C}\mathcal{D}_{t}^{\Phi_1,\Phi_2} \left[\sigma_2 T(t) - (\sigma_1 + \mu) R(t)\right].
\end{aligned} \tag{10}
$$

For convenient evaluations, the equations in (10) are redefined as,

$$
\begin{cases}
\mathcal{J}_1(S, I, T, R) = \psi + \sigma_1 R(t) - \alpha_1 S(t) I(t) - \mu S(t), \\
\mathcal{J}_2(S, I, T, R) = \alpha_1 S(t) I(t) + \kappa T(t) - \alpha_2 I(t) R(t) - (\beta + \delta_1 + \mu) I(t), \\
\mathcal{J}_3(S, I, T, R) = \alpha_2 I(t) R(t) \beta I(t) - (\mu + \kappa + \sigma_2) T(t), \\
\mathcal{J}_4(S, I, T, R) = \sigma_2 T(t) - (\sigma_1 + \mu) R(t).
\end{cases} \tag{11}
$$

Now through the Riemann-Liouville integral operator, the fractal-fractional Ebola disease model (9) suffices that;

$$
\begin{aligned}
{}^{RL}\mathcal{D}_{t}^{\Phi_1} S(t) &= \Phi_{2_*} t^{*\Phi_2 - 1} \mathcal{J}_1(S, I, T, R), \\
{}^{RL}\mathcal{D}_{t}^{\Phi_1} I(t) &= \Phi_{2_*} t^{*\Phi_2 - 1} \mathcal{J}_2(S, I, T, R), \\
{}^{RL}\mathcal{D}_{t}^{\Phi_1} T(t) &= \Phi_{2_*} t^{*\Phi_2 - 1} \mathcal{J}_3(S, I, T, R), \\
{}^{RL}\mathcal{D}_{t}^{\Phi_1} R(t) &= \Phi_{2_*} t^{*\Phi_2 - 1} \mathcal{J}_4(S, I, T, R).
\end{aligned} \tag{12}
$$

Now in order to solve the model, Eq. (12) is reformulated as an initial value problem

$$
\begin{cases}
{}^{RL}\mathcal{D}_{t}^{\Phi_1} \mathcal{Q}(t^*) = \Phi_{2_*} t^{*\Phi_2 - 1} \mathcal{J}(t, \mathcal{Q}(t)) \\
\quad \mathcal{Q}(0) = \mathcal{Q}_0, \qquad \Phi_1, \Phi_{2_*} \in (0, 1],
\end{cases} \tag{13}
$$

where $t^* \in \mathcal{U}$, such that

$$\begin{aligned} \mathcal{Q}(t^*) &= (S(t^*), I(t^*), T(t^*), R(t^*)), \\ \mathcal{Q}(0) &= (S_0, I_0, T_0, R_0)^t. \end{aligned} \tag{14}$$

Also,

$$\mathcal{J}(t, \mathcal{Q}(t)) = \begin{cases} \mathcal{J}_1(S(t^*), I(t^*), T(t^*), R(t^*)), \\ \mathcal{J}_2(S(t^*), I(t^*), T(t^*), R(t^*)), \\ \mathcal{J}_3(S(t^*), I(t^*), T(t^*), R(t^*)), \\ \mathcal{J}_4(S(t^*), I(t^*), T(t^*), R(t^*)). \end{cases} \tag{15}$$

Now by applying the fundamental theorem of calculus to (13), we obtain

$$\mathcal{Q}(t^*) = \mathcal{Q}(0) + \frac{\Phi_{2_*}}{\Gamma(\Phi_1^*)} \int_0^{t^*} \Omega^{*\Phi_{2_*}-1}(t^* - \Omega^*)^{\Phi_1^*-1} \mathcal{J}(\Omega^* \mathcal{Q}(\Omega^*)) h^* \Omega^*, \tag{16}$$

thus, leading to the following relations:

$$\begin{aligned} S(t^*) &= S(0) + \frac{\Phi_{2_*}}{\Gamma(\Phi_1^*)} \int_0^{t^*} \Omega^{*\Phi_{2_*}-1}(t^* - \Omega^*)^{\Phi_2^*-1} \mathcal{J}_1 \\ &\quad \times [S(\Omega^*), I(\Omega^*), T(\Omega^*), R(\Omega^*)], \\ I(t^*) &= I(0) + \frac{\Phi_{2_*}}{\Gamma(\Phi_1^*)} \int_0^{t^*} \Omega^{*\Phi_{2_*}-1}(t^* - \Omega^*)^{\Phi_2^*-1} \mathcal{J}_2 \\ &\quad \times [S(\Omega^*), I(\Omega^*), T(\Omega^*), R(\Omega^*)], \\ T(t^*) &= T(0) + \frac{\Phi_{2_*}}{\Gamma(\Phi_1^*)} \int_0^{t^*} \Omega^{*\Phi_{2_*}-1}(t^* - \Omega^*)^{\Phi_2^*-1} \mathcal{J}_3 \\ &\quad \times [S(\Omega^*), I(\Omega^*), T(\Omega^*), R(\Omega^*)], \\ R(t^*) &= R(0) + \frac{\Phi_{2_*}}{\Gamma(\Phi_1^*)} \int_0^{t^*} \Omega^{*\Phi_{2_*}-1}(t^* - \Omega^*)^{\Phi_2^*-1} \mathcal{J}_4 \\ &\quad \times [S(\Omega^*), I(\Omega^*), T(\Omega^*), R(\Omega^*)]. \end{aligned} \tag{17}$$

Now model (9) is reconstructed as a fixed point problem by using the fixed point theory technique. We initially suppose that the given dual function $\mathcal{W} = \mathcal{H}^* \longrightarrow \mathcal{H}^*$ be defined as

$$\mathcal{W}[\mathcal{Q}(t^*)] = \mathcal{Q}(0) + \frac{\Phi_{2_*}}{\Gamma(\Phi_1)} \int_0^{t^*} \Omega^{*\Phi_{2_*}-1}(t^* - \Omega^*)^{\Phi_1^*-1} \mathcal{J}(\Omega^* \mathcal{Q}(\Omega^*)) h^* \Omega^*. \tag{18}$$

We explicitly define the fixed point theorem for $\Theta^* - \psi^*$ contractions to suffice our proof.

Theorem 1 *([35]) Let us suppose a complete metric space is stated such that $\psi^* \in \mathcal{B}, \Theta^* : \mathcal{H}^{*2} \longrightarrow \mathbb{R}$, and $\mathcal{W} : \mathcal{H}^* \longrightarrow H^*$ which is an $\Theta^* - \psi^*$ contraction such that the following properties are valid:*
a. $\mathcal{W}$ is θ^* permissible.
b. We have h_0, which is in the function $\mathcal{H}^*$ such that $\Theta^*(\psi_0^*, \mathcal{W}\psi_0^*) \geq 1$.
c. Supposing that for any $h_{\psi_*}^*$ which is an improper subset of $\mathcal{W}^*$ where $h_{\psi_*}^* \longrightarrow h^*$ and $\Theta^*(h_{\psi_*}^*, h_{\psi_*+1}^*) \geq 1, \forall \psi^* \geq 1$, then there exists $\Theta^*(h_{\psi_*}^*, h^*) \geq 1$ for every $\psi^* \geq 1$.

The proof of the theorem is carried out through $\Theta^* - \psi^*$ contractions.

Theorem 2 *Let us suppose that we have a φ^* such that $\mathcal{R} \times \mathcal{R} \longrightarrow \mathcal{R}$ and also there is an $\psi^* \in \mathcal{B}$ for any given operator $\mathcal{J} \in \mathcal{W}(\mathcal{K} \times \mathcal{H}^*, \mathcal{H}^*)$. Also, B1 for any given $\mathcal{J}_1, \mathcal{J}_2, \mathcal{J}_3, \mathcal{J}_4 \in \mathcal{H}^*$ and there is $t^* \in \mathcal{A}$,*

$$|\mathcal{J}(t^*, \mathcal{Q}_1(t^*) - \mathcal{J}(t^*, \mathcal{Q}_2(t^*)| \leq \Theta^* \vartheta^*(|\mathcal{Q}_1(t^*) - \mathcal{Q}_2(t^*)|),$$

also realising that $\chi^*(\mathcal{Q}_1(t^*), \mathcal{Q}_2(t^*)) \geq 0$ and also $\vartheta^* = \frac{\Gamma(\Phi_{2_*}+\Phi_{1_*})}{\Phi_{2_*}\eta^{\Phi_{2_*}+\Phi_{1_*}-1}\Gamma(\Phi_{2_*})}$.
G2 Also, for any given $t^* \in \mathcal{A}$ there is a $\mathcal{Q}_0 \in \mathcal{H}^*$ such that

$$a^*(\mathcal{Q}_0(t^*), \mathcal{C}(\mathcal{Q}_0(t^*))) \geq 0,$$

given further that

$$a^*(\mathcal{Q}_1(t^*), \mathcal{Q}_2(t^*)) \geq 0 \longrightarrow a^*(\mathcal{C}(\mathcal{Q}_0(t^*)), \mathcal{C}(\mathcal{Q}_0(t^*))) \geq 0.$$

G3 Supposing that $\{\mathcal{Q}_{\psi^*}\}_{\psi^* \geq 1} \subseteq \mathcal{H}^*$ for $\mathcal{Q}_{n^*} \longrightarrow \mathcal{Q}$, such that

$$a^*(\mathcal{Q}_{\psi^*}(t^*), \mathcal{Q}_{\psi^*+1}(t^*)) \geq 0 \longrightarrow a^*(\mathcal{Q}_{\psi^*}(t^*)), (\mathcal{Q}(t^*)) \geq 0,$$

with any given ψ^* and $t^* \in \mathcal{A}$.
We hereby validate the Caputo fractal-fractional Ebola model to have a solution by the proof below.

Proof Let us suppose that there exists the functions $\mathcal{J}_1, \mathcal{J}_2, \mathcal{J}_3, \mathcal{J}_4 \in \mathcal{H}$ such that $\mathcal{J}_1(t^*), \mathcal{J}_2(t^*), \mathcal{J}_3(t^*), \mathcal{J}_4(t^*)$ are non-negative given any time dimension $t^* \in \mathcal{A}$. Applying some basic mathematical ideas in addition to the beta function yields the following;

$$\begin{aligned}
|\mathcal{W}(\mathcal{Q}_1(t^*)) - \mathcal{W}(\mathcal{Q}_2(t^*))| &\leq \frac{\Phi_{2_*}}{\Gamma(\Phi_1^*)} \int_0^{t^*} \Omega^{*\phi_{2_*}-1}(t^* - \Omega^*)^{\Phi_1^*-1} \\
&\quad \times |\mathcal{J}(\Omega^* \mathcal{Q}_1(\Omega^*)) - \mathcal{J}(\Omega^* \mathcal{Q}_2(\Omega^*))| d^*\Omega^* \\
&\leq \frac{\Phi_{2_*}}{\Gamma(\Phi_1^*)} \int_0^{t^*} \Omega^{*\Phi_{2_*}-1}(t^* - \Omega^*)^{\Phi_1^*-1} \Theta^* \eta^*(|\mathcal{Q}_1(\Omega^*) - \mathcal{Q}_2(\Omega^*)|) d^*\Omega^* \\
&\leq \frac{\Phi_{2_*}\eta^*\eta^{\Phi_{2_*}+\Phi_{1^*}-1}\mathbb{B}(\Phi_{2_*}, \Phi_{1_*})}{\Gamma(\Phi_{1_*})} \Theta^*(\|\mathcal{Q}_1 - \mathcal{Q}_2\|_{\mathcal{H}^*}) \qquad (19) \\
&\leq \frac{\Phi_{2_*}\eta^{\Phi_{2_*}+\Phi_{1^*}-1}\Gamma(\Phi_{2_*})}{\Gamma(\Phi_{1_*} + \Phi_{1^*})} \eta^* \Theta^*(\|\mathcal{Q}_1 - \mathcal{Q}_2\|_{\mathcal{H}^*}).
\end{aligned}$$

This suffices that

$$\|\mathcal{W}(\mathcal{Q}_1) - \mathcal{W}(\mathcal{Q}_2)\|_{\mathcal{H}^*} \leq \frac{\Phi_{2_*}\eta^{\Phi_{2_*}+\Phi_{1^*}-1}\Gamma(\Phi_{2_*})}{\Gamma(\Phi_{1_*} + \Phi_{1^*})} \eta^* \Theta^*(\|\mathcal{Q}_1 - \mathcal{Q}_2\|_{\mathcal{H}^*}) = \Theta^*(\|\mathcal{Q}_1 - \mathcal{Q}_2\|_{\mathcal{H}^*}).$$

Supposing further that given any values for $\mathcal{Q}_1, \mathcal{Q}_2\mathcal{H}^*$, we assume that Θ^* is defined to be $\mathcal{H}^* \times \mathcal{H}^* \longrightarrow [0, \infty)$ as stated in

$$\Theta^*(\mathcal{Q}_1, \mathcal{Q}_2) = \begin{cases} 1, & \text{if } a^*(\mathcal{Q}_1(t^*) \geq 0, \\ 0, & \text{otherwise,} \end{cases} \qquad (20)$$

which suffices that,

$$\mathcal{Q}_1, \mathcal{Q}_2 \in \mathcal{H}^*(\mathcal{W}(\mathcal{Q}_1), \mathcal{W}(\mathcal{Q}_2)) \leq (\mathcal{Q}_1, \mathcal{Q}_2),$$

for any $\mathcal{Q}_1, \mathcal{Q}_2 \in \mathcal{H}^*$.

We hereby establish the function $\mathcal{W}$ to be $\Theta^* - \psi^*$ contraction. Whenever there are $\mathcal{Q}_1, \mathcal{Q}_2 \in \mathcal{H}^*$, we observe that $\mathcal{Q}_1, \mathcal{Q}_2 \in \mathcal{H}^* \geq 1$. Stating explicitly the properties of Θ^*, it implies that $a^*(\mathcal{Q}_1(t^*), \mathcal{Q}_2(t^*))$ as non-negative. Then from (G2), we see that $a^*(\mathcal{W}(\mathcal{Q}_1(t^*)), \mathcal{W}(\mathcal{Q}_2(t^*)))$ is non-negative. Then we have Θ^* implying that $\Theta^*(\mathcal{W}(\mathcal{Q}_1(t^*)), \mathcal{W}(\mathcal{Q}_2(t^*))) \geq 1$. This explicitly suffices that the operator $\mathcal{W}$ is a Θ^* admissible.

We then strongly see that (G2) implies that there exist an $\mathcal{Q}_0 \in \mathcal{H}^*$. This then suffices that $t^*(\mathcal{Q}_0(t^*), \mathcal{W}(\mathcal{Q}_0(t^*)))$ is non-negative for any given t^* in the set $\mathcal{H}$ and

$$\Theta^*(\mathcal{Q}_0, \mathcal{W}(\mathcal{Q}_0)) \geq 1.$$

We can further assume that $\mathcal{Q}_{\psi^*>1}$ is an improper subset of the set $\mathcal{H}^*$ such that $\mathcal{Q}_{\psi^*}$ has a limit point $\mathcal{Q}$ anytime $\Theta^*(\mathcal{Q}_{\psi^*}, \mathcal{Q}_{\psi^*+1}) \geq 1$. It is explicitly seen in Θ^* that

$$a^*(\mathcal{Q}_{\psi^*}(t^*), \mathcal{Q}_{\psi^*+1}(t^*)) \geq 0.$$

This then suffices from (G3) that $a^*(\mathcal{Q}_{\psi^*}(t^*), \mathcal{Q}(t^*)) \geq 0$, implying further that $\Theta^*(\mathcal{Q}_{\psi^*}(t^*), \mathcal{Q}) \geq 1$ for every given ψ^*. Now from Theorem 1, it is observed that there is an $\mathcal{Q}^*\mathcal{H}^*$ in a manner that $\mathcal{W}(\mathcal{Q}^*) = \mathcal{Q}^*$. This then suffices that $\mathcal{Q}^* = (S^*, I^*, T^*, R^*)^T$ is a solution to the Caputo fractal-fractional Ebola disease model.

Theorem 3 *([43]) By assuming that $\mathcal{H}^*$ is said to be a Banach space, which is a convex function $\mathcal{O}$ which is bounded and closed in $\mathcal{H}^*$, and we have $\alpha \in \mathcal{O}$ which is an open set for $0 \in \alpha$. By defining $\mathcal{P} : \alpha \longrightarrow \mathcal{O}$ to be continuous and compact, then it is either*
a. There exists $b^{**} \in \mathcal{O}$ such that $\mathcal{P}(b^{**}) = b^{**}$, or
b. There is $b^* \in \mu\mathcal{O}$ and $v^* \in (0,1)$ such that $v^*\mathcal{P}(b^*) = b^*$
should hold.

Remark 1 *Let us define the relation*

$$\Delta = \mathcal{J}_0, \tag{21}$$

and also

$$\circledast = \frac{\Phi_{2_*}\eta^{\Phi_{2_*}+\Phi_{1^*}-1}\Gamma(\Phi_{2_*})}{\Gamma(\Phi_{2_*}+\Phi_{1^*})}. \tag{22}$$

Theorem 4 *Assuming that the function $\mathcal{J} \in C(\mathbb{Q} \times \mathcal{H}^*, \mathcal{H}^*)$. Then;*
M1: we have $\Theta^* \in \mathcal{N}^1(\mathbb{Q}, \mathbb{R}_+)$ and there have also a non decreasing monotonic function $\mathbb{K} \in C([0,\infty), \mathbb{R}_+)$, implying that for any $t^* \in \mathbb{Q}$ and also $\mathcal{Q} \in \mathcal{H}^*$, we have

$$|\mathcal{J}(t^*), \mathcal{Q}(t^*)| \leq \Theta^*(t^*)\mathbf{G}(|\mathcal{Q}(t^*)|).$$

M1: If there exists $\mathcal{X}$ that is positive and also

$$\frac{\mathcal{X}}{\lambda+\zeta\Theta^*(t^*\mathbf{P}(\mathcal{X}))}>1,$$

where $\Theta^{**}=\sup_{t^*\in\mathbb{Q}}|\Theta^*t^*|$ and also λ,ζ are defined in Eq. (20) and Eq. (19). We then say that the Caputo fractal-fractional Measles disease model's solution exists.

Proof Let us consider $\mathcal{W}:\mathcal{H}^*\longrightarrow\mathcal{H}^*$ as defined in (18) and

$$\mathcal{N}_\nu=\{\mathcal{Q}\in\mathcal{H}^*:\|\mathcal{Q}\|_{\mathcal{H}^*}\leq\nu\},\forall\delta>0.$$

Consequently, the operator $\mathcal{W}$ is obtained from the continuous and limited operator $\mathcal{J}$. Then for $\mathcal{Q}\in\mathcal{N}_\nu$ there is;

$$\begin{aligned}|\mathcal{W}(\mathcal{Q}(t^*))|&\leq|\mathcal{Q}(0)|+\frac{\Phi_{2_*}}{\Gamma(\Phi_1^*)}\int_0^{t^*}\Omega^{*\Phi_{2_*}-1}(t^*-\Omega^*)^{\Phi_1^*-1}|\mathcal{J}(\Omega^*,\mathcal{Q}(k^*))|dk^*\\&\leq\mathcal{Q}_0+\frac{\Phi_{2_*}}{\Gamma(\Phi_1^*)}\int_0^{t^*}\Omega^{*\Phi_{2_*}-1}(t^*-\Omega^*)^{\Phi_1^*-1}\Theta^*(k^*)\mathbb{G}|\mathcal{J}(\mathcal{Q}(k^*))|d\Omega^*\\&\leq\mathcal{Q}_0+\frac{\Phi_{2_*}\eta^*\eta^{\Phi_{2_*}+\Phi_{1^*}-1}\mathbb{B}(\Phi_{2_*},\Phi_{1_*})}{\Gamma(\Phi_{1_*})}\Theta^*0^*\mathbf{A}(\|\mathcal{Q}\|_{\mathcal{H}^*})\\&\leq\lambda+\zeta\Theta^*0^*\mathbf{A}(\nu).\end{aligned}\tag{23}$$

Implying further that

$$\|\mathcal{W}\mathcal{Q}\|\leq\lambda+\zeta\Theta^*0^*\mathbf{A}(\nu)<\infty.\tag{24}$$

We then obtain a complete continuous operator of $\mathcal{W}$ from $\mathcal{H}^*$. Let us now suppose some arbitrary values $t^*,t^{**}\in[0.T]$ such that $t^*\leq t^{**}$ and also $\mathcal{Q}\in\mathcal{N}_\nu$ with the assumption that

$$\sup_{(t^*,\mathcal{Q})\in\mathcal{A}\times\mathcal{N}_\nu}|\mathcal{J}(\Omega^*,\mathcal{Q}(t^*))|=\mathcal{J}^*<\infty.$$

It then suffices that

$$\begin{aligned}|\mathcal{W}(\mathcal{Q}(t^{**}))-\mathcal{W}(\mathcal{Q}(t^*))|&=|\frac{\Phi_{2_*}}{\Gamma(\Phi_1^*)}\int_0^{t^{**}}\Omega^{*\Phi_{2_*}-1}(t^{**}-\Omega^*)^{\Phi_1^*-1}|\mathcal{J}(\Omega^*,\mathcal{Q}(k^*))|dk^*\\&\quad-\frac{\Phi_{2_*}}{\Gamma(\Phi_1^*)}\int_0^{t^*}\Omega^{*\Phi_{2_*}-1}(t^*-\Omega^*)^{\Phi_1^*-1}\Theta^*(k^*)\mathcal{J}|\mathcal{J}(\mathcal{Q}(k^*))|d\Omega^*\\&\leq\frac{\psi_{2_*}\mathcal{P}^*}{\Gamma(\psi_1^*)}|\int_0^{\flat^{**}}\Omega^{*\Phi_{2_*}-1}(t^{**}-\Omega^*)^{\Phi_1^*-1}dk^*-\int_0^{t^*}\Omega^{*\Phi_{2_*}-1}(t^*-\Omega^*)^{\Phi_1^*-1}dk^*|\\&\leq\frac{\Phi_{2_*}\mathbb{B}(\Phi_{2_*},\Phi_1)\mathcal{J}^*}{\Gamma(\Phi_1^*)}[t^{**\Phi_{2_*}+\Phi_{1^*}-1}-t^{*\Phi_{2_*}+\Phi_{1^*}-1}]\\&\leq\frac{\Phi_{2_*}\Gamma(\Phi_{2_*})\mathcal{J}^*}{\Gamma(\Phi_1^*+\Phi_{1^*})}[(t^{**})^{\Phi_{2_*}+\Phi_{1^*}-1}-t^{*\Phi_{2_*}+\Phi_{1^*}-1}],\end{aligned}\tag{25}$$

we therefore observe that $\mathcal{Q}$ is independent of t^{**} has a limit point in t^*, then the RHS of Eq. (25)

is asymptotic to 0. This leads to

$$\|\mathcal{W}(\mathcal{Q}(t^{**})) - \mathcal{W}(\mathcal{Q}(t^{*}))\|_{\mathcal{H}^{*}} \longrightarrow 0.$$

We then observe from the above that the function $\mathcal{W}$ is equi-continuous and we further show the compactness of $\mathcal{W}$ on $\mathcal{N}_{\nu}$ through means of the Arzela and Ascoli theorem. It is observed in furtherance that the assumptions given in Theorem 3 are explicitly valid on the function $\mathcal{V}$. This implies that either (a) or (b) is valid. From (M1), we formulate;

$$\mathcal{R} = \{\mathcal{Q} \in \mathcal{H}_{*} : \|\mathcal{Q}\|_{\mathcal{H}_{*}} < \mathcal{Z}\},$$

where we define the function $\mathcal{Z}$ to be positive through

$$\lambda + \zeta\Theta^{*}0^{*}\mathcal{B}(\mathcal{Z}).$$

Now by applying (M1) on Eq. (25) we derive the relation

$$\|\mathcal{W}\mathcal{Q}\|_{\mathcal{H}_{*}} \leq \lambda + \zeta\Theta^{*}0^{*}\mathbf{A}(\mathcal{Q}). \tag{26}$$

Now from the existence of the operator $\mathcal{Q} \in \beta\mathcal{R}$ and $\beta \in (0,1)$ in a manner that $\mathcal{Q} = \varrho\mathcal{W}(\mathcal{Q})$. Now by the given function $\mathcal{Q}$ in the domain β, then from Eq. (26), we have,

$$\mathcal{Z} = \|\mathcal{Q}\|_{\mathcal{H}^{*}} = \beta\|\mathcal{W}(\mathcal{Q})\|_{\mathcal{H}^{*}} < \lambda + \zeta\Theta^{*}0^{*}\mathbf{A}(\|\mathcal{Q}\|_{\mathcal{H}^{*}}) < \lambda + \zeta\Theta^{*}0^{*}\mathcal{Z}(\mathcal{R}) < \mathcal{R}.$$

From the above, we observe that we cannot validate it. This implies that (b) is invalid and the operator $\mathcal{W}$ has a solution or a fixed point in the function $\mathcal{R}$ from Theorem 3. Then, the Caputo fractal-fractional model has at least one solution.
Now we establish explicitly that the Caputo fractal-fractional model has only one solution. We begin by stating the lemma below;

Lemma 1 *Supposing that there exist the following functions:*
$(S, I, T, R, S^{*}, I^{*}, T^{*}, R^{*}) \in \mathcal{G} = C(\mathcal{N}, \mathcal{Y})$ *and there is the norm*
(N1): $\|S\| \leq \mathfrak{I}_1, \|I\| \leq \mathfrak{I}_2, \|T\| \leq \mathfrak{I}_3, \|R\| \leq \mathfrak{I}_4$ *where* $\mathfrak{I}_1, \mathfrak{I}_2, \mathfrak{I}_3, \mathfrak{I}_4$ *are positive, and the given norms suffices the criteria of the least upper bound-norm regarding* t^{*}. *Now, further considering the case where,* $\mathcal{J}_1, \mathcal{J}_2, \mathcal{J}_3, \mathcal{J}_4$ *in view that equation the individual components in* (11) *meets the Lipschitz criterion of boundedness anytime there is* $\mathcal{K}_1, \mathcal{K}_2, \mathcal{K}_3, \mathcal{K}_4 > 0$ *where*

$$\begin{aligned}
\mathcal{K}_1 &= \alpha + \mu, \\
\mathcal{K}_2 &= (\alpha - \beta + \delta_1 + \mu), \\
\mathcal{K}_3 &= (\mu + \kappa + \sigma_2), \\
\mathcal{K}_4 &= \sigma_1 + \mu.
\end{aligned}$$

Proof Given the first operator $\mathcal{P}_1$, for the dual functions, S, S^{*}, we compute;

$$\begin{aligned}
&\|\mathcal{J}_1(t^{*}, S(t^{*}), I(t^{*}), T(t^{*}), R(t^{*})) - \mathcal{J}_1(t_{*}, S^{*}(t^{*}), I^{*}(t^{*}), T^{*}(t^{*}), R^{*}(t^{*}))\| \\
&\leq \|\psi + \sigma_1 R(t) - \alpha_1 S(t) I(t) - \mu S(t)\| \leq -\alpha(S - S^{*}) - \mu(S - S^{*}) \\
&\leq \mathcal{K}_1\|S - S^{*}\|.
\end{aligned}$$

We observe from the above that the function $\mathcal{J}_1$ about the compartment S for the constant $\mathcal{K}_1$ is positive and therefore bounded. Also, let us consider $\mathcal{J}_2$, for the dual functions, I, I^*, we obtain;

$$\begin{aligned}
&\|\mathcal{J}_1(t^*, S^*(t^*), I^*(t^*), T^*(t^*), R^*(t^*)) - \mathcal{J}_1(t_*, S^*(t^*), I^*(t^*), T^*(t^*), R^*(t^*))\| \\
&\leq \|\alpha_1 S(t)I(t) + \kappa T(t) - \alpha_2 I(t)R(t) - (\beta + \delta_1 + \mu)I(t)\| \\
&\leq [-\alpha - (\beta + \delta_1 + \mu)](I - I^*) \\
&\leq -[\alpha - (\beta + \delta_1 + \mu)]\|I - I^*\| \\
&\leq (\alpha - \beta + \delta_1 + \mu)\|I - I^*\| \\
&\leq \mathcal{K}_2\|I - I^*\|.
\end{aligned}$$

We further observe that the function $\mathcal{J}_2$ about the compartment I for the constant $\mathcal{K}_2$ is positive and also bounded. Let us again consider $\mathcal{J}_3$, for the dual functions, T, T^*, we have;

$$\begin{aligned}
&\|\mathcal{J}_1(t^*, S(t^*), I(t^*), T(t^*), R(t^*)) - \mathcal{J}_1(t_*, S^*(t^*), I^*(t^*), T^*(t^*), R^*(t^*))\| \\
&\leq \|\alpha_2 I(t)R(t)\beta I(t) - (\mu + \kappa + \sigma_2)T(t)\| \\
&\leq -(\mu + \kappa + \sigma_2)(T - T^*) \\
&\leq (\mu + \kappa + \sigma_2)\|T - T^*\| \\
&\leq \mathcal{K}_3\|T - T^*\|.
\end{aligned}$$

In addition, we see again that the function $\mathcal{J}_3$ about the compartment T for the constant $\mathcal{K}_3$ is positive and therefore bounded. Let us finally consider $\mathcal{J}_4$, for the dual functions, R, R^*, we derive;

$$\begin{aligned}
&\|\mathcal{J}_1(t^*, S(t^*), I(t^*), T(t^*), R(t^*)) - \mathcal{J}_1(t_*, S^*(t^*), I^*(t^*), T^*(t^*), R^*(t^*))\| \\
&\leq \|\sigma_2 T(t) - (\sigma_1 + \mu)R(t)\| \\
&\leq -(\sigma_1 + \mu)(R - R^*) \\
&\leq (\sigma_1 + \mu)\beta\|R - R^*\| \\
&\leq (\sigma_1 + \mu)\|R - R^*\| \\
&\leq \mathcal{K}_4\|R - R^*\|.
\end{aligned}$$

Finally, we observe that the function $\mathcal{J}_4$ about the state variable R for the constant $\mathcal{K}_4$ is positive and therefore bounded. This suffices that the constants $\mathcal{K}_1, \mathcal{K}_2, \mathcal{K}_3, \mathcal{K}_4$ meets the Lipscitz criterion for boundedness.
Let us finally state and prove the theorem below.

Theorem 5 *By assuming further that the condition (N1) is true, it is obvious that the Caputo fractal-fractional Ebola disease model admits only one solution whenever*

$$\circledast\mathcal{K}_\Omega < 1, \qquad \Omega \in \{1, 2, 3, 4\}, \tag{27}$$

recalling the definition of $\circledast$ *in Eq.* (22).

Proof By recalling and applying the concept of proof by contradiction, the study posits that the Caputo fractal-fractional Ebola model admits several solutions. We then commence the proof by assuming that there exists another solution to the Caputo fractal-fractional Ebola model, which is given as $(S^*(t^*), I^*(t^*), T^*(t^*), R^*(t^*))$ with the following initial values; (S_0, I_0, T_0, R_0) such that

Eq. (18) yields;

$$\begin{aligned}
S^*(t^*) &= S_0 + \frac{\Phi_{2_*}}{\Gamma(\Phi_{1^*})}\int_0^{\flat^*} \Omega^{*\Phi_{2_*}-1}(t^*-\Omega^*)^{\Phi_1^*-1} \\
&\quad \times \mathcal{J}_1(\Omega^*, S^*(\Omega^*), I^*(\Omega^*), T^*(\Omega^*), R^*(\Omega^*))g^*\Omega^*, \\
I^*(t^*) &= I_0 + \frac{\Phi_{2_*}}{\Gamma(\Phi_{1^*})}\int_0^{\flat^*} \Omega^{*\Phi_{2_*}-1}(t^*-\Omega^*)^{\Phi_1^*-1} \\
&\quad \times \mathcal{J}_2(\Omega^*, S^*(\Omega^*), I^*(\Omega^*), T^*(\Omega^*), R^*(\Omega^*))g^*\Omega^*, \\
T^*(t^*) &= T_0 + \frac{\Phi_{2_*}}{\Gamma(\Phi_{1^*})}\int_0^{\flat^*} \Omega^{*\Phi_{2_*}-1}(t^*-\Omega^*)^{\Phi_1^*-1} \\
&\quad \times \mathcal{J}_3(\Omega^*, S^*(\Omega^*), I^*(\Omega^*), T^*(\Omega^*), R^*(\Omega^*))g^*\Omega^*, \\
R^*(t^*) &= R_0 + \frac{\Phi_{2_*}}{\Gamma(\Phi_{1^*})}\int_0^{\flat^*} \Omega^{*\Phi_{2_*}-1}(t^*-\Omega^*)^{\Phi_1^*-1} \\
&\quad \times \mathcal{J}_4(\Omega^*, S^*(\Omega^*), I^*(\Omega^*), T^*(\Omega^*), R^*(\Omega^*))g^*\Omega^*.
\end{aligned} \tag{28}$$

We then obtain the following results;

$$\begin{aligned}
|S(t^*) - S^*(t^*)| &\leq S_0 + \frac{\Phi_{2_*}}{\Gamma(\Phi_{1^*})}\int_0^{t^*} \Omega^{*\Phi_{2_*}-1}(t^*-\Omega^*)^{\Phi_1^*-1} \\
&\quad \times |\mathcal{J}_1(\Omega^*, S(\Omega^*), I(\Omega^*), T(\Omega^*), R(\Omega^*)) \\
&\quad - \mathcal{J}_1(\Omega^*, S(\Omega^*), I(\Omega^*), T(\Omega^*), R(\Omega^*))|g^*\Omega^* \\
&\leq \frac{\Phi_{2_*}}{\Gamma(\Phi_{1^*})}\int_0^{t^*} \Omega^{*\Phi_{2_*}-1}(t^*-\Omega^*)^{\Phi_1^*-1} m_1 \|S - S^*\| g^*\Omega^* \\
&\leq \circledast \mathcal{K}_1 \|S - S^*\|,
\end{aligned} \tag{29}$$

which in this case results in

$$(1 - \circledast \mathcal{K}_1)\|S - S^*\| \leq 0.$$

It is therefore obvious from Eq. (29) the inequality above will be true if $\|S - S^*\| = 0$ or S being the same as S^*.

Also considering the infected compartment, that is, $I(t)$, we obtain;

$$\begin{aligned}
|I(t^*) - I^*(t^*)| &\leq I_0 + \frac{\Phi_{2_*}}{\Gamma(\Phi_{1^*})}\int_0^{t^*} \Omega^{*\Phi_{2_*}-1}(t^*-\Omega^*)^{\Phi_1^*-1} \\
&\quad \times |\mathcal{J}_2(\Omega^*, S(\Omega^*), I(\Omega^*), T(\Omega^*), R(\Omega^*)) \\
&\quad - \mathcal{J}_2(\Omega^*, S(\Omega^*), I(\Omega^*), T(\Omega^*), R(\Omega^*))|g^*\Omega^* \\
&\leq \frac{\Phi_{2_*}}{\Gamma(\Phi_{1^*})}\int_0^{t^*} \Omega^{*\Phi_{2_*}-1}(t^*-\Omega^*)^{\Phi_1^*-1} m_1 \|I - I^*\| g^*\Omega^* \\
&\leq \circledast \mathcal{K}_2 \|I - I^*\|,
\end{aligned} \tag{30}$$

which in this case results in

$$(1 - \circledast \mathcal{K}_2)\|V_1 - V_1^*\| \leq 0.$$

It is then an obvious observation that from Eq. (30), the above inequality will be valid if $\|I - I^*\| = 0$ or I being the same as I^*.
Let us consider also the third compartment, that is, $T(t)$, we have;

$$\begin{aligned}|T(t^*) - T^*(t^*)| &\leq T_0 + \frac{\Phi_{2_*}}{\Gamma(\Phi_{1^*})}\int_0^{t^*} \Omega^{*\Phi_{2_*}-1}(t^* - \Omega^*)^{\Phi_1^*-1} \\ &\times |\mathcal{J}_3(\Omega^*, S(\Omega^*), I(\Omega^*), T(\Omega^*), R(\Omega^*)) \\ &- \mathcal{J}_3(\Omega^*, S(\Omega^*), I(\Omega^*), T(\Omega^*), R(\Omega^*))|g^*\Omega^* \\ &\leq \frac{\Phi_{2_*}}{\Gamma(\Phi_{1^*})}\int_0^{t^*} \Omega^{*\Phi_{2_*}-1}(t^* - \Omega^*)^{\Phi_1^*-1} m_1\|T - T^*\|g^*\Omega^* \\ &\leq \circledast\mathcal{K}_3\|T - T^*\|,\end{aligned} \tag{31}$$

which also leads to

$$(1 - \circledast\mathcal{K}_3)\|T - T^*\| \leq 0.$$

We also see that from Eq. (31) the above inequality will be correct if $\|T - T^*\| = 0$ or T being the same as T^*.
Finally, considering the last state variable, that is, $R(t)$, we obtain;

$$\begin{aligned}|R(t^*) - R^*(t^*)| &\leq R_0 + \frac{\Phi_{2_*}}{\Gamma(\Phi_{1^*})}\int_0^{t^*} \Omega^{*\Phi_{2_*}-1}(t^* - \Omega^*)^{\Phi_1^*-1} \\ &\times |\mathcal{J}_4(\Omega^*, S(\Omega^*), I(\Omega^*), T(\Omega^*), R(\Omega^*)) \\ &- \mathcal{J}_4(\Omega^*, S(\Omega^*), I(\Omega^*), T(\Omega^*), R(\Omega^*))|g^*\Omega^* \\ &\leq \frac{\Phi_{2_*}}{\Gamma(\Phi_{1^*})}\int_0^{t^*} \Omega^{*\Phi_{2_*}-1}(t^* - \Omega^*)^{\Phi_1^*-1} m_1\|R - R^*\|g^*\Omega^* \\ &\leq \circledast\mathcal{K}_4\|R - R^*\|,\end{aligned} \tag{32}$$

a similar result is obtained as

$$(1 - \circledast\mathcal{K}_4)\|R - R^*\| \leq 0.$$

It is therefore obvious from Eq. (32) the inequality above will be true if $\|R - R^*\| = 0$ or R being the same as R^*.
From the above results, it is implied that the current solution $(S^*(t^*), I^*(t^*), T^*(t^*), R^*(t^*))$ and the previous solution $(S(t^*), I(t^*), T(t^*), R(t^*))$ are the same. This suffices therefore that the Caputo fractal-fractional Ebola disease model admits a single solution. This ends the proof.

Hyers-Ulam and Hyers-Ulam-Rassias stability of the Caputo fractal-fractional Ebola model

This section is dedicated to the stability analysis of the model in Eq. (9). Stability analysis is carried out in this study to establish that the solutions of the model obtained are not absolutely dependent on the changes that may occur in the neighbourhood. This is essential as biological systems undergo changes sometimes and this may affect the nature of the solution obtained. The stability studies are therefore carried out to find out if a small change in the neighbourhood may exert the same small amount of change in the solution of the model. To conduct this study, we employ the Hyers-Ulam (HU) stability criterion [44] and its extended form referred to as

the Hyers-Ulam-Rassias stability (HUR) criterion [45]. Also, many models do not have exact solutions therefore resulting in mostly reliance on numerical solutions which also come from approximation algorithms. The HU and HUR stability criteria have shown enough strength in studying instabilities that may occur. This section therefore deals with applying the HU and HUR stability criteria to understand the stability patterns of the Caputo Ebola fractal-fractional model's solution.

Definition 4 *Let us suppose that the Caputo fractal-fractional Ebola model meets the HU stability criterion whenever there exist* $D_{\mathcal{J}_i} > 0 \in \mathbb{R}$ *for* $i = 1, 2, 3, 4$ *such that* $\forall \wp > 0$ *and also for every* S^*, I^*, T^*, R^* *in the set* $\mathcal{S}^*$*, then we have,*

$$\begin{aligned}
|{}^{FFC}\mathcal{D}_{0,t^*}^{\Phi_1^*,\Phi_{2*}} S(t^*) - \mathcal{J}_1(S^*(t^*), I^*(t^*), T^*(t^*), R^*(t^*))| < \wp_1,\\
|{}^{FFC}\mathcal{D}_{0,t^*}^{\Phi_1^*,\Phi_{2*}} I(t^*) - \mathcal{J}_2(S^*(t^*), I^*(t^*), T^*(t^*), R^*(t^*))| < \wp_2,\\
|{}^{FFC}\mathcal{D}_{0,t^*}^{\Phi_1^*,\Phi_{2*}} T(t^*) - \mathcal{J}_3(S^*(t^*), I^*(t^*), T^*(t^*), R^*(t^*))| < \wp_3,\\
|{}^{FFC}\mathcal{D}_{0,t^*}^{\Phi_1^*,\Phi_{2*}} R(t^*) - \mathcal{J}_4(S^*(t^*), I^*(t^*), T^*(t^*), R^*(t^*))| < \wp_4,
\end{aligned} \tag{33}$$

and noting also that there exists $(S, I, T, R) \in \mathcal{S}^*$ *then it is obvious that the Caputo fractal-fractional Ebola disease model satisfy*

$$\begin{aligned}
|S^*(t^*) - S(t^*)| < D_{\mathcal{J}_1}\wp_1,\\
|I^*(t^*) - I(t^*)| < D_{\mathcal{J}_2}\wp_2,\\
|T^*(t^*) - T(t^*)| < D_{\mathcal{J}_3}\wp_3,\\
|R^*(t^*) - R(t^*)| < D_{\mathcal{J}_4}\wp_4.
\end{aligned} \tag{34}$$

Remark 2 *We then suppose that* $(S^*, I^*, T^*, R^*) \in \mathcal{G}^*$ *is a solution to the Caputo fractal-fractional Ebola model whenever we have* $\ell_1, \ell_2, \ell_3, \ell_4 \in \mathcal{C}([0, T], \mathbb{R})$ *(based on* (S^*, I^*, T^*, R^*) *respectively) such that* $\forall t^* \in (V, (\Omega)).|\ell_\Omega(t^*)| < \wp_\Omega$ *for* $\Omega = 1, 2, 3, 4$*, given*

$$\begin{aligned}
{}^{FFC}\mathcal{D}_{0,t^*}^{\Phi_1^*,\Phi_{2*}} S^*(t^*) = \mathcal{J}_1(S^*(t^*), I^*(t^*), T^*(t^*), R^*(t^*))| + \wp_1(t^*),\\
{}^{FFC}\mathcal{D}_{0,t^*}^{\Phi_1^*,\Phi_{2*}} I^*(t^*) = \mathcal{J}_2(S^*(t^*), I^*(t^*), T^*(t^*), R^*(t^*))| + \wp_2(t^*),\\
{}^{FFC}\mathcal{D}_{0,t^*}^{\Phi_1^*,\Phi_{2*}} T^*(t^*) = \mathcal{J}_3(S^*(t^*), I^*(t^*), T^*(t^*), R^*(t^*))| + \wp_3(t^*),\\
{}^{FFC}\mathcal{D}_{0,t^*}^{\Phi_1^*,\Phi_{2*}} R^*(t^*) = \mathcal{J}_4(S^*(t^*), I^*(t^*), T^*(t^*), R^*(t^*))| + \wp_4(t^*).
\end{aligned} \tag{35}$$

Definition 5 *We assume that the Caputo fractal-fractional Ebola model is HUR stable whenever we have a function* Φ_i *for* $i = 1, 2, 3, 4$ *for* $D_{\mathcal{J}_i,\Phi_i} > 0 \in \mathbb{R}$ *for* $i = 1, 2, 3, 4$ *such that for every* $\wp_i > 0$ *and also anytime* $(S^*, I^*, T^*, R^*) \in \mathbb{S}^*$ *satisfying*

$$\begin{aligned}
|{}^{FFC}\mathcal{D}_{0,t^*}^{\Phi_1^*,\Phi_{2*}} S(t^*) - \mathcal{J}_1(S^*(t^*), I^*(t^*), T^*(t^*), R^*(t^*))| < \wp_1\Phi_1(t^*),\\
|{}^{FFC}\mathcal{D}_{0,t^*}^{\Phi_1^*,\Phi_{2*}} I(t^*) - \mathcal{J}_2(S^*(t^*), I^*(t^*), T^*(t^*), R^*(t^*))| < \wp_2\Phi_2(t^*),\\
|{}^{FFC}\mathcal{D}_{0,t^*}^{\Phi_1^*,\Phi_{2*}} T(t^*) - \mathcal{J}_3(S^*(t^*), I^*(t^*), T^*(t^*), R^*(t^*))| < \wp_3\Phi_3(t^*),\\
|{}^{FFC}\mathcal{D}_{0,t^*}^{\Phi_1^*,\Phi_{2*}} R(t^*) - \mathcal{J}_4(S^*(t^*), I^*(t^*), T^*(t^*), R^*(t^*))| < \wp_4\Phi_4(t^*),
\end{aligned} \tag{36}$$

this implies that $(S^*, I^*, T^*, R^*) \in \mathcal{U}^*$ *satisfying the Caputo fractal-fractional Ebola model as given in*

$$\begin{aligned} |S^*(t^*) - S(t^*)| &< D_{\mathcal{J}_1\Phi_1}\wp_1\Phi_1(t^*), \\ |I^*(t^*) - I(t^*)| &< D_{\mathcal{J}_2\Phi_2}\wp_2\Phi_2(t^*), \\ |T^*(t^*) - T(t^*)| &< D_{\mathcal{J}_3\Phi_3}\wp_3\Phi_3(t^*), \\ |R^*(t^*) - R(t^*)| &< D_{\mathcal{J}_4\Phi_4}\wp_4\Phi_4(t^*). \end{aligned} \tag{37}$$

Remark 3 *We then assume further that* $(S^*, I^*, T^*, R^*) \in \mathcal{U}^*$ *is a solution to the Caputo fractal-fractional Ebola model whenever we have* $\ell_1, \ell_2, \ell_3, \ell_4 \in \mathcal{C}([0, T], \mathbb{R})$ *(depending on* (S^*, I^*, T^*, R^*) *respectively) such that* $\forall t^* \in (M, (\Omega)).|\ell_\Omega(t^*)| < \Phi_i\wp_\Omega$ *for* $\Omega = 1, 2, 3, 4$, *given that*

$$\begin{aligned} {}^{FFC}\mathcal{D}^{\Phi_1^*,\Phi_{2*}}_{0,t^*} S^*(t^*) &= \mathcal{J}_1(S^*(t^*), I^*(t^*), T^*(t^*), R^*(t^*))| + \wp_1(t^*), \\ {}^{FFC}\mathcal{D}^{\Phi_1^*,\Phi_{2*}}_{0,t^*} I^*(t^*) &= \mathcal{J}_2(S^*(t^*), I^*(t^*), T^*(t^*), R^*(t^*))| + \wp_2(t^*), \\ {}^{FFC}\mathcal{D}^{\Phi_1^*,\Phi_{2*}}_{0,t^*} T^*(t^*) &= \mathcal{J}_3(S^*(t^*), I^*(t^*), T^*(t^*), R^*(t^*))| + \wp_3(t^*), \\ {}^{FFC}\mathcal{D}^{\Phi_1^*,\Phi_{2*}}_{0,t^*} R^*(t^*) &= \mathcal{J}_4(S^*(t^*), I^*(t^*), T^*(t^*), R^*(t^*))| + \wp_4(t^*). \end{aligned} \tag{38}$$

Theorem 6 *Let us suppose that the Caputo fractal-fractional Ebola model is HU stable and satisfies the condition that* $U := [0, T]$ *such that* $\circledast\mathcal{K}_i$ *for* $i = 1, 2, 3, 4$, *and* $\circledast$ *as defined in Eq. (22) and the axiom* $N1$ *is true.*

Proof By assuming that $\wp > 0$ and also we define $S^* \in \mathcal{G}$ given further that

$$|{}^{FFC}\mathcal{D}^{\Phi_1^*,\Phi_{2*}}_{0,t} S^*(t) - \mathcal{J}_1(S^*, I^*, T^*, R^*)| < \wp_1,$$

we then have ℓ_1 which is deduced from the condition in Remark 2, this then implies that;

$$\begin{aligned} {}^{FFC}\mathcal{D}^{\Phi_1^*,\Phi_{2*}}_{0,t} S^*(t) &= \mathcal{J}_1(S^*, I^*, T^*, R^*) \\ &< \ell_1(t^*), \end{aligned} \tag{39}$$

where $|\ell_1(t) \leq \wp_1|$. This results in,

$$\begin{aligned} S^*(t^*) = S_0 + \frac{\Phi_{2*}}{\Gamma(\Phi_1^*)}\int_0^{t^*}(t^* - \Omega^*)^{\Phi_1 - 1}\mathcal{J}_1(S^*(\Omega^*), I^*(\Omega^*), T^*(\Omega^*), R^*(\Omega^*))d\Omega^* \\ + \frac{\Phi_{2*}}{\Gamma(\Phi_1^*)}\int_0^{t^{**}}(t^* - \Theta^*)^{\Phi_1^2 - 1}\wp_1(\Theta^*)d\Omega^*. \end{aligned} \tag{40}$$

Now from Theorem 5, we let $S \in \mathcal{G}$ to be a unique solution of the measles disease model with Caputo fractal-fractional operators. The function $S(\flat^*)$ in the form

$$\begin{aligned} S^*(t^*) = S_0 + \frac{\Phi_{2*}}{\Gamma(\Phi_1^*)}\int_0^{t^*}(t^* - \Omega^*)^{\Phi_1 - 1} \\ \times \mathcal{J}_1(S^*(\Omega^*), I^*(\Omega^*), T^*(\Omega^*), R^*(\Omega^*))d\Omega^*, \end{aligned} \tag{41}$$

and this leads to,

$$|S^*(t^*) - S(t^*)| \leq \frac{\Phi_{2_*}}{\Gamma(\Phi_1^*)} \int_0^{t^*} (t^* - \Omega^*)^{\Phi_1 - 1} |\wp_1(\Omega^*)| d\Omega^* + \frac{\Phi_{2_*}}{\Gamma(\Phi_1^*)} \int_0^{t^*} (t^* - \Omega^*)^{\Phi_1 - 1} \times |\mathcal{J}_1(S^*(\Omega^*), I^*(\Omega^*), T^*(\Omega^*), R^*(\Omega^*)) d\Omega^* - \mathcal{A}_1(S(\Omega^*), I(\Omega^*), T(\Omega^*), R(\Omega^*)) d\Omega^* \leq \circledast \wp_1 + \circledast \mathcal{K}_1 \|S^* - S\|. \tag{42}$$

We then have;

$$\|S^* - S\| \leq \frac{\circledast \wp_1}{1 - \circledast \mathcal{K}_1}.$$

It is supposed that $D_{\mathcal{J}_1} = \frac{\circledast}{1 - \circledast \mathcal{K}_1}$, this then results in the norm $\|S^* - S\| \leq D_{\mathcal{J}_1, \wp_1}$. By following the same approach for the other state variables of the model, we obtain the norms below;

$$\begin{aligned} \|I^* - I\| &\leq D_{\mathcal{J}_2, \wp_2}, \\ \|T^* - T\| &\leq D_{\mathcal{J}_3, \wp_3}, \\ \|R^* - R\| &\leq D_{\mathcal{J}_4, \wp_4}. \end{aligned} \tag{43}$$

Since we have the results $D_{\mathcal{J}_i, \wp_i} = \frac{\circledast}{1 - \circledast \mathcal{K}_i}$ for $i = 2, 3, 4$, then the condition for stability is satisfied. Hence we posit that the Caputo fractal-fractional Ebola model meets the Hyers-Ulam stability criterion.

Theorem 7 *By assuming further that (N1) is valid, and we have some non-decreasing maps Φ_i contained in the set $C([0, T], \mathbb{R})$ for $i = 1, 2, 3, 4$ and also there exist some $\ell_{\Phi_i} > 0$ such that $\forall t^* \in U$, then we have*

$${}^{FFC}\mathcal{D}_{0,t}^{\Phi_1^*, \Phi_{2_*}} \Phi_i(t^*) < \ell_{\Phi_i} \Phi_i(t^*), \qquad i = 1, 2, 3, 4.$$

Whenever condition (N1) is satisfied, we say that the Caputo fractal-fractional Ebola model is Hyers-Ulam-Rassias stable.

Proof Given that $\wp > 0$ and also $S^* \in \mathcal{G}$, thius results in

$$|{}^{FFC}\mathcal{D}_{0,t}^{\Phi_1^*, \Phi_{2_*}} S^*(t^*) - \mathcal{J}_1 S^*(t^*), I^*(t^*), T^*(t^*), R^*(t^*)| < \wp_1 \Phi_i(t^*).$$

Now assuming that there is $\ell_1(t^*)$ such that;

$${}^{FFC}\mathcal{D}_{0,t}^{\Phi_1^*, \Phi_{2_*}} S^*(t^*) = \mathcal{J}_1 S^*(t^*), I^*(t^*), T^*(t^*), R^*(t^*) + \ell(t^*),$$

noting that $|\ell_1(t^*) \leq \wp_1 \Phi_1(t^*)|$, leading to,

$$\begin{aligned} S^*(t^*) = S_0 &+ \frac{\Phi_{2_*}}{\Gamma(\Phi_1^*)} \int_0^{t^*} (t^* - \Omega^*)^{\Phi_1 - 1} \mathcal{J}_1(S^*(\Omega^*), I^*(\Omega^*), T^*(\Omega^*), R^*(\Omega^*)) d\Omega^* \\ &+ \frac{\Phi_{2_*}}{\Gamma(\Phi_1^*)} \int_0^{t^{**}} (t^* - \Omega^*)^{\Phi_1^2 - 1} \ell_1(\Omega^*) d\Omega^*. \end{aligned} \tag{44}$$

In addition, we recall from Theorem 5 and suppose that there exists a unique solution to the Caputo fractal-fractional Ebola model, relating to the state variable $S \in \mathcal{G}$. We then obtain the

function $S(t^*)$ in the form

$$\begin{aligned} S^*(t^*) = S_0 + \frac{\Phi_{2_*}}{\Gamma(\Phi_1^*)} \int_0^{t^*} (t^* - \Omega^*)^{\Phi_1 - 1} \\ \times \mathcal{J}_1(S^*(\Omega^*), I^*(\Omega^*), T^*(\Omega^*), R^*(\Omega^*)) d\Omega^*, \end{aligned} \tag{45}$$

which then leads to,

$$\begin{aligned} |S^*(t^*) - S(t^*)| &\leq \frac{\Phi_{2_*}}{\Gamma(\Phi_1^*)} \int_0^{t^*} (t^* - \Omega^*)^{\Phi_1 - 1} |\wp_1(\Omega^*)| d\Omega^* \\ &+ \frac{\Phi_{2_*}}{\Gamma(\Phi_1^*)} \int_0^{t^*} (t^* - \Omega^*)^{\Phi_1 - 1} \\ &\times |\mathcal{J}_1(S^*(\Omega^*), I^*(\Omega^*), T^*(\Omega^*), R^*(\Omega^*)) d\Omega^* \\ &- \mathcal{A}_1(S(\Omega^*), I(\Omega^*), T(\Omega^*), R(\Omega^*)) d\Omega^* \\ &\leq \frac{\wp_1 \Phi_{2_*}}{\Gamma(\Phi_1^*)} \int_0^{t^*} (t^* - \Omega^*)^{\Phi_1 - 1} \Phi_1(t^*) + \circledast \mathcal{K}_1 \|S^* - S\| \\ &\leq \wp_1 \ell_{\Phi_1} \Phi_1(t^*) + \circledast \mathcal{K}_1 \|S^* - S\|. \end{aligned} \tag{46}$$

It is observed that the state variable S is in the form;

$$\|S^* - S\| \leq \frac{\wp_1 \ell_{\Phi_1} \Phi_1(t^*)}{1 - \circledast \mathcal{K}_1}.$$

By concluding on this, from the above we define $D_{\mathcal{J}_1} = \frac{\ell_{\Phi_1}}{1 - \circledast \mathcal{K}_1}$, implying that the norm $\|S^* - S\| \leq \wp_1 D_{\mathcal{J}_1, \Phi_1} \Phi_1(t^*)$ is satisfied. Applying the same procedures we obtain the norms for the remaining state variables;

$$\begin{aligned} \|I^* - I\| &\leq \wp_2 D_{\mathcal{J}_2, \Phi_2} \Phi_2(t^*), \\ \|T^* - T\| &\leq \wp_3 D_{\mathcal{J}_3, \Phi_3} \Phi_3(t^*), \\ \|R^* - R\| &\leq \wp_4 D_{\mathcal{J}_4, \Phi_4} \Phi_4(t^*). \end{aligned} \tag{47}$$

Finally, we recall that $D_{\mathcal{J}_i, \Phi_i} = \frac{\ell_{\Phi_i}}{1 - \circledast \mathcal{K}_i}$ for $i = 2, 3, 4$. It is then easy to conclude that the Caputo fractal-fractional Ebola model meets the Hyers-Ulam-Razzias stability criterion. This completes the proof.

6 Estimation of parameters

In this section, the estimation of parameters from real Ebola data is done for the model which is a crucial element of epidemiological modelling [46]. Future outcomes can be predicted using the model and advance our comprehension of the factors that influence the transmission of disease. Additionally, this method effectively finds the parameters that are very close to their actual data while producing the appropriate curve generated from actual data [47, 48]. In this study, the parameters of the model were obtained by applying the least-squares technique as used in literature, see for instance [49–52] and this yields estimated parameters that have the highest likelihood of being accurate, assuming certain crucial assumptions are met. Nonlinear least-squares analysis is a collection of numerical methods used to determine the best value for the parameters in a vector form based on experimental data. As a result, the model's solution is

accurately adjusted using the epidemic's real data. Eq. (48) provides the method of least-squares that we apply to investigate the model system. The method is to choose initial approximations and pre-calculated model parameters that offer a good fit or incorporate all of the data points by minimising the sum of the squared discrepancies between the model's solution and the observed data $\amalg(g,\tilde{m})$ [53, 54], such that:

$$\amalg(\tilde{m}) = \sum_{g=1}^{n} (\tilde{m}_g - \amalg(g,\tilde{m}))^2. \tag{48}$$

Data from the Ebola cases that took place in Uganda between September 10, 2022, and November 2, 2022, were utilised for the model fitting, and it is displayed in Table 1. As mentioned in [55, 56], the set of data was sourced from GitHub. In collaboration with the WHO Regional Office for Africa (WHO AFRO), the Ministry of Health in Uganda, and the ECDC surveillance provided the data. According to the data obtained from the Worldometer, the total population of Uganda was estimated to be 47,249,585 in 2022 [57]. Therefore, we chose this number to represent the entire population of Uganda, $N(0) = 47249585$. Initial populations of the state variables were selected as follows: $I(0) = 58, T(0) = 0, R(0) = 0$, and the initial number of susceptible humans is computed as $S(0) = N(0) - (I(0)) + T(0) + R(0)) = 47249527$. The incubation period, normally lasts between 2 and 21 days, by the WHO [58]. As per [2], 64.06 years was Uganda's life expectancy in 2022. Thus, the natural mortality rate is estimated to be $\mu = \frac{1}{64.06\times365}$. Hence, the rate at which people are recruited to join the susceptible class is computed as $\psi = \mu \times N = 2020$. Figure 1 displays the model fitting to the entire set of real data in Table 1. The data listed above and some educated guesses regarding the parameters were used to accomplish this. Table 2 displays the model parameters derived from the model calibration shown in Figure 1.

Table 1. Ebola disease human cases, from 10th October, 2022 to 2nd November, 2022

Day	Cases	Day	Cases
10/15/2022	58	10/25/2022	109
10/16/2022	60	10/26/2022	115
10/17/2022	60	10/27/2022	121
10/18/2022	61	10/28/2022	126
10/19/2022	64	10/29/2022	128
10/20/2022	65	10/30/2022	129
10/21/2022	71	10/31/2022	130
10/22/2022	75	11/01/2022	131
10/23/2022	90	11/02/2022	131
10/24/2022	95		

Table 2. Ebola model parameters

Parameter	Value/day	Source	Parameter	Value/day	Source
ψ	2020	Estimated	β	0.298548	Fitted
μ	$\frac{1}{64.06\times365}$	Estimated	σ_2	0.004703	Fitted
α_1	0.000019×10^{-3}	Fitted	δ_1	0.603885	Fitted
σ_1	0.002182	Fitted	α_2	0.023848	Fitted
κ	0.096099	Fitted			

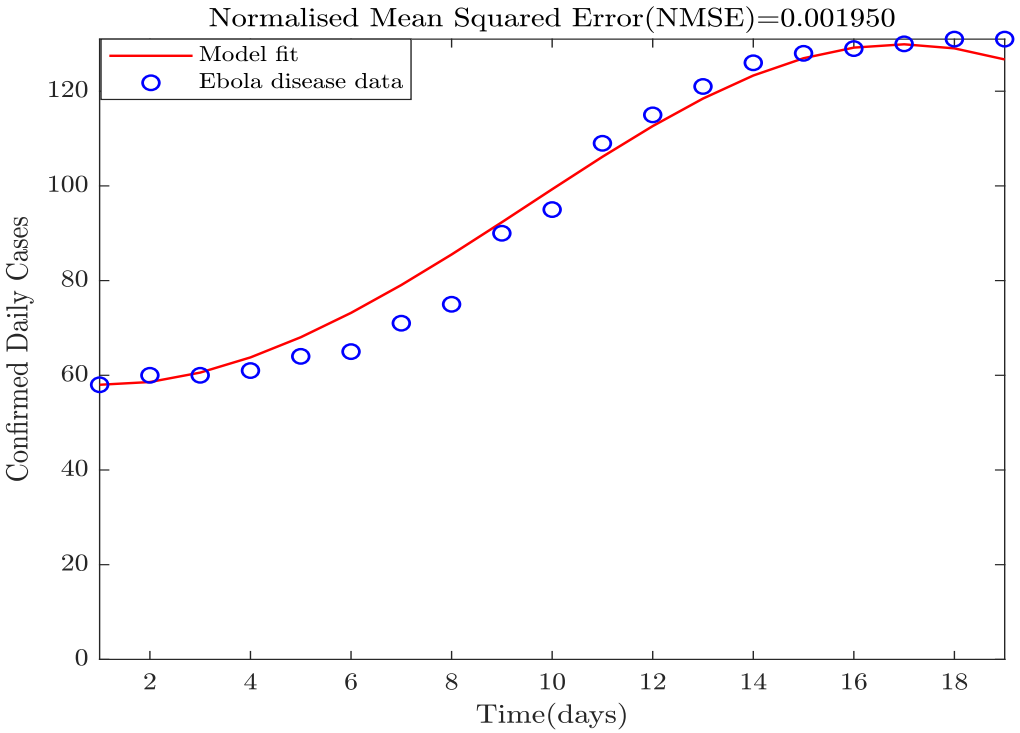

Figure 1. Comparison of the real data (blue dots) for the number of Ebola-infected individuals with the model under fractal-fractional Caputo derivative when $\Phi_1 = 0.80$ and $\Phi_2 = 0.86$ from 10th October, 2022 to 2nd November, 2022

7 Equilibrium points, stability of equilibrium points, and basic reproduction number

Disease-free equilibrium

The disease-free equilibrium denotes a situation where there is no disease in the population. It can be obtained in this model by setting S, I, T and R to zero in Eq. (1) and the resulting solution is given as

$$E_0 = \left(\frac{\psi}{\mu}, 0, 0, 0\right). \tag{49}$$

The fundamental reproduction number

The reproduction number(R_0) is the mean number of subsequent infections introduced into a fully susceptible population by a single infected individual [1]. In epidemiology, R_0 is essential for comprehending how infectious diseases spread, directing public health initiatives, and assessing pathogen infectiousness for efficient disease control and prevention [28]. The R_0 value below 1 signifies the end of a disease outbreak, while an R_0 value above 1 suggests a potential epidemic. A reduction in reproduction numbers due to vaccination, social isolation, or quarantine measures indicates containment. Employing next-generation matrix approach, we derive the R_0 of the model (1) to be;

$$R_0 = \frac{1}{(\beta + \mu + \delta_1)}\left[\frac{\alpha_1 \psi}{\mu} + \frac{\beta k}{(\mu + k + \sigma_2)}\right]. \tag{50}$$

Analysis of disease-free equilibrium

In this subsection, we prove the local stability of E_0.

Theorem 8 *The disease-free equilibrium is locally asymptotically stable if* $R_0 < 1$ *and* $(\beta+\mu+\delta_1)+(\mu+k+\sigma_2) > \alpha_1\frac{\psi}{\mu}$ *and unstable if* $R_0 > 1$.

Proof The corresponding Jacobian matrix of model (1) at E_0 is given by

$$J(E_0) = \begin{bmatrix} -\mu & -\alpha_1\dfrac{\psi}{\mu} & 0 & \sigma_1 \\ 0 & \alpha_1\dfrac{\psi}{\mu} - (\beta+\mu+\delta_1) & \kappa & 0 \\ 0 & \beta & -(\sigma_2+\kappa+\mu) & 0 \\ 0 & 0 & \sigma_2 & -(\mu+\sigma_1) \end{bmatrix}. \tag{51}$$

It is obvious that Eq. (51) has two negative roots $\epsilon_1 = -\mu$ and $\epsilon_2 = -\mu-\sigma_1$. The rest of the roots would be obtained from the characteristic equation below

$$\epsilon^2 + [(\beta+\mu+\delta_1)+(\mu+\kappa+\sigma_2)]\,\epsilon + (\beta+\mu+\delta_1)(\mu+\kappa+\sigma_2)(1-R_0). \tag{52}$$

From Eq. (51),

$$det(\epsilon_3\epsilon_4) = (\beta+\mu+\delta_1)(\mu+\kappa+\sigma_2)(1-R_0). \tag{53}$$

Also,

$$tr(\epsilon_3+\epsilon_4) = \alpha_1\frac{\psi}{\mu} - (\beta+\mu+\delta_1) - (\mu+\kappa+\sigma_2). \tag{54}$$

It is obvious that, since its trace is negative and its determinant is positive. $det(\epsilon_3\epsilon_4) > 0$ if $R_0 < 1$. If

$$(\beta+\mu+\delta_1)+(\mu+\kappa+\sigma_2) > \alpha_1\frac{\psi}{\mu}, \tag{55}$$

then $tr(\epsilon_3+\epsilon_4) < 0$, implying that model (1) is asymptotically stable.

Existence of endemic equilibrium

Here, we examine the requirements for model (1)'s endemic equilibrium. The endemic equilibrium denoted by $E_1^{**} = (S^{**}, I^{**}, T^{**}, R^{**})$ is obtained by substituting the derivatives in the left-hand side of the model (1) and equate it to zero. We then solve the associated system of S^{**}, I^{**}, T^{**}, and R^{**}, we obtain

$$\begin{aligned} S^{**} &= \frac{\psi(\mu+\sigma_1)(\mu+k+\sigma_2)+\sigma_2 I^{**}(\psi\alpha_2+\sigma_1\beta)}{(\alpha_1 I^{**}+\mu)[(\mu+\sigma_1)(\mu+k+\sigma_2)-\alpha_2\sigma_2 I^{**}]}, \\ T^{**} &= \frac{\beta(\mu+\sigma_1)I^{**}}{(\mu+\sigma_1)(\mu+k+\sigma_2)-\alpha_2\sigma_2 I^{**}}, \\ R^{**} &= \frac{\beta\alpha_2\sigma_2 I^{**}}{(\mu+\sigma_1)(\mu+k+\sigma_2)-\alpha_2\sigma_2 I^{**}}. \end{aligned} \tag{56}$$

The endemic equilibrium (56) satisfies

$$P(I^{**}) = I^{**}(Q_1 I^{**})^2 + Q_2 I^{**} + Q_3) = 0, \tag{57}$$

where

$$\begin{aligned}
Q_1 &= \alpha_1\alpha_2\sigma_2(\mu+\delta_1),\\
Q_2 &= \alpha_2\sigma_2[\psi\alpha_1 + \mu(\mu+\delta_1)] + \alpha_1\eta\sigma_2 + \alpha_1(\eta+\mu)[k\beta - (k+\mu+\sigma_2)(\beta+\mu+\delta_1)],\\
Q_3 &= (k+\mu+\sigma_2)(\beta+\mu+\delta_1)(\eta+\mu)(R_0-1).
\end{aligned}$$

The root $I^{**} = 0$ of Eq. (57) corresponds to disease-free equilibrium. Thus, we regard the quadratic equation

$$P(I^{**}) = Q_1(I^{**})^2 + Q_2 I^{**} + Q_3 = 0, \tag{58}$$

in determining the existence of endemic equilibrium. It should be noted that the positive root of the equation provides the endemic equilibrium (56).

One can easily see that $Q_1 > 0$ whether $R_0 > 1$ or not. If $R_0 > 1$, $Q_3 > 0$ and if $Q_2 < 0$ when $R_0 > 1$, then the graph of the polynomial (58) indicates that model (1) has one endemic equilibrium. If $R_0 < 1$, and $Q_3 < 0$. Then model (1) has no endemic equilibrium. If $R_0 = 1$, $Q_2 > 0$ and $Q_3 = 0$, then Eq. (58) has no positive root. In conclusion, we arrive at the results below.

Theorem 9 *The model* (1) *has a unique endemic equilibrium if* $Q_2 < 0$ *and* $R_0 > 1$, *and no endemic equilibrium when* $R_0 \leq 1$.

Local stability of endemic equilibrium and bifurcation analysis

We examine the possibility of bifurcation and discuss the local stability of endemic equilibrium. The bifurcation phenomenon is established in this section by using the centre manifold theory as explained in Theorem 4.1 by both Carlos Castillo-Chavez et al. [59] and Buonomo et al. [60] respectively as follows:

We consider the transmission rate of Ebola α_1 as the bifurcation parameter so that $R_0 = 1$ if and only if

$$\alpha_1 = \alpha_1^* = \frac{\mu(\beta+\mu+\delta_1)(\mu+k+\sigma_2) - \beta k\mu}{\psi(\mu+k+\sigma_2)}.$$

Introducing $S = x_1$, $I = x_2$, $T = x_3$, and $R = x_4$, model (1) becomes

$$\begin{aligned}
f_1 &= x_1' = \psi + \sigma_1 x_4 - \alpha_1 x_1 x_2 - \mu x_1,\\
f_2 &= x_2' = \alpha_1 x_1 x_2 + k x_3 - \alpha_2 x_2 x_4 - (\beta+\mu+\delta_1)x_2,\\
f_3 &= x_3' = \alpha_2 x_2 x_4 + \beta x_2 - (\mu+k+\sigma_2)x_3,\\
f_4 &= x_4' = \phi x_3 - (\mu+\sigma_1)x_4.
\end{aligned} \tag{59}$$

We know that the Ebola-free equilibrium is $\left[x_1^* = \frac{\psi}{\mu}, x_2^* = 0, x_3^* = 0, x_4^* = 0\right]$. We linearised the matrix of the model (59) around the disease-free equilibrium when $\alpha_1 = \alpha_1^*$ and obtained

$$J(E_1^0) = \begin{bmatrix} -\mu & -\alpha_1\frac{\psi}{\mu} & 0 & \sigma_1 \\ 0 & \alpha_1\frac{\psi}{\mu} - (\beta+\mu+\delta_1) & \kappa & 0 \\ 0 & \beta & -(\sigma_2+\kappa+\mu) & 0 \\ 0 & 0 & \sigma_2 & -(\mu+\sigma_1) \end{bmatrix}. \tag{60}$$

The matrix $J(E_1^0)$ possesses a simple eigenvalue, with other eigenvalues endowed with negative real parts. Therefore, the centre manifold theorem as performed in [2] can be applied. We therefore need to derive the values of a and b. We begin this by calculating the right and left eigenvalues of $J(E_1^0)$ denoted by

$$W = [w_1, w_2, w_3, w_4]^T \quad \text{and} \quad V = [v_1, v_2, v_3, v_4], \quad \text{respectively.}$$

We obtain

$$w_1 = -\frac{\psi\alpha_1^*(\mu+k+\sigma_2)(\mu+\sigma_1)+\sigma_2\sigma_1\beta\mu}{\mu^2\beta\sigma_2}, \quad w_2 = \frac{(\mu+k+\sigma_2)(\mu+\sigma_1)}{\beta\sigma_2}, \quad w_3 = \frac{(\mu+\eta)}{\sigma_2},$$
$$w_4 = 1,$$

and

$$v_1 = 0, \quad v_2 = \frac{(\mu+k+\sigma_2)}{k}, \quad v_3 = 1, \quad \text{and} \quad v_4 = 0.$$

Next, we compute the values of a and b. From model (59), all the associated partial derivatives of $F = (f_1, f_2, f_3, f_4)^T$ in (59) are zero at the Ebola-free equilibrium (DFE) except the following:

$$\frac{\partial^2 f_1}{\partial x_1 \partial x_2} = \frac{\partial f_1}{\partial x_2 \partial x_1} = -\alpha_1^*, \quad \frac{\partial^2 f_2}{\partial x_1 \partial x_2} = \frac{\partial^2 f_2}{\partial x_2 \partial x_1} = \alpha_1^*, \quad \frac{\partial^2 f_2}{\partial x_2 \partial x_4} = \frac{\partial^2 f_2}{\partial x_4 \partial x_2} = -\alpha_2,$$

$$\frac{\partial^2 f_3}{\partial x_2 \partial x_4} = \frac{\partial^2 f_3}{\partial x_4 \partial x_2} = \alpha_2, \quad \frac{\partial^2 f_2}{\partial x_2 \partial \alpha_1^*} = \alpha_2, \quad \frac{\partial^2 f_2}{\partial x_3 \partial \alpha_1^*} = \frac{\psi}{\mu}.$$

Substituting the above equations into a and b in

$$a = \sum_{k,i,j=1}^{n} v_k \omega_i \omega_j \frac{\partial^2 f_k}{\partial x_i \partial x_j(0,0)},$$
$$b = \sum_{k,i=1}^{n} v_k \omega_i \frac{\partial^3 f_k}{\partial x_i \partial \phi}(0,0),$$

it follows that

$$
\begin{aligned}
a &= 2v_2w_1w_2\frac{\partial^2 f_2}{\partial x_1\partial x_2} + 2v_2w_2w_4\frac{\partial^2 f_2}{\partial x_2\partial x_4} + 2v_3w_2w_4\frac{\partial^2 f_3}{\partial x_2\partial x_4} \\
&= 2v_2w_1w_2\alpha_1^* - 2v_2w_2w_4\alpha_2 + 2v_3w_2w_4\alpha_2 \\
&= \frac{2(\mu+k+\sigma_2)^2(\mu+\sigma_1)}{k\beta^2\mu^2\sigma_2^2}\left[\frac{\alpha_2}{(\mu+k+\sigma_2)} - \left(\psi\alpha_1^{*2}(\mu+k+\sigma_2)(\mu+\sigma_1) + \beta\mu(\alpha_2\mu+\sigma_2\sigma_1)\right)\right] > 0, \\
b &= v_2w_2\frac{\partial^2 f_2}{\partial x_2\partial\alpha_1^*} + v_3w_3\frac{\partial^2 f_2}{\partial x_3\partial\alpha_1^*} \\
&= \frac{\psi(k+\sigma_2+\mu)^2(\mu+\sigma_1)}{\beta\mu k\sigma_2} > 0.
\end{aligned}
$$

Here, it is obvious that the coefficient $b > 0$. It follows from the results given in [61], that model (1) undergoes backward bifurcation whenever $a > 0$, that is $\frac{\alpha_2}{(\mu+k+\sigma_2)} > \left(\psi\alpha_1^{*2}(\mu+k+\sigma_2)(\mu+\sigma_1) + \beta\mu(\alpha_2\mu+\alpha$ and would be a forward bifurcation whenever $a < 0$, that is $\frac{\alpha_2}{(\mu+k+\sigma_2)} < \left(\psi\alpha_1^{*2}(\mu+k+\sigma_2)(\mu+\sigma_1) + \beta\mu(\alpha_2\mu+\sigma_2\sigma_1)\right)$. The endemic equilibrium, which exists whenever $R_0 > 1$, is locally asymptotically stable whenever $R_0 > 1$ and $\alpha_1^* < \alpha_1$ with α_1 close to α_1^*.

Theorem 10 *The unique endemic equilibrium of model* (59) *is locally asymptotically stable when* $R_0 > 1$.

8 Sensitivity analysis of R_0

In this subsection, we conduct a sensitivity analysis of some key parameters in support of the graphs in Figure 6. The significance of conducting the sensitivity analysis is to identify parameters influencing the R_0. It is a useful tool for determining essential parameters to be considered while developing intervention strategies [2, 62, 63]. The forward normalised sensitivity index of R_0 is employed in this section. It is therefore defined as:

$$\chi_\ell^{R_0} = \frac{\partial R_0}{\partial \ell} \times \frac{\ell}{R_0}, \tag{61}$$

where ℓ denotes the parameters in the R_0. The resulting sensitivity indices utilising Eq. (4) and the parameter values in Table 2 are given in Table 3 below.

Table 3. Sensitivity analysis of R_0 to parameters for the Ebola model

Number	Parameter	Index
1	α_1	$+0.99968$
2	ψ	$+0.99968$
3	κ	$+1.49150 \times 10^{-5}$
4	μ	-0.99973
5	β	-0.33049
6	δ_1	-0.66914
7	σ_2	-1.47801×10^{-5}

Parameters with negative sensitivity indices lower R_0 value as the values assigned to them are increased. Parameters with positive indices increase R_0 value as the values assigned to the

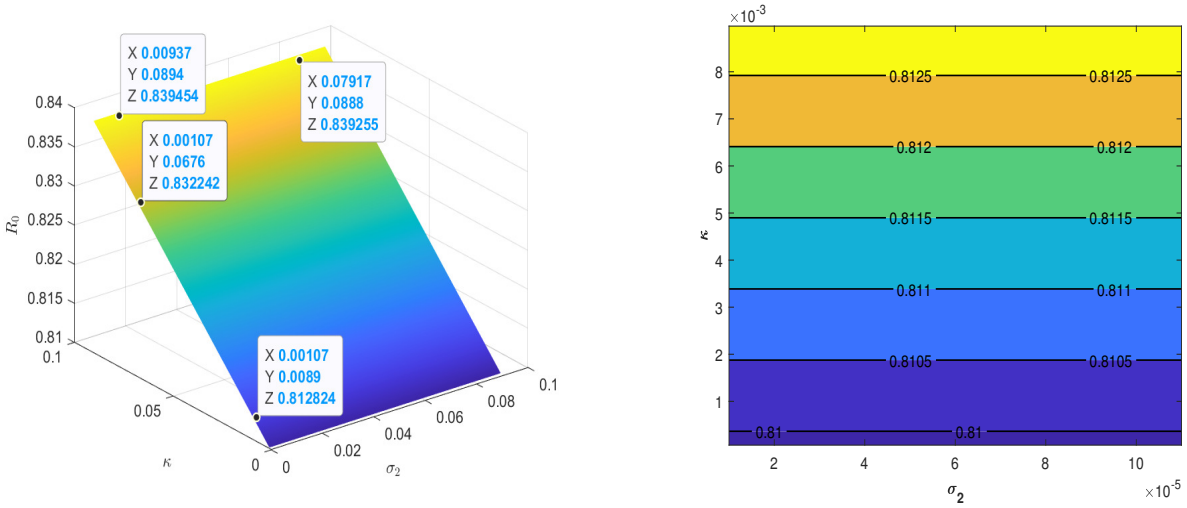

(a) 3D plot of κ and σ_2 on R_0 **(b)** Contour plot

Figure 2. The effect of κ and σ_2 on R_0

parameters are increased. It can be seen from Table 3 that α_1, κ and ψ are positive. Therefore, increasing their values increases the value of R_0. For instance, increasing α_1 by 10% raises or reduces the R_0 value by 9.9968%. Figure 2 indicates the 3D and contour plots in support of the impact of relapse rate, κ and the recovery rate, σ_2 on R_0. It can be seen in Figure 2a and Figure 2b that the value of R_0 increases as the values of κ increase. Also, the R_0 value decreases as the value of σ_2 increases. This implies that Ebola transmission can be reduced if the values of κ are reduced while increasing the value of σ_2 so that the value of R_0 would be less than unity. This can be achieved by educating the susceptible to ensure personal protection against Ebola, disinfecting the environment of the infectious and Ebola-related death victims, and advising the infectious individuals to visit health centres for treatment and vaccination of susceptible individuals. Also, $\beta, \delta_1, \sigma_2$, and μ have negative values. Therefore, an increase in any of them decreases the R_0. For instance, raising or lowering β by 10% raises or lowers the R_0 value by 3.3049%. This implies that if infectious people are advised to visit treatment centres Ebola infection decreases. Moreover, the rate of recovery of the infectious populace has been dominant. Thus, a reduction in R_0 to less than one will be possible if infected persons recover early from Ebola. However, the natural mortality rate, the disease-related death rate, and the recruitment rate cannot be used as control measures to eradicate the transmission of disease in our communities.

9 Numerical trajectories and discussion of results

In this subsection, the numerical results and the discussion of the outcomes of the analysis that was conducted in this study are presented. Based on the fractal-fractional Caputo, our model of the Ebola outbreak in Uganda may be numerically examined and utilised to predict the disease's trajectory. We used Newton's polynomial numerical scheme to carry out extensive numerical simulations, taking into consideration the estimated parameter values provided in Table 2. The numerical simulations were carried out using these initial state variable values: $S(0) = 47249527$, $I(0) = 58$, $T(0) = 0$, $R(0) = 0$, and the parameter values given in Table 2. Numerous simulations were conducted to assess the influence of the parameters on the Ebola virus disease state variables. Additionally, we performed sensitivity analyses on some of the key parameters to see how they affect the possibility of Ebola disease transmission.

The graphical results for our model's compartments, S, I, T, and R, utilising different fractal-fractional order values are presented in Figure 3, Figure 4, and Figure 5 accordingly. It is observed

that all the state variables' trajectories show a consistent pattern of convergence toward the precise endemic equilibrium point. This portrays the real dynamics of the Ebola virus disease outbreak. First, we show the numerical solution for both the integer order and the fractal-fractal Caputo orders of model (2) in Figure 3. It is obvious from Figure 3a, Figure 3b, Figure 3c and Figure 3d that integer model with $\Phi_1 = \Phi_2 = 1$ recorded a lower count of susceptible whiles infectious, treatment and recovery classes recorded a higher count as compared to the fractal-fractional order models. The integer order raises the impact of Ebola. An interesting result was observed in Figure 3b. The number of individuals infected with the Ebola virus increases more quickly as the fractional values get closer to unity, but after 18 days, it begins to decline sharply. The disease's trajectory seems to record a moderate growing pace, we record greater sensitivity to it at $\Phi_1 = \Phi_2 = 1$. A similar result was obtained in Figure 4b and Figure 5b.

The simulation results in Figure 4 depict the impact of keeping the fractal dimension constant at $\Phi_1 = 1$ while varying the fractional order value. It was observed in Figure 4a, Figure 4b, Figure 4c, and Figure 4d that, individuals in the susceptible class increase as fractional order values decrease. Also, individuals in the infectious, treatment, and recovery classes reduce as the fractional value reduces. As shown in Figure 5a, Figure 5b, Figure 5c, and Figure 5d, increasing the fractal dimension for a constant fractional order value produces dynamics that are similar to those obtained by keeping the fractal dimension constant at $\Phi_1 = 1$ and varying the fractional order. The findings underscore the significance of employing fractal-fractional models modelling infectious diseases. Hidden patterns and structures in the natural phenomena of Ebola transmission have been discovered by the application of fractal-fractional Caputo derivatives. Additionally, we analysed the contribution of some key parameters to the Ebola transmission and presented the results in Figure 6a, Figure 6b, Figure 6c and Figure 6d. We observed that, as the values of transmission rate outside the treatment centres, α_1, and the relapse rate, κ increase, the number of Ebola infectious individuals increases as indicated in Figure 6a, and Figure 6d respectively. This implies that α_1, and κ significantly contribute to the endemic status of the disease by increasing the value of the reproduction ratio. They are among the essential components that need to be considered while developing intervention strategies to curb the Ebola outbreak. We suggest that the provision of an immune booster vaccination after treatment could offer active, long-term protection, lower relapse rates, and prevent fatal outcomes. Furthermore, implementing control measures like quarantine, isolation, and disinfecting the environment in Ebola-affected communities could potentially help many individuals recover from the disease. Moreover, we considered the transmission rate at treatment centres, α_2, and the rate of transfer from the treated class to the infected class, β. We observed from Figure 6c and Figure 6b that recovery increases at treatment centres as the transmission rate within treatment centres, α_2 decreases in value. Also, as the value of β increases, the rate of Ebola infection declines, as depicted in Figure 6b. This implies if many infectious individuals are advised to visit treatment centres, Ebola transmission reduced, in communities. This also implies that transmission of Ebola disease could be controlled if proper measures are put in place at treatment centres. For instance, the implementation of clinical daily surveillance or prophylaxis after exposure (PEP) with favipiravir, health care worker training, and the provision of personal protective equipment (PPE) items may all contribute to the reduction of infection rates within Ebola treatment centres. Again, Figure 7 indicates the effects of σ_2 on the R_0. It is obvious that as the value of σ_2 increases the number of Ebola infectious individuals decreases. Hence reduction in its value increases recovery of the disease. This suggests that if the transmission rate is lowered, the number of subsequent infections in the community can be decreased and the relapse rate of Ebola is reduced. These can be achieved through personal protection against the disease, vaccination, and treatment, and disinfecting the surroundings of the deceased Ebola victims. Finally, it is obvious that the fractional model is essential to comprehend the vital factors

and attain accuracy and consistency. Its memory effects are demonstrated through graphs, unlike the integer-order models. According to the World Health Organisation (WHO), the Ebola virus disease is severe and recorded a mortality rate of up to 90% in humans. Notwithstanding this, it further reports that by carrying out effective treatment strategies, the mortality rate has decreased drastically from 90% to 25% in current epidemics. This report is in line with the results from our study since when proper precautions are put in place at the treatment centres we observed an increase in the recovery compartment which implies a decline in the disease-induced mortality rate.

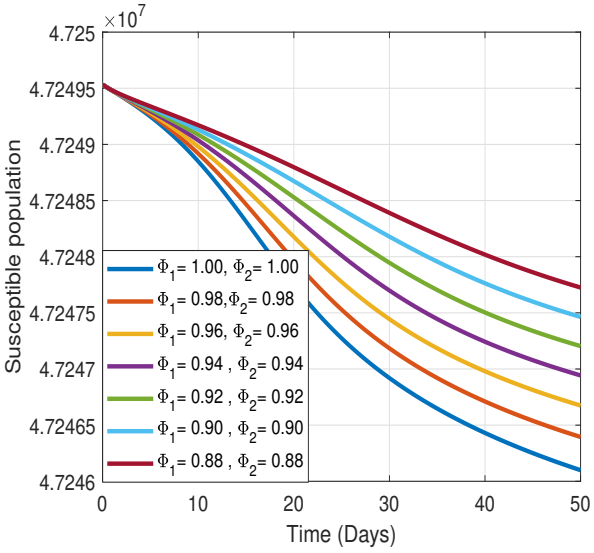

(a) Effect of Fractal-Fractional order on the susceptible class, $S(t)$

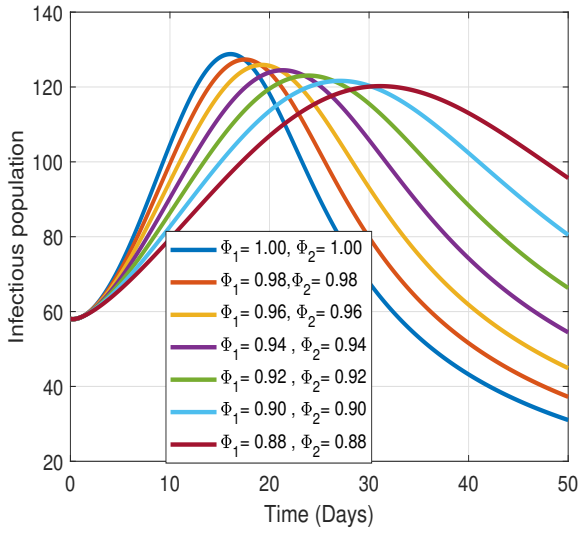

(b) Effect of Fractal-Fractional order on the infectious class, $I(t)$

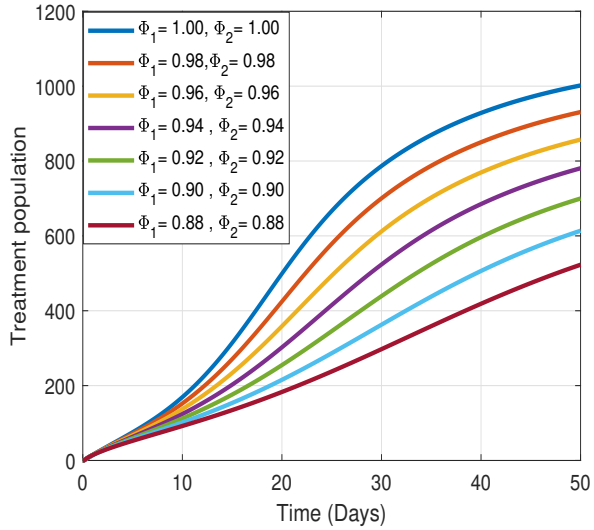

(c) Effect of Fractal-Fractional order on the treatment class, $T(t)$

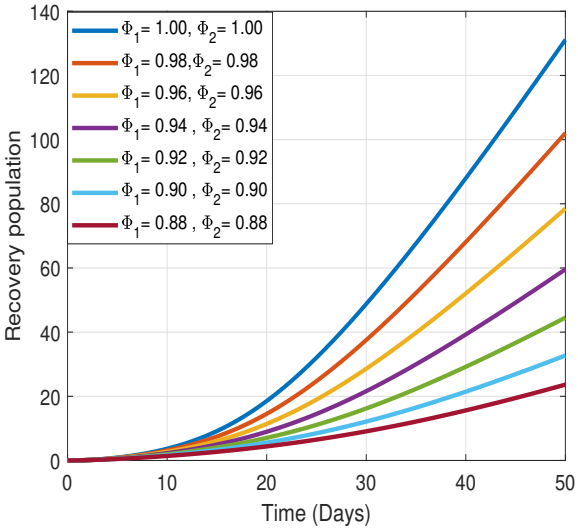

(d) Effect of Fractal-Fractional order on the recovery class, $R(t)$

Figure 3. Effect of Fractal-Fractional order on the $S(t), I(t), T(t)$, and $R(t)$ respectively. Considering $\Phi_1 = \Phi_2 = 1, 0.98, 0.96, 0.94, 0.92, 0.90, 0.88$

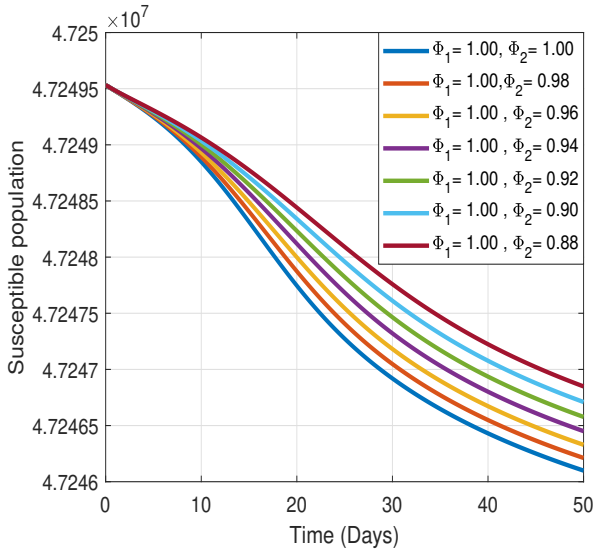

(a) Effect of Fractional order on the susceptible class, $S(t)$

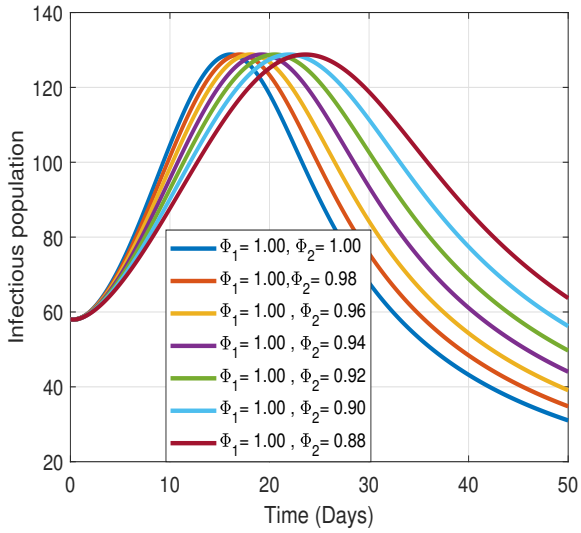

(b) Effect of Fractional order on the infectious class, $I(t)$

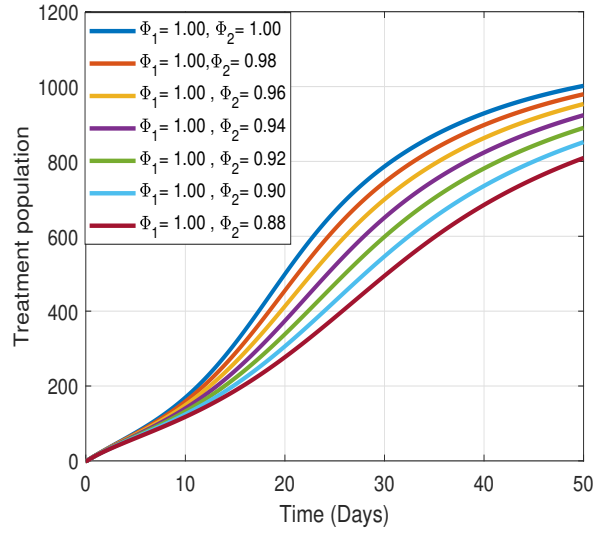

(c) Effect of Fractional order on the treatment class, $T(t)$

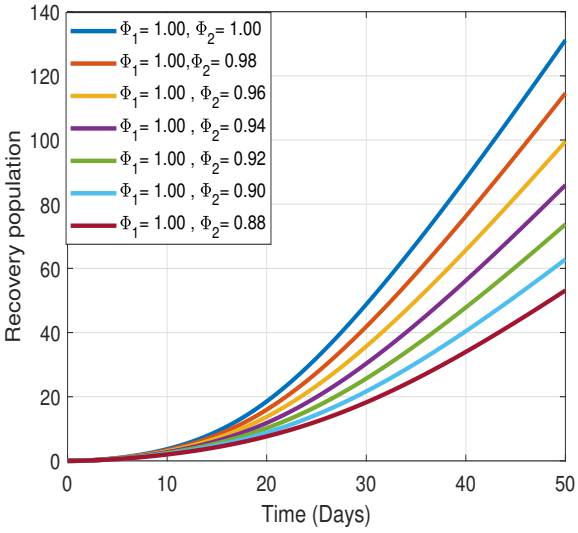

(d) Effect of fractional order on the recovery class, $R(t)$

Figure 4. Effect of fractional order on the $S(t), I(t), T(t)$, and $R(t)$ respectively. Considering $\Phi_1 = 1$ and $\Phi_2 = 1, 0.98, 0.96, 0.94, 0.92, 0.90, 0.88$

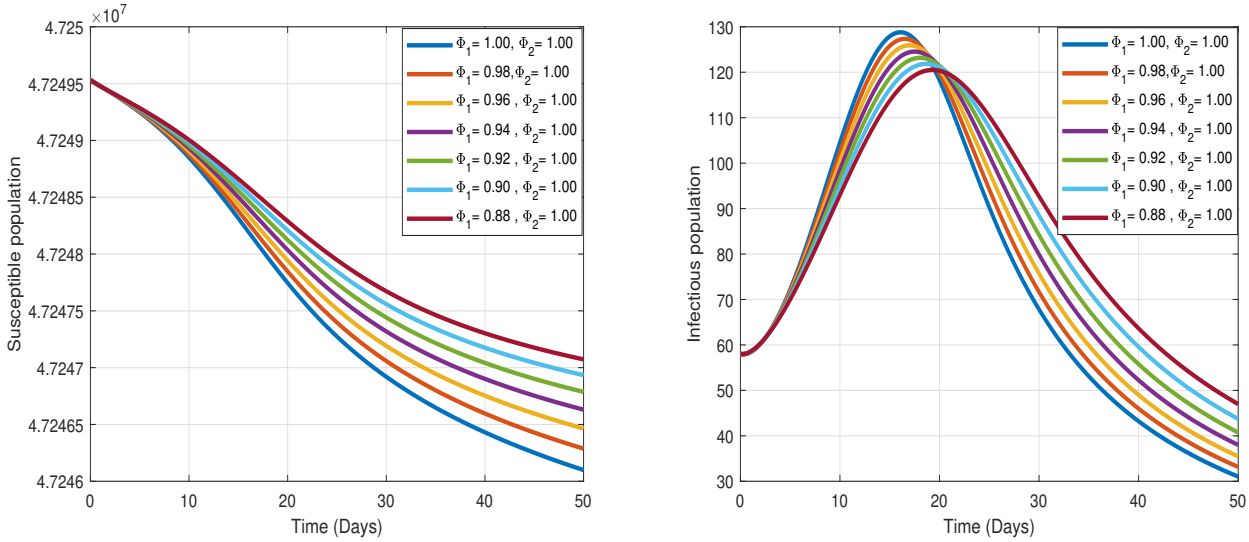

(a) Effect of Fractal order on the susceptible class, $S(t)$ **(b)** Effect of Fractal order on the infectious class, $I(t)$

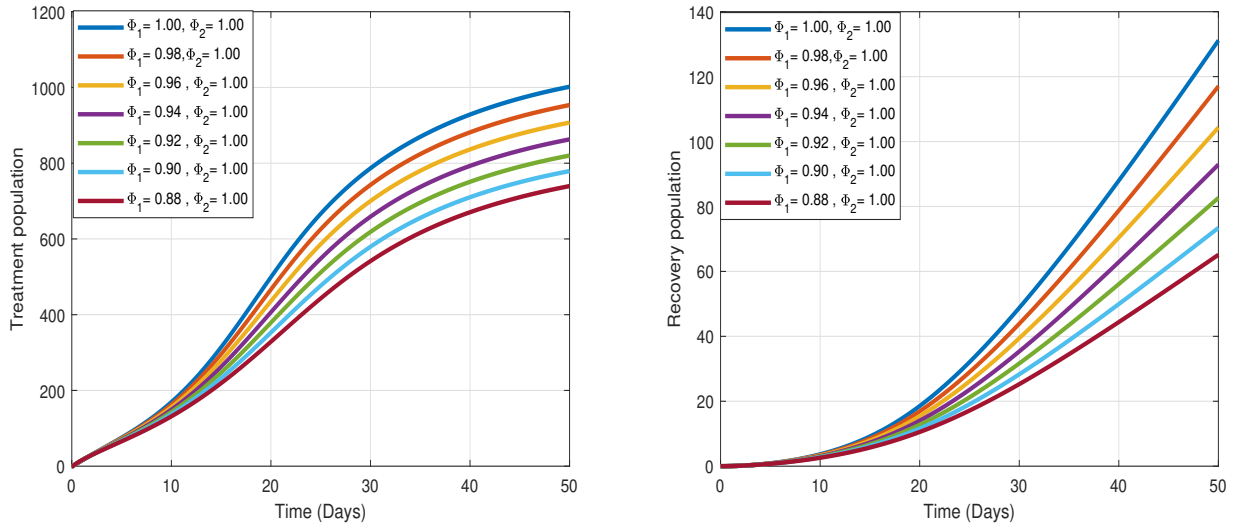

(c) Effect of Fractal order on the treatment class, $T(t)$ **(d)** Effect of Fractal order on the recovery class, $R(t)$

Figure 5. Effect of Fractal order on the $S(t), I(t), T(t)$, and $R(t)$ respectively. Considering $\Phi_1 = 1, 0.98, 0.96, 0.94, 0.92, 0.90, 0.88$ and $\Phi_2 = 1$

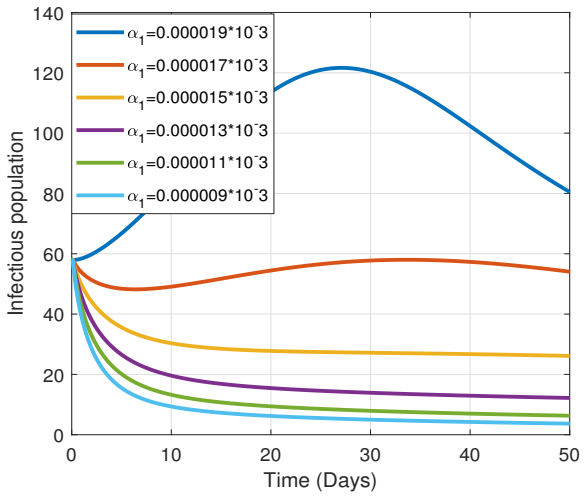

(a) Effect of α_1 on the infectious class, I(t) at $\Phi_1 = \Phi_2 = 0.90$

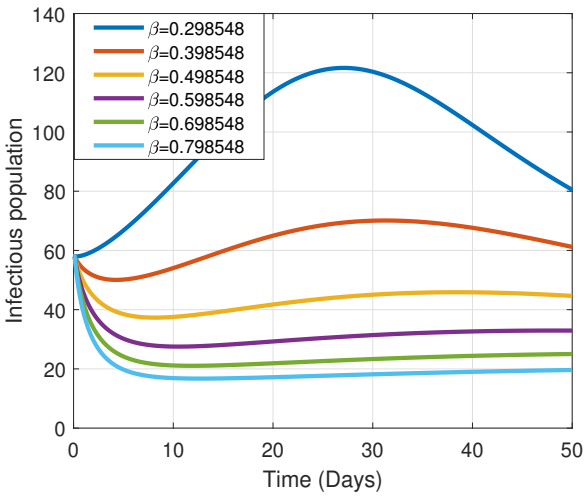

(b) Effect of β on the,infectious class, I(t) at $\Phi_1 = \Phi_2 = 0.90$

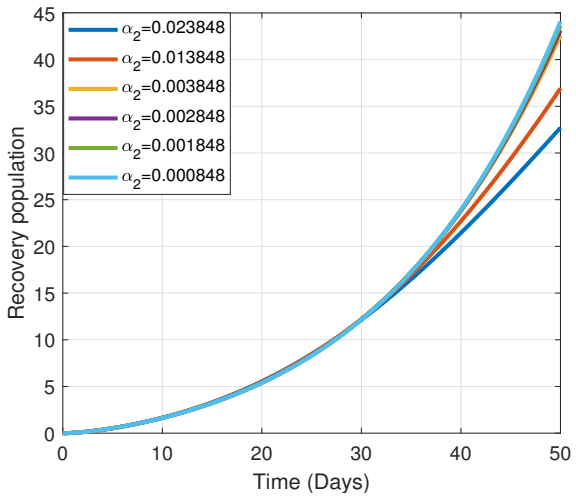

(c) Effect of α_2 on the recovery class, R(t) at $\Phi_1 = \Phi_2 = 0.90$

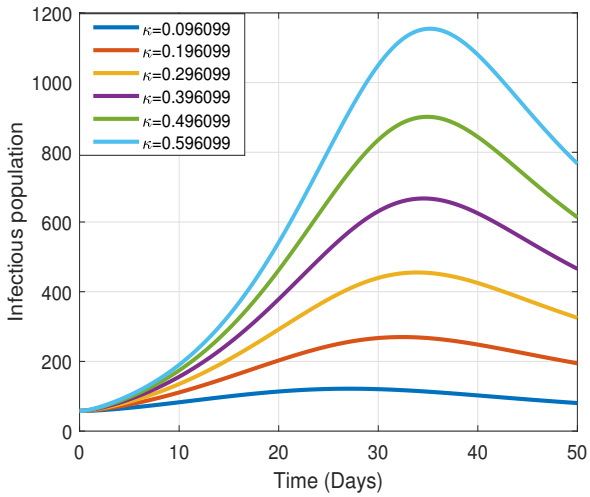

(d) Effect of κ on the infectious class, I(t) at $\Phi_1 = \Phi_2 = 0.90$

Figure 6. Effect of α_1,β,κ on the infectious class, I(t) and α_2 on the recovery class, R(t) at $\Phi_1 = \Phi_2 = 0.90$

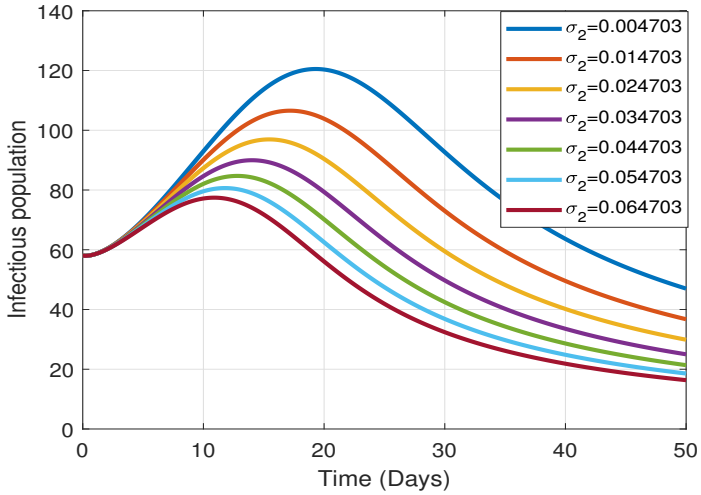

Figure 7. Effect of σ_2 on the infectious class, I(t) at $\Phi_1 = \Phi_2 = 0.90$

10 Conclusion

In this paper, the dynamics of the Ebola virus disease are investigated with a keen focus on the transmission of the Ebola virus disease at the treatment centres and also how the virus persists in the immunological sites of the treated patient which mostly results in the relapse of the disease. These dynamics of the Ebola virus disease are essential and contribute massively to the spread of the disease in the population. Therefore a Caputo fractal-fractional Ebola model was formulated to study how to control the disease in the population. The fractional operators were employed due to their ability to capture the memory effect exhibited by the Ebola virus disease. Through the fixed point theory, it was established that the Caputo fractal-fractional Ebola model possesses a unique solution. The study further applied the HU and HUR stability criteria to establish that the model was stable. In the studies, all parameters were fitted to real data from Uganda making the model's parameter values more reliable. It was observed from the sensitivity analysis that parameters like α_1, ψ and κ have a direct relationship with the spread of the disease whereas parameters like μ, β, δ_1 and σ_2 are inversely related to the fundamental reproductive number. From the numerical simulations, it was discovered that the hidden patterns or dynamics of the Ebola virus disease are well captured using fractional operators. It was observed that the transmission rate outside the treatment centres and relapse rate resulted in a high number of infections as compared to the transmission rate at the treatment centres. The study therefore suggests that infected individuals be sent to the treatment centres and proper treatment should also be carried out. The studies hence suggest that transmission of Ebola disease could be mitigated if proper measures are carried out at the treatment centres. Therefore, the implementation of clinical daily surveillance or prophylaxis after exposure (PEP) with favipiravir, health care worker training, and the provision of personal protective equipment (PPE) items may all contribute to the reduction of infection rates within Ebola treatment centres. By doing this, the Ebola disease will gradually die from the population. In the near future, the study will be extended to conduct an optimal control analysis into the Ebola disease by considering the results reported in this current study.

Declarations

Use of AI tools

The authors declare that they have not used Artificial Intelligence (AI) tools in the creation of this article.

Data availability statement

All data employed in this study for the parameter estimation have been duly referenced in this article.

Ethical approval (optional)

The authors state that this research complies with ethical standards. This research does not involve either human participants or animals.

Consent for publication

Not applicable

Conflicts of interest

The authors declare that they have no conflict of interest.

Funding

No funding was received for this research.

Author's contributions

I.K.A.: Conceptualization, Writing-Original draft preparation, Data Curation, Writing - Review & Editing, Methodology, Software, Formal Analysis. F.A.W.: Conceptualization, Writing Original draft preparation, Data Curation, Writing - Review & Editing, Methodology, Software, Formal Analysis. S.A.A.: Writing - Review & Editing, Methodology, Formal Analysis. G.O.A.: Writing-Original draft preparation, Methodology, Formal Analysis. All the authors were involved in the discussion of the entire results of this research and contributed to the final manuscript.

Acknowledgements

Not applicable

References

[1] Adu, I.K., Wireko, F.A., Nana-Kyere, S., Appiagyei, E., Osman, M.A.L. and Asamoah, J.K.K. Modelling the dynamics of Ebola disease transmission with optimal control analysis. *Modeling Earth Systems and Environment,* 10, 4731-4757, (2024). [CrossRef]

[2] Adu, I.K., Wireko, F.A., Osman, M.A.L. and Asamoah, J.K.K. A fractional order Ebola transmission model for dogs and humans. *Scientific African,* 24, e02230, (2024). [CrossRef]

[3] Gonzalez, A., Nikparvar, B., Matson, M.J., Seifert, S.N., Ross, H.D., Munster, V. and Bharti, N. Human movement and transmission dynamics early in Ebola outbreaks. *medRxiv,* (2023). [CrossRef]

[4] Savini, H., Janvier, F., Karkowski, L., Billhot, M., Aletti, M., Bordes, J. et al. Occupational exposures to Ebola virus in Ebola treatment center, Conakry, Guinea. *Emerging Infectious Diseases,* 23(8), 1380-1383, (2017). [CrossRef]

[5] Madelain, V., Nguyen, T.H.T., Olivo, A., De Lamballerie, X., Guedj, J., Taburet, A. and Mentré, F. Ebola virus infection: review of the pharmacokinetic and pharmacodynamic properties of drugs considered for testing in human efficacy trials. *Clinical Pharmacokinetics,* 55, 907-923, (2016). [CrossRef]

[6] Billioux, B.J., Smith, B. and Nath, A. Neurological complications of Ebola virus infection. *Neurotherapeutics,* 13(3), 461-470, (2016). [CrossRef]

[7] Adu, I.K., Wireko, F.A., Sebil, C. and Asamoah, J.K.K. A fractal-fractional model of Ebola with reinfection. *Results in Physics,* 52, 106893, (2023). [CrossRef]

[8] Thom, R., Tipton, T., Strecker, T., Hall, Y., Bore, J.A., Maes, P. et al. Longitudinal antibody and T cell responses in Ebola virus disease survivors and contacts: an observational cohort study. *The Lancet Infectious Diseases,* 21(4), 507-516, (2021). [CrossRef]

[9] Rugarabamu, S., Mboera, L., Rweyemamu, M., Mwanyika, G., Lutwama, J., Paweska, J. and Misinzo, G. Forty-two years of responding to Ebola virus outbreaks in Sub-Saharan Africa: a review. *BMJ Global Health,* 5(3), e001955, (2020). [CrossRef]

[10] Karaagac, B., Owolabi, K.M. and Pindza, E. A computational technique for the Caputo fractal-fractional diabetes mellitus model without genetic factors. *International Journal of Dynamics and Control,* 11, 2161-2178, (2023). [CrossRef]

[11] Wireko, F.A., Adu, I.K., Gyamfi, K.A. and Asamoah, J.K.K. Modelling the transmission be-

havior of Measles disease considering contaminated environment through a fractal-fractional Mittag-Leffler kernel. *Physica Scripta,*, 99, 075025, (2024). [CrossRef]

[12] Wireko, F.A., Adu, I.K., Sebil, C. and Asamoah, J.K.K. A fractal-fractional order model for exploring the dynamics of Monkeypox disease. *Decision Analytics Journal,* 8, 100300, (2023). [CrossRef]

[13] Nana-Kyere, S., Boateng, F.A., Jonathan, P., Donkor, A., Hoggar, G.K., Titus, B.D. et al. Global analysis and optimal control model of COVID-19. *Computational and Mathematical Methods in Medicine,* 2022, 9491847, (2022). [CrossRef]

[14] Qureshi, S. and Atangana, A. Fractal-fractional differentiation for the modeling and mathematical analysis of nonlinear diarrhea transmission dynamics under the use of real data. *Chaos, Solitons & Fractals,* 136, 109812, (2020). [CrossRef]

[15] Asamoah, J.K.K., Okyere, E., Yankson, E., Opoku, A.A., Adom-Konadu, A., Acheampong, E. and Arthur, Y.D. Non-fractional and fractional mathematical analysis and simulations for Q fever. *Chaos, Solitons & Fractals,* 156, 111821, (2022). [CrossRef]

[16] Alzahrani, E.O. and Khan, M.A. Modeling the dynamics of Hepatitis E with optimal control. *Chaos, Solitons & Fractals,* 116, 287-301, (2018). [CrossRef]

[17] Liana, Y.A. and Chuma, F.M. Mathematical modeling of giardiasis transmission dynamics with control strategies in the presence of carriers. *Journal of Applied Mathematics,* 2023, 1562207, (2023). [CrossRef]

[18] Eikenberry, S.E. and Gumel, A.B. Mathematical modeling of climate change and malaria transmission dynamics: a historical review. *Journal of Mathematical Biology,* 77, 857-933, (2018). [CrossRef]

[19] Byamukama, M., Kajunguri, D. and Karuhanga, M. Optimal control analysis of pneumonia and HIV/AIDS co-infection model. *Mathematics Open,* 3, 2450006, (2024). [CrossRef]

[20] Cetin, M.A. and Araz, S.I. Prediction of COVID-19 spread with models in different patterns: A case study of Russia. *Open Physics,* 22(1), 20240009, (2024). [CrossRef]

[21] Arik, I.A., Sari, H.K. and Araz, S.İ. Numerical simulation of Covid-19 model with integer and non-integer order: The effect of environment and social distancing. *Results in Physics,* 51, 106725, (2023). [CrossRef]

[22] Djiomba Njankou, S.D. and Nyabadza, F. Modelling the role of human behaviour in Ebola virus disease (EVD) transmission dynamics. *Computational and Mathematical Methods in Medicine,* 2022, 150043, (2022). [CrossRef]

[23] Rafiq, M., Ahmad, W., Abbas, M. and Baleanu, D. A reliable and competitive mathematical analysis of Ebola epidemic model. *Advances in Difference Equations,* 2020, 540, (2020). [CrossRef]

[24] Nazir, A., Ahmed, N., Khan, U., Mohyud-Din, S.T., Nisar, K.S. and Khan, I. An advanced version of a conformable mathematical model of Ebola virus disease in Africa. *Alexandria Engineering Journal,* 59(5), 3261-3268, (2020). [CrossRef]

[25] Rachah, A. and Torres, D.F.M. Mathematical modelling, simulation, and optimal control of the 2014 Ebola outbreak in West Africa. *Discrete Dynamics in Nature and Society,* 2015, 842792, (2015). [CrossRef]

[26] Singh, H. Analysis for fractional dynamics of Ebola virus model. *Chaos, Solitons & Fractals,* 138, 109992, (2020). [CrossRef]

[27] Farman, M., Akgül, A., Abdeljawad, T., Naik, P.A., Bukhari, N. and Ahmad, A. Modeling

and analysis of fractional order Ebola virus model with Mittag-Leffler kernel. *Alexandria Engineering Journal*,, 61(3), 2062-2073, (2022). [CrossRef]

[28] Adu, I.K. and Wireko, F.A. On SITR theoretical model of Ebola virus propagation with relapse and reinfection. *International Journal of Innovation and Development*, 1(3), (2023).

[29] Addai, E., Zhang, L., Preko, A.K. and Asamoah, J.K.K. Fractional order epidemiological model of SARS-CoV-2 dynamism involving Alzheimer's disease. *Healthcare Analytics*, 2, 100114, (2022). [CrossRef]

[30] Qureshi, A.I., Chughtai, M., Loua, T.O., Pe Kolie, J., Camara, H.F.S., Ishfaq, M.F. et al. Study of Ebola virus disease survivors in Guinea. *Clinical Infectious Diseases*, 61(7), 1035-1042, (2015). [CrossRef]

[31] Kengne, J.N. and Tadmon, C. Ebola virus disease model with a nonlinear incidence rate and density-dependent treatment. *Infectious Disease Modelling*, 9(3), 775-804, (2024). [CrossRef]

[32] MacIntyre, C.R. and Chughtai, A.A. Recurrence and reinfection-a new paradigm for the management of Ebola virus disease. *International Journal of Infectious Diseases*, 43, 58-61, (2016). [CrossRef]

[33] Rezapour, S., Asamoah, J.K.K., Hussain, A., Ahmad, H., Banerjee, R., Etemad, S. and Botmart, T. A theoretical and numerical analysis of a fractal-fractional two-strain model of meningitis. *Results in Physics*, 39, 105775, (2022). [CrossRef]

[34] Atangana, A. Fractal-fractional differentiation and integration: connecting fractal calculus and fractional calculus to predict complex system. *Chaos, Solitons & Fractals*, 102, 396-406, (2017). [CrossRef]

[35] Samet, B., Vetro, C. and Vetro, P. Fixed point theorems for α-ψ-contractive type mappings. *Nonlinear Analysis: Theory, Methods & Applications*, 75(4), 2154-2165, (2012). [CrossRef]

[36] Jiang, S., Zhang, J., Zhang, Q. and Zhang, Z. Fast evaluation of the Caputo fractional derivative and its applications to fractional diffusion equations. *Communications in Computational Physics*, 21(3), 650-678, (2017). [CrossRef]

[37] Padder, A., Almutairi, L., Qureshi, S., Soomro, A., Afroz, A., Hincal, E. and Tassaddiq, A. Dynamical analysis of generalized tumor model with Caputo fractional-order derivative. *Fractal and Fractional*, 7(3), 258, (2023). [CrossRef]

[38] Sikora, B. Remarks on the Caputo fractional derivative. *Minut*, 5, 76-84, (2023).

[39] Baba, I.A., Ahmed, I., Al-Mdallal, Q. M., Jarad, F. and Yunusa, S. Numerical and theoretical analysis of an awareness COVID-19 epidemic model via generalized Atangana-Baleanu fractional derivative. *Journal of Applied Mathematics and Computational Mechanics*, 21(1), 7-18, (2022). [CrossRef]

[40] Ahmed, I., Yusuf, A., Ibrahim, A., Kumam, P. and Ibrahim, M.J. A mathematical model of the ongoing coronavirus disease (COVID-19) pandemic: a case study in Turkey. *Science & Technology Asia*, 27(4), 248-258, (2022).[CrossRef]

[41] Hussain, A., Ahmed, I., Yusuf, A. and Ibrahim, M.J. Existence and stability analysis of a fractional-order COVID-19 model. *Bangmod International Journal of Mathematical and Computational Science*, 7, 102-125, (2021).

[42] Ahmed, I., Yusuf, A., Tariboon, J., Muhammad, M., Jarad, F. and Mikailu, B.B. A Dynamical and sensitivity analysis of the Caputo fractional-order Ebola virus model: implications for control measures. *Science & Technology Asia*, 28(4), 26-37, (2023).

[43] Granas, A. and Dugundji, J. *Fixed Point Theory*. Springer: New York, (2003). [CrossRef]

[44] Hyers, D.H. On the stability of the linear functional equation. *Proceedings of the National Academy of Sciences,* 27(4), 222-224, (1941). [CrossRef]

[45] Rassias, T.M. On the stability of the linear mapping in Banach spaces. *Proceedings of the American Mathematical Society,* 72, 297-300, (1978). [CrossRef]

[46] Gopal, K., Lee, L.S. and Seow, H.V. Parameter estimation of compartmental epidemiological model using harmony search algorithm and its variants. *Applied Sciences,* 11(3), 1138, (2021). [CrossRef]

[47] Asamoah, J.K.K., Owusu, M.A., Jin, Z., Oduro, F.T., Abidemi, A. and Gyasi, E.O. Global stability and cost-effectiveness analysis of COVID-19 considering the impact of the environment: using data from Ghana. *Chaos, Solitons & Fractals,* 140, 110103, (2020). [CrossRef]

[48] Asamoah, J.K.K., Jin, Z., Sun, G.Q., Seidu, B., Yankson, E., Abidemi, A. et al. Sensitivity assessment and optimal economic evaluation of a new COVID-19 compartmental epidemic model with control interventions. *Chaos, Solitons & Fractals,* 146, 110885, (2021). [CrossRef]

[49] Allahamou, A., Azroul, E., Hammouch, Z. and Alaoui, A.L. Modeling and numerical investigation of a conformable co-infection model for describing Hantavirus of the European moles. *Mathematical Methods in the Applied Sciences,* 45(5), 2736-2759, (2022). [CrossRef]

[50] Hamou, A.A., Rasul, R.R.Q., Hammouch, Z. and Özdemir, N. Analysis and dynamics of a mathematical model to predict unreported cases of COVID-19 epidemic in Morocco. *Computational and Applied Mathematics,* 41, 289, (2022). [CrossRef]

[51] Alla Hamou, A., Azroul, E. and Lamrani Alaoui, A. Fractional model and numerical algorithms for predicting COVID-19 with isolation and quarantine strategies. *International Journal of Applied and Computational Mathematics, Springer,* 7, 142, (2021). [CrossRef]

[52] Hamou, A.A., Azroul, E., Hammouch, Z. and Alaoui, A.L. A fractional multi-order model to predict the COVID-19 outbreak in Morocco. *Applied and Computational Mathematics,* 20(1), 177-203, (2020).

[53] Martcheva, M. *An Introduction to Mathematical Epidemiology* (Vol. 61). Springer: New York, (2015). [CrossRef]

[54] Asamoah, J.K.K. A fractional mathematical model of heartwater transmission dynamics considering nymph and adult amblyomma ticks. *Chaos, Solitons & Fractals,* 174, 113905, (2023). [CrossRef]

[55] Branda, F. and Maruotti, A. 2022 Uganda Ebola outbreak: Early descriptions and open data. *Journal of Medical Virology,* 95, e28344, (2023). [CrossRef]

[56] Branda, F., Mahal, A., Maruotti, A., Pierini, M. and Mazzoli, S. The challenges of open data for future epidemic preparedness: The experience of the 2022 Ebolavirus outbreak in Uganda. *Frontiers in Pharmacology,* 14, 1101894, (2023). [CrossRef]

[57] Worldometer. Population of Uganda, (2022). *World Population Prospects: The 2022 Revision, Frontiers Media SA* 1, (2022). https://www.worldometers.info/world-population/uganda-population.

[58] World Health Organization (WHO). Ebola Virus Disease, (2023). https://www.who.int/news-room/fact-sheets/detail/ebola-virus-disease.

[59] Castillo-Chavez, C. and Song, B. Dynamical models of tuberculosis and their applications. *Mathematical Biosciences and Engineering,* 1(2), 361-404, (2004). [CrossRef]

[60] Gemperli, A., Vounatsou, P., Sogoba, N. and Smith, T. Malaria mapping using transmission models: application to survey data from Mali. *American Journal of Epidemiology,* 163(3), 289-297, (2006). [CrossRef]

[61] Chen, J., Huang, J., Beier, J.C., Cantrell, R.S., Cosner, C., Fuller, D.O. et al. Modeling and control of local outbreaks of West Nile virus in the United States. *Discrete and Continuous Dynamical Systems-B*, 21(8), 2423-2449, (2016). [CrossRef]

[62] Ahmed, I., Kiataramkul, C., Muhammad, M. and Tariboon, J. Existence and sensitivity analysis of a Caputo fractional-order diphtheria epidemic model. *Mathematics,* 12(13), 2033, (2024). [CrossRef]

[63] Ahmed, I., Ibrahim, M.J., Abdullahi, M. and Saje, A.U. A mathematical analysis of a Caputo fractional-order cholera model and its sensitivity analysis. In *Modelling in Fractional-Order Systems with Applications in Engineering* (pp. 1-23). Lahore, Pakistan: Ptolemy Scientific Research Press, (2023).

Mathematical Modelling and Numerical Simulation with Applications (MMNSA)
(https://dergipark.org.tr/en/pub/mmnsa)

How to cite this article: Adu, I.K., Wireko, F.A., Adarkwa, S.A. and Agyekum, G.O. (2024). Mathematical analysis of Ebola considering transmission at treatment centres and survivor relapse using fractal-fractional Caputo derivatives in Uganda. *Mathematical Modelling and Numerical Simulation with Applications,* 4(3), 296-334. https://doi.org/10.53391/mmnsa.1514196

Mathematical Modelling and Numerical Simulation with Applications, 2024, 4(3), 335–350

https://dergipark.org.tr/en/pub/mmnsa

ISSN Online: 2791-8564 / Open Access

https://doi.org/10.53391/mmnsa.1492749

RESEARCH PAPER

Column generation approach for 1.5-dimensional cutting stock problem with technical constraints

Müjgan Sağır [1,*,‡] and **Tuğba Saraç** [1,‡]

[1]Eskişehir Osmangazi University, Faculty of Engineering and Architecture, Department of Industrial Engineering, 26040 Odunpazarı, Eskişehir, Türkiye

* Corresponding Author

‡ mujgan.sagir@gmail.com (Müjgan Sağır); tsarac@ogu.edu.tr (Tuğba Saraç)

Abstract

In this study, the 1.5-dimensional cutting stock problem with technical constraints is considered. In the literature, this problem is also defined as a strip packing or open dimension problem. When given a strip of infinite length and bounded width, the problem is to define a packing of rectangular objects into a strip that minimizes its final length. Technical constraints, such as the order type and the number of strips, are indispensable in real life; however, they are often neglected in the literature because they make the problem difficult to solve. Only one study was reached in the literature that took into account technical constraints, but in that mentioned study, only a mathematical model was proposed for the problem. In this context, our aim is to solve the problem with a more effective approach. The research question in this study is the usability of the column generation technique to solve the 1.5-dimensional cutting stock problem. In this study, the column generation approach was proposed for the first time for the considered problem. To demonstrate the performance of the proposed solution method, randomly generated test problems were solved with GAMS/Cplex. As we report the results, proposed column generation approach (CG) reaches very close (such as 1% and 2% error) solutions to integrated mathematical model (IM) for small sized problems in a second. On the other hand, while CG solved all the problems in a reasonable time, IM could not produce a feasible solution to some problems. Numerical experiments showed that the column generation algorithm outperforms the integrated mathematical model for the problem.

Keywords: 1.5-dimensional cutting problem; column generation; mixed-integer linear programming

AMS 2020 Classification: 90C06; 90C10; 90C11; 90C90

1 Introduction and literature survey

The essential characteristics to be considered to generate the cutting plans are the number of dimensions of the stock material and the order of pieces. Cutting items such as paper rolls and metal

➤ **Received:** 30.05.2024 ➤ **Revised:** 27.08.2024 ➤ **Accepted:** 16.09.2024 ➤ **Published:** 30.09.2024

rods are one-dimensional. The problems, such as pallet placement and cutting small rectangular order pieces from large rectangular stock materials, are two-dimensional, and problems such as container insertion and packing into packing boxes, are three-dimensional. Four-dimensional problems can arise when the time dimension is added to a three-dimensional problem.

One-and-a-half-dimensional problems are a particular case of two-dimensional problems. Such problems arise when rectangular order pieces are to be placed on very long rolls. Although rectangular order pieces are being cut, the problem is not two-dimensional because the side waste along the stock material can be defined by one dimension.

Dyckhoff et al. (1985) made significant contributions to the literature on cutting problems and named the one-dimensional cutting stock problem in continuous form as one plus half-dimensional, 1.5-dimensional [1]. This definition in Dyckhoff's classification has not been included much in the literature. The related problems are defined as 'one-dimensional and various-sized stock materials cut-off' instead of the 1.5-dimensional problem [2]. Moreover, in the following years, Dyckhoff grouped the problems according to their dimensions as one, two, three, and $N-$dimensional ($N > 3$) problems. This classification does not include the 1.5- dimensional problems [3].

Song et al. (2006) defined the 1.5-dimensional problem differently. Accordingly, the 1.5- dimensional cutting stock problem is cutting smaller rectangular order pieces from large rectangular stock materials. In this problem, the order piece requested by the customers can sometimes be longer than the primary material. In this case, several stock materials are brought together so that their total length matches the size of the order pieces. This problem is also defined as a 1.5-dimensional problem because of the assumption that the stock materials can be combined [4]. In the definitions above, the 1.5-dimensional problem is the placement of rectangular order pieces to the stock material, which can be accepted as a fixed width and continuous form. Although this problem is not mentioned as much as other cutting problems in the literature, it has a significant area, especially in production environments with inputs such as paper, metal, sheet metal.

Saraç and Özdemir (2003) discussed the 1.5-dimensional cutting stock problem with the limited number of strips, piece types, and stock material selection. They proposed a two-step approach to solve the problem. The cutting plans are derived for the first stage, and complete enumeration is considered under the constraints of the number of strips and the order of piece type. In the second stage, a bi-objective, nonlinear, mixed-integer mathematical model is proposed to determine which cutting plans and stock materials will be selected. A genetic algorithm has been developed because a mathematical model cannot solve real-life problems [5]. Gasimov et al. (2007) developed a new multi-objective mixed-integer linear mathematical model for the 1.5-dimensional cutting stock and stock material selection problem. This model requires the cutting plans to be derived in advance [6]. Kokten and Sel (2022) developed a nonlinear mixed-integer mathematical model for the 1.5-dimensional cutting stock and stock material selection problem. They used a decomposition method in which the sub-models were solved sequentially to solve the problem [7]. Saraç and Sağır (2021) developed a mixed-integer linear mathematical model for the 1.5-dimensional cutting stock problem with limited part type and strip number that does not need to be derived in advance of cutting plans [8]. Duysak et al. (2022) proposed a metaheuristic algorithm for the 1.5-dimensional cutting and assortment problem. They considered the due dates of the cutting parts [9]. Vasilyev et al. (2023) proposed a few mathematical models and two solution algorithms for the problem [10]. Liu et al. (2023) dealt with two aspects of the problem: the uncertain demand for items and the need for diverse types of strips to cater to varying customer needs. They proposed a robust optimization model to cope with these difficulties [11].

The variations of the considered problem have also been referred to in the literature as strip packing or open dimensional problems. The strip packing problem is defined as follows. Consider

a set of n rectangular items with dimensions (wj, h_j) where wj and h_j represent the width and the height of item j, respectively, and wj is an integer value. Let R be a rectangular object (strip) with fixed width W and height H large enough (infinite height) to pack all items. The objective of the strip packing problem is to pack all items without overlapping while minimizing the height of the strip [12]. On the other hand, according to Wäscher et al. (2007), 2D strip packing corresponds to the Two-Dimensional Rectangular Open Dimension Problem [13].

A few studies solve the strip packing problem with column generation. In their study, Sugi et al. (2020) considered the rectangular strip packing problem with a three-stage guillotine cutting constraint and the limitations of slitter blades. They propose a new algorithm based on the column-generation technique for this problem [14]. While Cintra et al. (2008) and Bettinelli et al. (2008) developed solution approaches based on the column generation technique for the classical two-dimensional level strip packing problem [15, 16], respectively, Cui et al. (2017) suggested it for the rectangular level strip packing problem [17]. When it comes to level, the structure of the problem differs significantly from that of the classical problem since the cutting process is done on a level basis. The problems addressed in these studies are different from our problems. Order type and strip number constraints were not considered together in any of these studies. In summary, we have reached only one study [8] in the literature that considers technical constraints. Furthermore, when considering the 1.5-dimensional cutting problem literature, it becomes evident that the column generation solution approach has not been applied to this problem previously. In other words, in this study, the column generation approach was proposed for the first time for the considered problem.

The following Section 2 presents the problem in detail and gives the mathematical model of the problem. Section 3 proposes a column generation approach to solve the problem. Section 4 provides experimental results, Section 5 gives the discussion, and Section 6 presents the conclusion.

2 Problem definition and mathematical model

n rectangular order pieces of different dimensions are cut from G-width stock material. The length (L) of the stock material is long enough to neglect the length restriction when creating cutting plans. For this reason, cutting plans are created by considering only the 'width' constraints. Then, the total lengths are calculated separately for each order piece included in a cutting plan. The largest of these determines the size of the cutting plan. The number of knives $(t-1)$ that can cut the stock material into strips by cutting parallel to the length is limited. Therefore, the stock material can be cut into a maximum of t strips. In other words, a maximum t order pieces can be placed on the stock material. While cutting the order pieces, they cannot be rotated; that is, cutting should be made so that the width of the order piece is parallel to the width and length of the stock material. Also, the maximum number of order piece types (c) that can be included in a cutting plan is limited.

An integrated mathematical model (IM) proposed by Saraç and Sağır (2021) generates and selects cutting plans for 1.5-dimensional cutting stock problems with technical constraints [8]. Table 1 gives the indices of the mathematical model, Table 2 shows the parameters, and Table 3 shows the decision variables.

Table 1. Indices

r	Quantity index with the order piece at the width of the cutting plan $r \in \{1, \ldots, enb_j\{q_j\}\}$
j	Order piece index $j \in \{1, \ldots, n\}$
k	Cutting plan index $k \in \{1, \ldots, m\}$

Table 2. Parameters

n	number of order pieces
m	maximum number of cutting plans that can be derived
e_j	width of the order piece j (cm)
b_j	length of the order piece j (cm)
d	the demand of the order piece
q_j	the quantity that the order piece j can fit in the width of the stock material $q_j = \left\lfloor \frac{G}{e_j} \right\rfloor$
G	width of the stock material (cm)
L	length of the stock material (cm)
t	maximum number of strips that can be included in a cutting plan
c	maximum variety of order parts that can be included in a cutting plan

Table 3. Decision variables

μ_{jk}	the total amount of order piece j included in the cutting plan k
y_{jk}	the quantity that the order piece j can fit in the width of the k^{th} cutting pattern
z_k	1, if k^{th} cutting pattern is used, 0 otherwise
w_{jk}	1, if j^{th} order is included in the k^{th} cutting pattern, 0 otherwise
x_k	Net amount to be used from the k^{th} cutting pattern (cm)
s_{jkr}	1, if there is an r row of the order j at the width of the cutting pattern k, 0 otherwise
$\propto_{jk}$	the quantity of the order piece j can fit in the length of the cutting pattern k
σ_k	amount to be used from the k^{th} cutting pattern (Each cutting plan is assumed as 100 cm. In the mathematical model, and σ_k decision variable shows how many times 100 cm cutting patterns are used. Therefore, the number of uses of the cutting patterns also means how many meters are used
M'	a big positive number $M' = \left\lfloor \frac{G}{e_j} \right\rfloor \left\lfloor \frac{L}{b_j} \right\rfloor$
M''	a big positive number $M'' = \max q_j$

The IM model is given below:

$$\sum_k \mu_{jk} \geq d_j, \qquad \forall j, \tag{1}$$

$$\sum_j e_j y_{jk} \leq G z_k, \qquad \forall k, \tag{2}$$

$$\sum_k x_k \leq L, \tag{3}$$

$$\mu_{jk} \leq y_{jk} M', \qquad \forall j, k, \tag{4}$$

$$\mu_{jk} \geq y_{jk}, \qquad \forall j, k, \tag{5}$$

$$\propto_{jk} \leq \frac{100\sigma_k}{b_j}, \qquad \forall j, k, \tag{6}$$

$$\mu_{jk} \leq r \propto_{jk} + (1 - s_{jkr}) M', \qquad \forall j, k, r | r \leq q_j, \tag{7}$$

$$y_{jk} = \sum_{r | r \leq q_j} r s_{jkr}, \qquad \forall j, k, \tag{8}$$

$$\sum_{r | r \leq q_j} s_{jkr} \leq 1, \qquad \forall j, k, \tag{9}$$

$$\sum_{j}\sum_{r|r\leq q_j} s_{jkr} \leq c, \qquad \forall k, \tag{10}$$

$$\sum_{j} y_{jk} \leq t, \qquad \forall k, \tag{11}$$

$$\sum_{j} y_{jk} \leq \sigma_k M'', \qquad \forall k, \tag{12}$$

$$\sigma_k \geq z_k, \qquad \forall k, \tag{13}$$

$$\sigma_k \leq L\, z_k, \qquad \forall k, \tag{14}$$

$$x_k \geq b_j \propto_{jk}, \qquad \forall j,k, \tag{15}$$

$$x_k \geq 0, \qquad \forall k, \tag{16}$$

$$y_{jk} \geq 0 \text{ and integer}, \qquad \forall j,k, \tag{17}$$

$$\mu_{jk} \geq 0 \text{ and integer}, \qquad \forall j,k, \tag{18}$$

$$z_k \in \{0,1\}, \qquad \forall k, \tag{19}$$

$$w_{jk} \in \{0,1\}, \qquad \forall j,k, \tag{20}$$

$$s_{jkr} \in \{0,1\}, \qquad \forall j,k,r, \tag{21}$$

$$\sigma_k \geq 0 \text{ and integer}, \qquad \forall k, \tag{22}$$

$$\propto_{jk} \geq 0 \text{ and integer}, \qquad \forall j,k. \tag{23}$$

Objective function

$$f = enk \sum_{k} \frac{x_k}{L} + \sum_{k} \frac{Z_k}{m}. \tag{24}$$

Constraint (1) is the demand constraint. It is ensured by constraint (2) that the total width of all order pieces placed in a cutting plan does not exceed the width of the stock material. The constraint (3) is for the total amount of cutting plan used not to exceed the length of the stock material. The constraints (4) and (5) are the relationship constraints between variables μ_{jk} and y_{jk}. If y_{jk} is zero, they ensure that the variable μ_{jk} is also zero. Constraint (6) calculates how many times the order pieces j are included in the cutting plan k considering only its length. Decision variable σ_k indicates how many pieces of the cutting plan are used, and it is multiplied by 100 to convert to cm. Constraint (7) calculates exactly how many pieces of order j are included in the total amount of cutting plan k. Constraint (8) calculates how many pieces of order j are included in a cutting plan considering only its width. Constraint (9) indicates that if an order piece is used in a cutting plan, the amount that can fit in the end can be a single value. Constraint (10) indicates that maximum c different order pieces can be included in the cutting plan. Constraint (11) indicates that there may be no more than t order pieces that can be cut across a cutting plan. The constraint number (12) is the relational constraint between y_{jk} and σ_k. Constraints (13) and (14) are the relational constraints between σ_k and z_k. The constraint number (15) calculates the net used amount of the cutting plan. (16) - (23) constraints are sign constraints. The objective function (24) is to minimize the total length and type of cutting plan used. These terms are combined using the weighted sum scalarization method.

3 Problem-solving with column generation

Although mathematical models are developed to give the best solution for t his problem, they cannot be solved when the problem size increases. In addition, the problem has some special

technical limitations that have not been included in the literature by now. Our motivation comes from this need to solve the model more effectively and quickly by using the column generation method, as well as to take into account more realistic constraints are aimed, as we explained before. This section presents the column generation method.

Column generation method

Column Generation is a technique for solving linear programs where the numbers of variables are hard to enumerate. According to this approach, only a few variables are needed to determine the optimal solution, as most will assume a zero value [18]. In each step, the master model looks for the best solution, considering only a certain number of variables (equivalent columns). The sub-problem (knapsack problem) investigates whether new columns are added to the master problem in the next increment, reducing the objective function. The objective function of the knapsack problem is the reduced cost of the columns concerning the optimal dual variables corresponding to the optimal solution of the current master problem. If there is a column with a negative reduced cost, that column is added to the master problem and proceeded to the next iteration; otherwise, optimality is achieved [18].

Figure 1 gives the flow chart of the column generation algorithm.

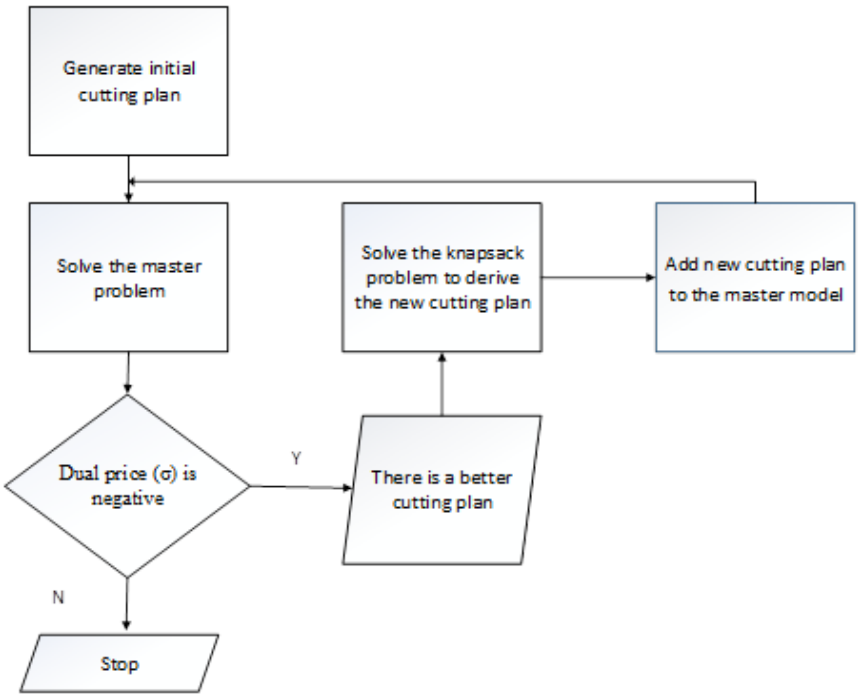

Figure 1. Main steps of the CG algorithm

According to the algorithm, initial cutting plans are derived. The master model is solved using these cutting plans. If the dual price (σ) is negative, there is a better cutting pattern. From the solution of the master model, the dual variable of the related constraint is sent to the knapsack model. The knapsack model is solved, and the new cutting plan will be added to the master model. Then, the loop continues until no better cutting plan is derived.

The complexity of column generation depends on the structure of the main problem and the pricing sub-problems. Because the process involves solving a constrained main problem and a set of sub-problems iteratively to create new columns, the computational burden is usually incurred

by solving the sub-problems and can be complex and time-consuming, especially when these problems involve combinational structures. For the problem considered in this study, a significant reduction is observed in the complexity of the sub-problem compared to the complexity of the integrated problem. The solution times given in Section 5 are an indicator of this reduction.
The column generation technique is used to solve many problems in the literature. Kamran et al. (2020) used a column-generation-based heuristic algorithm and Benders' decomposition technique to schedule patients in operating rooms. With the growth in the number of patients, the feasible sequencing plans grow exponentially. On the other hand, the CG method does not need to price out all the columns, and this makes it beneficial [19].
Faiz et al. (2019) used a column generation framework to solve large-scale instances of vehicle scheduling and routing problems. They first suggest various linear programming models for the problem. According to the experimental results, the column-generation-based approach provides better solutions in terms of solution time [20].
Changchun et al. (2018) developed a column generation-based distributed scheduling algorithm for a constrained project scheduling problem. They decomposed the problem into two parts as: production planning and vehicle scheduling [21].
Section 3 presents the proposed column generation algorithm's main and sub (knapsack) problems and the mathematical models developed to solve them.

Master and knapsack models

Master and knapsack models are developed as below, respectively. Since the indices, parameters, and decision variables are explained in Section 2, only the newly defined ones are included here.
Master model
Parameters

y'_{jk} : the quantity that the order piece j can fit in the width of the k^{th} cutting pattern.

Constraints are given by the following equations including Eq. (3),

$$\propto_{jk} \leq \frac{100x_k}{b_j}, \qquad \forall j,k, \tag{25}$$

$$\sum_k \propto_{jk} y'_{jk} \geq d_j, \qquad \forall j, \tag{26}$$

$$x_k \geq z_k, \qquad \forall k, \tag{27}$$

$$x_k \leq L\, z_k, \qquad \forall k, \tag{28}$$

$$x_k \geq b_j \propto_{jk}, \qquad \forall j,k. \tag{29}$$

Objective function

$$f = min \sum_k x_k. \tag{30}$$

Constraint (25) calculates how many times order piece j is included in the cutting plan k considering only its length. Decision variable x_k indicates how long cutting plans are used in meters, and it is multiplied by 100 to convert to centimeters. Constraint (26) is demand constraint. Constraints (27) and (28) are the relational constraints between x_k and z_k. Constraint (29) calculates the net amount to be used from the k^{th} cutting pattern (cm).
The objective function (30) minimizes the total net amount used from the cutting patterns.

Knapsack Model

Parameters

y_j : the quantity that the order piece j can fit in the width of the cutting pattern,
w_j : 1, if j^{th} order is included in the cutting pattern, *0* otherwise,
φ_j : dual variables of constraint (26) of main model.

$$y_j \leq t w_j, \qquad \forall j, \tag{31}$$
$$y_j \geq w_j, \qquad \forall j, \tag{32}$$
$$\sum_j e_j y_j \leq G, \tag{33}$$
$$\sum_j w_j \leq c, \tag{34}$$
$$\sum_j y_j \leq t, \tag{35}$$
$$y_j \geq 0, \qquad \forall j, \tag{36}$$
$$w_j \in \{0,1\}, \qquad \forall j, \tag{37}$$

$$f = min\left(1 - \sum_j \varphi_j\, y_j\, (\frac{1}{b_j})\right). \tag{38}$$

Constraints (31) and (32) indicate that if an order piece is included in the cutting pattern, at least one and no more than t order pieces can be cut across the cutting plan. It is ensured by constraint (33) that the total width of all order pieces placed in a cutting plan does not exceed the width of the stock material. Constraint (34) indicates that maximum c different order pieces can be included in the cutting plan. Constraint (35) indicates that there may be no more than t order pieces that can be cut across a cutting plan. (36) - (37) are sign constraints. The objective function is given in Eq. (38).

4 Experimental results

An instance taken from the literature with different numbers of orders is solved both with MI and CG. CPLEX solver of GAMS (version 24.0.2) is used on a PC with 3.60 GHz Intel Core i7 and 16 GB RAM. The time limit of 86,400 CPU seconds is applied for CPLEX runs.
The following section presents the test problems, followed by the toy problem and the test results, which are introduced in the first and second subsection of Section 4, respectively.

Test problems

The first four samples (problem instances) are taken from [8]. The remaining are obtained by adapting the examples generated for one-dimensional cutting problems by Kasımbeyli et al. (2011) [22]. The widths of the order pieces in the one-dimensional problem are multiplied by a parameter, and the length values are obtained. The parameter values of all samples are given below.

Sample 1.

$$n = 5, \quad G = 110, \quad e = (10,20,30,40,60), \quad b = (13,26,39,52,78), \quad d = (6,11,4,20,15).$$

Sample 2.

$$
\begin{aligned}
n &= 10, \quad G = 120, \\
e &= (10, 20, 30, 40, 60, 15, 25, 35, 45, 65), \\
b &= (13, 26, 39, 52, 78, 19, 32, 45, 58, 84), \\
d &= (7, 11, 3, 20, 15, 5, 10, 13, 20, 15).
\end{aligned}
$$

Sample 3.

$$
\begin{aligned}
n &= 20, \quad G = 130, \\
e &= (10, 20, 30, 40, 60, 15, 25, 35, 45, 65, 11, 12, 13, 14, 21, 22, 23, 24, 31, 32), \\
b &= (13, 26, 39, 52, 78, 19, 32, 45, 58, 84, 14, 15, 16, 18, 27, 28, 29, 31, 40, 41), \\
d &= (16, 11, 13, 20, 15, 15, 10, 13, 20, 15, 15, 11, 13, 20, 15, 15, 10, 13, 2, 15).
\end{aligned}
$$

Sample 4.

$$
\begin{aligned}
n &= 30, \quad G = 280, \\
e &= (10, 20, 30, 40, 60, 15, 25, 35, 45, 65, 11, 12, 13, 14, 21, 22, 23, 24, 31, 32, 33, 34, 41, 42, 43, 44, 51, \\
&\quad 52, 53, 54), \\
b &= (13, 26, 39, 52, 78, 19, 32, 45, 58, 84, 14, 15, 16, 18, 27, 28, 29, 31, 40, 41, 42, 44, 53, 54, 55, 57, 66, \\
&\quad 67, 68, 70), \\
d &= (5, 11, 3, 20, 15, 5, 10, 13, 20, 15, 5, 11, 3, 20, 15, 5, 10, 13, 20, 15, 5, 11, 3, 20, 15, 5, 10, 13, 20, 15).
\end{aligned}
$$

Sample 5.

$$
\begin{aligned}
n &= 40, \quad G = 130, \\
e &= (10, 20, 30, 40, 60, 15, 25, 35, 45, 65, 11, 12, 13, 14, 21, 22, 23, 24, 31, 32, 33, 34, 41, 42, 43, 44, 51, \\
&\quad 52, 53, 54, 61, 62, 63, 64, 66, 67, 68, 69, 70, 71), \\
b &= (13, 26, 39, 52, 78, 19, 32, 45, 58, 84, 14, 15, 16, 18, 27, 28, 29, 31, 40, 41, 42, 44, 53, 54, 55, 57, 66, \\
&\quad 67, 68, 70, 79, 80, 81, 83, 85, 87, 88, 89, 91, 92), \\
d &= (5, 11, 3, 20, 15, 5, 10, 13, 20, 15, 5, 11, 3, 20, 15, 5, 10, 13, 20, 15, \\
&\quad 5, 11, 3, 20, 15, 5, 10, 13, 20, 15, 5, 11, 3, 20, 15, 5, 10, 13, 20, 15).
\end{aligned}
$$

Sample 6.

$$
\begin{aligned}
n &= 40, \quad G = 10000, \\
e &= (732, 1746, 1210, 290, 1212, 715, 1471, 1405, 1974, 344, 1699, 172, 351, 1227, 1739, 272, 1903, \\
&\quad 1121, 1326, 107, 726, 1917, 1116, 501, 1599, 439, 821, 485, 361, 860, 1252, 562, 1131, 271, 1075, \\
&\quad 987, 1171, 1979, 228, 1370), \\
b &= (951, 2269, 1573, 377, 1575, 929, 1912, 1826, 2566, 447, 2208, 223, 456, 1595, 2260, 353, 2473, \\
&\quad 1457, 1723, 139, 943, 2492, 1450, 651, 2078, 570, 1067, 630, 469, 1118, 1627, 730, 1470, 352, \\
&\quad 1397, 1283, 1522, 2572, 296, 1781),
\end{aligned}
$$

$$d = (217, 232, 265, 249, 266, 269, 215, 215, 213, 267, 299, 259, 287, 284, 277, 223, 200, 255, 269, 226, 240, 209, 266, 254, 241, 264, 229, 257, 285, 204, 255, 257, 283, 222, 218, 289, 244, 214, 223, 290).$$

Sample 7.

$$n = 100, \quad G = 800,$$
$$e = (1, 2, 3, 4, 5, 6, 7, 8, 9, 10, 11, 12, 13, 14, 15, 16, 17, 18, 19, 20, 21, 22, 23, 24, 25, 26, 27, 28, 29, 30, 31, 32, 33, 34, 35, 36, 37, 38, 39, 40, 41, 42, 43, 44, 45, 46, 47, 48, 49, 50, 51, 52, 53, 54, 55, 56, 57, 58, 59, 60, 61, 62, 63, 64, 65, 66, 67, 68, 69, 70, 71, 72, 73, 74, 75, 76, 77, 78, 79, 80, 81, 82, 83, 84, 85, 86, 87, 88, 89, 90, 91, 92, 93, 94, 95, 96, 97, 98, 99, 100),$$
$$b = (1, 2, 3, 5, 6, 7, 9, 10, 11, 13, 14, 15, 16, 18, 19, 20, 22, 23, 24, 26, 27, 28, 29, 31, 32, 33, 35, 36, 37, 39, 40, 41, 42, 44, 45, 46, 48, 49, 50, 52, 53, 54, 55, 57, 58, 59, 61, 62, 63, 65, 66, 67, 68, 70, 71, 72, 74, 75, 76, 78, 79, 80, 81, 83, 84, 85, 87, 88, 89, 91, 92, 93, 94, 96, 97, 98, 100, 101, 102, 104, 105, 106, 107, 109, 110, 111, 113, 114, 115, 117, 118, 119, 120, 122, 123, 124, 126, 127, 128, 130),$$
$$d = (5, 11, 3, 20, 15, 5, 10, 13, 20, 15, 5, 11, 3, 20, 15, 5, 10, 13, 20, 15, 5, 11, 3, 20, 15, 5, 10, 13, 20, 15, 5, 11, 3, 20, 15, 5, 10, 13, 20, 15, 13, 13, 13, 13, 13, 13, 13, 13, 13, 14, 14, 14, 14, 14, 14, 14, 14, 14, 14, 14, 14, 14, 14, 14, 14, 14, 15, 15, 15, 15, 15, 15, 15, 15, 15, 15, 15, 15, 15, 15, 15, 16, 16, 16, 16, 16, 16, 16, 16, 16, 16, 16, 16, 16, 16, 17, 17).$$

Sample 8.

$$n = 20, \quad G = 110,$$
$$e = (50, 51, 52, 53, 54, 55, 56, 57, 58, 59, 32, 33, 42, 44, 27, 19, 10, 40, 20, 30),$$
$$b = (65, 66, 67, 68, 70, 71, 72, 74, 75, 76, 41, 42, 54, 57, 35, 24, 13, 52, 26, 39),$$
$$d = (273, 20, 27, 19, 32, 28, 100, 82, 55, 42, 48, 35, 29, 50, 35, 40, 23, 42, 51, 32).$$

Sample 9.

$$n = 200, \quad G = 1400,$$
$$e = (1, 2, 3, 4, 5, 6, 7, 8, 9, 10, 11, 12, 13, 14, 15, 16, 17, 18, 19, 20, 21, 22, 23, 24, 25, 26, 27, 28, 29, 30, 31, 32, 33, 34, 35, 36, 37, 38, 39, 40, 41, 42, 43, 44, 45, 46, 47, 48, 49, 50, 51, 52, 53, 54, 55, 56, 57, 58, 59, 60, 61, 62, 63, 64, 65, 66, 67, 68, 69, 70, 71, 72, 73, 74, 75, 76, 77, 78, 79, 80, 81, 82, 83, 84, 85, 86, 87, 88, 89, 90, 91, 92, 93, 94, 95, 96, 97, 98, 99, 100, 101, 102, 103, 104, 105, 106, 107, 108, 109, 110, 111, 112, 113, 114, 115, 116, 117, 118, 119, 120, 121, 122, 123, 124, 125, 126, 127, 128, 129, 130, 131, 132, 133, 134, 135, 136, 137, 138, 139, 140, 141, 142, 143, 144, 145, 146, 147, 148, 149, 150, 151, 152, 153, 154, 155, 156, 157, 158, 159, 160, 161, 162, 163, 164, 165, 166, 167, 168, 169, 170, 171, 172, 173, 174, 175, 176, 177, 178, 179, 180, 181, 182, 183, 184, 185, 186, 187, 188, 189, 190, 191, 192, 193, 194, 195, 196, 197, 198, 199, 200),$$
$$b = (1, 2, 3, 5, 6, 7, 9, 10, 11, 13, 14, 15, 16, 18, 19, 20, 22, 23, 24, 26, 27, 28, 29, 31, 32, 33, 35, 36, 37, 39, 40, 41, 42, 44, 45, 46, 48, 49, 50, 52, 53, 54, 55, 57, 58, 59, 61, 62, 63, 65, 66, 67, 68, 70, 71, 72, 74, 75, 76, 78, 79, 80, 81, 83, 84, 85, 87, 88, 89, 91, 92, 93, 94, 96, 97, 98, 100, 101, 102, 104, 105,$$

106, 107, 109, 110, 111, 113, 114, 115, 117, 118, 119, 120, 122, 123, 124, 126, 127, 128, 130, 131, 132, 133, 135, 136, 137, 139, 140, 141, 143, 144, 145, 146, 148, 149, 150, 152, 153, 154, 156, 157, 158, 159, 161, 162, 163, 165, 166, 167, 169, 170, 171, 172, 174, 175, 176, 178, 179, 180, 182, 183, 184, 185, 187, 188, 189, 191, 192, 193, 195, 196, 197, 198, 200, 201, 202, 204, 205, 206, 208, 209, 210, 211, 213, 214, 215, 217, 218, 219, 221, 222, 223, 224, 226, 227, 228, 230, 231, 232, 234, 235, 236, 237, 239, 240, 241, 243, 244, 245, 247, 248, 249, 250, 252, 253, 254, 256, 257, 258, 260),

d = (5, 11, 3, 20, 15, 5, 10, 13, 20, 15, 5, 11, 3, 20, 15, 5, 10, 13, 20, 15, 5, 11, 3, 20, 15, 5, 10, 13, 20, 15, 5, 11, 3, 20, 15, 5, 10, 13, 20, 15, 13, 13, 13, 13, 13, 13, 13, 13, 14, 14, 14, 14, 14, 14, 14, 14, 14, 14, 14, 14, 14, 14, 14, 14, 14, 14, 15, 15, 15, 15, 15, 15, 15, 15, 15, 15, 15, 15, 15, 15, 15, 16, 16, 16, 16, 16, 16, 16, 16, 16, 16, 16, 16, 16, 16, 16, 16, 16, 16, 16, 17, 17, 16, 16, 17, 17, 17, 17, 17, 17, 17, 17, 17, 17, 17, 17, 17, 17, 17, 17, 17, 17, 17, 17, 17, 18, 18, 18, 18, 18, 18, 18, 18, 18, 18, 18, 18, 18, 18, 18, 18, 18, 18, 18, 19, 19, 19, 19, 19, 19, 19, 19, 19, 19, 19, 19, 19, 19, 19, 19, 19, 19, 19, 20, 20, 20, 20, 20, 20, 20, 20, 20, 20, 20, 20, 20, 20, 20, 20, 20, 20, 20, 20, 20, 20, 20, 21, 21, 21, 21, 21, 21, 21, 21, 21, 21, 21, 21, 21, 21, 21, 21, 21, 21, 21, 21, 21, 22, 22, 22).

Two cases are considered for all samples: Cutting plans can be included (1) at most two kinds of order pieces and eight strips ($c = 2$ and $t = 8$) and (2) at most three types of parts and sixteen strips ($c = 4$ and $t = 16$).

Toy problem

Toy problem includes four order pieces, P1, P2, P3, P4, with sizes as 10×13, 20×26, 30×39, 40×52, respectively. The stock material's width is 50. Demands are 4, 5, 3, and 2, respectively.
The toy problem was solved with both CG and IM, and the same solution was obtained. However, while CG achieved this solution in 0.48 seconds, MI runs to the time limit of 86400 seconds. Obtained cutting plans are presented in the following Figure 2, Figure 3, and Figure 4.

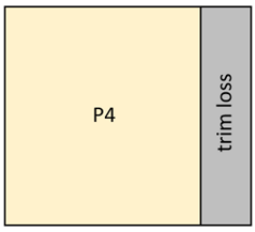

Figure 2. Cutting Plane 1

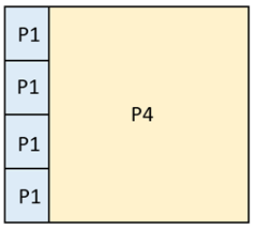

Figure 3. Cutting Plane 2

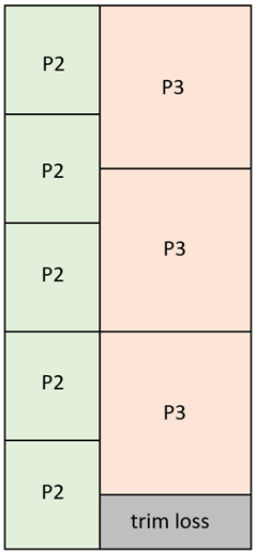

Figure 4. Cutting Plane 3

5 Test results and discussion

Samples have been solved both with IM and CG for two parameter sets: set 1 ($c = 2$ and $t = 8$) and set 2 ($c = 4$ and $t = 16$). The results obtained with set 1 are given in Table 4 and set 2 in Table 5. According to Table 4, IM obtains only the optimum solution for Samples 1 and 2. CG reaches very close solutions (1% and 2% error) to IM in a second. IM could not achieve any feasible solution for other problems in reasonable times. On the other hand, feasible solutions are achieved in reasonable times with CG. For none of the instances in Table 5, an optimum solution is achieved for IM, but feasible solutions are obtained for Samples 1, 2, and 8. For sample 1, both IM and CG obtained the same solution. The solution time of CG is only one second, while the solution time of IM is 86400 seconds (IM stopped by the time limit). For Sample 2, in a second, CG approaches 1% close to the solution obtained by MI in 31288 seconds. For sample 8, on the other hand, CG achieved a more successful objective function value in a much shorter time than IM. CG obtained feasible solutions in reasonable times for the rest of the instances. On the other hand, IM has not obtained a solution within the time limit for these instances. Due to the difference in d values (much bigger than the other instances' d values), the z_{CG} value in Sample 6 for CG is obtained bigger than the other z_{CG} values.

Table 4. Test results for $c = 2$ and $t = 8$

	IM	IM	CG	CG
	z_{IM}	t_{IM}	z_{CG}	t_{CG}
*sample*1	1248	6244	1261	1
*sample*2	2531	1181	2587	1
*sample*3	-	86400	3002	141
*sample*4	-	86400	2714	822
*sample*5	-	86400	10980	86400
*sample*6	-	86400	1672106	28561
*sample*7	-	86400	3240	1
*sample*8	-	86400	28239	3
*sample*9	-	86400	69514	86400

Table 5. Test results for $c = 4$ and $t = 16$

	IM z_{IM}	IM t_{IM}	CG z_{CG}	CG t_{CG}
*sample*1	1222	86400	1222	1
*sample*2	2510	31288*	2533	1
*sample*3	-	86400	2976	4322
*sample*4	-	86400	2754	288
*sample*5	-	86400	10948	86400
*sample*6	-	86400	1661374	86400
*sample*7	-	86400	9604	86400
*sample*8	28621	86400	28144	11777
*sample*9	-	86400	52265	86400

*out of memory.

When Table 4 and Table 5 are examined regarding the effects of different parameter sets on the objective function and solution times, it is observed that when the c and t parameters are increased, generally better objective function values can be obtained, but the solution time is prolonged.

When the experimental results are evaluated in general, it is observed that the mathematical modeling method has some critical limitations for the 1.5-dimensional cutting stock problem with technical constraints. In particular, it has been determined that as the problem size increases, the solution times with traditional mathematical models increase dramatically, and even in some cases, a feasible solution cannot be found. This situation shows that complex constraints and high-dimensional problem structures are difficult to cope with only using classical mathematical modeling techniques.

In this context, the proposed Column Generation (CG) solution method has emerged as an effective alternative, especially for cutting stock problems with large-scale and complex constraints. The CG method offers an approach that can divide the problem into smaller sub-problems and solve each of them in reasonable times. In the numerical experiments, it has been observed that this method produces faster and more successful solutions even for large-sized problems. In particular, it has been concluded that it is successful in coping with technical constraints and therefore can be used as a practical solution method in real-world applications.

6 Conclusion

In this study, the 1.5-dimensional cutting stock problem is considered. This problem covers situations where materials of certain widths and lengths commonly encountered in industrial production processes need to be cut with minimum waste. Unlike the studies in the literature, technical constraints such as order type and number of strips are taken into account together in this study. This approach allows obtaining results closer to real-world applications. In order to solve the problem, a column generation technique, which has been proven to be effective in large-scale and complex cutting stock problems, is proposed. This technique was developed to increase the solution time and accuracy even in high-dimensional problems.

In order to test the accuracy and effectiveness of the study, the test problems and a linear integrated mathematical model from the literature were used. The numerical experiments revealed that as the problem size increases, the solution time of the mathematical model increases dramatically, and even in some cases, a feasible solution cannot be found. However, the proposed column generation approach produces faster and more successful solutions even for large-sized problems. The column generation algorithm performed better than the mathematical model. The column generation approach is not limited to the problem considered in this study but can also be applied to other cutting stock problems in the future. This approach provides a valuable solution, especially

for researchers dealing with large data sets and complex production processes.
The CG solution approach may be insufficient when the problem dimensions are very large, such as in big data. Applying heuristic methods to solve the sub-problem may be a solution in this case.

Declarations

Use of AI tools

The authors declare that they have not used Artificial Intelligence (AI) tools in the creation of this article.

Data availability statement

There are no external data associated with the manuscript.

Ethical approval (optional)

The authors state that this research complies with ethical standards. This research does not involve either human participants or animals.

Consent for publication

Not applicable

Conflicts of interest

The authors declare that they have no conflict of interest.

Funding

No funding was received for this research.

Author's contributions

M.S.: Conceptualization, Methodology, Validation, Writing-Original draft preparation, Software. T.S.: Conceptualization, Methodology, Validation, Writing-Original draft preparation, Data Curation, Software. All authors have read and agreed to the published version of the manuscript.

Acknowledgements

Not applicable

References

[1] Dyckhoff, H., Kruse, H.J., Abel, D. and Gal, T. Trim loss and related problems. *Omega*, 13(1), 59-72, (1985). [CrossRef]

[2] Adakçı, S. *Stok Kesme Problemi: Alüminyum Sektöründe Uygulaması*. Yüksek Lisans Tezi, İstanbul Teknik Üniversitesi Fen Bilimleri Enstitüsü, İstanbul, (2001).

[3] Dyckhoff, H. A typology of cutting and packing problems. *European Journal of Operational Research*, 44(2), 145-159, (1990). [CrossRef]

[4] Song, X., Chu, C.B., Nie, Y.Y. and Bennell, J.A. An iterative sequential heuristic procedure to a real-life 1.5-dimensional cutting stock problem. *European Journal of Operational Research*, 175(3), 1870-1889, (2006). [CrossRef]

[5] Saraç, T. and Özdemir, M.S. A genetic algorithm for 1.5 dimensional assortment problems with multiple objectives. In Proceedings, *International Conference on Industrial, Engineering and*

Other Applications of Applied Intelligent Systems (IEA/AIE), pp. 41-51, Heidelberg, Berlin, (2003, June). [CrossRef]

[6] Gasimov, R.N., Sipahioglu, A. and Saraç, T. A multi-objective programming approach to 1.5-dimensional assortment problem. *European Journal of Operational Research,* 179(1), 64-79, (2007). [CrossRef]

[7] Kokten, E.S. and Sel, Ç. A cutting stock problem in the wood products industry: a two-stage solution approach. *International Transactions in Operational Research,* 29(2), 879-907, (2022). [CrossRef]

[8] Saraç, T. and Sağır, M. Mixed-Integer programming models for 1.5-dimensional cutting problem with technical constraints. *Journal of the Faculty of Engineering and Architecture of Gazi University,* 36(1), 291-302, (2021). [CrossRef]

[9] Duysak, E., Dülger, İ., Yıldız, N.S., Gümüş, S. and Saraç, T. Teslim zamanlarinin dikkate alındığı 1,5 boyutlu kesme Ve ana malzeme seçimi problemi için bir matsezgisel algoritma. *Endüstri Mühendisliği,* 33(2), 402-412, (2022). [CrossRef]

[10] Vasilyev, I., Ushakov, A.V., Zhang, D. and Ren, J. Generalized multiple strip packing problem: Formulations, applications, and solution algorithms. *Computers & Industrial Engineering,* 178, 109096, (2023). [CrossRef]

[11] Liu, K., Zhang, H., Wang, C., Li, H., Chen, Y. and Chen, Q. Robust optimization for the two-dimensional strip-packing problem with variable-sized bins. *Mathematics,* 11(23), 4781, (2023). [CrossRef]

[12] Bezerra, V.M.R., Leao, A.A.S., Oliveira, J.F. and Santos, M.O. Models for the two-dimensional level strip packing problem-a review and a computational evaluation. *Journal of the Operational Research Society,* 71(4), 606–627, (2020). [CrossRef]

[13] Wäscher, G., Haußner, H. and Schumann, H. An improved typology of cutting and packing problems. *European Journal of Operational Research,* 183(3), 1109-1130, (2007). [CrossRef]

[14] Sugi, M., Shiomi, Y., Okubo, T., Nagai, H., Inoue, K. and Ota, J. Solution of the rectangular strip packing problem considering a 3-stage guillotine cutting constraint with finite slitter blades. *International Journal of Automation Technology,* 14(3), 447-458, (2020). [CrossRef]

[15] Cintra, G.F., Miyazawa, F.K., Wakabayashi, Y. and Xavier, E.C. Algorithms for two-dimensional cutting stock and strip packing problems using dynamic programming and column generation. *European Journal of Operational Research,* 191(1), 61-85, (2008). [CrossRef]

[16] Bettinelli, A., Ceselli, A. and Righini, G. A branch-and-price algorithm for the two-dimensional level strip packing problem. *4OR,* 6, 361-374, (2008). [CrossRef]

[17] Cui, Y.P., Zhou, Y. and Cui, Y. Triple-solution approach for the strip packing problem with two-staged patterns. *Journal of Combinatorial Optimization,* 34, 588-604, (2017). [CrossRef]

[18] Bertoli, F., Kilby, P. and Urli, T. A column-generation-based approach to fleet design problems mixing owned and hired vehicles. *International Transactions in Operational Research,* 27(2), 899-923, (2020). [CrossRef]

[19] Kamran, M.A., Karimi, B. and Dellaert, N. A column-generation-heuristic-based benders' decomposition for solving adaptive allocation scheduling of patients in operating rooms. *Computers & Industrial Engineering,* 148, 106698, (2020). [CrossRef]

[20] Faiz, T.I., Vogiatzis, C. and Noor-E-Alam, M. A column generation algorithm for vehicle scheduling and routing problems. *Computers & Industrial Engineering,* 130, 222-236, (2019). [CrossRef]

[21] Changchun, L., Xi, X., Canrong, Z., Qiang, W. and Li, Z. A column generation based distributed scheduling algorithm for multi-mode resource constrained project scheduling problem. *Computers & Industrial Engineering*, 125, 258-278, (2018). [CrossRef]

[22] Kasimbeyli, N., Saraç, T. and Kasimbeyli, R. A two-objective mathematical model without cutting patterns for one-dimensional assortment problems. *Journal of Computational and Applied Mathematics*, 235(16), 4663-4674, (2011). [CrossRef]

Mathematical Modelling and Numerical Simulation with Applications (MMNSA)
(https://dergipark.org.tr/en/pub/mmnsa)

How to cite this article: Sağır, M. & Saraç, T. (2024). Column generation approach for 1.5-dimensional cutting stock problem with technical constraints. *Mathematical Modelling and Numerical Simulation with Applications*, 4(3), 335-350. https://doi.org/10.53391/mmnsa.1492749

Mathematical Modelling and Numerical Simulation with Applications, 2024, 4(3), 351–369

https://dergipark.org.tr/en/pub/mmnsa
ISSN Online: 2791-8564 / Open Access
https://doi.org/10.53391/mmnsa.1406374

RESEARCH PAPER

A multi-step mathematical model-based predictive strategy for software release timing during testing stage

Poonam Panwar [1,‡], **Satish Kumar** [2,‡], **Shakuntala Singla** [3,‡] **and Yeliz Karaca** [4,*,‡]

[1]University School of Computing, Rayat Bahra University, Mohali-140301, India, [2]Faculty of Agriculture, Maharishi Markandeshwar (Deemed to be University), Mullana, Ambala-133207, India, [3]Department of Mathematics and Humanities, MMEC, Maharishi Markandeshwar (Deemed to be University), Mullana, Ambala-133207, India, [4]University of Massachusetts Chan Medical School, Worcester, MA 01655, USA

* Corresponding Author
‡ rana.poonam1@gmail.com (Poonam Panwar); satishrana.biotech@gmail.com (Satish Kumar); shakusingla@gmail.com (Shakuntala Singla); yeliz.karaca@ieee.org (Yeliz Karaca)

Abstract

Mathematically precise modeling is important to be established to accurately examine the quantitative relationship between software testing and software reliability. Software testing process is complex since it is concerned with various factors such as test case execution, defect debugging, tester expertise, test case selection, and so forth. For this reason, it is required to be meticulous in formulating the software testing process in a manner which is mathematically concise. The software release life cycle or sequential release timeline, referring to the process related to the development, testing and distribution of a software product comprises several critical stages, and the length of this particular life cycle reveals variations depending on different factors like the type of product, the intended use of it, industry security, general standards and compliance. One consideration software engineers have is related to the release date of the software so that future commitments about the software's release time can be formulated beforehand. In view of these aspects, a multi-step strategy for predicting software release dates is proposed in the current study along with the following stages: firstly, the proposed technique selects the utmost reliability growth model that very well fits the observed test data halfway through the testing period, and then employs it to forecast the probable date of release. This technique entails approximating the unknown parameters of suitable Software Reliability Growth Models (SRGMs). Finally, the chosen SRGM is used to forecast the release date of the software under test by fitting it to available fault data. The proposed method is straightforward and applied to test on a total of ten actual datasets collected from the literature. The results of the proposed technique reveal that in the majority of the situations, nearly exact approximation of date of release can be made halfway through the testing period. Moreover, the proposed method's performance is also compared to that of a number of previous strategies present in the literature. The outcomes obtained by our study demonstrate that the proposed strategy may be used to forecast the release date of software in practical situations.

Keywords: Nonhomogeneous Poisson process; mathematical prediction modeling; software reliability

model; stochastic processes; error content function; software source code; goodness of fit

AMS 2020 Classification: 60G35; 93E10; 60G55; 60J45; 94B70

1 Introduction

Mathematical modeling, describing a system by a set of equations and variables, is employed for establishing relationships among them, and in control of the system, it has a critical value for the accurate examination of the quantitative relationship between software testing and software reliability. Software testing process, as a complex one, is concerned with various factors such as test case execution, defect debugging, tester expertise, test case selection, and so on. For this reason, it is required to be meticulous in formulating the software testing process in a reliable manner. Computer software is used in practically every facet of human endeavor, and it is of utmost significance to devise, build and test the software appropriately before being released. Software development takes a long time and comes with a substantial amount of financial burden. When software is developed, it is thoroughly tested before being released to ensure that it is bug-free and hence trustworthy. In reality, reliability is the most crucial characteristic for a well-designed software application. Accordingly, a software reliability model indicates the form of a random process defining the behavior of software failures to time, and these models have emerged as more understanding has become a requisite to examine the features of the way and reason software fails, with an attempt to quantify software reliability. Musa and Okumoto [1] defined reliability of any software application as the likelihood of operation with no failures in any given environment for a specific amount of time. In practice, project managers find it challenging to assess software reliability. A variety of Software Reliability Growth Models (SRGMs) has been proposed since the early 1970s [1–4] for the evaluation of reliability growth of systems throughout software developments specially during the completing and testing periods of the software concerned. The number of expected failures within a certain time period is a widely accepted indicator for assessing a product's reliability. Failures are the result of software code faults, and even a single flaw can result in several failures. Furthermore, software engineers are often interested in projecting the software's expected release date while it is still in development so that future delivery commitments can be made timely. With this in mind, software engineers used specialized development approaches to reduce the overall risk and support rapid change. As a result, there is a significant issue in predicting the likely release date of software in development with sufficient accuracy. Existing techniques, such as a cumulative flow methodology, release backlogs are used in software development to anticipate and set release dates; however, because this does not take software reliability into account when projecting release dates, there is a risk that software at the predicted release date may be unreliable. Software system availability depends on reliability, and SRGMs can be used to determine whether sufficient defects have been eliminated in order to release the software.

A software economic policy was developed by Huang et al. [5] offering a thorough examination of software based on test efficiency and cost. Project managers may also benefit from the strategy by using it to assist them decide when to finish testing in preparation for market release. A SRGM that takes into account the impact of imprecise fault debugging and error creation was proposed by Kapur et al. [6]. The suggested model is used to define the release time problem, which minimizes the estimated cost while meeting the minimal dependability level that must be met by the release time. By creating a software cost model with a risk component, Singh

➤ **Received:** 29.12.2023 ➤ **Revised:** 14.09.2024 ➤ **Accepted:** 25.09.2024 ➤ **Published:** 30.09.2024

and Kumar [7] provided a technique for determining when to conclude the testing phase and deliver the program to the end user. They addressed the question of how to determine when to finish testing and release the product. A method for building a software reliability growth model based on the Non-Homogeneous Poisson Process was presented by Quadri et al. [8]. Despite the fact that several testing-effort functions based on the non-homogeneous Poisson process (NHPP) have been developed for the software reliability growth model. They examined the scenario in which the Generalized Exponential Distribution (GED) describes the time-dependent behaviors of testing-effort expenditures. The NHPP is used to create SRGMs, which include the (GED) testing-effort spent during the software-testing phase. A mathematical modeling approach for numerous software product releases is proposed by Kapur et al. [9]. Their suggested model uses a Cobb Douglas production function to simulate the failure process using a software reliability growth model, accounting for the combined effects of schedule pressure and resource constraints. A technique for choosing SRGMs to forecast the overall amount of errors in software was suggested by Panwar and Lal [10]. To assess how effectively the technique predicts the predicted total number of software failures, it is used to a case study consisting of three datasets of defect reports from system testing of three versions of a big medical record system. In order to offer more accurate predictions, Choudhary and Baghel [11] provide an efficient software dependability modeling based on Cuckoo Search optimization, Ensemble Empirical Mode Decomposition, and Autoregressive Integrated Moving Average (ARIMA) modeling of time series. Panwar and Kaur [12] suggest a method for estimating the number of software defects that remain by utilizing both perfect and imperfect software reliability growth models. A software metrics-based technique for software reliability prediction is presented by Shi et al. [13]. Metric measurement outcomes are linked to quantitative reliability forecasts by taking into account defect data and operational conditions.

Although numerous models have been presented researched, and implemented, the majority of them are failure count models that do not account for the many development scenarios like developers team structure or a substantial reduction in development time. As a result, standard models are unable to reliably estimate the release dates. Hence, in the present study, a method for obtaining reliability estimations is proposed which can determine the product's likely release date during the product testing stage. Previously, only basic SRGMs were employed in the studies, however the proposed method, as a novelty, suggests that NHPP SRGMs can model the circumstances more practically. The objective of this study is to respond to the following questions:

- Is it possible to forecast software release dates using NHPP SRGMs?
- Is our proposed method more accurate than the previously proposed methods in terms of predicting the release dates?

The following can be put forth among the contributions to the proposed work.

- A multi-step strategy for predicting software release time by dividing development time into various degrees of testing.
- A method for estimating the release date forecast precision by specifying a desired level of confidence.
- An evaluation result demonstrating that our prediction method outperforms previous models.

The following is a breakdown of the paper's structure. Section 2 provides a basic introduction to SRGMs. Section 3 describes the suggested strategy, which is then tested on 10 real datasets in Section 4 to see how effective it is. Finally, in Section 5, conclusions based on the current study along with the future directions are drawn and discussed.

2 Non-homogeneous Poisson process software reliability growth models

NHPP class of SRGMs has been broadly used in the literature [14–18]. These models use test data from failure history, predicting the software application's projected total number of faults and forthcoming reliability. This class of models can also be used to approximate the sum of remaining software faults and the amount of time period it will take to identify these. Mean value function is used is each model of this category, which is dependent on diverse conventions about the equations of error content and the defect finding rate. The NHPP SRGMs models are commonly categorized as follows based on the patterns of their mean value functions, which are the concave models and S-shaped models.

The defect debugging process is depicted naturally in concave models, in which the faults discovered accumulate as the testing activity proceeds, and the aggregated faults propagates at a gradual pace before approaching asymptotic behaviour as the software behavior stabilizes. On the other side, S-shaped curve models show a steady fault discovery at the beginning of the debugging stage [19]. As testing progresses, the rate of defect identification increases, and the cumulative defects curve finally approaches asymptotic behavior [20]. This class also distinguishes between finite and infinite failure models. Finite failure models presume that a fault-free product may be developed in the end, as well as an asymptotic methodology to a predictable value. The failure models of infinite class, on the other hand, presume that the count of observed faults is inestimable, implying that the function of mean value is unrestrained. Numerous models similarly imply that whilst correcting existing issues, new bugs may be introduced inadvertently. These are denoted as imperfect debugging models [21]. Five concave, nine S-shaped, and two more models that can perform as a concave otherwise S-shaped are employed in our proposed study.

3 Multi-step mathematical model-based predictive strategy

In the literature, various methods and practices for selecting appropriate SRGM are suggested [22–32]. However, the majority of those are dependent on the particular situation and may not be applied with certainty in all situations. Present study proposes a method for selecting the best SRGM along with using that one to forecast the likely date of release with the intention to make required arrangements and revisions ahead of time to fulfil any deadlines. The procedure is straightforward and has shown to be beneficial in the recent study. It entails choosing an SRGM that almost fits the existing error content and then use it next to forecast the date of software release. The proposed technique demands calculating the unknown variables/parameters of applicable SRGMs before ordering these according to their behavior on observed failure data. Finally, best chosen SRGM is utilized for forecasting the date of release of any software under test. The strategy proposed is not scenario-specific and can be used to any situation. It works in the way whose specific details are provided in the remaining parts of our study.

Estimation of model parameters

NHPP SRGM has some unknown parameters that must be determined from observed test failure data. Maximum Likelihood Estimation (MLE) or Least Squares Estimate (LSE) are the two methods which can be used on the currently available test data, to determine the value of these unknown parameters [33, 34]. The MLE method estimate these parameters by solving a set of simultaneous equations whereas LSE reduces the TSS (total sum of square of variation) between observed and probable faults depending on the hypothetical chosen model. There are also a number of tools available to estimate the value of these unknown parameters like Curve Fitting MATLAB [35] which is based on the LSE technique. Moreover, our individual proficiency has also proved that the LSE provides more appropriate parameter values as contrasted to MLE, allowing the model

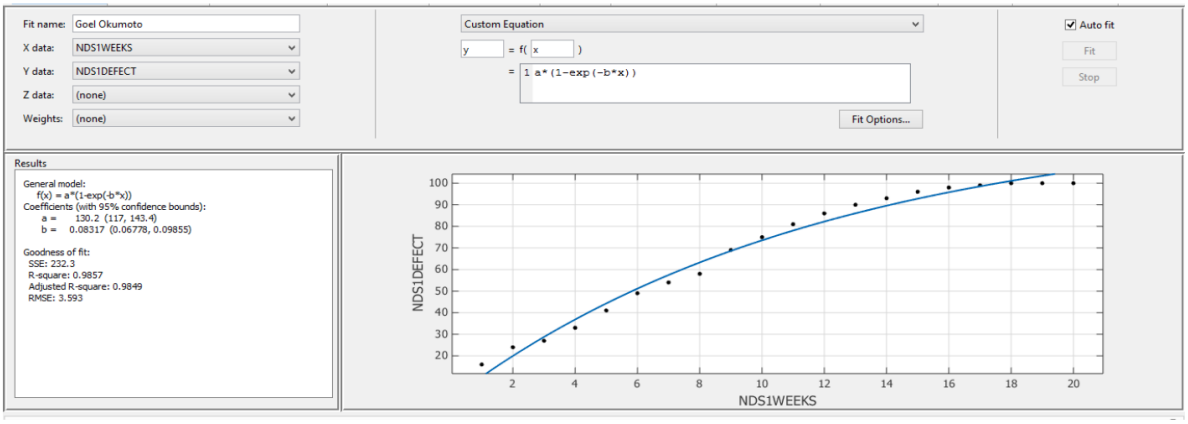

Figure 1. Estimation of unknown parameters by MATLAB curve fitting tool

to better fit the actual data. As a result, we chose to employ the LSE technique for parameter estimation in using MATLAB's curve fitting tool. After analyzing the existing test data, we first determine which models appear to be more suitable for fitting this data, and then calculate the values of RSq and RMSE for each of these SRGMs to determine which one best matches the data. Figure 1 shows how the Curve Fitting tool fits the SRGM to the given test data and computes the values of parameters that are unknown in nature.

Ranking of models

In the second step of proposed technique, a comparison criterion (1) is proposed to compare models realistically in order to examine the efficiency of software reliability growth models employed in the proposed study. Based on our experience, using a vast set of comparison criteria is not necessary, and in most situations, it does not even assure trustworthy forecasts. Hence, we discovered that the subsequent modest criterion may be implemented to rank rival models of software reliability in order to choose an optimal SRGM for more accurate release date predictions.

$$\text{Rank Index} = \frac{1}{2}\left[\frac{RSq_j}{max_j^n(RSq_j)} + \frac{minjn(RMSEj}{RMSEj)}\right]. \tag{1}$$

The relative amount of variation in the actual test data and the test data estimated by the matching SRGM is shown by RSq. The higher the RSq score, the greater variation there is in the actual and estimated test data values. The RSq is computed as the proportion of the residuals sum of squares (SSR) and the total sum of squares (SST). Here, j denotes the number of the SRGM as provided in Table 1. Also, we have

$$RS_q = \frac{SSR}{SSQ}, \tag{2}$$

where SSR is defined as

$$SSR = \left(\sum_{i=1}^{n} \widehat{m(t_i)} - \sum_{i=1}^{n} \frac{(m(t_i))}{n}\right)^2. \tag{3}$$

The sum of squares about the mean, or SST, is defined as: In (3) and (4) i signifies the test period and $m(t_i)$ the real number of faults discovered up to time t_i. Next $m(t_i)$ represents the calculated

value of cumulative failures until time ti as determined by SRGM under study and $m(t)$ represent the mean value of reported total failures. The regression's fit standard error is denoted by $RMSE$ in (1). It is a calculation of the random component's standard deviation, and it is defined as:

$$RMSE = \sqrt{MSE}. \tag{4}$$

$MSE = SSE/v$ is the "mean square error" or "the residual mean square" whereas SSE is the aggregate divergence of the genuine measured faults from the approximated of faults using SRGM. SSE can be calculated by using equation $SSE = \sum_{i=1}^{n} (m(t_i) - (mt_i)^2$ and v is the degree of freedom. The number of fitted coefficients m subtracted from the total count of response values n is the degree of freedom. All competing models' rank index values are obtained in (1), and next they are ordered in increasing sequence of these values. The model with the highest rank index value receives rank 1. If it results in a draw (any two or more models have identical values of rank index), they are together regarded to be of same rank. The most appropriate model that best captures the behavior of the test data is model ranked one.

Forecasting the release date

In the next step, using the chosen model and the error content function $(a(t))$ of the selected rank 1 SRGM, we estimate the total number of predicted errors in the software. The total number of errors that may occur in software over its lifetime is the value of the error content function. The error content function $(a(t))$ of each model is given in Table 1. The following equation is used to measure the software's reliability over time using the mean value function and error content function stated in Table 1.

$$R(t) = m(t)/a(t). \tag{5}$$

The conditional reliability $(R(s|t))$ in interval $(t, t+s)$ is estimated using

$$R(s|t) = e^{[m(t+s)-m(t)]}. \tag{6}$$

The likelihood that the obtained reliability at any point of time t may not alter in this gap is given by conditional reliability $(t, t+s)$. By increasing the value of time t stepwise in Eq. (5) and Eq. (6) the future prediction about reliability and conditional reliability is done. We increase the value of t by 1 in each step and finally time of release t is considered the time when $R(t) \geq 0.960$ and $R(s|t) \geq 0.500$ for $s = 1$ and $R(s|t) \geq 0.350$ for $s = 2$.

The proposed method with its relevant stages

- Estimate the length of the testing period when the program is ready for testing and continue testing until at least 50% of the testing time has passed.
- Choose the acceptable models from Table 1 that should fit the data into the best of your ability.
- Calculate the unknown parameters of the selected models using Section 3, Then use Section 3 to choose the model with the highest rank.
- This model is then used to calculate $R(t)$ and $R(s|t)$.
- Take this as the time of release if $R(t)$ which meets the necessary level of reliability and $R(s|t)$ for the next two-time units is acceptable. If the anticipated release date is to be met, adapt the testing infrastructure accordingly. When around 75% of the expected release time has passed, it is often recommended to update the estimations again.

Table 1. SRGMs investigated

No	Model	Category	Mean Value (m(t)) Equation	Remarks
1	Goel-Okumoto (GO) [2]	Concave	$m(t) = a(1-e^{-bt})$, $a(t) = a,\ b(t) = b,$	Known as the exponential growth model
2	Generalized Goel [2]	Concave	$m(t) = a(1-e^{-bt^c})$, $a(t) = a,\ b(t) = b,$	Goodness-of-fit is better than the GO-Model. For $c = 1$, the same as the GO-Model
3	Modified Duane [19]	Concave	$m(t) = a[1-(b/(b+t))^c]$, $a(t) = a,\ b(t) = b,$	Assume independence of failure occurrences
4	Musa-Okumoto [2]	Concave	$m(t) = a\ln(1+bt)$, $a(t) = a,\ b(t) = b,$	Assumes that the severity of failure decreases exponentially as the predicted number of errors increases
5	Yamada Exponential [36]	Concave	$m(t) = a(1-e^{r\alpha}(1-e^{\beta t}))$, $a(t) = a, b(t) = r\alpha\beta e^{-\beta t},$	Make an attempt to account for the time spent testing
6	Gompert [37]	S-Shaped	$m(t) = ake^{-bt}$, $a(t) = a,$ $b(t) = b,$	Estimates the severity of software errors. In addition, it forecasts demand, economic growth, and future population
7	Inflection S-Shaped [38]	S-Shaped	$m(t) = (a(1-e^{bt}))/(1+\beta e^{-bt})$, $a(t) = a,$ $b(t) = b/1+\beta e^{-bt},$	With the GO model, a technical problem is solved. If $k = 0$, the result is the same as GO-Model
8	Logistic Growth [24]	S-Shaped	$m(t) = a/(1+ke^{-bt})$,	Calculates the amount of error in software systems
9	Delayed S-Shaped [36]	Concave	$m(t) = a(1-(1+bt)e^{-bt}$, $a(t) = a,$ $b(t) = (b^2t)/(1+bt),$	The GO model has been modified to become S-shaped
10	Yamada-Imperfect-Debugging Model I [36]	S-Shaped	$m(t) = ab/(\alpha+b)(e^{\alpha t}-e^{bt})$, $a(t) = ae^{\alpha}t,$ $b(t) = b,$	Assumes a constant fault detection rate and an exponential fault content function
11	Yamada-Imperfect-Debugging Model II [36]	S-Shaped	$m(t) = a[1-e^{-bt}][1-\alpha/b] + \alpha at,$ $a(t) = a(1+\alpha t),$ $b(t) = b,$	Assumes constant rate of introduction α and a constant rate of fault detection
12	Yamada-Rayleigh [36]	S-Shaped	$m(t) = a(1-e^{-r\alpha(1-e^{(\beta t^2/2)})})$, $a(t) = a,$ $b(t) = r\alpha\beta te^{-\beta t^2/2},$	Make an effort to report the time spent testing
13	Pham-Zhang-IFD [39]	S-Shaped	$m(t) = a-ae^{-bt}(1+(b+d)t + bdt^2),$ $a(t) = a,$ $b(t) = b,$	Maintains an initial constant function fault count and an imperfect detection rate of fault considering fault introduction phenomenon
14	Zhang-Teng-Pham [40] model (ZT Pham)	S-Shaped	$m(t) = a/(p-\beta)[(1-(1+\alpha)e^{-bt}/1+\alpha e^{-bt})^{(c/b(p-\beta))}]$, $a(t) = \beta(t)m(t),$ $b(t) = c/(1+\alpha e^{-bt}), \beta(t) = \beta,$	Considers a constant rate of fault introduction and a non-decreasing function of fault detection rate
15	Pham-Nordman-Zhang [41] (PNZ Model)	S-Shaped & Concave	$m(t) = (a(1-e^{-bt})(1-\alpha/b) + \alpha at)/(1+\beta e^{-bt})$, $a(t) = a(1+\alpha t),$ $b(t) = b/(1+\beta e^{(}-bt)),$	Considers that the fault detection rate is non-decreasing and the introduction rate is a linear
16	Pham-Zhang model (PZ Model) [40]	S-Shaped & Concave	$m(t) = 1/(1+\beta e^{-bt})$ $((c+a)(1-e^{-bt})$ $-ab/(b-\alpha)(e^{-\alpha t}-e^{-bt}))$, $a(t) = c+a(1-e^{-\alpha t}),$ $b(t) = b/(1+\beta e^{-bt}),$	The exponential rate of introduction is and non-decreasing rate of fault detection

Table 2. Tandom computer software failure (dataset 1)

Time (in weeks)	Processor hours	Faults found	Time (in weeks)	Processor hours	Faults found
1	519	16	11	6539	81
2	968	24	12	7083	86
3	1430	27	13	7487	90
4	1893	33	14	7846	93
5	2490	41	15	8205	96
6	3058	49	16	8564	98
7	3625	54	17	8923	99
8	4422	58	18	9282	100
9	5218	69	19	9641	100
10	5823	75	20	10000	100

4 Implementation on testing data

In this section, the suggested approach is applied on 10 real datasets from the literature [4, 22, 23, 25, 26, 42]. In this study, 16 NHPP SRGMs, which are given in Table 1 are applied on all the datasets. In the same table, the characteristics of these SRGMs are also summarized. The proposed strategy is used at three levels of testing, when 50% of the testing is finished, next after 75% of the testing is ready, and lastly, once the testing of software finished. The presented technique's operation is described in more depth using various examples below.

Example 1 *A dataset (DS1) with 100 observed faults was gathered from the public domain of literature for examination; the dataset is listed in Table 2 and was acquired from a subsection of artifacts for four different Tandem Computers Company software versions. The count of errors was normalized as 0 to 100 to eliminate confidentiality concerns, and the amount of energy consumed was translated correspondingly into the scale (0 to 10,000) [23, 25, 26].*

To evaluate the unknown parameters of SRGMs, LSE approach was utilized for NHPP SRGMs considered under study, with confidence bounds of 95%. The parameters were estimated using MATLAB at time $t = 10$ weeks, as indicated in Section 3; this is when 50% of the testing is completed. Table 3 shows the estimated values of the parameters for each of the 16 models. Following that, using Eqs. (2)-(5), the values of the comparison criteria (RSq and RMSE) presented in this study paper were obtained. Table 4 shows the estimated RSq and RMSE values for dataset 1 with $t = 10$ weeks (i.e. this is the time when almost half of the testing is complete).

The rank index is then determined using (1). The models are next ranked accordingly in descending rank index values based on the value of the derived rank index (i.e. model with the highest value of rank index is allotted rank 1). Table 5 shows the predicted rank index values and model ranking of dataset 1 considering the fault data of ten weeks.

Table 5 further demonstrates that at this stage of testing, when only half of the test data is available, Gompertz has ranked one model. As a result, Gompertz is now utilized to predict software delivery dates utilizing Eqs. (5) and (6). With the given level of reliability and conditional reliability, the projected release time at this stage of testing is 35 weeks. Table 6 shows the estimated value of the release date, reliability, and conditional reliability with this data.

The same process is repeated again when testing has been done up to 15 weeks (i.e., 75% test plan is complete). At this point, the top-ranking model has been identified as logistic growth. Table 6 shows the estimated time of release with conditional reliability and reliability which can be reached upon this day. The method was again repeated using 20 weeks of full test data to get the conditional reliability and reliability values at the factual date of release. Table 6 summarizes all the results. We may deduce from the outcomes of this dataset that predicting the release is doable even when only 50% of the failure data is available. We also tried to see if we could make accurate forecasts sooner than ten weeks. For this, we carried out the

Table 3. Unknown parameter approximation of SRGMs for dataset 1

Model Name	Values
Delayed S-Shaped	$a = 126.8, b = 0.2426$
Generalized Goel	$a = 172.5, b = 0.04078, c = 1.235$
Goel Okumoto	$a = 528, b = 0.01773$
Gompertz	$a = 152.7, b = 0.08441, c = 0.8835$
Inflection S-Shaped	$a = 127.3, b = 0.2412, \beta = 3.524$
Logistic Growth	$a = 104, b = 0.2767, k = 6.371$
Modified Duane	$a = 420.7, b = 27.19, c = 1.206$
Musa Okumoto	$a = 497.8, b = 0.0188$
Pham Zhang IFD	$a = 127.4, b = 0.2414, d = 0.22e-14$
Pham Nordman Zhang (PNZ Model)	$a = 9.163, \alpha = 0.709, b = 21.89, \beta = 0.001809$
Pham Zhang model (PZ Model)	$a = 0.001194, \alpha = 3570, b = 0.2412, \beta = 3.524, c = 127.2$
Yamada Exponential	$a = 300, \alpha = 2.307, \beta = 0.006354, r = 2.361$
Yamada Imperfect Debugging Model 1	$a = 528.1, \alpha = 1.595e-08, b = 0.01773$
Yamada Imperfect Debugging Model II	$a = 8.997, \alpha = 0.7221, b = 49.81$
Yamada Rayleigh	$a = 142.2, \alpha = 1.198, \beta = 0.02026, r = 1.302$
Zeng Teng Pham	$a = 29.91, \alpha = 5.214, b = 0.2286, \beta = 0.6015, c = 0.841,$ $p = 0.8238$

Table 4. Estimation of RSquare and RMSE using ten weeks failure data for dataset 1

Model Name	RSq	RMSE
Delayed S-Shaped	0.903	6.524
Generalized Goel	0.984	2.852
Goel Okumoto	0.972	3.529
Gompertz	0.994	1.707
Inflection S-Shaped	0.972	3.773
Logistic Growth	0.993	1.849
Modified Duane	0.984	2.849
Musa Okumoto	0.974	3.382
Pham Zhang IFD	0.903	6.524
Pham Nordman Zhang (PNZ Model)	0.993	2.001
Pham Zhang model (PZ Model)	0.991	2.515
Yamada Exponential	0.927	6.532
Yamada Imperfect Debugging Model 1	0.975	3.544
Yamada Imperfect Debugging Model II	0.993	1.853
Yamada Rayleigh	0.866	8.860
Zeng Teng Pham	0.995	2.204

computations at seven weeks (about 35% data) also but the results obtained at this stage were not compatible with the later date of prediction.

Example 2 *We used a separate dataset to assess the applicability of the suggested technique to diverse datasets [23]. This failure dataset was compiled out of three versions of a big medical record software with 188 components. Numerous files are included in each component. The package originally comprised of 173 software components. All the three updates have improved the product's functionality. A total of 15 components were added to the three releases. In each release, three to seven new components were included. As a result of the increased capability, some other components were adjusted in all three editions. Table 7 shows the results of applying the proposed approach to release 1 of this dataset. The same step-by-step process was used for this dataset as it was for the SRGM rating and release date prediction in Example 1. Table 8 provides the results, which show that logistic growth is ranked first using the results acquired (1). The same model of logistic growth is ranked 1 in all stages of testing for this dataset. At all three stages, the*

Table 5. SRGMs ranking using rank index for dataset 1 at $t = 10$ weeks

Model Name	Rank Index	Rank
Delayed S-Shaped	0.5848	14
Generalized Goel	0.7939	8
Goel Okumoto	0.7303	11
Gompertz	0.9999	1
Inflection S-Shaped	0.7147	12
Logistic Growth	0.9609	2
Modified Duane	0.7943	7
Musa Okumoto	0.7420	9
Pham Zhang IFD	0.5848	15
PNZ Model	0.9259	4
PZ Model	0.8376	6
Yamada Exponential	0.5968	13
Yamada Imperfect Debugging Model 1	0.7310	10
Yamada Imperfect Debugging Model II	0.9601	3
Yamada Rayleigh	0.5316	16
Zeng Teng Pham	0.8873	5

Table 6. SRGMs ranking using rank index for dataset 1 at $t = 10$ weeks

The dataset as well as the actual release date	Testing data used (in weeks)	Model chosen	Date of expected release (in weeks)	Expected level of reliability $(R(t))$	Conditional reliability $(R(s\|t))$ to be accomplished	
					For $s = 1$	For $s = 2$
(20 weeks)	10	Gompertz	35	0.970	0.570	0.350
	15	Logistic Growth	21	0.980	0.590	0.400
	20	ZT Pham	18	0.980	0.580	0.400

Table 7. Data of a significant medical record system's failures: release-1 (dataset 2)

Weeks	Aggregated failures	Weeks	Aggregated failures
1	28	10	125
2	29	11	139
3	29	12	152
4	29	13	164
5	29	14	164
6	37	15	165
7	63	16	168
8	92	17	170
9	116	18	176

estimated release date is the same. As a result, it can be stated that if the selected model is the same at each step of testing, more accurate predictions about the software release date can be made.

Similarly, eight more datasets from the available literature were used to assess the applicability of the suggested approach. Table 9 shows the anticipated value of release time for all the datasets, as well as to be expected value of conditional reliability and reliability. We have also evaluated the anticipated date of release by our presented technique with the factual date of release and

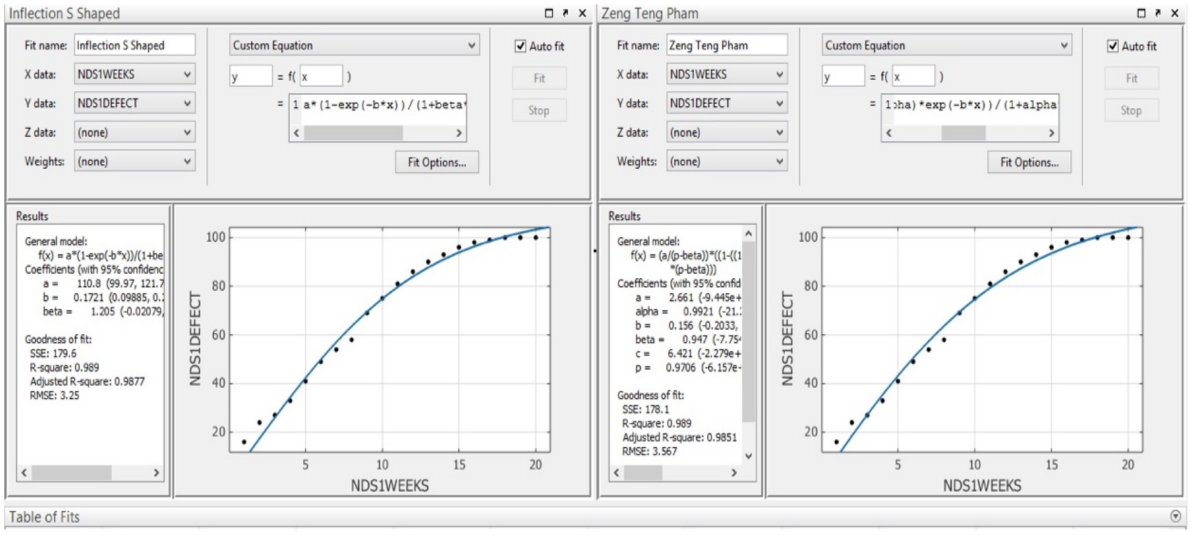

Figure 2. Comparison for dataset 1 using the models identified by presented methodology with the best model considered in existing studies

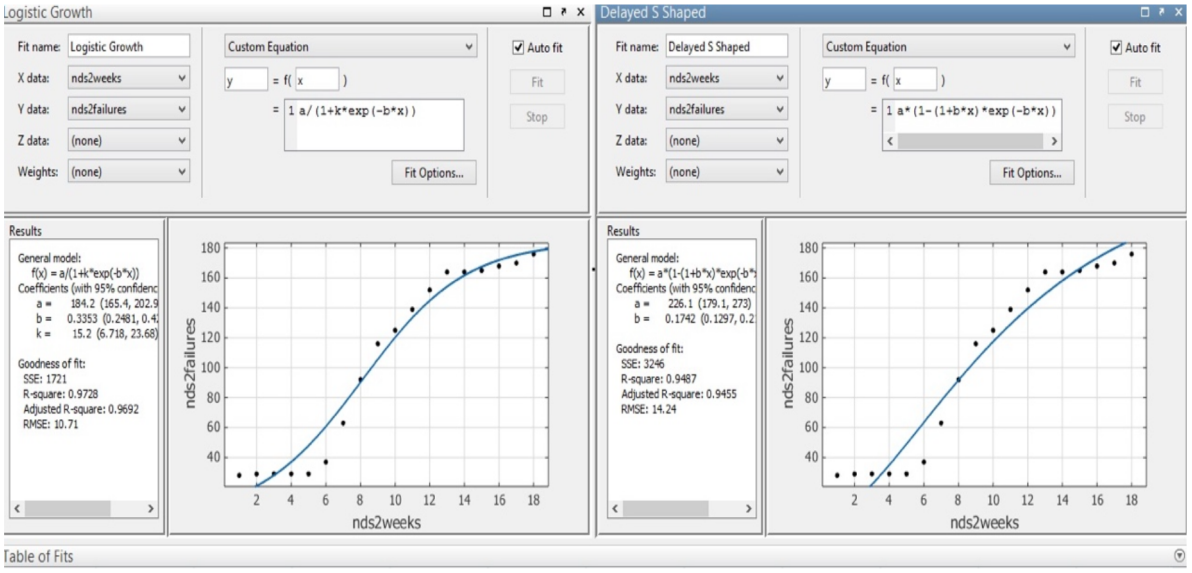

Figure 3. Comparison for dataset 2 using the models identified by presented methodology with the best model considered in existing studies

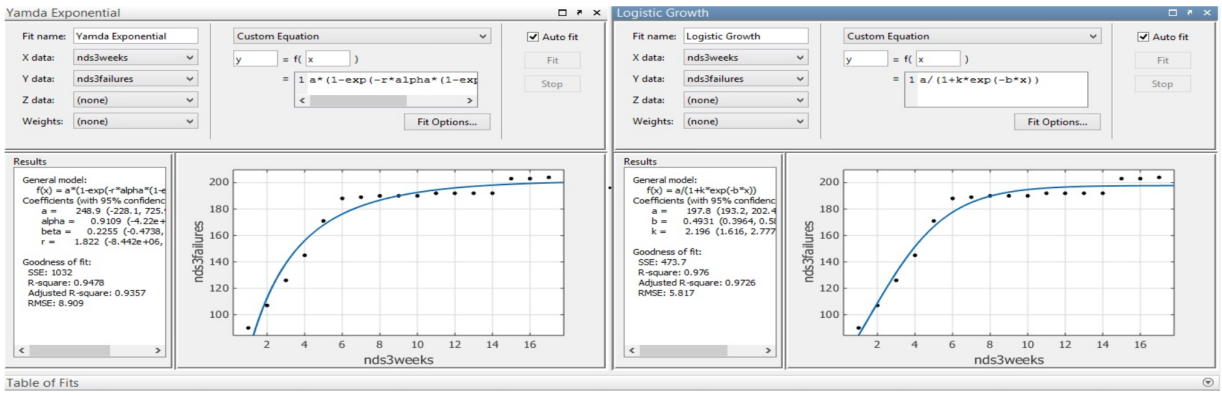

Figure 4. Comparison for dataset 3 using the models identified by presented methodology with the best model considered in existing studies

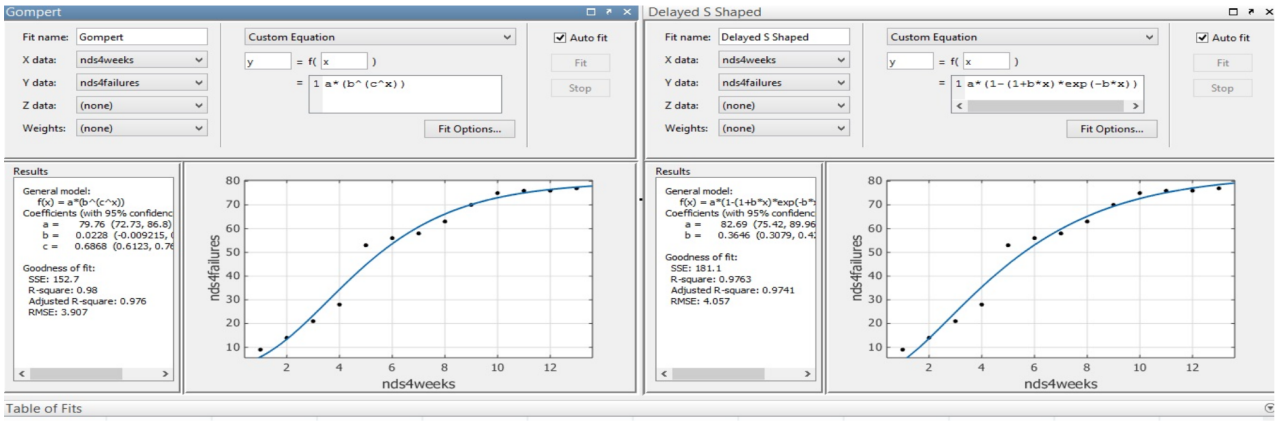

Figure 5. Comparison for dataset 4 using the models identified by presented methodology with the best model considered in existing studies

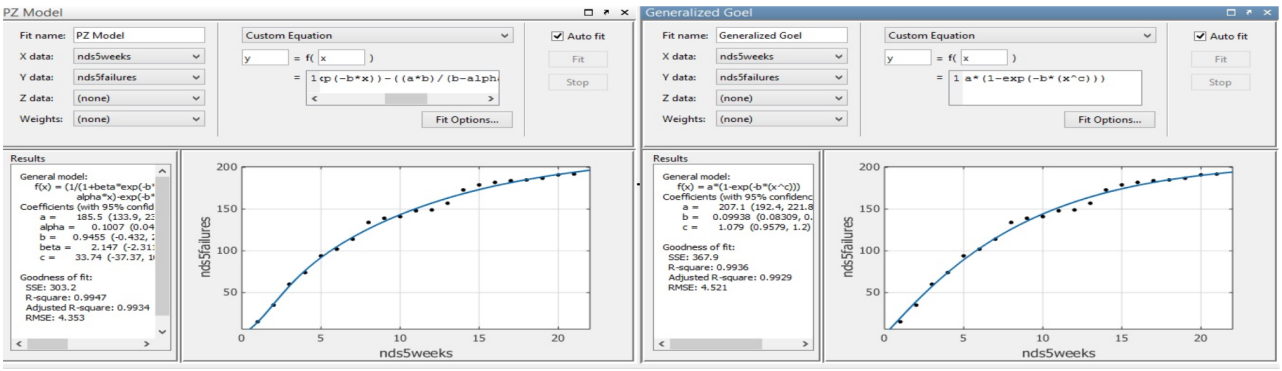

Figure 6. Comparison for dataset 5 using the models identified by presented methodology with the best model considered in existing studies

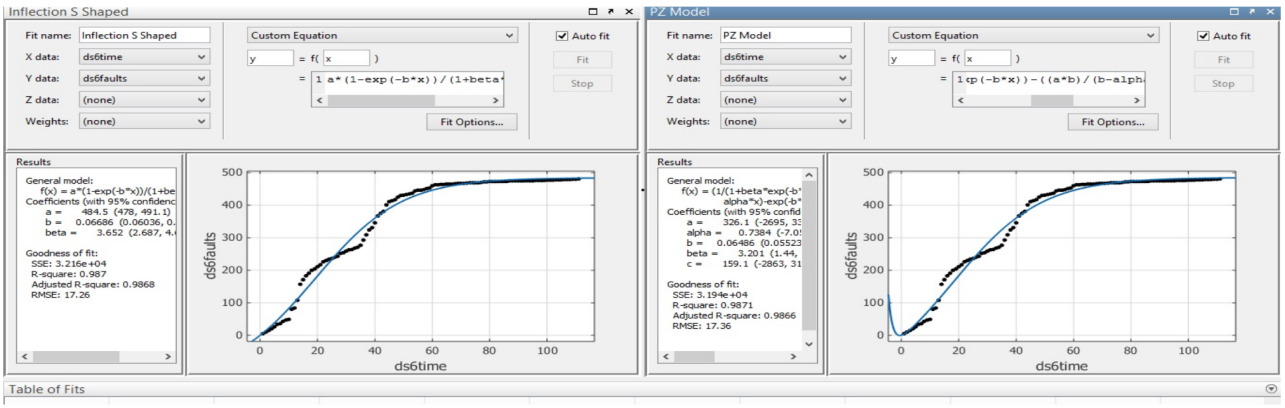

Figure 7. Comparison for dataset 6 using the models identified by presented methodology with the best model considered in existing studies

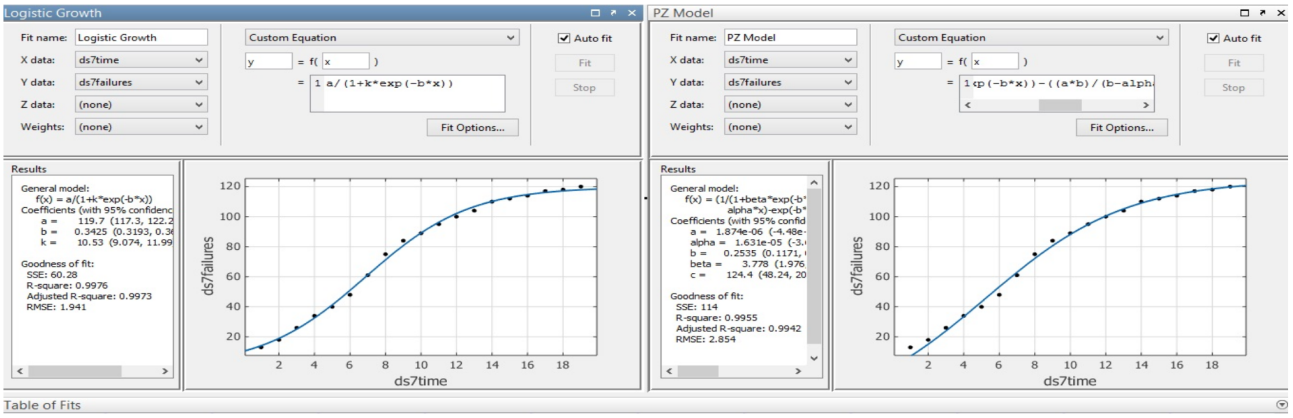

Figure 8. Comparison for dataset 7 using the models identified by presented methodology with the best model considered in existing studies

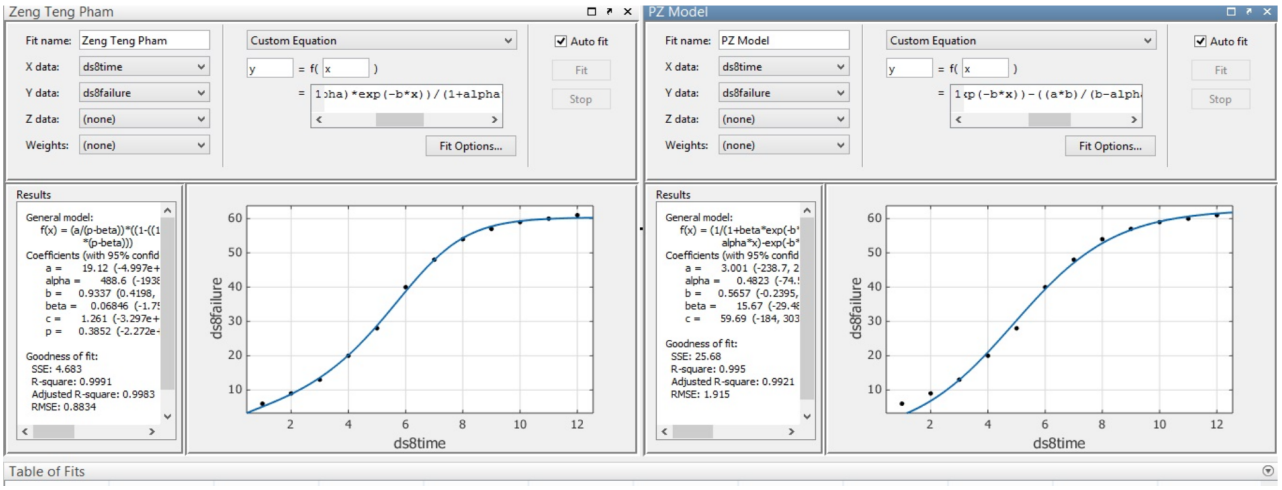

Figure 9. Comparison for dataset 8 using the models identified by presented methodology with the best model considered in existing studies

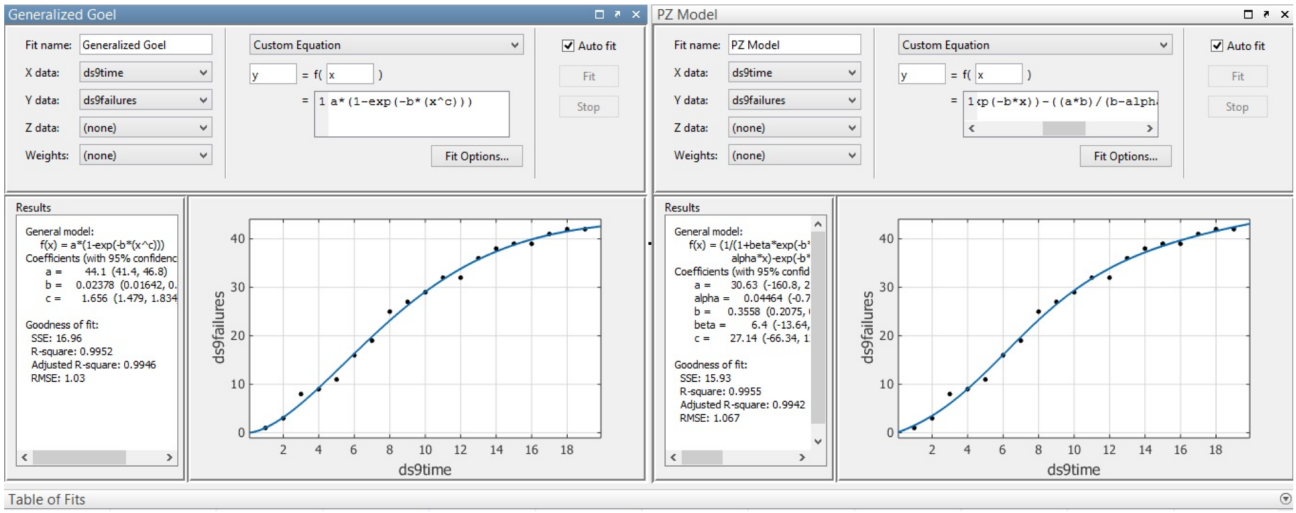

Figure 10. Comparison for dataset 9 using the models identified by presented methodology with the best model considered in existing studies

Table 8. Predicted dataset 2 release time, with expected values of conditional reliability and reliability

The dataset as well as the actual release date	Testing data used (in weeks)	Model chosen	Date of expected release (in weeks)	Expected level of reliability (R(t))	Conditional reliability (R(s | t)) to be accomplished	
					For $s = 1$	For $s = 2$
Dataset 2 (18 weeks)	10	Logistic Growth	24	0.990	0.550	0.350
	15	Logistic Growth	24	0.990	0.690	0.520
	18	Logistic Growth	22	0.990	0.610	0.430

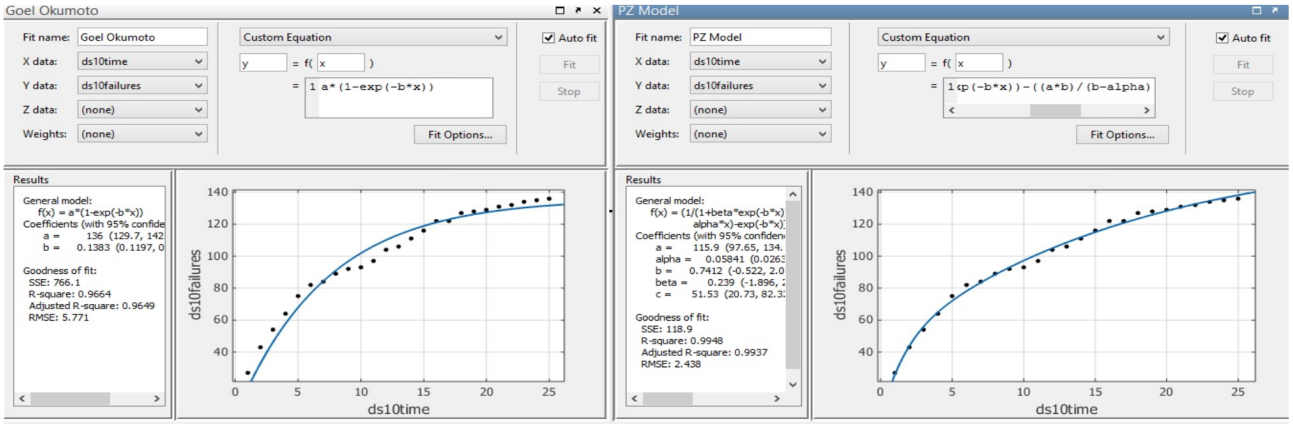

Figure 11. Comparison for dataset 10 using the models identified by presented methodology with the best model considered in existing studies

the estimated date of release by the best models identifies in existing studies for the datasets utilised in current study to evaluate the performance of our proposed method. From Figure 2 to Figure 11 depict the comparison. The findings shown in Figure 11 reveal that with the exception of datasets 3 and 6, our suggested approach can forecast dependability early and timely virtually in all circumstances.

5 Conclusions, outcomes and future directions

Formulating the software testing process in a mathematically rigorous manner is important in software testing which acts as a major apparatus for software quality assurance, and this process is known to be complex since it comprises many factors such as test case execution, test case selection, defect debugging, tester's knowledge and experience, and so forth. This study has investigated how to choose the best software reliability model for predicting the most likely release date. Section 3 outlines the proposed strategy, allowing the user to anticipate the expected release date even after nearly half of the estimated test period has passed. We used the proposed approach at various phases of testing (e.g., once 50% of the testing is done, 75% of the testing is accomplished, at the actual release date). Our findings reveal that when the current technique is employed to the test dataset 7 and 50% of the test plan period has passed, the proposed method's anticipated release date is nearly identical to the actual release date. In the case of datasets 1, 2, 4, 5, 7, 8, 9, and 10, the anticipated date of release based on 50% of the data is inside 1 to 2 weeks of the factual release date. The expected date of release for dataset 3 is, however, significantly sooner

Table 9. Anticipated time of release for datasets considered in present work with expected to be attained value of conditional reliability and reliability

Factual date of release (in weeks and dataset)	Prediction time (in weeks)	Selected model	Release date (in weeks)	Expected level of reliability	To be attained conditional reliability For $s = 1$	For $s = 2$
Dataset 1	10	Gompertz	35	0.970	0.570	0.350
(20 weeks)	15	Logistic Growth	21	0.980	0.590	0.400
	20	ZT Pham	18	0.980	0.580	0.400
Dataset 2	10	Logistic Growth	24	0.990	0.550	0.350
(18 weeks)	15	Logistic Growth	24	0.990	0.690	0.520
	18	Logistic Growth	22	0.990	0.610	0.430
Dataset 3	10	ZT Pham	10	1.000	0.900	0.860
(17 weeks)	15	Logistic Growth	11	0.990	0.540	0.370
	17	Logistic Growth	12	0.990	0.640	0.480
Dataset 4	7	Logistic Growth	9	0.980	0.530	0.400
(13 weeks)	14	Gompertz	14	0.980	0.620	0.440
Dataset 5	10	Generalized Goel	19	0.990	0.560	0.360
(21 weeks)	15	Generalized Goel	27	0.980	0.580	0.370
	21	Generalized Goel	30	0.980	0.580	0.360
Dataset 6	55	Generalized Goel	232	0.970	0.590	0.350
(111 weeks)	84	Generalized Goel	90	0.980	0.600	0.370
	111	Inflection S-Shaped	85	0.980	0.620	0.390
Dataset 7	10	Logistic Growth	19	0.990	0.610	0.430
(19 weeks)	15	Logistic Growth	18	0.980	0.560	0.370
	19	Logistic Growth	19	0.980	0.590	0.400
Dataset 8	7	Logistic Growth	14	0.980	0.600	0.440
(12 weeks)	12	ZT Pham	10	0.980	0.740	0.650
Dataset 9	10	Inflection S-Shaped	15	0.980	0.750	0.620
(19 weeks)	15	Delayed S-Shaped	26	0.970	0.770	0.620
	19	Generalized Goel	20	0.960	0.690	0.520
Dataset 10	13	Generalized Goel	23	0.960	0.690	0.520
(25 weeks)	19	Gompertz	25	0.970	0.590	0.380
	25	PZ Model	28	0.990	0.590	0.350

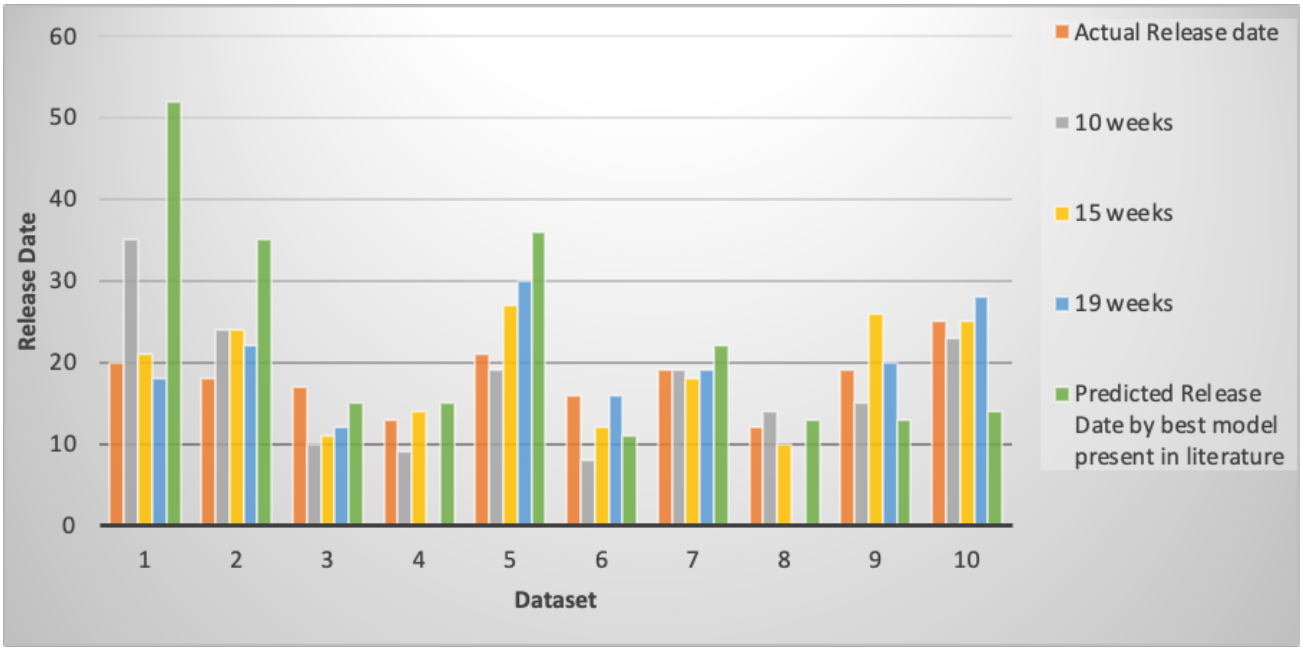

Figure 12. Comparison of the expected release time of the datasets in the proposed study with the actual release date, as well as the best models provided in the literature

than the actual release date. Interestingly, when 50% of the dataset is used to forecast the release date, the estimated date is 232 weeks, which is substantially far ahead than the actual date of 111 weeks. When a likelihood is generated using around 75% of the data, the estimated date of release is once again quite near to the factual release date, and it is dramatically lowered to 90 weeks. Even if all available data is used, the estimated release timeframe is 85 weeks. This indicates that testing may have been overdone, or that software adjustments were made in the interim. In all situations, we also tried with lower than 50% of test plan data and found that estimates were not reliable in common. Table 9 and Figure 11 show that when utilizing the proposed method, the anticipated release dates with models picked by us, even when using midway test data, are generally better than the similar outcomes achieved for these datasets when exploring the methods given in literature. Since NHPP SRGMs cannot handle time-dependent variables, the suggested approach is limited to software development circumstances that are time-independent. We intend to change the time-dependence of these models in the future, which will allow us to more exactly anticipate the number of faults found. We also intend to apply the proposed strategy to other software development methodologies, such as agile development. The comparison of the results with those available in literature shows that the proposed approach is able to select a model that fits the present data closely. Therefore, the selected model can be used for future predictions, and the selected models estimates by our proposed method are closer to the actual number of failures found by that time in each case.

Declarations

Use of AI tools

The authors declare that they have not used Artificial Intelligence (AI) tools in the creation of this article.

Data availability statement

There are no external data associated with the manuscript.

Ethical approval (optional)

The authors state that this research complies with ethical standards. This research does not involve either human participants or animals.

Consent for publication

Not applicable

Conflicts of interest

The authors declare that they have no conflict of interest.

Funding

No funding was received for this research.

Author's contributions

All authors have contributed equally to the manuscript. All authors have read and agreed to the published version of the manuscript.

Acknowledgements

Not applicable

Abbreviations

NHPP: Non-Homogeneous Poisson Process; SRGMs: Software Reliability Growth Models; LSE: Least Squared Estimation; GOF: Goodness of Fit; RMSE: Root-Mean-Square Error; RSq: R-Square; SSE: Sum-of-Squared Errors.

References

[1] Musa, J.D. and Okumoto, K. A logarithmic Poisson execution time model for software reliability measurement. In Proceedings, *7th International Conference on Software Engineering*, pp. 230–238, Orlando, Florida, (1984, March).

[2] Goel, A.L. and Okumoto, K. An analysis of recurrent software errors in a real-time control system. In Proceedings, *Proceedings of the 1978 Annual Conference (ACM)*, pp. 496–501, Washington, DC, USA, (1978, December). [CrossRef]

[3] Goel, A.L. Software reliability models: assumptions, limitations, and applicability. *IEEE Transactions on Software Engineering*, SE-11(12), 1411–1423, (1985). [CrossRef]

[4] Bauer, E., Zhang, X. and Kimber, D.A. *Practical System Reliability*. John Wiley & Sons: New Jersey, (2009).

[5] Huang, C.Y. and Lyu, M.R. Optimal release time for software systems considering cost, testing-effort, and test efficiency. *IEEE Transactions on Reliability*, 54(4), 583–591, (2005). [CrossRef]

[6] Kapur, P.K., Gupta, D., Gupta, A. and Jha, P.C. Effect of introduction of fault and imperfect debugging on release time. *Ratio Mathematica*, 18, 62–90, (2008).

[7] Singh, Y. and Kumar, P. Determination of software release instant of three-tier client server software system. *International Journal of Software Engineering*, 1(3), 51–62, (2010).

[8] Quadri, S.M.K., Ahmad, N. and Farooq, S.U. Software reliability growth modeling with generalized exponential testing-effort and optimal software release policy. *Global Journal of Computer Science and Technology*, 11(2), 26-41, (2011).

[9] Kapur, P.K., Pham, H., Aggarwal, A.G. and Kaur, G. Two dimensional multi-release software reliability modeling and optimal release planning. *IEEE Transactions on Reliability,* 61(3), 758–768, (2012). [CrossRef]

[10] Panwar, P. and Lal, A.K. Predicting total number of failures in a software using NHPP software reliability growth models. In Proceedings, *Third International Conference on Soft Computing for Problem Solving (SocProS),* pp. 715–727, New Delhi, India, (2014, December). [CrossRef]

[11] Choudhary, A. and Baghel, A.S. Software reliability prediction using cuckoo search optimization, empirical mode decomposition, and ARIMA model: CS-EEMD-ARIMA based SRGM. *International Journal of Open Source Software and Processes,* 7(4), 39–54, (2016). [CrossRef]

[12] Panwar, P. and Kaur, R. Effect of imperfect debugging on prediction of remaining faults in software. In Proceedings, *Fifth International Conference on Soft Computing for Problem Solving (SocProS)*, pp. 175–185, Uttarakhand, India, (2016, December). [CrossRef]

[13] Shi, Y., Li, M., Arndt, S. and Smidts, C. Metric-based software reliability prediction approach and its application. *Empirical Software Engineering,* 22, 1579–1633, (2017). [CrossRef]

[14] Pandey, S. and Kumar, K. Software fault prediction for imbalanced data: A survey on recent developments. *Procedia Computer Science,* 218, 1815-1824, (2023). [CrossRef]

[15] Luo, H., Xu, L., He, L., Jiang, L. and Long, T. A novel software reliability growth model based on generalized imperfect debugging NHPP framework. *IEEE Access,* 11, 71573-71593, (2023). [CrossRef]

[16] Samal, U., Kushwaha, S. and Kumar, A. A testing-effort based Srgm incorporating imperfect debugging and change point. *Reliability: Theory & Applications*, 18(1), 86-93, (2023). [CrossRef]

[17] Pradhan, V., Kumar, A. and Dhar, J. Modeling multi-release open source software reliability growth process with generalized modified weibull distribution. *Evolving Software Processes: Trends and Future Directions,* 123–133, (2022). [CrossRef]

[18] Quadri, S.M.K., Ahmad, N. and Peer, M.A. Software optimal release policy and reliability growth modeling. In Proceedings, *2nd National Conference on on Computing for Nation Development (INDIACom)*, pp. 423–431, New Delhi, India, (2008).

[19] Kapur, P.K., Pham, H., Anand, S. and Yadav, K. A unified approach for developing software reliability growth models in the presence of imperfect debugging and error generation. *IEEE Transactions on Reliability,* 60(1), 331–340, (2011). [CrossRef]

[20] Huang, C.Y., Lyu, M.R. and Kuo, S.Y. A unified scheme of some nonhomogenous poisson process models for software reliability estimation. *IEEE Transactions on Software Engineering,* 29(3), 261–269, (2003). [CrossRef]

[21] Shatnawi, O. Discrete time NHPP models for software reliability growth phenomenon. *The International Arab Journal of Information Technology,* 6(2), 124-131, (2009).

[22] Wood, A. Software reliability growth models. *Tandem Technical Report,* 96(130056), 900, (1996).

[23] Stringfellow, C. and Andrews, A.A. An empirical method for selecting software reliability growth models. *Empirical Software Engineering,* 7, 319–343, (2002). [CrossRef]

[24] Andersson, C. A replicated empirical study of a selection method for software reliability growth models. *Empirical Software Engineering,* 12, 161–182, (2007). [CrossRef]

[25] Garg, R., Sharma, K., Kumar, R. and Garg, R.K. Performance analysis of software reliability models using matrix method. *International Journal of Computer and Information Engineering,*

5(2), 113-120, (2010).

[26] Sharma, K., Garg, R., Nagpal, C.K. and Garg, R.K. Selection of optimal software reliability growth models using a distance based approach. *IEEE Transactions on Reliability,* 59(2), 266–276, (2010). [CrossRef]

[27] Ullah, N., Morisio, M. and Vetrò, A. Selecting the best reliability model to predict residual defects in open source software. *Computer,* 48(6), 50–58, (2014). [CrossRef]

[28] Kumar, V., Singh, V.B., Garg, A. and Kumar, G. Selection of optimal software reliability growth models: a fuzzy DEA ranking approach. In *Quality, IT and Business Operations,* (pp. 347–357). Singapore: Springer, (2018). [Crossref]

[29] Li, Q. and Pham, H. A generalized software reliability growth model with consideration of the uncertainty of operating environments. *IEEE Access,* 7, 84253–84267, (2019). [CrossRef]

[30] Kumar, V., Saxena, P. and Garg, H. Selection of optimal software reliability growth models using an integrated entropy–Technique for Order Preference by Similarity to an Ideal Solution (TOPSIS) approach. *Mathematical Methods in the Applied Sciences,* 1-21, (2021). [CrossRef]

[31] Asraful Haque, M. and Ahmad, N. Modified Goel-Okumoto software reliability model considering uncertainty parameter. In Proceedings, *Mathematical Modeling, Computational Intelligence Techniques and Renewable Energy (MMCITRE)*, pp. 369–379. Gandhinagar, India, (2022). [CrossRef]

[32] Bibyan, R. and Anand, S. Ranking of multi-release software reliability growth model using weighted distance-based approach. *Optimization Models in Software Reliability,* (pp. 355–373). Singapore, Springer, (2022). [CrossRef]

[33] Shanmugam, L. and Florence, L. A comparison of parameter best estimation method for software reliability models. *International Journal of Software Engineering & Applications,* 3(5), 91-102, (2012). [CrossRef]

[34] Song, K.Y., Chang, I.H. and Lee, S.W. Predictions of MLE and LSE in NHPP Software Reliability Model. *Journal of the Chosun Natural Science,* 6(2), 111–117, (2013). [CrossRef]

[35] The MathWorks, Inc., MATLAB 2022 version 9.12.0 (R2022a), Software, Natick, MA, (2022).

[36] Yamada, S., Tokuno, K. and Osaki, S. Imperfect debugging models with fault introduction rate for software reliability assessment. *International Journal of Systems Science,* 23(12), 2241–2252, (1992). [CrossRef]

[37] Pham, H. *Software Reliability*. Springer Science & Business Media, Singapore, (2000).

[38] Pham, H. *System Software Reliability*. Springer, London, (2007).

[39] Pham, H. and Zhang, X. An NHPP software reliability model and its comparison. *International Journal of Reliability, Quality and Safety Engineering,* 4(03), 269–282, (1997). [CrossRef]

[40] Zhang, X., Teng, X. and Pham, H. Considering fault removal efficiency in software reliability assessment. *IEEE Transactions on Systems, Man, and Cybernetics-Part A: Systems and Humans,* 33(1), 114–120, (2003). [CrossRef]

[41] Pham, H., Nordmann, L. and Zhang, Z. A general imperfect-software-debugging model with S-shaped fault-detection rate. *IEEE Transactions on Reliability,* 48(2), 169–175, (1999). [CrossRef]

[42] Wood, A. Predicting software reliability. *Computer,* 29(11), 69–77, (1996). [CrossRef]

Mathematical Modelling and Numerical Simulation with Applications (MMNSA)
(https://dergipark.org.tr/en/pub/mmnsa)

How to cite this article: Panwar, P., Kumar, S., Singla, S. & Karaca, Y. (2024). A multi-step mathematical model-based predictive strategy for software release timing during testing stage. *Mathematical Modelling and Numerical Simulation with Applications,* 4(3), 351-369. https://doi.org/10.53391/mmnsa.1406374

Mathematical Modelling and Numerical Simulation with Applications, 2024, 4(3), 370–394

https://dergipark.org.tr/en/pub/mmnsa

ISSN Online: 2791-8564 / Open Access

https://doi.org/10.53391/mmnsa.1517843

RESEARCH PAPER

A seismic-risk-based bi-objective stochastic optimization framework for the pre-disaster allocation of earthquake search and rescue units

Nadi Serhan Aydın [1,*,‡]

[1]Department of Industrial Engineering, Faculty of Engineering and Natural Sciences, Istinye University, Sarıyer 34396, Istanbul, Türkiye

* Corresponding Author

‡ serhan.aydin@istinye.edu.tr (Nadi Serhan Aydın)

Abstract

Accurately predicting earthquakes' time, location and size is nearly impossible with today's technology. Severe earthquakes require prompt and effective mobilization of available resources, as the speed of intervention has a direct impact on the number of people rescued alive. This, in turn, calls for a strategic pre-disaster allocation of search and rescue (SAR) units, both teams and equipment, to make the deployment of resources as quick and equitable as possible. In this paper, a seismic risk-based framework is introduced that takes into account distance-based contingencies between cities. This framework is then integrated into a mixed-integer non-linear programming (MINLP) problem for the allocation of SAR units under uncertainty. The two minimization objectives considered are the expected maximum deployment time of different SAR units and the expected mean absolute deviation of the fulfillment rates. We recover the best vulnerability-adjusted routes for each size-location scenario as input to the optimization model using the dynamic programming (DP) approach as part of the broader area of reinforcement learning (RL). The results of the hypothetical example indicate that the comprehensive model is feasible in various risk scenarios and can be used to make allocation-deployment decisions under uncertainty. The results of the sensitivity analysis verify that the model behaves reasonably against changes in selected parameters, namely the number of allowed facilities and weights of individual objectives. Under the assumption that the two objectives are equally important, the model achieves a total deviation of 3.5% from the objectives with an expected maximum dispatch time of 1.1327 hours and an expected mean absolute deviation of 0.01%.

Keywords: Earthquake response; SAR units allocation; mixed-integer nonlinear programming (MINLP); stochastic optimization; dynamic programming

AMS 2020 Classification: 90B06; 90C11; 90C15; 90C39

➤ **Received:** 17.07.2024 ➤ **Revised:** 26.09.2024 ➤ **Accepted:** 29.09.2024 ➤ **Published:** 30.09.2024

1 Background

Disasters due to natural hazards rarely occur, but once they occur, they can cause extreme fatalities and physical damages. World Health Organization (WHO) estimates that, between 1998-2017, earthquakes claimed nearly 750,000 lives worldwide, which is more than 50% of all deaths related to natural disasters [1]. Disaster risk from earthquakes can be mitigated by decreasing both the exposure of the property to active fault zones and its fragility. On the other hand, the effects of SAR on disaster fatality have long been recognised and explored (see, e.g., [2, 3]). That being said, there is also a need for effective pre-disaster allocation of search-and-rescue (SAR) units for the response to the earthquake to be timely and life-saving. It is a well-known fact that the likelihood of finding survivors in any location is inversely related to time [4]. Research has shown that many more victims could survive if medical care in SAR was provided quickly and effectively [5]. With data collected from the China Earthquake Database for 51 earthquakes globally, Figure 1 aims to highlight the difference in SAR efficiency for earthquakes with different scales, where the completion ratio denotes the ratio of cumulative death toll up to the current time to the final death toll. It is clear that larger-scale earthquakes are associated with slower growth in the percentage of victims reached, thus lower SAR efficiency, especially during the *golden 72 hours* into the earthquake's occurrence. This implies that there is an ample room for improving SAR efficiency by making a better use of the available resources. The efficient planning of SAR operations has a significant role in saving lives in the response phase to disasters [6]. To guarantee an adequate and timely response, effective prepositioning of different SAR units to certain locations and in certain quantities is crucial [7].

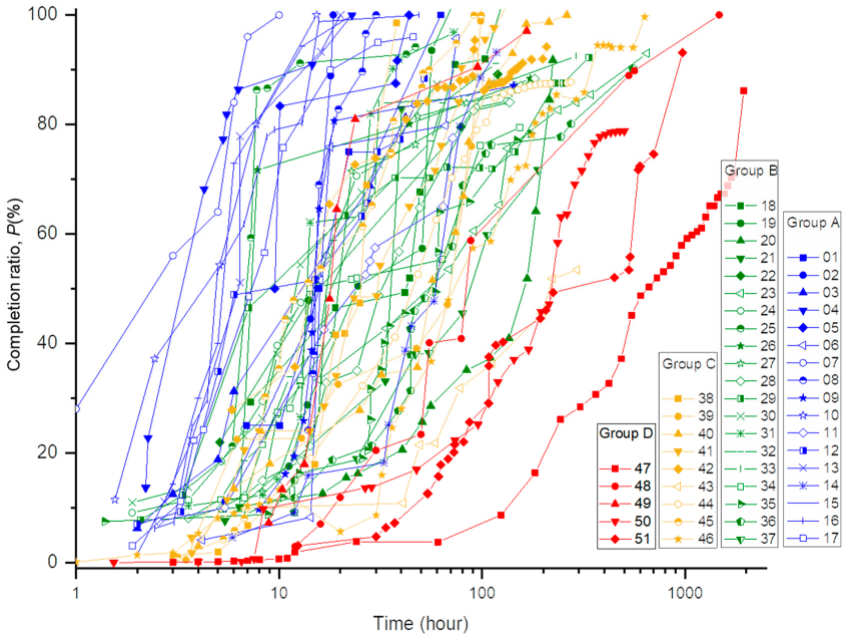

Figure 1. SAR completion ratio curves for the reported death tolls in earthquakes globally [8] (Groups A-D represent earthquakes with death tools < 100, $100 - 1,000$, $1,000 - 10,000$ and $> 10,000$, respectively)

All in all, disaster risk management problems are strongly characterized by random outcomes, which indicates the importance of using mathematical tools that can thoroughly take into account the stochastic nature of these problems [9]. In this study, our primary focus is on the humanitarian losses due to devastating earthquakes, and we classify the latter mainly into the following groups:

- Those captured under and lost lives immediately after the earthquake happens due to collapse

of buildings,
- Those captured under and lost lives after a period since they could not be rescued on time,
- Those rescued from wreckage but could not been hospitalized timely.

As only the losses belonging to the second and third group are preventable with the collective availability of rescue entities (i.e., rescue teams, ambulances, and heavy equipment), the present study seeks to optimize the pre-disaster allocation of SAR units through minimizing two objectives, namely, the expected maximum time it takes to dispatch all needed SAR units and the expected mean percentage deviation of fulfillment rates across all cities.

In this regard, starting from a fault map, the present study focuses on designing a pre-disaster framework for allocating disaster rescue teams and equipment with a view to minimizing both the maximum of the average delivery times associated with each SAR unit type to entire earthquake region and absolute deviation of fulfillment rates across cities. The first objective can be justified by the reasonable assumption that entities will largely be dysfunctional without one another. To give an example, rescue teams without excavators, ambulances without rescue teams, or excavators without ambulances will not be able to perform their functions. Therefore, one entity can start performing its rescue action only after other entity types arrive. This, in turn, calls for the minimization of the longest time period it takes for a specific entity to arrive at the disaster site. The second objective, on the other hand, will ensure that SAR units will not be clustered in one location to prioritize only the city with highest conditional disaster risk.

The study aims to develop an integrated and flexible framework for SAR unit allocation and deployment, combining a seismic risk framework similar to that in [10] with a MINLP model to achieve the joint objective of minimizing the dispatch time of SAR units and variation between response rates. Particularly, the incorporation of seismic risk components and consideration of conditional damage on infrastructure to calculate shortest routes constitute significant research gaps that the present study seeks to address. The rest of the study is organized as follows: Section 2 offers a summary of the related literature. Section 3 provides the details of the risk-based model, including the seismic hazard framework as well as the DP model for recovering vulnerability-adjusted shortest routes and the main MINLP model. Section 4 presents a numerical example on the comprehensive model introduced in Section 3. In Section 5, we give results and the related discussion. Section 6 then concludes.

2 Related literature

The literature on planning the allocation and displacement of earthquake SAR units is broad and focuses on a variety of methods ranging from mixed integer programming (MIP) to stochastic programming and meta-heuristics. Fairly comprehensive reviews of the literature on the use of optimization methods in disaster response are presented, e.g., in [11–13]. We refer the interested reader to these studies.

Stochastic programming

Authors such as, but not limited to, [14–18] presented stochastic programming (SP) models, some of which are multi-stage. For example, [14] applied multi-stage SP for deploying urban search and rescue teams with a view to maximizing the total expected number of people rescued. To make the model more realistic, the likelihood of survival is assumed to diminish over time. Using a two-stage model, [15] sought to minimize the total cost of facility location, inventory holding, transportation and shortage in the context of a humanitarian relief problem. [18] proposed a tri-objective model for pre-and post-earthquake decisions, whereas a novel multi-objective particle swarm optimization (PSO) algorithm was used for solving the model. [17] introduced a stochastic

multi-objective mixed-integer mathematical programming logistic distribution and evacuation planning during earthquake. [19] used a stochastic modeling framework to incorporate various uncertainties such as facility damage and casualty losses as a function of the magnitude of the earthquake, and developed an evolutionary optimization *heuristic* aided by an innovative mixed integer programming (MIP) model that was used to initialize the algorithm. The model was showcased with an application to a region that is prone to earthquakes.

Integer programming

Some other authors like [20–22] opted for pure integer programming (IP) models —linear or non-linear— to tackle the allocation problem. [21] proposed an integer nonlinear multi-objective, multi-period, multi-commodity model to minimize the travel time and total cost and increases reliability of the routes from distribution centers. [20] employed a multi-objective integer nonlinear programming model for assigning rescue teams to disaster sites. The model aimed to minimize the maximum arrival time of all rescue teams to the affected areas and, at the same time, maximize the satisfaction of rescue teams for their assignments. Methods such as NSGA-II, C-METRIC and fuzzy logic were then used to solve the model. The model was then applied to a real earthquake event. [23] combined simulation with a two-phase IP model whereby the first phase aimed to minimize the total distance to be covered for distributing relief supplies by determining the optimal amount of these supplies each neighborhood sent and/or received and, the second phase, to minimize the total number of facilities. [24] proposed a two-stage robust scenario-based optimization problem to facilitate decisions regarding, inter alia, suitable locations for shelters, the optimal route for evacuating people, total rescue time, required budget. NSGA-II was proposed as the solution method. [25] designed a bi-objective robust mixed-integer linear programming (MILP) model for rescue units' allocation and scheduling also by considering the learning feature of rescue units. [6] offered a robust decision support framework for post-earthquake planning SAR resource deployment. In this regard, a two-stage MIP-based decomposition approach was proposed where the first phase performs the allocation of SAR units for maximizing fair and effective demand coverage and the second phase deals with the routing of resources with the aim of minimizing the weighted sum of fulfillment times. [26] developed a decision support model, namely, a MINLP, that minimizes the sum of completion times of incidents weighted by their severity and compared several *heuristics* and *meta-heuristics*.

Other modelling approaches

In [27], a dynamic combinatorial optimization model was introduced to find the best assignment of available resources to operational areas, thereby minimizing the total number of fatalities. First three days after an earthquake takes place were considered to be essential to the success of relief efforts. *Heuristics*, namely, Simulated Annealing (SA) and Tabu Search (TS), were used to solve the model. [28] presented a simulation-based approach for probabilistic modelling to improve post-disaster relief and recovery operations.

Incorporating a seismic-risk model

[10] presented a risk-based approach that incorporates hazard, exposure and vulnerability data, for the pre-positioning of relief resources in appropriate locations. Again, a MILP model used in the study aimed to allocate assets to the locations with the highest levels of risk and then minimize the residual risk. Applying the model on 87 counties Wyoming and Colorado, US, authors reported an at least 33% improvement in residual risk when compared to historical allocations. [7] proposed a two-phase framework based on a compound stochastic process that models' disaster attributes

such as occurrence time, intensity and severity. [29] developed a machine learning framework to predict the casualty rate and direct economic loss induced by earthquakes. They found earthquake magnitude, position, and population density to be the leading indicators for loss prediction.
Table 1-Table 2 summarize the relevant literature in a tabular format and in comparison with the present work. Against this background, methodological as well as managerial contributions of the current study can be outlined as follows. Unlike the majority of the previous studies, this paper:

- Presents an integrated and flexible approach that can be adapted to various hazard / fragility / exposure scenarios. Yet, the model's ability to adapt is partly undermined by
- Links the resource allocation and dispatching problem to a seismic risk modelling framework. This aspect is missing from a vast majority of the studies reviewed.
- Incorporates vulnerability-adjusted shortest routes into the problem for more realistic resource allocation. This is achieved through identifying post-disaster optimal routes for each possible scenario through dynamic programming.
- Helps policymakers make more equitable earthquake dispatchment decisions by understanding its marginal impact on the speed of dispatchment. This aspect is also usually omitted in the existing literature.

3 Model description

In this paper, we apply a seismic-risk-based stochastic bi-objective pre-disaster resource allocation framework modelled as a mixed-integer non-linear programming (MINLP) model, starting from the formulation of a seismic hazard framework and incorporating the vulnerability of cities through fragility curves. The framework deals with the question of how the available SAR resources should be located throughout an earthquake zone, with a view to minimizing not only the expected maximum time it takes for each SAR unit type to be dispatched to the cities affected but also the expected mean absolute deviation of fulfillment rates across cities.
More specifically, we present a stochastic resource allocation model that takes the map of existing fault lines on an IxJ grid, with their hazard (i.e., probability) of producing an earthquake with a certain demand parameter g in the planning period (e.g., 10 years) as input and decides on the optimal allocation of SAR units to facilities and dispatch of these units to earthquake zones based on the realized scenarios, and taking into account their post-earthquake accessibilities which will be affected by potential damages in the transportation infrastructure.
SAR units considered in this study consist of 4 types: rescue teams, excavators or bulldozers, trucks, and ambulances. These units are needed to make the first intervention in any earthquake rescue operation. As explained later, the number of available units from each type k will be set to the conditionally expected number of collapsed buildings (i.e., conditional risk of disaster) provided that an earthquake occurs, multiplied by a factor α_k that determines the quantity of equipment needed per collapsed building.
We start by introducing fault zones $z \in \mathcal{Z}$ where fault zone z has n_z fault segments, each with a city on it. A fault segment will be activated during a seismic event and cause an earthquake with a peak ground acceleration (PGA) value $g \in \mathcal{G}$.[1] Each segment on a fault zone is assumed to have even probability of being epicenter to an earthquake. When an earthquake occurs, it is known that the *hazard* of natural disaster is transformed into the *risk* of environmental / economic / social disaster through vulnerability (or fragility) of cities and property stock's level of exposure. Fragility curves, in this regard, are widely used to associate the demand parameter of the earthquake with the

1 ground motion, of which PGA is a measure, is argued to be related more closely to the level of damage to buildings and infrastructure in an earthquake, rather than the magnitude of the earthquake itself.

Table 1. Tabular literature and present study

Citation	Disaster phase	Optimization model	Uncertainty handling	Seismic model	Decision	Objective	Solution method/tool	Case study / example
This study	Pre/post	Stochastic programming model (nonlinear)	Stochastic	Yes	Locate SAR facilities and dispatch SAR units	Minimize maximum dispatch time; minimize mean absolute deviation between fulfillment rates	Sample Average Approximation	Numerical
[24]	Post	Two-stage multi-objective multi-period robust scenario-based optimization model	Robust opt.	None	Locate temporary shelters and assign injured people to the shelters	Minimize time and the cost of the relief operation in various scenarios	NSGA-II	Real (Tehran, Iran)
[6]	Post	Two-stage MILP model	Robust opt.	None	Robust allocation and routing of search and rescue resources	Maximize the demand coverage for the district with the lowest coverage score (minimize the gap between coverage scores)	Direct	Scenario (Tehran, Iran)
[30]	Pre	Scenario-based stochastic program (non-linear)	Stochastic	None	Storage facility location and material prepositioning decisions (pre-disaster) and service allocation (post-disaster)	Minimize total system costs across all scenarios (facility set-up cost, material prepositioning cost, transportation cost, and victims' deprivation cost)	Direct	Numerical (US)
[17]	Pre/post	Stochastic multi-objective mixed-integer mathematical programming	Stochastic	None	Location of distribution and care centers, amount and distribution of commodities	Minimize expected value of maximum weighted percentage of untreated injured people	Chance constraint; epsilon-constraint, NSGA-II	Real (Tahran, Iran)
[25]	Post	Bi-objective mixed-integer linear programming (MILP) model	Robust opt.	None	Allocating and scheduling disaster rescue units	Minimize total weighted time to complete all the rescue operations; minimize the total weighted delay in all the rescue operations	Multi-choice goal programming	Mazandaran, Iran
[10]	Pre	Mixed-integer programming model (linear)	Probabilistic	Yes	Pre-positioning of relief resources in appropriate locations	Minimize the sum of the residual risk values across the entire overall region	Direct	Colorado /Wyoming

Table 2. Tabular literature and present study (cont'd)

[31]	Pre, post	Bi-level stochastic optimization model	Stochastic	None	budget allocation for improving the efficiency of the transportation network in pre- and post-disaster	Minimize the overall network travel time; minimize the expected number of casualties	Particle Swarm Optimization (PSO)	Numerical
[7]	Pre	Two-stage stochastic programming model	Stochastic	Yes	Location, number and capacity of distribution centres, and quantity of emergency items to keep	Minimize total transportation and procurement costs; minimize total penalty associated with satisfying demands	Monte Carlo, Sample Average Approximation	North Carolina, US
[21]	Post	Integer nonlinear multi-objective, multi-period, multi-commodity model	None	None	Locate distribution centers for timely distribution of relief, vehicles routing and emergency roadway repair operations	Minimize maximum vehicle route traveling time; minimize total cost; maximize minimum reliability of route	NSGA-II, MOPSO	Test problems
[20]	Post	Multi-objective multistage integer nonlinear programming model	None	None	Emergency rescue team assignment in the disaster chain	Minimize maximum arrival time of all rescue teams to affected areas; maximize satisfaction of rescue teams assignment	NSGA-II, C-METRIC and fuzzy logic	Wenchuan, China
[18]	Pre, post	Three-objective stochastic programming model	Stochastic	None	Numbers and locations of distribution centres, stocking levels of relief items, commodity flow amounts	Maximize total expected demand coverage; minimize total expected cost; minimize difference in satisfaction rates	MOPSO, NSGA-II	Tehran, Iran
[19]	Pre	Stochastic optimization model	Stochastic	No	Location and capacity of distribution centers	Minimize total expected costs (facilities, supplies and fatalities) by determining the capacity and location of DCs	MIP (initial solution) and evolutionary heuristics	Los Angeles, California, US
[22]	Pre	Mixed-integer programming (MIP) model / network flow model	None	None	Locate and allocate temporary distribution centers in different time periods	Minimize logistics and penalty costs	Direct	South Carolina, US

conditional probability of a certain damage state (e.g., total damage or collapse) occurring.
As stated earlier, the objective of our model is to minimize the preventable humanitarian losses through the optimal allocation of SAR units to have them timely and equitably dispatched to disaster sites. As the preventable losses increases with time due to lack of SAR units and as different types of units have to work together (*inter-dependence*), our objective of *timeliness* will be based on shortening the arrival time of the latest-arriving SAR unit type.
Severe earthquakes are extremely rare events yet with huge conditional impact. One challenge for policymakers is therefore to decide on the quantity of SAR units to be kept available at SAR facilities. A conservative but unrealistic strategy is to make available the amount of equipment that is adequate for the worst-case size-location scenario assuming that it will materialize. An alternative yet opposite approach would be based on the unconditional risk of disaster. A flowchart of the modelling methodology followed in this paper in presented in Figure 2. We first introduce a seismic risk methodology based on hazard, vulnerability and exposure maps. This framework provides conditional risk values (expected demand for SAR units) as an input to the bi-objective optimization model, whereas the conditional shortest routes are served by the DP model for each earthquake scenario and city pair. The optimization model is then solved using the weighted sum approach and for different values of the selected parameters.

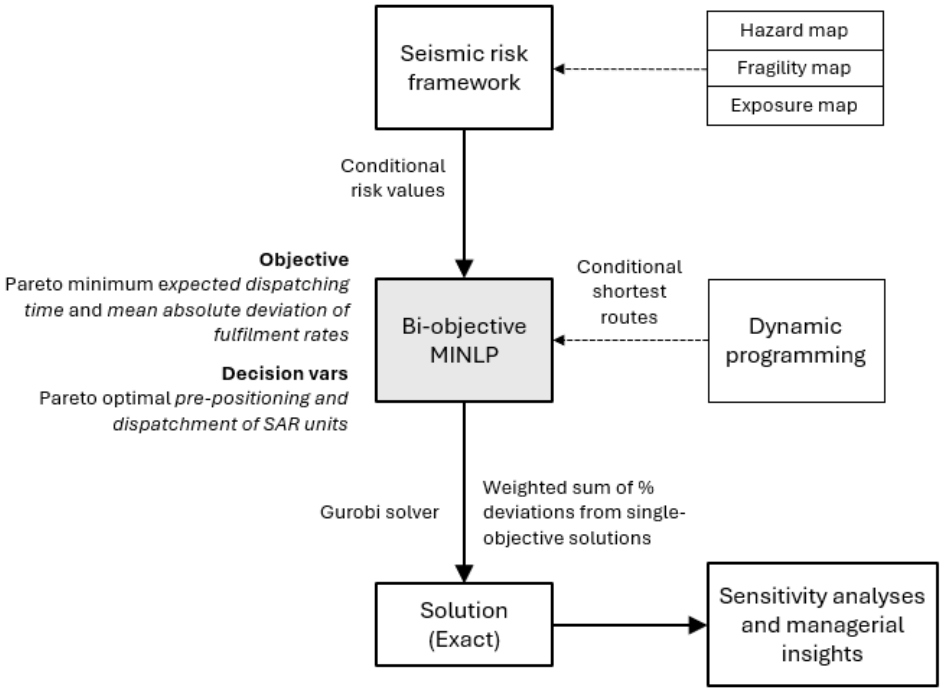

Figure 2. Methodology flowchart

Mathematical model

Model assumptions, sets and indices

Model assumptions that are made to avoid some undesired complexities can be stated as follows:

i. Each city will have at most one earthquake over the planning period,
ii. Earthquakes are independent among fault zones, i.e., they will not happen around the same time,
iii. A break can occur at any segment of a fault zone with even probability,
iv. Each city can only be in a single fault zone,

v. The Impact of an earthquake on a city is homogeneous,
vi. Distribution of the residential property stock in a city is homogeneous,
vii. Residential properties have an equal number of independent units each with an equal number of residents,
viii. SAR facilities and units are not affected by the earthquake,
ix. There is no setup time or minimum batch size for SAR units to mobilize.

The sets, indices and parameters related to the model are given in Table 3 and Table 4.

Table 3. Sets and indices

i :	Index of vertical coordinate ($i \in \mathcal{I}$ where $\mathcal{I} = \{1, 2, \dots, I\}$)
j :	Index of horizontal coordinate ($j \in \mathcal{J}$ where $\mathcal{J} = \{1, 2, \dots, J\}$)
f :	Index of facilities ($f \in \mathcal{F}$ where $\mathcal{F} = \{f_1, f_2, \dots\}$)
c :	Index of cities ($c \in \mathcal{C}$ where $\mathcal{C} = \{c_1, c_2, \dots\}$)
k :	Index of equipment types ($k \in \mathcal{K}$ where $\mathcal{K} = \{k_1, k_2, \dots\}$)
s :	Index of spatial states of earthquake ($s \in \mathcal{S}$ where $\mathcal{S} = \{s_1, s_2, \dots\}$)
g :	Index of PGA states of an earthquake ($g \in \mathcal{G}$ where $\mathcal{G} = \{g_1, g_2, \dots\}$)
ξ_z :	Sets of fault zones ($z \in \mathcal{Z}$ where $\mathcal{Z} = \{1, 2, \dots, Z\}$) indicating cities in the fault zone

Table 4. Parameters

n_z	Number of cities located on fault zone ξ_z
n_F^k	Number of facilities allowed for SAR unit type k
Av_k	Number of available SAR units of type k
β_c	Current building stock in city c
α_k	The number of SAR unit type k needed for each collapsed building
v_k	Average velocity (in 100 mph) of SAR unit type k under normal conditions

Seismic risk framework

Let n_z be the number of cities on the fault zone z. Assuming that the fault zone can fail in any part of it with even probability, the hazard of city c on fault zone z for being the epicenter to a devastating earthquake with a demand parameter g can be defined as

$$EP_{cg} = I_{\{c \in \xi_z\}} \frac{p_{zg}}{n_z}, \quad \forall c \in \mathcal{C}, g \in \mathcal{G}, \tag{1}$$

where p_{zg} is the probability of fault zone z being activated and causing a PGA of g. However, any city c will also be contingent on other cities geographically, which means that the hazard of an earthquake in any city s will also add to the total hazard of city c by a factor relative to the distance between them. We define the contingency between any two cities c and s in terms of their proximity and using an arbitrary function of the Euclidean distance d_{cs} as follows:

$$Co_{cs} = \frac{1}{2^{d_{cs}}}, \quad \forall c \in \mathcal{C}, s \in \mathcal{S}. \tag{2}$$

Note that the choice of Co_{cs} is not our primary concern and the framework can accommodate any reasonable function. Further discussion on the relation between PGA and distance can be found in [32] and the references therein. To illustrate; if the distance between two (not necessarily adjacent

cities) is 200 miles, then an earthquake of demand parameter g in city s is assumed to be felt as an earthquake of size $0.25g$ in city c. In other words, the hazard of city s being epicenter to an earthquake of size g will contribute to the total hazard in city c for an earthquake of the same size by 25%. The hazard in city c for being affected from an earthquake of size g in city s can then be written as

$$H_{csg} = Co_{cs} EP_{sg}, \quad \forall c \in \mathcal{C}, s \in \mathcal{S}, g \in \mathcal{G}. \tag{3}$$

Note that (3) boils down to EP_{cg} for any city that hosts the eartquake. Integrating over all scenarios, we can find the cumulative hazard in city c as

$$H_{cg} = \sum_{s} H_{csg} = \sum_{s} Co_{cs} EP_{sg} = EP_{cg} + \sum_{s \neq c} Co_{cs} EP_{sg}, \quad \forall c \in \mathcal{C}, s \in \mathcal{S}, g \in \mathcal{G}. \tag{4}$$

Therefore, the cumulative hazard of city c is the probability that city c will be the epicenter of the next devastating earthquake, plus the sum of the same probabilities for other cities in $\mathcal{C}$ adjusted by a factor of geographical contingency.

As stated previously, the level of damage from an earthquake is determined collectively by its hazard together with the vulnerability of infrastructure as well as exposure of property stock. Given an earthquake of parameter g occurs in city c, the probabilistic vulnerability (i.e., conditional probability that the building stock in city c will exceed the *complete damage* or *collapse* threshold d_0) is determined by a fragility curve [33] and can be stated as

$$VP_{cg} = P_c(D > d_0 | G = g), \quad \forall c \in \mathcal{C}, g \in \mathcal{G}. \tag{5}$$

Therefore, given the building stock in city c is S_c, the expected number of buildings in city c reaching the complete damage state (i.e., collapse) given a devastating earthquake occurs can be computed as

$$V_{cg} = VP_{cg} S_c, \quad \forall c \in \mathcal{C}, g \in \mathcal{G}, \tag{6}$$

where, again, the conditional probability of collapse given the earthquake demand parameter g, V_{cg}, is recovered from the vulnerability curve that is specific to city c. Figure 3 illustrates sample curves which are constructed from log-normal CDFs with arbitrary μ values ranging from 0 to 1, and $\sigma = 0.5$. A discussion of the calibration of these curves to real earthquake data is beyond the scope of our work and can be found in [33] or [34]. Note that the fragility curves depicted here reflect varying vulnerability levels only for a single damage state, i.e., complete damage, which will be our focus in this study.[2]

Therefore, the risk of city c from a disaster due to an earthquake of size g in city s, that is, the expected number of buildings in city c reaching the total damage state, can be expressed as

$$R_{csg} = H_{csg} V_{cg}, \quad \forall c \in \mathcal{C}, s \in \mathcal{S}, g \in \mathcal{G}. \tag{7}$$

Summing over all possible size-location scenarios, we state the overall risk from an earthquake

2 In general, fragility curves are used to depict the conditional probability of exceeding certain damage levels for a given vulnerability level.

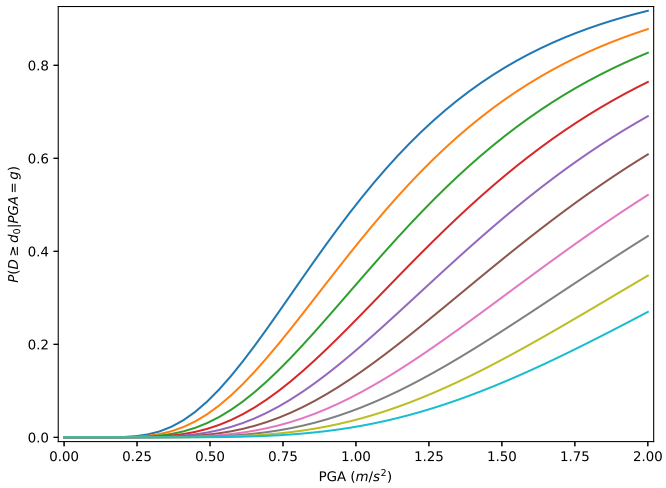

Figure 3. Probabilistic vulnerability curves (only the total damage state)

disaster in city c as

$$R_c = \sum_{s,g} R_{csg}, \quad \forall c \in \mathcal{C}. \tag{8}$$

Note that the risk values already incorporate the contingencies through the hazard values H. Given the seismic risk framework above, the expected demand of city c for SAR unit type k can be determined by the equation

$$\mathbb{E}\left[DM_{ck}\right] = \alpha_k R_c, \quad \forall c \in \mathcal{C}, k \in \mathcal{K}. \tag{9}$$

Since devastating earthquakes are considered as low-probability events (although with extreme conditional damage), one challenging task for the policymakers and relevant authorities is to determine the appropriate number of SAR units to keep ready because it is not rational for governments to ensure the availability of SAR units in an anticipation of the worst-case scenario (*vulnerability-based approach*) by setting

$$Av_k = \max_{s,g} \left\{ \alpha_k \sum_c \left(\frac{H_{csg}}{EP_{sg}} \right) V_{cg} \right\} = \max_{s,g} \left\{ \alpha_k \sum_c Co_{sc} V_{cg} \right\}, \quad \forall k \in \mathcal{K}. \tag{10}$$

On the contrary, taking a solely *risk-based approach* such that

$$Av_k = \alpha_k \sum_c R_c = \sum_c \mathbb{E}\left[DM_{ck}\right] = \mathbb{E}\left[DM_k\right], \quad \forall k \in \mathcal{K}, \tag{11}$$

would again be unrealistic as it will overlook the devastating conditional impact of severe earthquakes. In this paper, acknowledging the fact that predicting the size and/or location of an earthquake is much more difficult than predicting whether or not an earthquake will occur, we suggest that countries with high risks of earthquake can take a *conditional-risk-based approach* by assuming that there will be definitely an earthquake and basing their provision policies on the

conditional risk of an earthquake (i.e., given one of the cities becomes an epicenter with certainty):

$$\begin{aligned} Av_k = \mathbb{E}\left[DM_k|EP\right] &= \alpha_k \frac{\sum_c R_c}{\sum_{s,g} EP_{sg}} \\ &= \alpha_k \frac{\sum_{c,s,g} Co_{cs} EP_{sg} V_{cg}}{\sum_{s,g} EP_{sg}} = \alpha_k \sum_{c,s,g} Co_{cs} V_{cg} EP_{sg|EP}, \quad \forall k \in \mathcal{K}, \end{aligned}$$

where we introduced the conditional probability of city s being an epicenter to an earthquake of size g (given there is an earthquake) as

$$EP_{sg|EP} := \frac{EP_{sg}}{EP}, \quad \forall s \in \mathcal{S}, g \in \mathcal{G}, \tag{12}$$

with $EP = \sum_{s,g} EP_{sg}$. To summarize the three approaches,

i. *Vulnerability-based approach:* the worst-case scenario will happen with probability one.
ii. *Risk-based approach:* whether, where and at which size an earthquake will occur should be handled as an expected value.
iii. *Conditional-risk-based approach:* an earthquake will definitely happen, but we don't know where it will happen and at which size.

Vulnerability-adjusted fastest routes via RL: a DP approach

As an input to the mathematical optimization model to be discussed in Section 3, we also recover the fastest route between any two cities on the grid that takes into account accessibility during an earthquake using a DP approach. The explicit enumeration approach offers a relatively poor runtime performance on larger grids (e.g., it can take long hours to enumerate all paths on a 5x5 grid).

Given an earthquake of size g occurs in city s, the vulnerability-adjusted travel time of SAR unit type k between two adjacent cities c and c' is introduced as

$$\tilde{T}_{cc'ksg} = \frac{d_{cc'}}{v_k \left(1 - \frac{H_{csg} VP_{cg} + H_{c'sg} VP_{c'g}}{2}\right)} = \frac{d_{cc'}}{\tilde{v}_{cc'ksg}}, \quad \forall c, c' \in \mathcal{C}, k \in \mathcal{K}, s \in \mathcal{S}, g \in \mathcal{G}, \tag{13}$$

where $\tilde{v}_{cc'ksg}$ can be considered as the vulnerability-adjusted speed of unit type k between cities c and c' should there be an earthquake of size g in city s. It is obvious from Eq. (13) that if the probabilistic vulnerabilities of any pairs of cities (c, c') get closer to 1, then $\tilde{v}_{cc'ksg}$ will get close to 0, meaning that the route will be unusable.

We formulate the fastest route problem using the DP approach [35]. A policy π is the probabilities assigned to a certain set of actions $a \in \mathcal{A}$ (moves on the grid map in our case) for each state $c \in \mathcal{C}$. In particular, $\pi_{sg}(a|c)$ is the probability that the SAR entity will choose to make one of the eight possible moves ($\uparrow \nearrow \rightarrow \searrow \downarrow \swarrow \leftarrow \nwarrow$) given it is currently in city c. The value of an action a in city c under policy π (or the city-action value), denoted by $v^\pi(a|c)$, is determined by the sum of the immediate reward from transitioning to city c', denoted by $r(c'|c)$, and the continuation value $v^\pi(c')$

$$v^\pi_{sg}(c, a) = \sum_{c'} p(c'|c, a) \left(r_{sg}(c'|c) + v^\pi_{sg}(c')\right), \quad \forall s \in \mathcal{S}, g \in \mathcal{G}, \tag{14}$$

where $p(c'|c,a)$ is the probability of ending up in city c' by taking move a in city c (which is obviously 1 for the city in the direction of the move and 0 for others in our case). We set $r_{sg}(c'|c) = -\tilde{T}_{cc'ksg}$ depending on the equipment type k. Integrating (14) over all possible actions (each with appropriate probabilities $\pi(a|c)$ yields the city value function

$$v^{\pi}_{sg}(c) = \sum_{c'} p(c'|c) \left(r_{sg}(c'|c) + v^{\pi}_{sg}(c') \right), \quad \forall s \in \mathcal{S}, g \in \mathcal{G}, \tag{15}$$

where $p(c'|c) = \sum_{a \in \mathcal{A}} p(c'|c,a)\pi_{sg}(a|c)$. The optimal policy is then the one that maximizes the value of being in each city:

$$\pi^{*}_{sg} = \arg\max_{\pi} v^{\pi}_{sg}(c), \quad \forall c \in \mathcal{C}, s \in \mathcal{S}, g \in \mathcal{G}. \tag{16}$$

The search for π^{*}_{sg} involves two steps, namely, policy evaluation and policy iteration (improvement). Evaluation of an arbitrary policy is a recursive operation that runs until the value of $v_{\pi}(c)$ stabilizes across all cities. At each step, the value of $v^{\pi}(c)^{sg}$ is calculated by evaluating all possible actions for all cities through $v^{\pi}_{sg}(c,a)$. At policy iteration step, the policy is updated based on the re-calculated values of $v^{\pi}_{sg}(c)$ and $v^{\pi}_{sg}(c,a)$, $\forall c \in \mathcal{C}, a \in \mathcal{A}$.

As an example, the calculated values of the city value function as well as the corresponding optimal routes and travel times on a 4x4 grid for various endpoints, SAR unit types, scenarios and earthquake sizes are shown in Figure 4.

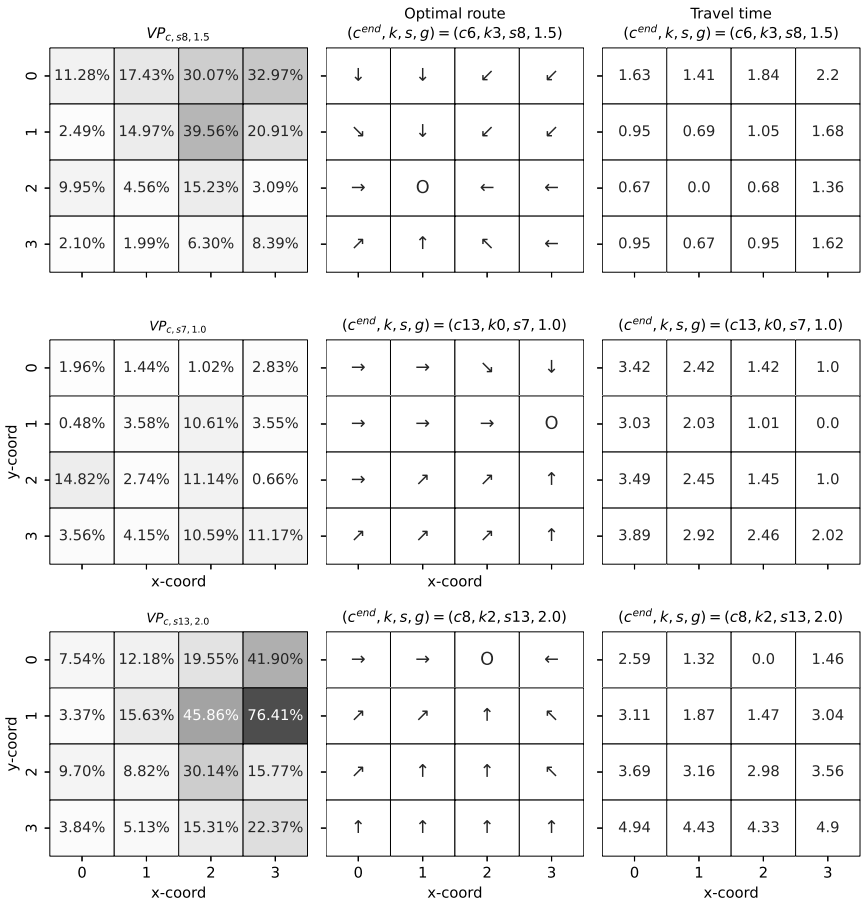

Figure 4. Percentage vulnerabilities (left), optimal routes (middle) and shortest travel times (right) on a 4x4 grid for different end-points and values of k, s, g

MINLP model variables, objectives and constraints

Decision and non-decision variables of the MINLP model and their explanations are provided in Table 5-Table 6.

Table 5. Decision variables defined in the MINLP model

$Z_{fk} \in \{0,1\}$	whether a facility f for SAR unit type k is established or not
$X_{fk} \in \mathbb{Z}^+$	amount of SAR unit type k to be allocated to facility f
$Y_{fcksg} \in \mathbb{Z}^+$	amount of SAR unit type k to be dispatched from facility f to city c in an earthquake of size g in city s

Table 6. Non-decision variables defined in the MINLP model

T_{ksg}	average dispatch time of SAR unit type k in an earthquake of size g in city s
T_{sg}^{max}	maximum average dispatch time across SAR unit types in an earthquake of size g in city s
T^{max}	Expected maximum average dispatch time
$Fulfill_{cksg} \in [0,1]$	proportion of demand by city c for SAR unit type k fulfilled given an earthquake of size g occurs in city s
$Fulfill_{ck} \in [0,1]$	expected proportion of demand by city c for SAR unit type k fulfilled
$Fulfill_{ksg} \in [0,1]$	proportion of demand for SAR unit type k fulfilled given an earthquake of size g occurs in city s
$Fulfill_{k} \in [0,1]$	expected proportion of demand for SAR unit type k fulfilled

Our two main objectives in this model is to minimize (i) the expected upper bound for the average dispatch time of SAR units taking into account all size-location scenarios, and (ii) the expected mean absolute deviation across fulfillment rates of cities. This will also help us minimize preventable humanitarian losses, as the survival rate is generally considered to be a decreasing function of time. To this end, we define the average time it takes to dispatch SAR unit type k under any scenario as the vulnerability-adjusted dispatch times between all facility-city pairs, $\tilde{T}_{fcksg}$, weighted by the percentage of flow:

$$T_{ksg} = \sum_{f,c} \tilde{T}_{fcksg} \frac{Y_{fcksg}}{\sum_{f,c} Y_{fcksg}}, \quad \forall k \in \mathcal{K}, s \in \mathcal{S}, g \in \mathcal{G}. \tag{17}$$

So, on average, all demand for SAR unit type k will have arrived at earthquake sites in T_{ksg} hours, should there be any earthquake of size g in city s. Since we assume that SAR units are interdependent (e.g., rescue teams on excavators, excavators on ambulances, ambulances on rescue teams), our aim is the minimize, in each scenario, the maximum of the average times across all cities for equipment type k, which is defined as

$$T_{sg}^{max} = \max\left\{T_{ksg} : k \in \mathcal{K}\right\}, \quad \forall s \in \mathcal{S}, g \in \mathcal{G}. \tag{18}$$

Expected maximum dispatch time is then the average of the maximum dispatch times T_{sg}^{max} weighted by the possibility of a given scenario:

$$T^{max} = \sum_{s,g} T_{sg}^{max} EP_{sg|EP}. \tag{19}$$

Accordingly, we can state our first objective as

$$\min \quad \theta_1 = T^{max}. \tag{20}$$

Our second objective will ensure the fair distribution of SAR assets by minimizing the mean absolute deviation of fulfillment rate for each city from the average fulfillment rate under each size-location scenario. The rate of fulfillment of demand from each city for SAR unit type k under scenario (s, g) is given by

$$Fulfill_{cksg} = \frac{\sum_f Y_{fcksg}}{DM_{cksg}}, \quad \forall c \in \mathcal{C}, k \in \mathcal{K}, s \in \mathcal{S}, g \in \mathcal{G}, \tag{21}$$

fulfillment of demand from each city for SAR unit type k is then the average of $Fulfill_{cksg}$ values weighted by the conditional probability of each scenario:

$$Fulfill_{ck} = \sum_{s,g} Fulfill_{cksg} EP_{sg|EP}, \quad \forall c \in \mathcal{C}, \forall k \in \mathcal{K}. \tag{22}$$

Similary, fulfillment of demand for SAR unit type k, both under each scenario and on average, can be expressed as

$$Fulfill_{ksg} = \frac{\sum_{f,c} Y_{fcksg}}{\sum_c DM_{cksg}}, \quad \forall k \in \mathcal{K}, s \in \mathcal{S}, g \in \mathcal{G}, \tag{23}$$

$$Fulfill_{k} = \sum_{s,g} Fulfill_{ksg} EP_{sg|EP}, \quad \forall k \in \mathcal{K}. \tag{24}$$

We then state mean absolute deviation for each size-location scenario and expected mean absolute deviation as

$$Fulfill^{\text{dev}}_{ksg} = \frac{\sum_c \left| Fulfill_{cksg} - Fulfill_{ksg} \right|}{|\mathcal{C}|)}, \quad \forall k \in \mathcal{K}, s \in \mathcal{S}, g \in \mathcal{G}, \tag{25}$$

and

$$Fulfill^{\text{dev}}_{k} = \sum_{s,g} Fulfill^{\text{dev}}_{ksg} EP_{sg|EP}, \quad \forall k \in \mathcal{K}, \tag{26}$$

respectively. Our second objective is therefore

$$\min \quad \theta_2 = Fulfill^{\text{dev}}_{k_0sg}. \tag{27}$$

In Eq. (27), we were able to change k to k_0 (i.e., SAR unit type 0) because availability of SAR units, and deployment to cities under each scenario, namely, Av_k and Y_{fcksg}, are proportional among SAR unit types (recall the *interdependence* argument).

On the other hand, we deal with the bi-objectiveness of the MINLP model by applying the weighted sum over the deviations of objectives given in Eq. (20) and Eq. (27) from their respective

best possible values, scaled by the difference between their respective best and worst values $\underline{\theta}$ and $\overline{\theta}$:

$$\min \quad \theta = w\left(\frac{\theta_1 - \underline{\theta}_1}{\overline{\theta}_1 - \underline{\theta}_1}\right) + (1-w)\left(\frac{\theta_2 - \underline{\theta}_2}{\overline{\theta}_2 - \underline{\theta}_2}\right). \tag{28}$$

Before implementing the objective (28), the model is first solved as single-objective for (20) to obtain best and worst values for θ_1 and θ_2, respectively, and then for (27) to obtain the best and worst values for θ_2 and θ_1, again, respectively.

Having defined the decision variables and objective functions, we can now express the constraints of the model to be satisfied while achieving the objective (28). First, we require all $\bar{T}_{ksg}$ values to be less than or equal to their supremum T_{sg}^{max}:

$$T_{ksg} \leq T_{sg}^{max}, \quad \forall k \in \mathcal{K}, s \in \mathcal{S}, g \in \mathcal{G}. \tag{29}$$

The total number of facilities for each SAR unit type should not exceed the allowed quantity:

$$\sum_f Z_{fk} \leq n_F^k, \quad \forall k \in \mathcal{K}. \tag{30}$$

Furthermore, decision-makers need to make sure that all available equipment is allocated to the facilities and, if allocated, that the facility is established:

$$\sum_f X_{fk} = Av_k, \quad \forall k \in \mathcal{K}, \tag{31}$$

$$X_{fk} \leq MZ_{fk}, \quad \forall f \in \mathcal{F}, k \in \mathcal{K}, \tag{32}$$

where M is a sufficiently large number. Amount of dispatch from facilities to earthquake sites should not exceed the respective capacities of those facilities:

$$\sum_c Y_{fcksg} \leq Z_{fk}X_{fk}, \quad \forall f \in \mathcal{F}, k \in \mathcal{K}, s \in \mathcal{S}, g \in \mathcal{G}. \tag{33}$$

If the sum of equipment k allocated to facilities is less than or equal to the total demand under any scenario, then the total amount of dispatch to earthquake sites should be equal to the amount available (otherwise, it should be equal to the demand), namely,

$$\sum_f X_{fk} \geq \sum_c DM_{cksg} \Longrightarrow \sum_{f,c} Y_{fcksg} = \sum_c DM_{cksg}, \quad \forall k \in \mathcal{K}, s \in \mathcal{S}, g \in \mathcal{G},$$

and

$$\sum_{f \in \mathcal{F}} X_{fk} < \sum_{c \in \mathcal{C}} DM_{cksg} \Longrightarrow \sum_{f,c} Y_{fcksg} = \sum_f X_{fk}, \quad \forall k \in \mathcal{K}, s \in \mathcal{S}, g \in \mathcal{G}.$$

In other words, amount of total deployment of SAR unit type k under each scenario should be the

minimum among the available and demanded amount of SAR units of type k:

$$\sum_{f,c} Y_{fcksg} = \min \left\{ \sum_{f} X_{fk}, \sum_{c} DM_{cksg} \right\}, \quad \forall k \in \mathcal{K}, s \in \mathcal{S}, g \in \mathcal{G}. \tag{34}$$

We linearize Eq. (34) to improve runtime.[3]
Amount of SAR units dispatched to any city should not exceed its demand under any scenario:

$$\sum_{f} Y_{fcksg} \leq DM_{cksg}, \quad \forall c \in \mathcal{C}, k \in \mathcal{K}, s \in \mathcal{S}, g \in \mathcal{G}. \tag{35}$$

Finally, the deployment of SAR units should preserve proportionality since they are interdependent:

$$\sum_{f} Y_{fcksg} = \alpha_k \sum_{f} Y_{fck_0sg}, \quad \forall c \in \mathcal{C}, k \in \{\mathcal{K} \setminus k_0\}, s \in \mathcal{S}, g \in \mathcal{G}. \tag{36}$$

The allocation-dispatchment model described through Eqs. (28)-(36) is obviously non-linear, with the non-linearity arising from the two objectives, namely, due to the maximum function in Eq. (18) and ratio of decision variables in Eq. (27). The non-linearity in Eq. (18) is eliminated through constraint (29). Handling Eq. (27) requires transformation of model variables, which is not straightforward. A further non-linearity is imposed by Eq. (34), which is also substituted with linear constraints. The remaining non-linearity, coupled with large number of constraints and arbitrarily generated initial problem settings, manifests itself high computation times (see Section 5). The comprehensive model presented throughout this section will be applied to a hypothetical example in Section 4 where we will also present some analysis of results and policy insights.

4 A numerical example

The numerical example presented in this section aims to illustrate the seismic-risk-based resource allocation and dispatch framework through a minimal example but is flexible enough to extend to cover higher-dimensional scenarios. Figure 5 (panels *i-vi*) displays the main components of the

3 This is done by representing Eq. (34) by the following constraints and restrictions:

$$\begin{aligned}
\sum_{f} X_{fk} &\geq \sum_{c} DM_{cksg} + M(u_{ksg} - 1), && \forall k \in \mathcal{K}, s \in \mathcal{S}, g \in \mathcal{G}, \\
\sum_{c} DM_{cksg} + M(u_{ksg} - 1) \leq \sum_{f,c} Y_{fcksg} &\leq \sum_{c} DM_{cksg} + M(1 - u_{ksg}), && \forall k \in \mathcal{K}, s \in \mathcal{S}, g \in \mathcal{G}, \\
\sum_{f} X_{fk} + \epsilon &\leq \sum_{c} DM_{cksg} + M(1 - u'_{ksg}), && \forall k \in \mathcal{K}, s \in \mathcal{S}, g \in \mathcal{G}, \\
\sum_{f} X_{fk} + M(u'_{ksg} - 1) \leq \sum_{f,c} Y_{fcksg} &\leq \sum_{f} X_{fk} + M(1 - u'_{ksg}), && \forall k \in \mathcal{K}, s \in \mathcal{S}, g \in \mathcal{G}, \\
u_{ksg} + u'_{ksg} &= 1, && \forall k \in \mathcal{K}, s \in \mathcal{S}, g \in \mathcal{G}, \\
u_{ksg}, u'_{ksg} &\in \{0, 1\}, && \forall k \in \mathcal{K}, s \in \mathcal{S}, g \in \mathcal{G}.
\end{aligned}$$

seismic hazard framework based on expectations.[4] There are 4 fault zones in the map (*i-ii*) and these zones can trigger earthquakes with assigned probabilities (*iii*). Together with contingencies, these probabilities constitute the overall hazard of earthquake (*iv*). Combined with percentage vulnerabilities for different demand parameters derived from fragility curves given in Figure 3, the level of exposure determines the risk of a disaster (*vi*).

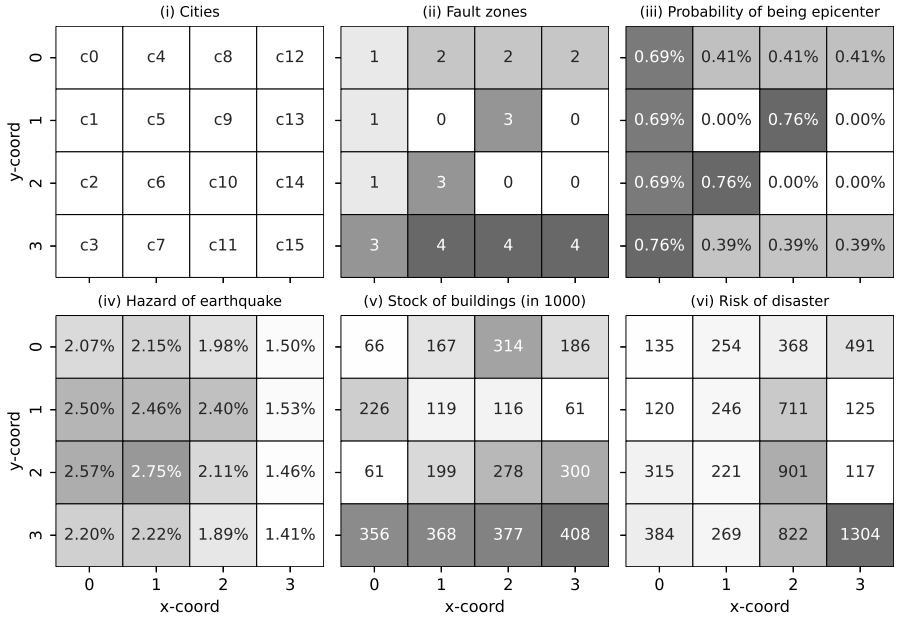

Figure 5. Main components of the seismic hazard framework

Figure 6, on the other hand, demonstrates a realized scenario, namely, $s = s_2$ and $g = 2.0$ (that is, an earthquake of size 2.0 occurs in city 2). Now, since the hazard is realized, the hazard map turns into a realized hazard map where the impact propagates based on distances. From the realized risk map (*iv*), we can see how many collapses this scenario can cause in different cities based on their vulnerabilities (*ii*) and building stocks (*iii*).

The optimization model presented in Section 3 is implemented using Gurobi solver on a workstation with an Intel(R) Xeon(R) W-2245 CPU @ 3.90GHz processor with a 64.0GB installed RAM. Figure 7 displays the optimal allocation of equipment type k_0 for $n_F = 7$ (top left), as well as conditional risk levels (top right), average dispatch times (bottom left) and fulfillment rates (bottom right) for a single scenario (i.e., $s = s_6$, $g = 1.0$) where we also arbitrarily set $w = 0.5$. Figure 8 illustrates the deployment plan for the sample scenario. The overall fulfillment rate for k_0 under this allocation plan is calculated as 83.4%. Expected fulfillment rates across cities for $n_F^k = 7\ \forall k$ are depicted in Figure 9 where we observe a small variation (thanks to our second objective function θ_2). For $w = 0.5$ and $n_F^k = 7\ \forall k$, the optimal values of θ_1 and θ_2 are calculated as 0.8281 hours and 0.025%. We present results for some more scenarios in Table 7.

We extend these results through a number sensitivity analyses based on two key model parameters, namely, the maximum number of facilities for SAR unit type k, n_F^k, and the objective weight factor, w. Figure 10 displays the sensitivity of each objective function value with respect to these two parameters whereas Table 7 presents these results in numerical format. As expected, optimal value

4 For reproducibility, we use seed 51 in Python's NumPy library, which is chosen as it yielded a lower computation time.

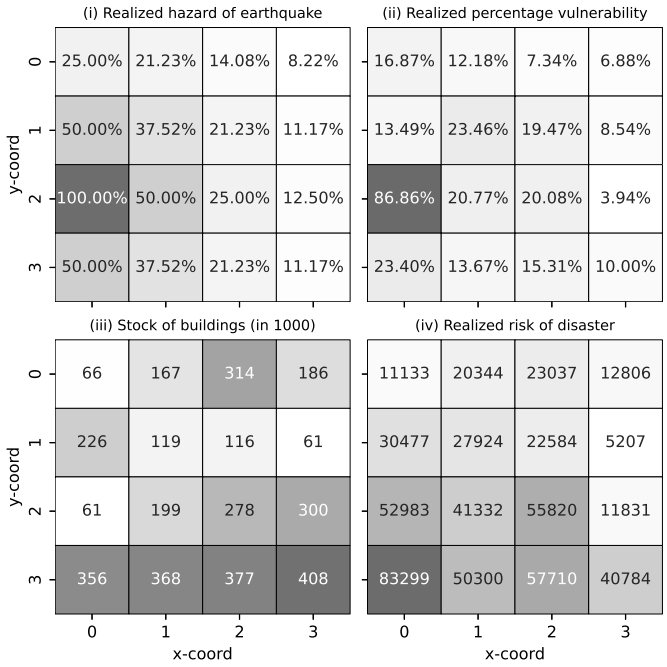

Figure 6. Main components of the seismic hazard framework (a realized scenario with $s = s_2$ and $g = 2.0$)

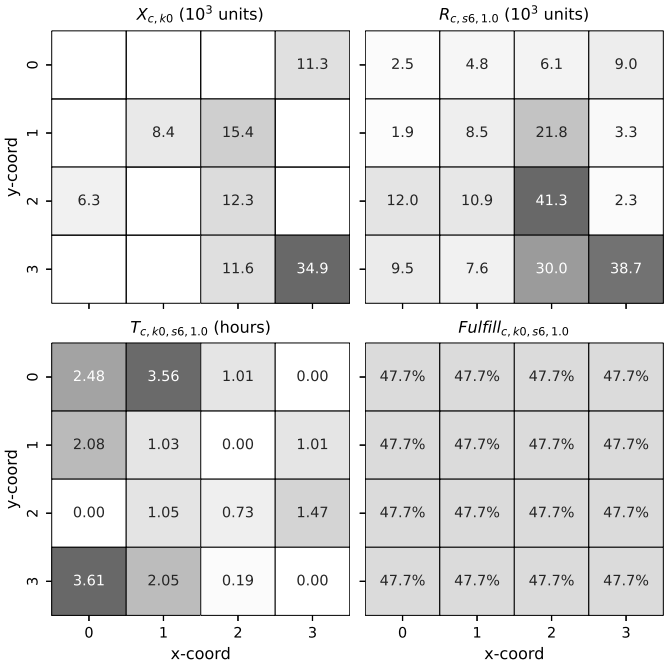

Figure 7. Optimal allocation of SAR unit type k_0 for $n_F = 7$ (top left), as well as realized risk (top right), average dispatch times (bottom left) and fulfillment rates (bottom right) for $s = s_6, g = 1.0$

of the expected maximum deployment time decreases with the number of allowed facilities (left). The impact of the latter on mean absolute deviation of fulfillment rates is somewhat reverse (mid). Increasing the number of facilities somehow worsens the optimal value of θ_2, leading to a higher deviation across fulfillment rates. As far as the main objective function θ is concerned (right), we can observe that the total percentage deviation from the two goals peaks at $(w, n_F) = (0.75, 6)$ with 6.98%. The sensitivity analyses can assist decision-makers in choosing the optimal number of facilities and devising an allocation-dispatchment plan. For example, if the primary focus is

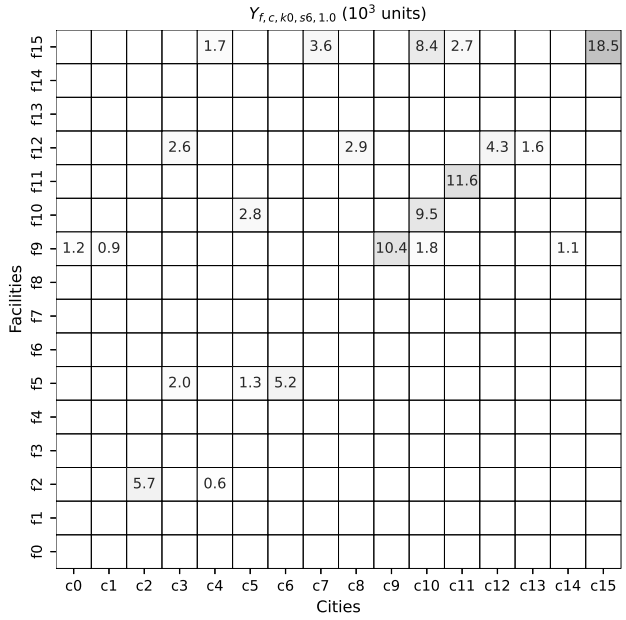

Figure 8. Optimal dispatching of SAR unit type k_0 for $n_F = 7$ and a single scenario ($s = s_6, g = 1.0$)

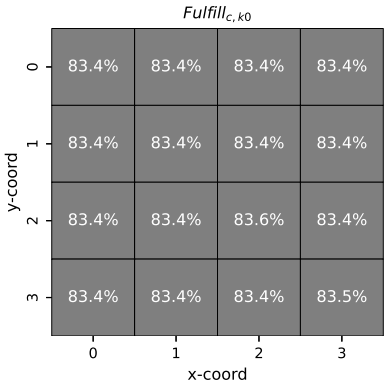

Figure 9. Expected fulfillment rate for SAR unit type k_0 and $n_F = 7$

on the speed of dispatchment, then the choice of $(w, n_F) = (1, 7)$ yields an expected maximum deployment time of as low as 0.3514 hours, although with an expected mean deviation of 10.94%. Or, if the policymakers are of the view that the deployment speed is three times as important as having an equitable deployment, namely, $(w, n_F) = (0.75, 7)$, then a 0.67% expected deviation can be achieved with an increase in expected maximum dispatch time to 0.6859 hours (again, Table 7).

5 Results and discussion

In real earthquake situations, survival rate is largely determined by the speed of intervention, whereas poor planning can result in the clustering of available resources in a subset of affected locations, resulting in an inequitable situation for victims. Recent big earthquakes, such as the two that struck 11 cities in southern Turkey in 2023, has shown that it is not the abundance of resources that matters for the well-functioning of disaster response but how these resources are pre-positioned and deployed.

Results from hypothetical examples (including the one presented in Section 4) indicate that the seismic-risk-based bi-objective MINLP model is feasible under various risk scenarios and can be

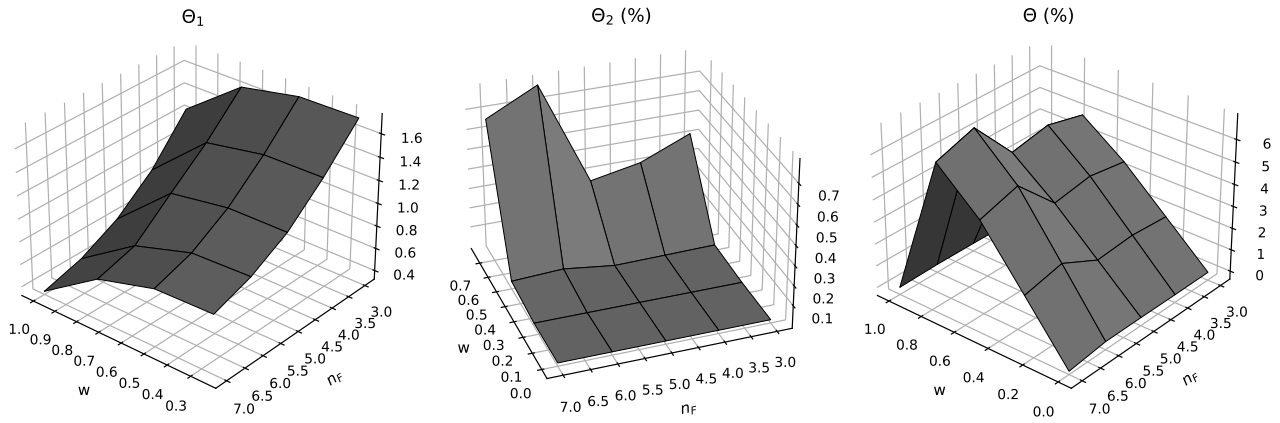

Figure 10. Sensitivity of objective values $\theta, \theta_1, \theta_2$ with respect to n_F and w

Table 7. Optimal values for various w and n_F

		n_F				
w		3	4	5	6	7
0	θ_1	8,0135	6,7374	7,5972	7,0617	8,0135
	θ_2	0,00%	0,00%	0,00%	0,00%	0,00%
	θ	-0,01%	-0,01%	0,00%	-0,01%	-0,23%
0.25	θ_1	1,7402	1,4128	1,1352	0,9547	0,8411
	θ_2	0,00%	0,00%	0,00%	0,00%	0,00%
	θ	1,75%	1,88%	1,75%	2,63%	2,25%
0.5	θ_1	1,7333	1,4084	1,1327	0,9363	0,8281
	θ_2	0,01%	0,01%	0,01%	0,04%	0,03%
	θ	3,51%	3,78%	3,50%	5,23%	4,70%
0.75	θ_1	1,6320	1,3171	1,0527	0,7811	0,6859
	θ_2	0,43%	0,32%	0,27%	0,80%	0,67%
	θ	4,91%	5,33%	5,00%	6,98%	6,40%
1	θ_1	1,2527	0,8765	0,6148	0,4470	0,3514
	θ_2	12,79%	12,24%	11,80%	11,30%	10,94%
	θ	-0,19%	-0,05%	-0,02%	-0,01%	-0,04%

applied to make allocation-deployment decisions when the size and location of earthquakes are uncertain. With equal weights for two objectives, the model achieves a total of 3.5% deviation from single-objective solutions (more precisely, the difference between negative and positive ideal solutions) with an expected maximum dispatch time of 1.1327 hours and expected mean absolute deviation of 0.01%. Sensitivity analysis results, on the other hand, verify that the model behaves in accordance with our expectations as far as the changes in the number of allowed facilities and weights of individual objectives are concerned.

Yet, the ability of the model to adapt to different problem sizes is hindered by rapidly growing computational complexity and runtimes, which is illustrated in Table 8.

Table 8. DP and MINLP model runtimes for different problem sizes (random seed: 51)

Grid size	DP runtime (sec, per scenario)	DP runtime (sec, total)	Number of constraints	MINLP model runtime (sec)
3x3	0.13	4.7	9,417	6.4
4x4	0.90	57.6	27,029	350
5x5	4.09	409	62,921	5,469

6 Conclusion

This paper sought to develop an integrated and versatile framework for SAR unit pre-allocation and deployment, incorporating a seismic risk component similar to the one discussed in [10] into a MINLP model to minimize the dispatch time of SAR units and deviation between response rates. The features of the model introduced in this paper are by no means exhaustive. In particular, the seismic risk framework presented here offers a simple yet flexible approach that can be adapted to various problem sizes and hazard maps, as well as vulnerability and exposure profiles. The bi-objective MINLP model then linked the seismic hazard framework with the resource allocation and dispatchment problem where the vulnerability-(or conditional-risk-)adjusted shortest routes were recovered from the computationally efficient DP algorithm. The bi-objectiveness of the problem under study is handled through derivation of a pareto optimality surface for the weighted sum of percentage deviations from the individual objectives.
The model's efficiency, however, is mainly limited by the runtime that is exponentially increasing with the problem size. Moreover, lack of a real case study might be concealing the potential hassles in representing real maps as simple grids (e.g., a single node might include multiple cities or vice versa). Besides, various assumptions made in the study (e.g., contingency structure assumed in Eq. (2), uniform distribution of property stock, even probability for any part of a fault line being activated, etc.) might render the model difficult to apply in real life. Thus, as an outlook, acquiring real seismic hazard and exposure data for model validation purposes, working with fragility curves calibrated to observed vulnerabilities, a critical review of the assumptions made through expert solicitations, integrating meta-heuristics for improving computational efficiency for larger problem sizes can further enhance the applicability of the model to real-life situations.

Declarations

Use of AI tools

The author declares that he has not used Artificial Intelligence (AI) tools in the creation of this article.

Data availability statement

There are no external data associated with the manuscript.

Ethical approval (optional)

The author states that this research complies with ethical standards. This research does not involve either human participants or animals.

Consent for publication

Not applicable

Conflicts of interest

The author declares that he has no conflict of interest.

Funding

No funding was received for this research.

Author's contributions

The author has written, read and agreed to the published version of the manuscript.

Acknowledgements

Not applicable

References

[1] World Health Organization (WHO), Earthquakes, (2024). https://www.who.int/health-topics/earthquakes#tab=tab_1

[2] Schweier, C. Geometry based estimation of trapped victims after earthquakes. In Proceedings *International Symposium on Strong Vrancea Earthquakes and Risk Mitigation*, pp. 4-6, Bucharest, Romania, (2007, October).

[3] Weber, M. Rural areas may suffer disproportionately in quakes. *Temblor,* (2020). [CrossRef]

[4] Noji, E.K. The public health consequences of disasters. *Prehospital and Disaster Medicine,* 15(4), 21-31, (2000). [CrossRef]

[5] Kunkle, R. Medical care of entrapped patients in confined spaces. In Proceedings, *International Workshop on Earthquake Injury Epidemiology: Implications for Mitigation and Response*, pp. 338-344, Baltimore, Maryland, USA, (1989, July). [CrossRef]

[6] Ahmadi, G., Tavakkoli-Moghaddam, R., Baboli, A. and Najafi, M. A decision support model for robust allocation and routing of search and rescue resources after earthquake: a case study. *Operational Research,* 22, 1039–1081, (2022). [CrossRef]

[7] Klibi, W., Ichoua, S. and Martel, A. Prepositioning emergency supplies to support disaster relief: a case study using stochastic programming. *INFOR: Information Systems and Operational Research,* 56(1), 50-81, (2018). [CrossRef]

[8] Chiu, Y.Y., Omura, H., Chen, H.E. and Chen, S.C. Indicators for post-disaster search and rescue efficiency developed using progressive death tolls. *Sustainability,* 12(19), 8262, (2020). [CrossRef]

[9] Condeixa, L.D., Leiras, A., Oliveira, F. and De Brito Jr, I. Disaster relief supply pre-positioning optimization: A risk analysis via shortage mitigation. *International Journal of Disaster Risk Reduction,* 25, 238-247, (2017). [CrossRef]

[10] Arnette, A.N. and Zobel, C.W. A risk-based approach to improving disaster relief asset pre-positioning. *Production and Operations Management,* 28(2), 457-478, (2019). [CrossRef]

[11] Caunhye, A.M., Nie, X. and Pokharel, S. Optimization models in emergency logistics: A literature review. *Socio-Economic Planning Sciences,* 46(1), 4-13, (2012). [CrossRef]

[12] Kaveh, A., Javadi, S.M. and Moghanni, R.M. Emergency management systems after disastrous earthquakes using optimization methods: A comprehensive review. *Advances in Engineering Software,* 149, 102885, (2020). [CrossRef]

[13] Boonmee, C., Arimura, M. and Asada, T. Facility location optimization model for emergency humanitarian logistics. *International Journal of Disaster Risk Reduction,* 24, 485-498, (2017). [CrossRef]

[14] Chen, L. and Miller-Hooks, E. Optimal team deployment in urban search and rescue. *Transportation Research Part B: Methodological,* 46(8), 984-999, (2012). [CrossRef]

[15] Döyen, A., Aras, N. and Barbarosoğlu, G. A two-echelon stochastic facility location model for humanitarian relief logistics. *Optimization Letters,* 6, 1123-1145, (2012). [CrossRef]

[16] Zhang, L., Liu, T. and Huang, J. Relief equipment layout model for natural disaster with uncertain demands. In Proceedings, *2009 International Conference on Management and Service*

Science, pp. 1-4, Beijing, China, (2009, September). [CrossRef]

[17] Ghasemi, P., Khalili-Damghani, K., Hafezalkotob, A. and Raissi, S. Stochastic optimization model for distribution and evacuation planning (A case study of Tehran earthquake). *Socio-Economic Planning Sciences*, 71, 100745, (2020). [CrossRef]

[18] Mohammadi, R., Ghomi, S.F. and Jolai, F. Prepositioning emergency earthquake response supplies: A new multi-objective particle swarm optimization algorithm. *Applied Mathematical Modelling*, 40(9-10), 5183-5199, (2016). [CrossRef]

[19] Paul, J.A. and MacDonald, L. Location and capacity allocations decisions to mitigate the impacts of unexpected disasters. *European Journal of Operational Research*, 251(1), 252-263, (2016). [CrossRef]

[20] Zhang, S., Guo, H., Zhu, K., Yu, S. and Li, J. Multistage assignment optimization for emergency rescue teams in the disaster chain. *Knowledge-Based Systems*, 137, 123-137, (2017). [CrossRef]

[21] Vahdani, B., Veysmoradi, D., Shekari, N. and Mousavi, S.M. Multi-objective, multi-period location-routing model to distribute relief after earthquake by considering emergency roadway repair. *Neural Computing and Applications*, 30, 835-854, (2018). [CrossRef]

[22] Khayal, D., Pradhananga, R., Pokharel, S. and Mutlu, F. A model for planning locations of temporary distribution facilities for emergency response. *Socio-Economic Planning Sciences*, 52, 22-30, (2015). [CrossRef]

[23] Sebatli, A., Cavdur, F. and Kose-Kucuk, M. Determination of relief supplies demands and allocation of temporary disaster response facilities. *Transportation Research Procedia*, 22, 245-254, (2017). [CrossRef]

[24] Aghaie, S. and Karimi, B. Location-allocation-routing for emergency shelters based on geographical information system (ArcGIS) by NSGA-II (case study: Earthquake occurrence in Tehran (District-1)). *Socio-Economic Planning Sciences*, 84, 101420, (2022). [CrossRef]

[25] Tirkolaee, E.B., Aydın, N.S., Ranjbar-Bourani, M. and Weber, G.W. A robust bi-objective mathematical model for disaster rescue units allocation and scheduling with learning effect. *Computers & Industrial Engineering*, 149, 106790, (2020). [CrossRef]

[26] Wex, F., Schryen, G., Feuerriegel, S. and Neumann, D. Emergency response in natural disaster management: Allocation and scheduling of rescue units. *European Journal of Operational Research*, 235(3), 697-708, (2014). [CrossRef]

[27] Fiedrich, F., Gehbauer, F. and Rickers, U. Optimized resource allocation for emergency response after earthquake disasters. *Safety Science*, 35(1-3), 41-57, (2000). [CrossRef]

[28] Sharif, S.V., Moshfegh, P.H. and Kashani, H. Simulation modeling of operation and coordination of agencies involved in post-disaster response and recovery. *Reliability Engineering & System Safety*, 235, 109219, (2023). [CrossRef]

[29] Chen, W. and Zhang, L. An automated machine learning approach for earthquake casualty rate and economic loss prediction. *Reliability Engineering & System Safety*, 225, 108645, (2022). [CrossRef]

[30] Zhang, L. and Cui, N. Pre-positioning facility location and resource allocation in humanitarian relief operations considering deprivation costs. *Sustainability*, 13(8), 4141, (2021). [CrossRef]

[31] Edrisi, A. and Askari, M. Probabilistic budget allocation for improving efficiency of transportation networks in pre-and post-disaster phases. *International Journal of Disaster Risk Reduction*, 39, 101113, (2019). [CrossRef]

[32] Bommer, J.J., Stafford, P.J., Alarcón, J.E. and Akkar, S. The influence of magnitude range on empirical ground-motion prediction. *Bulletin of the Seismological Society of America*, 97(6), 2152-2170, (2007). [CrossRef]

[33] Menichini, G., Nistri, V., Boschi, S., Del Monte, E., Orlando, M. and Vignoli, A. Calibration of vulnerability and fragility curves from moderate intensity Italian earthquake damage data. *International Journal of Disaster Risk Reduction*, 67, 102676, (2022). [CrossRef]

[34] Lallemant, D., Kiremidjian, A. and Burton, H. Statistical procedures for developing earthquake damage fragility curves. *Earthquake Engineering & Structural Dynamics*, 44(9), 1373-1389, (2015). [CrossRef]

[35] Sutton, R.S. and Barto, A.G. *Reinforcement Learning: An Introduction*. MIT Press: USA, (2018).

Mathematical Modelling and Numerical Simulation with Applications (MMNSA)
(https://dergipark.org.tr/en/pub/mmnsa)

How to cite this article: Aydın, N.S. (2024). A seismic-risk-based bi-objective stochastic optimization framework for the pre-disaster allocation of earthquake search and rescue units. *Mathematical Modelling and Numerical Simulation with Applications*, 4(3), 370-394. https://doi.org/10.53391/mmnsa.1517843